Universitat de Girona

STUDY OF BOND BEHAVIOUR BETWEEN FRP REINFORCEMENT AND CONCRETE

Marta BAENA MUÑOZ

ISBN: 978-84-694-2484-1
Dipòsit legal: GI-281-2011
http://hdl.handle.net/10803/7771

Universitat de Girona

PhD Thesis

Study of bond behaviour between FRP reinforcement and concrete

Marta Baena Muñoz

2010

Universitat de Girona

PhD Thesis

Study of bond behaviour between FRP reinforcement and concrete

Marta Baena Muñoz

2010

Technology Doctorate Program

Advisors

Dr. Lluís Torres Llinàs
Universitat de Girona, Spain

Dr. Albert Turon Travesa
Universitat de Girona, Spain

A thesis submitted for the degree of Doctor of Philosophy by the University of Girona

To whom it might concern,

Dr. Lluís Torres Llinàs, Professor at the *Universitat de Girona* of the Department of *Enginyeria Mecànica i de la Construcció Industrial*, and Dr. Albert Turon Travesa, lecturer at the *Universitat de Girona* of the Department of *Enginyeria Mecànica i de la Construcció Industrial*,

CERTIFY that the study entitled *Study of bond behaviour between FRP reinforcement and concrete* has been carried out under their supervision by Marta Baena Muñoz to apply the doctoral degree with the European Mention,

Girona, October 2010,

Dr. Lluís Torres Llinàs
Universitat de Girona, Spain

Dr. Albert Turon Travesa
Universitat de Girona, Spain

A mi familia

Agraïments - Agradecimientos - Acknowledgements

Als directors de la tesi, el Dr. Lluís Torres Llinàs i el Dr. Albert Turon Travesa, per la seva continua motivació i tutela. La seva experiència, consells i contribucions han fet possible la realització d'aquesta tesi.

Many thanks to Professor Kypros Pilakoutas and Dr. Maurizio Guadagnini for having offered me the possibility to visit the Department of Civil and Structural Engineering at the University of Sheffield.

Agraïr l'ajuda i assistència tècnica durant el treball experimental al personal del laboratori. Gràcies Sergi O., Francesc M., Jordi V. i Sergi S.

Voldria també agraïr a tots els companys i amics del grup de recerca AMADE. Un agraïment especial a en Jordi Renart, en Marc Gascons, l'Emili González, en Pere Maimí, en Pep Vicens i l'Elio Pajares, que em van rebre des d'un bon principi fent-me sentir part d'un grup de fantàstiques persones. Agraïr especialment l'amistat i la bona predisposició per ajudar-me en els assajos de laboratori a la Cristina Miàs, la Irene Vilanova i la Cristina Barris. Juntes hem "patit" i compartit molts moments inoblidables. Gràcies també a la resta de companys, amb els que espero continuar passant bons moments, Xavier C., Joan Andreu M., Norbert B., Dani T., Josep C., Dani S., Jaume V., Takeichi K., Raúl C., Pere B., Lierni Z. i Javi B.

Thank you to the colleagues at the University of Sheffield with whom I shared three unforgettable months, specially to Andreea, Angela, Panos, Kyriacos and Harris.

Agradezco a mis padres José y Mª Luisa y a mi hermana Elena sus incesantes muestras de apoyo, ánimos y confianza en mi capacidad, en éste y cada uno de los proyectos que he afrontado y afrontaré. Gracias por vuestro amor incondicional.

Finalment, el meu més sincer agraïment a la persona que m'ha ofert tot el seu recolzament, comprensió i inacabable paciència. Gràcies Jaume.

Funds

The author of this work acknowledges the Department of Mechanical Engineering and Industrial Construction of the University of Girona for the support provided throughout the course of this work and the research group Analysis and Advanced Materials for Structural Design for incorporating the carrying out of this work and experimental tests in their research.

The period of doctorate studies comprised between May of 2007 and December of 2007 has been supported by the University of Girona through the research grant *BR07/10*. The period of research has been funded by the Comissionat per a Universitats i Recerca del Departament d'Innovació, Universitats i Empresa de la Generalitat de Catalunya, and by European Social Funds, under a research grant *FI 2008 - Formació de Personal Investigador*, starting in January of 2008 and finishing in December of 2010.

Also, the present work has been partially funded by the Spanish Government research projects BIA−2004 − 05253 and BIA−2007 − 60222.

Part of the work has been carried out during a stage at the University of Sheffield, under the grant for mobility: *BE-2008* (of the Comissionat per a Universitats i Recerca del Departament d'Innovació, Universitats i Empresa de la Generalitat de Catalunya).

Abstract

The use of Fibre Reinforced Polymers (FRP) as reinforcement in concrete structures is considered to be a possible alternative to steel in those situations where corrosion is present. However, because of their more flexible but brittle behaviour, when compared to that of steel, different behaviour is expected for Fibre Reinforced Polymer Reinforced Concrete Structures (FRPRCS) compared to Steel Reinforced Concrete (SRC) structures. Therefore, the full acceptance of FRP reinforcement in concrete construction is contingent on a complete study and comprehension of all aspects of their structural performance. Bond development is one of the basic aspects of structural behaviour, since the transmission of load from reinforcement to concrete relies on it. Therefore, the quality of bond has a prominent influence on crack formation and hence affects the spacing between cracks and the crack width.

This thesis investigates the bond behaviour between Fiber Reinforced Polymer (FRP) reinforcement and concrete. Two experimental programs were conducted. In the first program the role of the variables which affect the bond behaviour (rebar diameter, type of fibres, surface treatment and concrete strength) was studied with 88 pullout tests. It was concluded that the non-standardized FRP bars surface treatment plays an important role on the activation of the different bond mechanisms that exist. However, this surface influence is less pronounced at low concrete compressive strengths.

In the second program, GFRP RC members were tested in tension to study their cracking response. The results of the tests confirm the conservative nature of the approach assumed in ACI provisions. In contrast, the approach of modified constitutive equation for reinforcement with progressive reduction in stiffness beyond

cracking load (used in EC2 and MC90) was found to be capable enough to account for the differences of FRP reinforcement. However, although the dependence of crack spacing on the ratio of rebar diameter to effective reinforcement ratio was confirmed with experimental results, EC2 proposal for the additional dependence on the concrete cover does not seem directly applicable to RC tensile members. Additional notched ties were tested with internally strain gauged FRP bars. The instrumentation was proven to be an effective tool to analyze cracking behaviour and understand the evolution of crack pattern, as well as the stress redistribution that takes place after crack formation.

A numerical model was developed to simulate the cracking behaviour of RC tensile members. The model reliability was proven at two levels: local reinforcement strain distribution and RC tie deformability. Since the model was flexible enough to include any "user-defined" bond-slip law and variable materials' properties, a parametric study was conducted to analyze which are the variables that influence the cracking behaviour. The normalized concrete post-cracking tensile response of RC ties was found to be less sensitive to changes in concrete compressive strength. The reinforcement ratio and the ratio of the modulus of elasticity of the materials were found to be the key parameters that can affect the post-cracking tensile response of RC members.

Resumen

Debido a los problemas de corrosión existentes en estructuras de hormigón armadas con acero sometidas a ambientes agresivos, el uso de barras de materiales compuestos (en adelante FRP "Fiber Reinforced Polymer") puede ser una alternativa efectiva. Sin embargo, las estructuras de hormigón armadas con barras de FRP se comportan de manera distinta que los elementos armados con acero, debido a su menor módulo de elasticidad y a la ausencia de límite elástico y plastificación. Por ello, la plena aceptación de los materiales FRP en el mundo de la construcción está condicionada al estudio y comprensión de todos los aspectos involucrados en su comportamiento estructural. En este sentido, la adherencia es uno de los aspectos fundamentales del comportamiento estructural ya que la correcta transmisión de cargas del refuerzo al hormigón depende de ella. Es por ello que la calidad de la adherencia tiene una destacada influencia sobre la fisuración, afectando así a la separación entre fisuras y el ancho de fisura.

Este trabajo estudia el comportamiento adherente entre barras de FRP y hormigón. Para ello, se han llevado a cabo dos programas de ensayos experimentales. El primero de ellos estudia la influencia de las variables involucradas en el comportamiento adherente, como son, el diámetro de la barra, el tipo de fibra, el acabado superficial y la resistencia del hormigón. Este estudio se realiza mediante 88 ensayos de pull-out. Del estudio se concluye que los diferentes acabados superficiales de las barras de FRP, que a diferencia de las barras de acero no se encuentran estandarizados, activan diferentes mecanismos de adherencia. No obstante, la influencia del acabado superficial sobre los mecanismos adherentes no es tan acusada cuando se utilizan hormigones de resistencias bajas.

En el segundo programa experimental se estudia el proceso de fisuración de tirantes de hormigón reforzados con barras de materiales compuestos de fibra de vidrio (en adelante GFRP "Glass Fibre Reinforced Polymer") mediante ensayo a tracción directa. Los resultados experimentales confirman que el enfoque que la guía de diseño norteamericana (ACI.224-2R, ACI 440.1R-06) realiza sobre el estudio de elementos reforzados tiene un carácter conservador. Sin embargo, la descripción del comportamiento de la barra de refuerzo mediante la asignación de una ley constitutiva modificada, cuya pendiente se ve progresivamente reducida para niveles de carga superiores a la carga de fisuración, se ha mostrado como una herramienta efectiva incluso para el estudio de refuerzo de FRP. Asimismo, se confirma la existencia de una dependencia entre el ratio "diametro de barra/cuantía mecánica" y la separación entre fisuras, tal y como se propone en EC-2. No obstante, la influencia adicional del recubrimiento sobre la separación entre fisuras, que se define en el código de diseño, no parece directamente extrapolable a elementos sometidos a tracción pura con recubrimientos notablemente distintos que en el caso de flexión. El programa experimental se completa con el estudio de dos tirantes con pre-fisura inducida e instrumentación interna de la barra de refuerzo. Esto permite el análisis del proceso de fisuración y un mejor entendimiento del mapa de fisuración final. De igual forma, el estudio del perfil de deformaciones en el refuerzo permite estudiar la redistribución de tensiones que tiene lugar a medida que se van formando las fisuras.

El trabajo se concluye con el desarrollo de un modelo numérico para la simulación del comportamiento de elementos de hormigón reforzado bajo cargas de tracción. La bondad del modelo se comprueba mediante la comparación de resultados numéricos y resultados experimentales, tanto a nivel local mediante la distribución de deformaciones del refuerzo, como a nivel global mediante la respuesta $P - \delta$ del tirante. La flexibilidad del modelo para incorporar cualquier ley de adherencia y propiedades de los materiales involucrados, lo convierte en una herramienta flexible para la realización de un estudio paramétrico sobre las variables que influyen en el proceso de fisuración. Basándose en la representación de la rigidez adicional surgida del fenómeno tenso-rigidez (en inglés, tension stiffening) mediante la modificación de la ley constitutiva del hormigón a tracción, el estudio concluye que el fenómeno tenso-rigidez para estos elementos se muestra poco sensible a la variación de la re-

sistencia del hormigón a compresión. En cambio, la cuantía geométrica y la relación de módulos de elasticidad de los materiales son las variables determinantes del comportamiento post-rotura de elementos de hormigón reforzado a tracción.

Contents

List of Figures

List of Tables

List of Symbols

Symbol	Description
A, B, C, D, E, F, G	Nondimensional empirical constants in Malvar bond-slip model.
A_{cr}	Cracked cross sectional area of RC tie.
A_e	Effective cross sectional area of RC tie.
A_g	Gross sectional area of RC tie.
A_r	Cross sectional area of rebar.
a_s	Area to space ratio.
c, c_y	Concrete cover.
CLR	Concrete lug ratio.
d_b	Rebar experimental diameter.
d_n	Rebar nominal diameter.
E_c	Modulus of elasticity of concrete.
E_{FRP}	Modulus of elasticity of FRP rebar.
E_r	Modulus of elasticity of reinforcing rebar.
E_{steel}	Modulus of elasticity of steel bar.
$f_c^{'}$	Concrete compressive strength.
$F_c(x), F_r(x)$	Axial force along the x-axis of concrete and reinforcement in the numerical model.
f_{cm}	Mean concrete compressive strength at the age of 28 days.
f_{ct}, f_t	Concrete tensile strength (in RC tensile tests).
f_{ctm}	Mean tensile strength of concrete.

Symbol	Description
f_{fu}	Rebar rupture tensile strength.
$f_{fu,exp}$	Rebar rupture tensile strength.
h	Notional size of cross section to compute shrinkage strain.
K_1	Factor to define the further cracking criterion in the numerical model.
k_1	Bond characteristic coefficient in mean crack spacing proposal of EC-2.
k_2	Load type coefficient in mean crack spacing proposal of EC-2.
k_b	Bond coefficient in maximum crack width proposal of ACI440.
k_t	Load type coefficient in crack width proposal of EC-2.
L	Bonded length in RC ties.
L_B	Half length of concrete block studied in the numerical procedure.
l_b	Bonded length in pull-out tests.
l_t	Transfer length.
M_{cr}	Cracking moment.
n	Modular ratio.
n_c	Number of transverse cracks.
P	Applied load.
p	Parameter to be calibrated in D.B.M. bond-slip model.
P_{add}	Initial tensile load on RC tie due to shrinkage.
P_c	Transfer load.
P_{crack}	First cracking load in RC tie.
p_r	Perimeter of the bar.
$P_{rupture}$	Rebar rupture tensile load.
P_{sta}	Cracking stabilization load in RC tie.
P_{ult}	RC tie ultimate load.
RH	Relative humidity.
R_r	Relative rib area.

Symbol	Description
$s(x)$	Slip between reinforcement and concrete along the x-axis in the numerical model.
s_m	Slip value at which bond strength is attained in B.E.P. bond-slip law.
$s_{m,le}, s_{m,ue}$	Slip value at which bond strength is attained for the loaded and unloaded end in experimental pull-out tests.
s_r	Parameter to be calibrated in C.M.R. bond-slip law.
$s_{r,max}$	Maximum crack spacing.
$s_{r,max,exp}$	Experimental maximum crack spacing.
$s_{r,min}$	Minimum crack spacing.
$s_{r,min,exp}$	Experimental minimum crack spacing.
s_{rm}	Average crack spacing.
$s_{rm,exp}$	Experimental average crack spacing.
t	Age of concrete.
$TOL1$	Tolerance to compute the transfer length, l_t, in numerical procedure.
$TOL2$	Tolerance in the check of concrete tensile strength attainment in numerical procedure.
t_s	Age of concrete at the beginning of shrinkage.
u	Perimeter of the cross section which is exposed to drying.
$u_c(x), u_r(x)$	Displacement along the x-axis of concrete and reinforcement in the numerical model.
w_c, w_f	Width of concrete and rebar lug.
w_m	Experimental average crack width.
α	Parameter to be calibrated in B.E.P., D.B.M. and mB.E.P. bond-slip models.
α_1, α_2	Parameters to be calibrated in concrete post-cracking response.

Symbol	Description
β	Parameter to be calibrated in C.M.R. and M.C.M.R. bond-slip models.
β_1	Bond characteristic coefficient in average strain proposal of EC-2.
β_2	Load type coefficient in average strain proposal of EC-2.
β_d	Reduction coefficient proposed in ACI to adapt steel code to FRP code.
β_{RH}	Factor for the computation of the notional shrinkage coefficient.
$\beta_s(t, t_s)$	Coefficient to describe the development of shrinkage with time.
β_{sc}	Coefficient accounting for cement type in the computation of shrinkage strain.
β_t	Factor for steel strain along the transmission length in MC90.
δ	Member elongation applied while testing.
δ_{ult}	Ultimate elongation.
ϵ_1, ϵ_2	Reinforcement strain calculated for the uncracked and fully cracked section.
$\epsilon_c(x), \epsilon_r(x)$	Tensile strain along the x-axis of concrete and reinforcement in the numerical model.
$\epsilon_{cs}(t, t_s)$	Total shrinkage strain.
ϵ_{cso}	Notional shrinkage coefficient.
ϵ_{ct}	Concrete tensile cracking strain.
ϵ_m	Average strain in reinforcement.
$\epsilon_{m,i}$	Member initial shortening due to shrinkage.
$\epsilon_s(f_{cm})$	Factor for the computation of the notional shrinkage coefficient.
$\epsilon_{sr1}, \epsilon_{sr2},$	Reinforcement strain calculated for the uncracked and fully cracked section when first crack has formed.
$\epsilon_{sm} - \epsilon_{cm}$	Difference between the mean strain of steel and concrete between cracks.
γ	Parameter to be calibrated in the M.C.M.R. bond-slip model.

Symbol	Description
η_1, η_2, η_3	Coefficient accounting for type of reinforcement in MC90 design bond stress equation proposal.
η_2	Coefficient accounting for position of bar during casting in MC90 design bond stress equation proposal.
η_3	Coefficient accounting for bar diameter in MC90 design bond stress equation proposal.
ρ	Reinforcement ratio.
ρ_b	Balanced reinforcement ratio.
ρ_{eff}	Effective reinforcement ratio.
$\sigma_c(x), \sigma_r(x)$	Tensile stress along the x-axis of concrete and reinforcement in the numerical model.
σ_{cr}	Tensile stress in reinforcement at cracked section when the first crack occurs.
σ_s	Tensile stress in steel reinforcement at cracked section at the actual load.
$\sigma_{sr1}, \sigma_{srn},$	Reinforcement stress at cracked section when first and last crack has formed.
τ_m	Bond strength in MC-90 proposal of bond-slip law.
τ_{max}	Bond strength in experimental pull-out tests.
τ_r, τ_{res}	Residual bond strength in experimental pull-out tests.

Chapter 1

Introduction and objectives

1.1 Introduction

Steel reinforced concrete (SRC) is the most widely used structural material in construction. However, corrosion of steel under certain environments can lead to deterioration of structural elements, deriving to large repair and rehabilitation costs. In order to prevent these high expenses, construction industry has tried several approaches to inhibit the corrosion of steel, but they normally appear to be either expensive or ineffective [1]. Therefore, the non-corrosive properties offered in Fiber Reinforced Polymer (FRP) materials has lead to a generalized acceptance for FRP reinforcement as a feasible alternative.

Although several shapes of FRP rebars can be made, the most common shape used is circular. However, in order to improve their bond characteristic in concrete, several techniques are used: surface deformations, sand coating, surface texture, indented grooves and helical wrapping.

As a composite material, mechanical properties of FRP bars vary significantly from one bar to another depending on the nature and volume of fibres, the mechanical properties of the resin and the fibre orientation. It is therefore not possible to establish universal values for the mechanical properties and only indicative values can be given. The elastic modulus of Glass Fibre Reinforced Polymer (GFRP) and Carbon Fibre Reinforced Polymer (CFRP) materials used in construction generally varies

between 20 to 70% of that of steel, respectively. As a result of these lower stiffness they develop higher strains, and consequently FRP reinforced concrete (FRP RC) elements are more flexible and perform higher deformations. Moreover, these materials are presented to have a brittle failure, unlike steel. Therefore, different behaviour is expected for FRP RC structures compared to SRC structures.

The full acceptance of FRP reinforcement in concrete construction is contingent on a complete study and comprehension of all aspects of their structural behaviour. Since existing codes of practice for SRC structures are not flexible enough to directly accommodate the design of FRP RC structures, a great amount of research is currently being carried out world-wide on FRP RC structures aiming towards the development of specific design guidelines for FRP RC structures [2].

One of the fundamental aspects of structural behaviour is bond development, since bond is the responsible to establish and to maintain the composite interaction between the reinforcement and surrounding concrete through load transfer from one to another. Therefore, the quality of bond has a prominent influence on crack formation and hence affects the spacing between cracks and the crack width. The bond behaviour between steel and concrete has been widely studied and an extensive amount of experimental, analytical and numerical work already exists [3]. The main mechanism in the development of bond in steel-concrete interface is the mechanical interaction between the ribbed or deformed surface of the reinforcing bar and the concrete. However, other mechanisms such as surface friction and chemical adhesion also play a role.

Research on the bond behaviour between FRP and concrete is not that extensive, specially if the influence of the non-standardized surface configuration of FRP is accounted for. Moreover, existing experimental research is mainly focused on the study of the bond behaviour through pull-out tests. However, results derived in pull-out test are said to be "qualitative" good, but can not be considered to be "quantitative" good, as the stress conditions performed in pull-out tests differ from that occurring in the tension zone of flexural members. In this sense, direct tensile tests are thought to better represent the bond behaviour, because a reinforced

concrete element that is subjected to axial loading is one of the most simple problems which incorporates several basic characteristics of reinforced concrete without coupling bending singularities. However, limited extension of the study of bond behaviour between FRP and concrete to FRP RC ties is available.

1.2 Objectives

The main objective of the present thesis is to investigate the bond behaviour between FRP and concrete, and how this bond performance affects the cracking behaviour of FRP RC tensile members. In order to achieve this aim, the following tasks were undertaken:

- Review the literature focused on the bond behaviour between FRP bars and concrete through both pull-out and direct tension test, so that the roles of the different variables involved in the bond transfer mechanism are identified.

- Experimentally investigate the main parameters that affect the bond behaviour: rebar diameter, kind of fibres, surface configuration and concrete compressive strength. Based on experimental results, the influence of the different variables on both bond development and bond failure mode of FRP specimens for pull-out tests should be defined.

- Experimentally investigate the cracking behaviour of FRP RC ties and check the validity of code predictions through comparison with experimental results on load-elongation relationship, crack spacing and crack width.

- Develop a numerical model to simulate the cracking behaviour of FRP RC tensile members, versatile enough to model the differences in bond behaviour of the different bars available in the market through the introduction of any "user-defined" bond-slip law. The flexibility of the model should be extended so that materials' properties (geometrical and mechanical) can also be modified. The final model would be used to analyze how the bond variables and the geometrical and mechanical variables affect the post-cracking behaviour of RC ties.

1.3 Thesis layout

According to the objectives previously described, the thesis is structured as follows:

In Chapter 2 a detailed review of the works on the study of bond behaviour between FRP and concrete available in the bibliography is given. First, a complete review of experimental and numerical programs on pull-out tests is presented. A special attention is given to the influence on the bond behaviour of the main variables involved (concrete strength, rebar diameter, surface configuration and fibre material). Moreover, the analytical works centered on providing bond-slip relationships that define the local bond behaviour are also presented. In a second part of the chapter, a review on the available experimental programs on FRP RC tensile members is reported. Furthermore, an inspection on the existent approaches to include the effects of the interaction between reinforcement and concrete on the response of RC tensile members is made.

Based on the analysis done in Chapter 2, the variables which can influence the bond behaviour are studied in detail in Chapter 3. In addition, details on the materials' properties and test set-up are given. The significant experimental results of the pull-out tests are shown and discussed in Chapter 4, and all the experimentally deduced bond-slip laws are included in related Appendix A.

In Chapter 5, the experimental program on direct tensile tests to investigate the cracking behavior of GFRP RC ties is presented. Details on all the phases of the experimental procedure are given. The tensile behavior of the ties is analyzed and the accuracy of existing codes, in particular EC-2 [4], MC90 [5] and a modified version of ACI 224.2R-92 [6], is discussed by comparing the predictions with experimental results. A summary of experimental data is included in related Appendix B.

In Chapter 6, a numerical model is presented, where finite difference method is used to solve the system of differential equations that describe the cracking behavior of RC tensile members. The verification of the model is performed by comparison with experimental data, previously presented in Chapter 5, on both reinforcement

strain distribution and P-δ relationships. The numerical model is thereafter used to conduct a parametric study to detect the influence of the different variables on the post-cracking behaviour of RC tensile members.

Finally, the thesis is concluded in Chapter 7 with a summary of its achievements and discussion of possible future research.

Chapter 2

Literature review on the bond behaviour of deformed steel and FRP bars

2.1 Bond of steel reinforcing bars to concrete

2.1.1 Steel bar-concrete interaction

Steel-to-concrete bond is the many-faceted phenomenon which allows longitudinal forces to be transferred from the reinforcement to the surrounding concrete in a reinforced concrete structure. Due to this transfer, the force in a reinforcing bar changes along its length, as does the force in the concrete embedment. Wherever steel strains differ from concrete strains, a relative displacement between the steel and the concrete (slip) does occur, but this lack of compliance is also the effect of the highly-localized strains in the concrete layer closest to the reinforcement (interface).

The resistant mechanisms upon which the steel-to-concrete bond is based are already well known, due to the many tests' results that have been gathered and analyzed by resorting to a variety of specimens and techniques [7]. The researchers who have contributed to the knowledge of the many aspects of bonding agree that the interaction between concrete and a bar subjected to a pull-out force is characterized by four different stages (Figure 2.1).

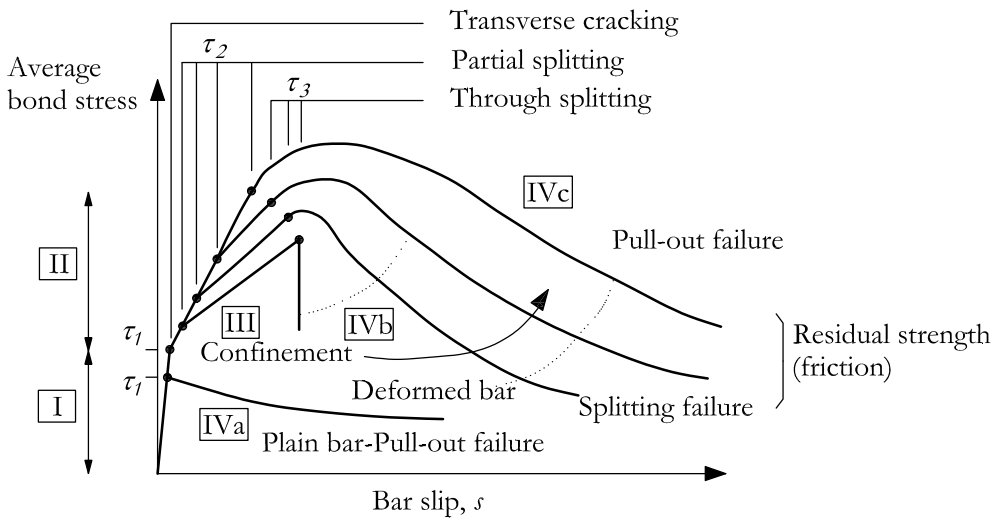

Figure 2.1: Steel-concrete local bond stress-slip law (after [7]).

Stage I (uncracked concrete): for low bond-stress values, $\tau \leq \tau_1 = (0.2 - 0.8) f_{ct}$, bond efficiency is assured mostly by chemical adhesion, and negligible bar slip occurs, but highly localized stresses arise close to lug tips (Figure 2.2(a)). Chemical adhesion is also accompanied by the micromechanical interaction associated with the microscopically rough steel surface, but on the whole chemical and physical adhesion plays a minor role, as confirmed by the low bond performances of plain bars, where chemical adhesion and microinterlocking are soon followed by the sliding of the bars (end of Stage IVa, which is highly affected by transverse pressure). Note that the relative displacement of the bar is always measured with reference to the undisturbed concrete and consists of two parts, the relative slip at the interface and the shear deformations in the concrete (Figure 2.2(b)); therefore, even if there is no bar slip, a certain displacement occurs owing to the localized strains close to the interface. This explains the slip in stage I.

Stage II (first cracking): for higher bond stress values, $\tau > \tau_1$, the chemical adhesion breaks down; in deformed bars the lugs induce large bearing stresses in the concrete (p*, Figure 2.3(a)) and transverse microcracks originate at the tips of the lugs allowing the bar to slip, but the wedging action of the lugs remains limited and there is no concrete splitting.

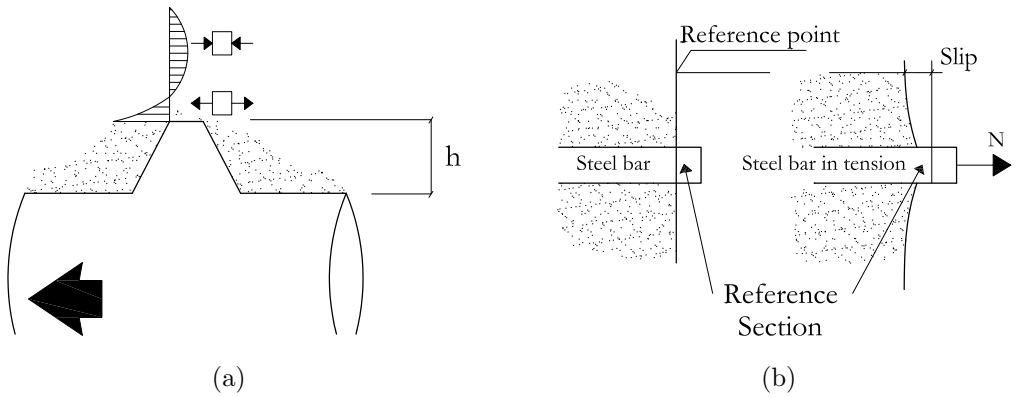

Figure 2.2: (a) Typical stress peaks in the elastic phase (deformed bars) and (b) Relative bar displacement (slip) (after [7]).

Stage III: for still higher bond stress values, $\tau > (1-3)f_{ct}$, the longitudinal cracks (splitting cracks, Figure 2.3(b)) spread radially, owing to the wedging action which is enhanced by the crushed concrete stuck to the front of the lugs. The outward component of the pressure (p**, Figure 2.3(a)) is resisted by the hoop stresses in the surrounding concrete; as a consequence, the surrounding concrete exerts a confinement action on the bar, and bond strength and stiffness are assured mostly by the interlocking among the reinforcement, the concrete struts radiating from the bar and the undamaged outer ring. In the case of light transverse reinforcement, this stage ends as soon as concrete splitting reaches the outer surface of the concrete member (through splitting τ_3). Afterwards, a more or less sudden failure occurs depending on the transverse confinement (Stage IVb, splitting failure). In the case of heavy transverse reinforcement or large concrete cover, through splitting is prevented by their confining action and concrete splitting remains limited to a cracked core around the bar (Stage IVc, pull-out failure).

Stage IVa: in plain bars this stage immediately follows the breakage of adhesive bond; force transfer is provided by friction and is strongly affected by the transverse pressure; concrete shrinkage and bar roughness favor friction.

Stage IVb: in the case of deformed bars confined by light-to-medium transverse reinforcement, the longitudinal crakcs (splitting cracks) break out through the cover and the bar spacing, and the bond tends to fail abruptly. On the other hand, if suf-

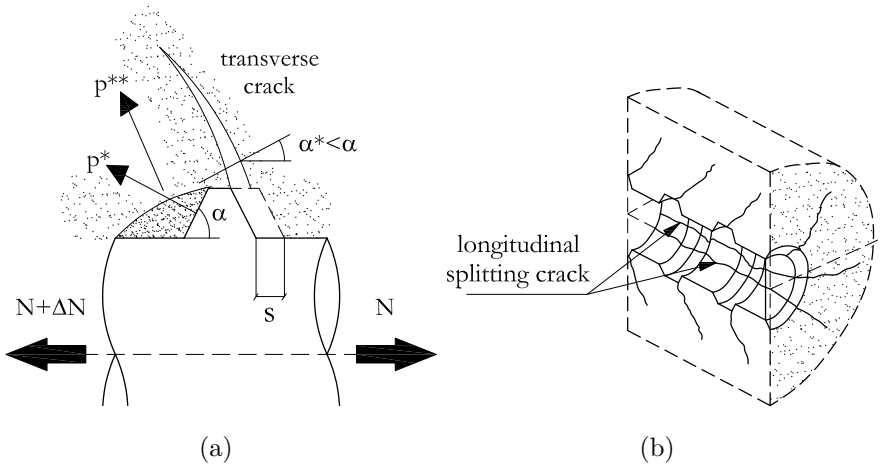

Figure 2.3: (a) Bar-concrete slip and wedging action of the bar and (b) Transverse cracks and splitting (after [7]).

ficient transverse reinforcement (namely stirrups) is provided, bond can be assured in spite of concrete splitting, because of the confinement action developed by the reinforcement.

Stage IVc: in the case of deformed bars confined by heavy transverse reinforcement, splitting does not occur and bond failure is caused by bar pull-out. The force transfer mechanism changes from rib bearing to friction.

2.1.2 Factors influencing bond behaviour

There are many factors that influence bond behaviour between concrete and steel reinforcement, thus influencing bond strength. It is important to understand how these factors influence bond when steel reinforcement is considered, so that comparison can be made when dealing with FRP reinforcement.

An extended explanation on which are the main parameters influencing bond is included in [7]. Some of the main parameters are presented next:

Concrete strength

Concrete strength is the most important factor to control if bond failure by splitting is not desired. Splitting failure takes place when the tensile hoop stresses exceed

the tensile strength of the surrounding concrete, which happens generally at a lower load than the pull-out mode of failure. As a consequence of splitting failure, bond stress in the bar is lost abruptly and the residual bond strength is practically zero.

The importance of concrete tensile strength is therefore recognized in different codes of practice like [8, 9] among others, as it is indirectly included in the anchorage length equations.

Bar diameter

The size of bar diameter influences the bond strength with bars with bigger diameters developing less bond strength than smaller bars. This effect is acknowledged in [8] by suggesting a reinforcement size factor in its development length formula.

Transverse pressure

Transverse pressure has a double influence on bond behaviour. Firstly, the existence of transverse pressure delays the onset of splitting failure and secondly it increases the frictional force in the steel-concrete failure surface. As a result, the presence of transverse pressure results in higher bond stresses and in reduced values of slip at a particular load.

2.2 FRP reinforcement for concrete structures

2.2.1 Introduction

A considerable amount of research investigating FRP materials as an effective solution for the replacement of ferrous-reinforcement in concrete structures has been conducted until now. The replacement from ferrous to non-ferrous reinforcement is not direct, due to their differences in properties. Therefore, it is possible to talk about strengths and weaknesses of FRP materials when compared to steel. The main advantages and disadvantages of FRP materials against steel are presented in [10] and are shown in Table 2.1

Variations in the nature of nowadays/actual developed non-ferrous reinforcement are expected because of the difference in their manufacturers. In most of the cases, the FRP products consist of continuous glass, carbon or aramid fibres impregnated

ADVANTAGES
• Higher ratio of strength to self weigth (10 to 15 times greater than steel). • Carbon and aramid fibre reinforcement have excellent fatigue characteristics. • Excellent corrosion resistance and electromagnetic neutrality. • Low axial coefficient of thermal expansion.
DISADVANTAGES
• Higher raw material cost. • Lower elastic modules (except some Carbon FRPs). • Glass FRP reinforcement suffers from stress corrosion (meaning that a piece of glass in tension will not last as much as expected). • Lack of ductility.

Table 2.1: Main advantages/disadvantages of FRP materials [10]

in a resin matrix (epoxy, vinyl ester and polyester).

The choice of a manufacturing process depends on the type of matrix and fibres, the temperature required to form the part, and to cure the matrix, and the cost effectiveness of the process. There are various manufacturing options available, including hand lay-up, filament winding and braiding among others, but pultrusion is the most common one. Pultrusion is a manufacturing process, similar to that shown in Figure 2.4, for producing continuous lengths of reinforced polymer structural shapes with constant cross-sections. Raw materials are a liquid resin mixture (containing resin, fillers and specialized additives) and flexible textile reinforcing fibres. The process involves pulling these raw materials through a heated steel forming die using a continuous pulling device. The reinforcement materials are in continuous forms such as rolls of fibreglass mat and doffs of fiberglass roving. As the reinforcements are pre-impregnated and saturated with the resin mixture in the resin bath and pulled through the die, the hardening of the resin is initiated by the heat from the die and a rigid, cured profile to correspond to the shape of the die.

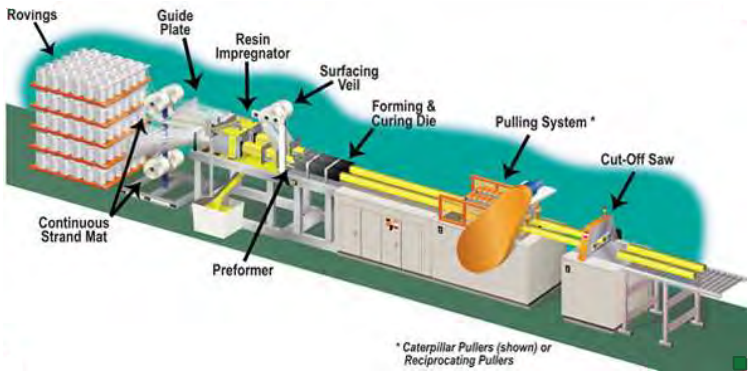

Figure 2.4: Pultrusion process (www.stronwell.com).

The performer is an array of tooling which squeezes away excess resin as the product is moving forward and shapes the materials prior to entering the die. FRP can easily be manufactured in any shape, unlike conventional reinforcing steel, while the resin has not cured. Cross-sectional shape influences because of the distribution of normal strains and stresses over different shaped bar cross-section.

FRP materials obtained with the same manufacturing process can have different

kind of surface deformations; the form of the bar deformations differs from manufacturer to manufacturer, consisting either on resin or on resin and fibre or, in some cases, on a combination of resin, fibre and additional sand particles attached to the surface of the bar. These differences in surface deformations can influence bond behaviour of these FRP bars.

2.2.2 Mechanical properties

As a composite material, mechanical properties of FRP bars vary significantly from one sample to another depending on the nature and volume of fibres, the mechanical properties of the resin and the fibre orientation. It is therefore not possible to establish universal values for the mechanical properties and only indicative values can be given. A comparison of FRP and steel bars mechanical properties is shown in Table 2.2.

Property	GFRP	CFRP	AFRP	Steel
Density (kg/cm^3)	1.25÷2.1	1.5÷1.6	1.25÷1.4	7.9
Longitudinal thermal expansion coefficient (10^{-6}/°C)	6÷10	-9÷0	-6÷-2	11.7
Transverse thermal expansion coefficient (10^{-6}/°C)	21-23	74-104	60-80	11.7
Yielding stress (MPa)	-	-	-	400÷500
Longitudinal tensile strength (MPa)	480÷1600	600÷3690	1720÷2540	550
Longitudinal modulus (GPa)	35÷50	120÷580	41÷125	200
Yielding longitudinal tensile strain (%)	-	-	-	0.20÷0.25
Ultimate longitudinal tensile strain (%)	1.2÷3.1	0.5÷1.7	1.9÷4.4	15÷20

Table 2.2: Typical FRP and steel reinforcement mechanical properties [10].

Unlike steel rebars, FRP bars are strongly anisotropic (i.e. their mechanical

properties are different in two transverse directions, having the longitudinal axis as the stronger one) and have no ductility. As it will be explained later, these properties in addition to other differences are expected to influence bond behaviour of the rebars.

Modulus of elasticity

The Young Modulus of FRP bars is generally lower than that of steel, having GFRP bars the lowest values. The modulus of elasticity of FRP bars remains practically constant up to the failure point (elastic brittle behaviour); for the case of steel bars, a ductile behaviour is expected and therefore considered in design codes. Besides, because of their lower values of modulus of elasticity, deformations expected in FRP reinforced concrete structures (FRPRCS) are larger than that of steel reinforced concrete structures.

These two differences in mechanical properties will affect bond behaviour and therefore it is important to have them in consideration when developing design codes.

Tensile strength

Generally, GFRP bars can develop more than twice the tensile strength of steel bars, whereas CFRP and AFRP can develop more than threefold, depending on the nature of fibres and matrix.

A comparison of the tensile properties of FRP and steel bars is shown in Figure 2.5.

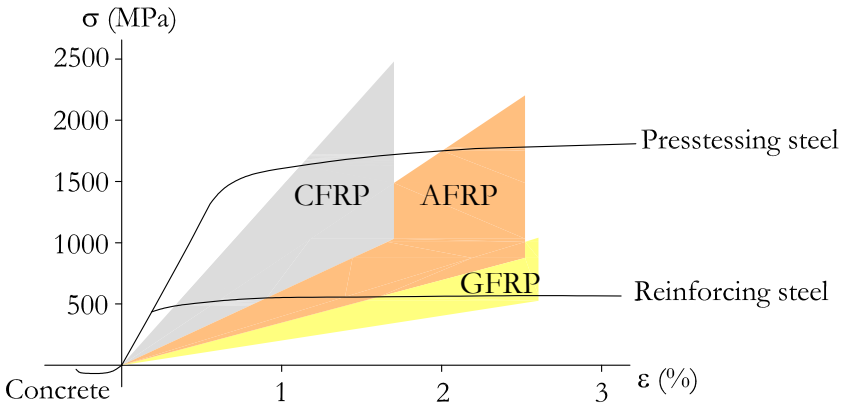

Figure 2.5: Typical stress-strain relationships for FRP and steel bars (after [10]).

Unlike steel bars, FRP bars have no constant tensile strength value, but a variable one with dependence on the cross sectional area. According to [7], when a FRP bar is pulled in tension through the surface, there can be a differential movement between the core an the surface fibres, which results in a non-uniform distribution of normal stresses through the cross section of the bar (i.e. fibres located near the center of the bar cross section are not subjected to as much stress as those near the outer surface).

2.3 Bond of FRP reinforcing bars to concrete

2.3.1 Introduction

The wider acceptance of FRP materials in the construction industry is limited to a better understanding of the composite action of FRP reinforced concrete and hence, bond between concrete and FRP needs to be understood. A good composite action is assured when forces are adequately transmitted from reinforcement to concrete. The bond behaviour of FRP bars to concrete is expected to vary from that of conventional steel bars since various key parameters that influence bond performance are different. Some of these parameters are [11]:

- The lower FRP modulus of elasticity when compared to that of steel, both in the lateral and the longitudinal direction.
- The shear stiffness is much lower than that of steel.
- The resin matrix shear strength is lower than that of steel, a factor that is expected to control the strength of the surface deformations of the bar.

2.3.2 FRP bar-concrete interaction

An accepted description of the bond performance between bar and concrete is presented in [7], being this behaviour different for the case of plain, deformed or surface treated bars.

When plain bars are considered, bond is found to be mainly governed either by the adhesion between the bar surface and the surrounding concrete or by the inter-laminar shear strength between successive layers of fibres at the surface of the bar. Due to the plain surface, no tensile cracking is likely to occur and splitting bond forces are unlikely to develop. The description of the deformed or surface treated FRP bar to concrete interaction is summarized in Figure 2.6.

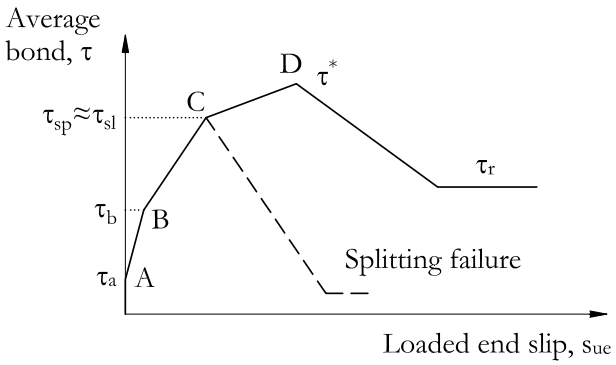

Figure 2.6: Typical average bond stress versus loaded end slip curve of an FRP short embedment (after [11]).

At the beginning of loading, *section OA*, the main mechanism resisting the external load is the chemical adhesion between the two materials. At this stage, no measurable slip is observed. For higher bond stress values($\tau > \tau_a$) the chemical adhesion breaks down and a different bond mechanism is set (*section AB*). The slip at the loaded end of the bar increases and the deformations of the bar induce large bearing stresses in the concrete, thus originating microcracks at the tips of the bar deformations allowing the bar to slip. It is believed that the onset of the microcracks is delayed because of the "softener" surface deformations of the FRP bars when compared to that of steel bars. As the slip of the bar increases, *section BC*, the bearing stresses increase considerably and the radial component from the bond forces is balanced against the rings of tensile stresses developed in concrete (Figure 2.7). If the bar is not adequately confined and the value of the tensile hoop of stresses exceeds the tensile strength of concrete, splitting cracks may appear along the length of the reinforcing bar. If sufficient resistance to splitting can be provided, *section CD*, the bond stress can reach the maximum bond strength (τ^*). As both ends of the bar (loaded and unloaded) are slipping, the bond stiffness decreases.

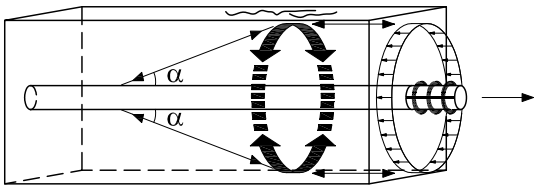

Figure 2.7: Balance of the radial components of the bond forces against the tensile stress rings (after [11]).

Depending on the ratio between concrete strength and shear strength of surface deformations, four different modes of bond failure can take place:

- *Shearing off part or all the surface deformations of the bar.* The bond strength of FRP bars is controlled by the shear strength between successive layers of fibre or by the shear strength of bar deformations. Therefore, an increase in concrete strength will not be corresponded with an increase in bond strength of the FRP bar.

- *Concrete shear failure.* The concrete is crushed in front of the bar deformations; therefore the bond strength is mainly controlled by the concrete shear strength.

- *Combined mode.* With intermediate levels of concrete strength, a combined mode of the above failure is likely to occur.

- *Squeeze through.* Due to the low stiffness in the radial direction, the bar can squeeze through the concrete. In this case bond is provided by the friction between the deformations of the bar and the concrete.

Once the maximum bond stress has been reached, the bearing mechanism breaks down. The residual bond strength is mainly dependent on the frictional resistance, τ_r.

The previously introduced average bond stress versus loaded end slip curve is widely explained in [7].

2.3.3 Bond mechanisms

In the following, a brief description of some studies investigating the bond mechanisms of different types of FRP bars, is presented.

An experimental program performing several tests on pull-out and beam specimens reinforced with FRP bars was conducted in [12]. GFRP, AFRP and CFRP bars with varying surface deformations (strands, deformed, braided) were used. The test specimens were designed to fail in a concrete splitting mode. A first attempt of classification for bond mechanism was made, defining friction resistance (for smooth and strand-shaped FRP bars) and bearing resistance (for ribbed FRP bars) as the two types of bond-resistant mechanisms. All the test data were collected and presented, but no recommendations on design equation were done.

Different surface treatments were considered in [13]; the authors studied bond behaviour performing bond tests with different types of deformed and sanded bars, made of carbon, aramid and glass continuous fibres embedded in an epoxy resin matrix. According to their results, sanding lead to an increase of chemical bond, resulting in a large increment of bond strength. However, sand-covered continuous fibre bars showed good bond performance initially, but the interface between sand grains and bars detached abruptly, with a brittle bond failure.

The results of an experimental program performing pull-out tests of GFRP rebars in concrete are presented in [14]. From the tests data the authors concluded that the anchorage design for steel rebars is not directly applicable on GFRP bars. For the same test conditions they observed that the average nominal bond stress at failure was greater for the steel rebars than for the GFRP rebars. They also observed that the slip of the rebars relative to the concrete surface was greater for GFRP rebars than for the steel rebars. For GFRP rebars with spiral indentation, adhesion and friction were the primary component of the bond.

Bond strength of FRP rebars was also experimentally investigated and compared to that of steel rebars in [15]. This study included two types of FRP bars, four nominal diameters of FRP and steel bars and three embedment lengths. The

study showed lower values of bond strength for GFRP bars compared to that of steel bars, with a range of values for bond strength varying from 5.1 to 12.63 MPa, depending on the rebar diameter and the embedment length. From bond tests on GFRP smooth rods, whose surface was subsequently deformed by helically winding the same kind of fibers, the authors concluded that adhesion and friction were the primary component of bond.

A complete investigation on the interface bond behaviour was conducted under the EUROCRETE project [16] in which some influential parameters like type of bar, embedment length and cross sectional shape were studied. The study involved more than 100 specimens which were tested in direct pull-out with short embedment lengths, failing all of them in pull-out mode. EUROCRETE GFRP and CFRP bars had a rough surface produced by a peel ply and were manufactured in different diameters and shapes (Figure 2.8).

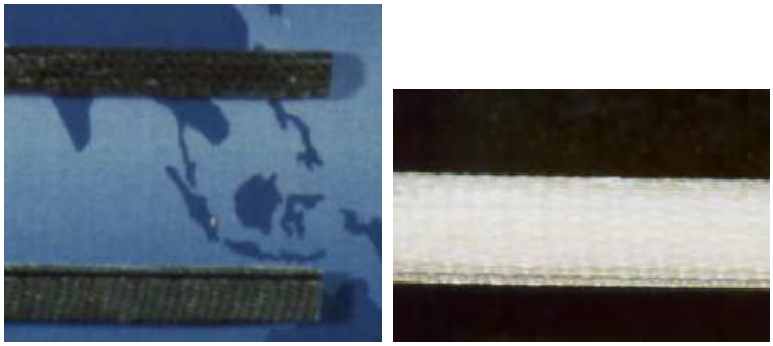

(a) (b)

Figure 2.8: Samples of the EUROCRETE CFRP and GFRP bars [11].

Results of the study are presented in [11, 17]. For concrete strengths greater than 30MPa the failure occurred in the surface of the bar, by peeling part of its surface layer, thus meaning that bond strength of the GFRP bars was not controlled much by concrete strength but appeared to be influenced by the interlaminar shear strength just below the resin rich surface layer of the bar. For concrete strengths less than 15MPa the concrete was crushed in front of the bar deformations and the bond strength was controlled mainly by the shear strength of concrete. Therefore, the authors concluded that the pull-out mechanism of the FRP reinforcements differs from that of deformed steel bars, whose bond behaviour is influenced by the

strength of the concrete matrix only.

Although differences in bond mechanism of FRP and steel rebars exist, there are two effects affecting bond behaviour that are present in both reinforcing materials. These two effects are the increase in bond strength derived from either a decrease in rebar diameter or a decrease in embedment length.

The rebar diameter appeared to play a perceptive role in the bond behaviour of steel bars to concrete in which is known in literature as the "*shear lag effect*" (see Figure 2.9). When a bar is pulled in tension by bond through the surface, there can be a differential strain between the core and the surface, because of the limited axial shear stiffness, which results in a non-uniform distribution of normal stresses through the cross section of the bar. The actual bond strength that is developed between the bar and the concrete is directly related to the value of the normal stress that occurs close to the surface of the bar (τ_{max}). Alternatively, the calculated bond strength that the user anticipates as the "real" bond strength is proportional to the average normal stress over the full cross-section of the bar (τ_{av}). As the diameter of the bar increases, the difference between τ_{max} and τ_{av} increases and therefore the "real" bond strength of the bar decreases. This "*shear lag effect*" is expected to be more pronounced in FRP reinforcing bars, because they offer a lower shear stiffness in the axial direction, whose value depends mainly on the shear stiffness of the bar resin and the shear strength capacity at the resin-fibre interface. Experimental results that confirm this behaviour can be found in [11, 17, 18].

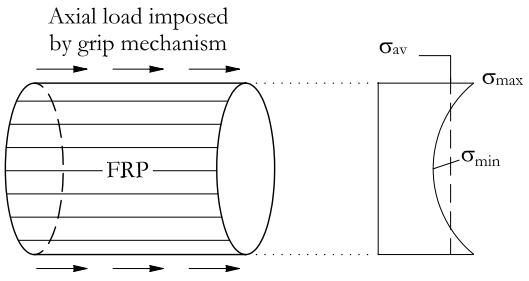

Figure 2.9: Distribution of normal stresses in an FRP bar cross-section subjected to axial tension (after [18]).

Besides, the embedment length appeared to influence the bond behaviour of steel bars to concrete because of the non-linear bond forces distribution. Therefore, the bond between steel rebars and concrete is usually studied through specimens with short embedment lengths. In the case of FRP rebars, larger differences between the loaded and unloaded end slips arise, thus denoting a higher non-linearity in bond forces distribution. However, depending on bar surface configuration, short embedment length desired to reduce the non-linear distribution could not be representative. Therefore, bond tests of FRP rebars are usually performed with longer embedment lengths, and the influence of non-linear distribution is expected to be more pronounced. Experimental results that confirm this behaviour can be found in [11, 15–17, 19–21].

2.3.4 Factors influencing bond behaviour

Like in steel reinforced concrete, there are many factors that influence bond behaviour between concrete and FRP reinforcement. Research on which are these factors and how they influence bond behaviour has been done and is still on, with the performance of different experimental and analytical programs. In the following, a description of some of these studies is presented. Unlike steel reinforcement, no standard surface configuration has been set for FRP bars. Research is therefore mainly focused on studying how these surface configurations affect bond behaviour.

An experimental program investigating the bond behaviour of GFRP bars in direct pull-out was conducted by [22]. The GFRP bars were supplied by a Canadian manufacturer (Pultrall Inc.) and had a smooth surface on which deformations were added by helical winding the same kind of fibers and by sand coating particles. Normal and high strength concretes (30MPa, 80MPa) were used. Three bar diameters were tested (12.7mm, 15.9mm, 19.1mm) and bars were embedded vertically in 150x300mm concrete cylinders having embedment lengths of 5 or 10 times the bar diameter. The authors concluded that bond strength of FRP bars did not depend on the concrete strength in the same way as steel (for concrete strengths ranging from 30 to 80MPa). For the GFRP rebars considered in the study, bond strength varied from 11.1 to 15.1MPa, with an average value of 12.9MPa, which is 62% to 84%

of that of steel deformed bars. Finally, the value of the anchorage length required to develop the ultimate tensile strength of GFRP rebars considered in the study depended on the rebar diameter, obtaining anchorage lengths that ranged from 10 to 20 times the rebar diameter.

The load transfer behaviour between FRP reinforcement and concrete was experimentally investigated in [23]. Measurements on bond strength using conventional direct pull-out tests were performed and both smooth and rough surface bars with embedment lengths of 5 and 10 bar diameters were tested. Three types of rough bars with different fibre/resin configuration were examined: glass-vinyl ester (GV), carbon-vinyl ester (CV) and carbon-epoxy (CE). The results showed that the bond strength of smooth bars (especially those with resin rich surface layer) was very low. On the other hand, GV and CV rough FRP bars developed average bond stresses of 13 and 14MPa respectively, whereas CE rough bars developed bond strengths of 23MPa. Steel deformed bars bond strength was around 15-20MPa. All the specimens reinforced with machined rods failed by shearing off of lugs followed by sliding, indicating that failure was controlled by strength and mechanical action of the deformations on the rod surface rather than adhesion and friction. The controlling factor in terms of bond strength appeared to be the resin type. For the range of concrete compressive strength studied (ranging from 42.7 to 66.1 MPa), failure mechanism did not change and insignificant influence on bond strength was found. The height of bar deformations (height examined: 1.3 and 0.75mm) had no significant effect on the bond strength and failure mode.

Test arrangement and materials used in [23] were used in [20] with the only difference on the placement of strain probe inside the FRP rod to monitor internal strain distribution (axial and hoop direction) at the region of the embedment length, without affecting the FRP/concrete interface. The strain probe consisted of a 3.9mm outside diameter (3.2mm inside diameter) aluminum tube with longitudinal and hoop strain gages (rosettes). Machined and wrapped bars with embedded lengths including 5 and 10 lugs, and different lug widths and heights were studied (Figure 2.10). Four concrete mixtures with strengths ranging from 32 to 66.1MPa were examined.

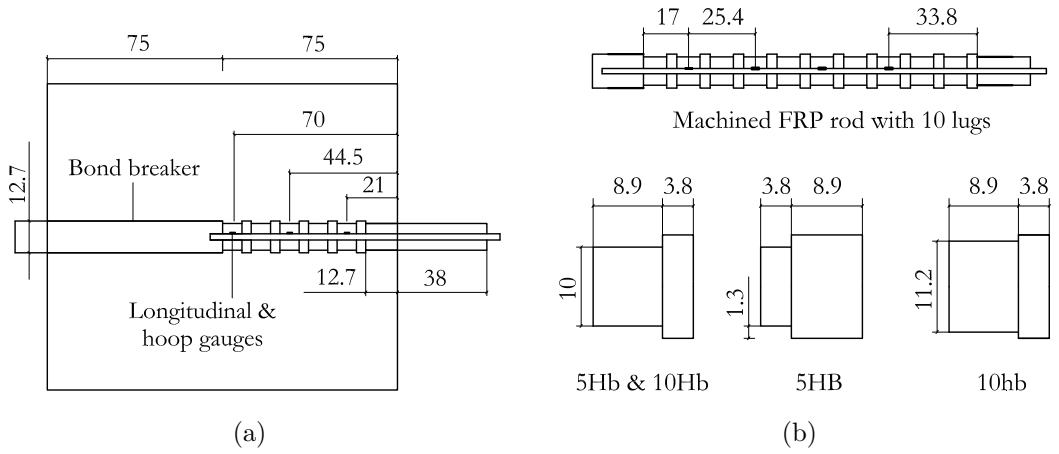

Figure 2.10: Machined FRP rod showing the strain probe location with (a) five lugs and (b) ten lugs, and lug dimensions (after [20], units in mm).

From experimental results on the machined FRP rods it was concluded that machined FRP rods with axisymmetric deformations had comparable shear stress-slip diagrams. For specimens with 3.8mm lug width the same failure mode was observed, consisting of shearing off of the lugs without any damage to the concrete, provided that there was enough concrete cover to avoid concrete splitting. Shear strength values of the GV and CV rods were 60-70% that of the CE rods, denoting that resin type rather than the fibre type appeared to control bond strength of FRP rods. Embedment length and lug height had no effect on the failure mode but doubling the embedment length and number of lugs reduced the nominal shear strength. Increasing the lug width from 3.8 to 8.9mm changed the failure mode from lug shearing to concrete shearing. Failure mode for wrapped FRP rods consisted of the shearing off of the lugs, after which load continued to increase, probably due to the higher resistance during the rod slippage offered by the significant residual wrap left on the bar surface (observed during the visual examination of the dislocated lugs after the tests), meaning a friction controlled bond mechanism after lug dislocation. As for the case of machined rods, resin was the controlling factor in terms of bond strength. When compared to machined FRP rods, wrapped FRP rods had significantly less shear strength, highlighting the significance of the method used for manufacturing.

Results of an experimental study on the bond performance of two types of GFRP bars and steel bars in high-strength concrete are presented in [24]. The experimental program consisted of testing 150mm concrete cube specimens prepared according to CSA S806-02 standard [25], with an embedded length of four times the rebar diameter. Six different concrete mix designs were prepared allowing the average concrete compressive strength to range from 25.2MPa to 93.2MPa. The nominal diameter of the bars was 12.7mm and different bond improvements were applied for each type (sand coating and helical wrapping with sand coating).

Differences in surface treatment lead to difference in bond behaviour, as the bond stress of the steel and the GFRP bars with sand coating dropped rapidly after attaining the maximum bond stress, whilst GFRP bars with helical wrapping and sand coating exhibited a gradual reduction of bond stress. Moreover, bond failure for steel bars occurred due to concrete crushing against the bar deformations, irrespective of the concrete compressive strength, meaning that bond strength was likely governed by the compressive strength of concrete. The bond strength and failure mode of the GFRP bars depended on the relative shear strengths of concrete-resin and resin-fibre interfaces, observing a concrete-resin interface failure when normal concrete was considered and a resin-fibre interface failure for high-strength concrete. To better study this dependence, the authors defined the ratio of the delaminated area (measured with a graphic software) to the total surface area, and observed an increase in the ratio when the concrete compressive strength increased. As a result, the increasing rate of the bond strength of the GFRP bars with respect to concrete strength depended on the ratio of the delaminated area.

A more comprehensive study on the effect of surface preconditioning on bond between carbon fibre reinforced polymer (CFRP) rod and concrete was performed by [26] by using pull-out tests. Considering the same smooth initial bar, two different surface treatments were applied, which consisted in a surface machining to create lugs on the rod with three different configurations and a surface sanding of the smooth CFRP rods with three types of sand of various grain sizes (Figure 2.11). Besides, smooth and ribbed steel bars were also considered. Specimens reinforced with the CFRP rods had an embedment length of both 5 and 10 times the rebar diameter, whilst an embedment length of 5 times the rebar diameter was consi-

dered for the steel reinforced specimens. Three different concrete strengths were considered, ranging from 34 to 65.7MPa.

(a) Sanded and machined CFRP rods (b) Lug dimensions

Figure 2.11: CFRP rods and lug dimensions (in mm) for CFRP rods used in [26].

Experimental results confirmed that smooth steel rebars performed higher bond strength than smooth CFRP rebars, due to low roughness of the smooth CFRP rods in comparison with that of steel. To better study the influence of the three different configurations of the machined rebars on bond performance, the Concrete Lug Ratio (CLR) was defined as:

$$\text{Concrete Lug Ratio (CLR)} = \frac{\text{concrete width}}{(\text{concrete} + \text{CFRP})\,\text{width}} = \frac{w_c}{(w_c + w_f)} \tag{2.1}$$

A CLR of 35% was found to be sufficient to ensure a bond strength equivalent to that of ribbed steel bars with bond failure due to shearing off of the concrete lugs. However, a CLR of 78% was found to be necessary to perform a better bond strength where failure occurs by the shearing off of the CFRP lugs (leading to a maximum pull-out load of the machined CFRP rods). The influence of grain sizes consisted on a decrease in ultimate bond strength of the sanded CFRP rods with the reduction of the sand size. Whether smooth, machined or sanded rebars were considered, bond strength was found to be higher for lower embedment lengths, due to the non-uniform distribution of the shear stress along the embedment length.

Recommendations on the optimal ratio of rebar ribs to rebar diameter were suggested in [27], where an extensive study on the effect of the rib geometry on bond-slip characteristics of GFRP ribbed rebars was performed using the *relative rib area*, R_r, as the descriptive term.

$$R_r = \frac{\text{projected rib area normal to bar axis}}{\text{nominal bar perimeter} \times \text{center-to-center rib spacing}} \tag{2.2}$$

According to experimental results, authors concluded that any increase in rib spacing (i.e. reduction in *relative rib area*) would cause a reduction in both initial stiffness and peak bond strength, whilst the loaded end slip value at the peak load would increase. This general trend was not confirmed for rib spacing being equal to 50% the rebar diameter, because the concrete rib resulting could not offer enough bearing action and could easily be cracked at relative low slip values. Conversely, the increase in rib height from 4% to 6% (i.e. increase in *relative rib area*) caused an increase in both initial stiffness and peak bond strength. However, the excessive reduction in cross-sectional area that would result from a greater increase in rib height (from 7% to 9%) overcame the improving trend with increasing rib height. Therefore, design recommendations were suggested that the optimal rib spacing is equal to the rebar diameter, and the optimal rib height is 6% of the rebar diameter. This optimal rib geometry derives in an optimal *relative rib area* equal to 0.06.

The effect of rod geometry on concrete bond strength and stand-alone tensile strength and modulus was experimentally (and analytically) investigated in [28], using commercially available FRP reinforcement rods with well-controlled variations in depth and pitch on indented wrappings. An increase in the bond strength when increasing indent depth was observed, but no particular dependence on indent pitch was displayed. The loaded end slip, at the onset of free end slip, increased with increasing embedment length and decreasing rod diameter and was relatively constant for rods with similar embedment length to diameter ratios.

Once the importance of the rib geometry of ribbed rebars on bond behaviour is asserted, a further step is to analyze this same influence at varying levels of confining pressure. With this aim, the bond characteristics of four different types of GFRP

reinforcing bars with different surface deformations embedded in lightweight concrete ($f_c^{'}$=29MPa) were experimentally analyzed by [29]. The types of bars are shown in Figure 2.12. Type A bars had an external helicoidal tow which both provided a protruding deformation and small indentation in the bar surface. The indentations on type B bars were obtained by a stressed surface tow during fabrication. Type D bars were manufactured similar to type B but an outer resin layer was also added to the surface to protect the fibres. Type C bars have a helicoidal tow glued to the surface to provide only surface deformations.

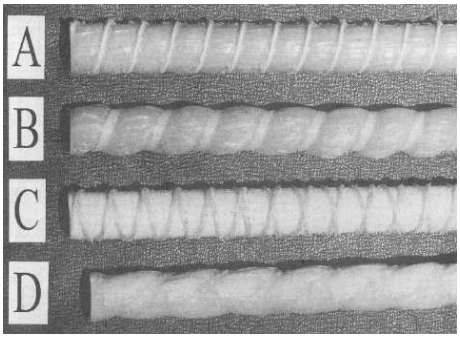

Figure 2.12: GFRP rebars used in [29].

Pull-out tests were performed with #6 GFRP bar (d_b=19mm) embedded in a 76mm diameter - 102mm long, precracked concrete cylinder subjected to a controlled amount of confining axisymmetric radial pressure. An embedment length of 67mm was considered (Figure 2.13).

For each type of reinforcing bars, bond stress-slip and bond stress-radial deformation relationships were obtained for five levels of confining pressure. The author concluded that the bond strength could be increased by increasing the confining pressure, but only when splitting of the concrete cylinder occurred. This was possible for rebars that presented a surface tow stressed so that indentations rather than deformations were obtained (rebars B and D), and for rebars with an external helicoidal tow providing a portruding deformation and small indentation which had an additional protection by an outer layer consisting exclusively of matrix material (rebar A). Small surface deformations, about 5.4% of the bar diameter, were thought to be sufficient to provide adequate bond behaviour similar to that obtained from steel bars. The bond strength of steel bars was between 1.2 and 1.5 times the bond strength of these types of GFRP bars for an identical amount of confinement.

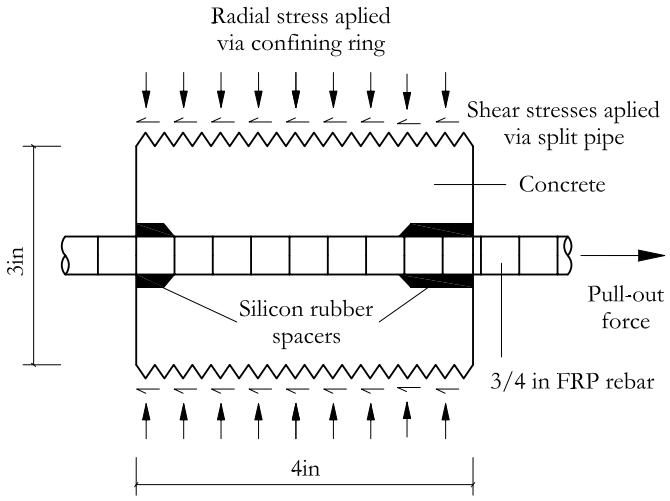

Figure 2.13: Test specimen used in [29] (units in inches; 1 in=25.4mm).

However, rebars with a surface tow glued to the exterior of the bar (rebar C) showed premature failure of the glued deformations, with bond resistance being only provided by friction between the rebar itself and the concrete. In this last case, no effect of the confining pressure was obtained.

The previous study was extended to four different types of CFRP rebars with different surface deformations embedded in lightweight concrete in [30]. The types of bars are shown in Figure 2.14. Type A bars had molded external deformations that mimic those of steel rebar, having a deformation height of about 0.6mm and a spacing of 7.6mm. The surface of type B bars was roughened to obtain very small deformations (0.0025mm high) very closely spaced (3mm). Type C bars were tendons fabricated by twisting and gluing seven separate CFRP smooth strands. The twist on the strands was low, resulting in an equivalent deformation spacing in excess of 150mm. Type D bars were also seven strand tendons.
In a first series of tests, specimens with the same dimensions as those of [29] were performed to obtain the local bond stress-slip data, as well as bond stress-radial deformation data, for four levels of confining axisymmetric radial pressure. In a second series of tests, the rebars were pulled out from 152mm diameter - 610mm long lightweight concrete specimens to provide preliminary data for development length assessment. This data was then used to calibrate an interface bond model presented in [31].

Figure 2.14: Carbon fiber reinforced polymer bar types used in [30].

The authors concluded that surface deformations with a height at least 6% of the nominal rebar diameter (i.e. similar to that of steel) and deformation spacing of not more than three times the rebar diameter, were sufficient to yield maximum bond stresses up to 8MPa, about twice the concrete tensile strength (type A and D bars). Bars with small surface deformation height of 0.3% of the nominal diameter squeezed through the concrete (type B), whilst bars with deformation spacing about 15 times the bar diameter twisted and squeezed through the concrete (type C). For types A and D bars (bars with adequate height and deformation spacing), bond strength could be increased more than twofold by increasing the confining pressure, whereas bars B and C could not induced significant lateral displacement, performing small bond strength increases with increasing confining pressure.

Up to this point, the main part of research was conducted in performing centric pull-out test, where the maximum bond strength of the FRP-concrete interface and its dependencies were examined. A parallel research on the concrete splitting tendency has also been performed, with the proposal of eccentric pull-out tests. Some studies with a combination of centric and eccentric pull-out tests are presented next.

In order to examine the bond behaviour of GFRP C-BARs (commercial name, f_{fu} ≅750MPa and E_{FRP}= 42GPa) to concrete, two series of pull-out tests, whose arrangement is shown in Figure 2.15, were performed by [32]. The tested bar was made of continuous glass fibres impregnated with polyester resin. The outermost layers were impregnated with urethane-modified vinyl ester and the surface had cir-

cumferential to the axis of bar inclined ribs connected to two longitudinal ribs.

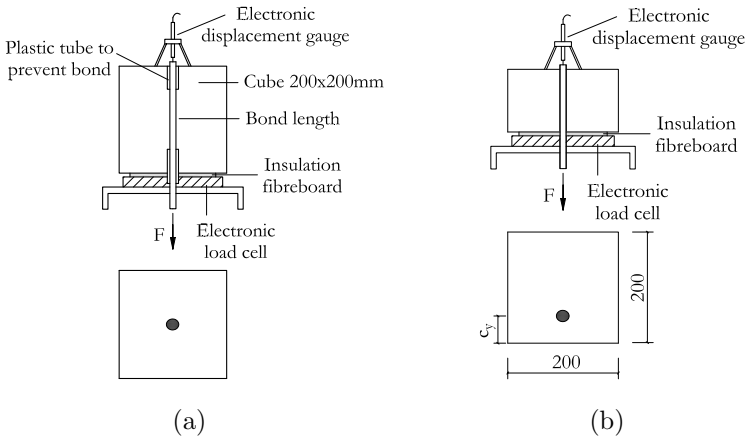

Figure 2.15: Pull-out test specimens with (a) central and (b) eccentric placement of bar (after [32]).

The centric pull-out tests series permitted the study of the ultimate bond strength. The bars used had diameters of 12 and 15mm, the embedment lengths examined were 3, 5 and 7 times the bar diameter and the concrete compressive strength was between 25 and 55MPa. The bars developed average bond strength of 20 and 15MPa, respectively. The authors concluded that the above bond values were similar to the ones developed by steel deformed bars and that the shear off strength of the bar ribs governed the bond strength of C-BARs at pull-out.

In the eccentric pull-out tests series, the concrete cover splitting tendency was examined. The embedment length was equal to 5 times the bar diameter. The concrete cover (c_y) varied between 1 and 2 times the bar diameter and the concrete strength varied between 25 and 55MPa. All the specimens failed by splitting. The cover splitting tendency along the bar was lower for the FRP bar than for steel bar (i.e. the pressure from the FRP bar cracked the concrete cover at a higher load than what was the case for steel bars). However, when the cover became split along the bar, the splitting tendency increased for the C-BAR and the final ultimate splitting crack pattern was formed and the cover was split off for a rupture load which was about 30% lower than that of steel bar.

The previously presented eccentric pull-out test was proposed in [18] to determine the concrete cover splitting resistance along the bar. In this publication [18] the clauses for steel presented in [5] were adapted for internal FRP reinforcement, in which was presented to be the easiest way to bring FRP materials into codes of practice. In this sense, test methods were proposed to estimate the coefficients η_1, η_2 and η_3 that represent the influence of the type of reinforcement, the position of the bar during casting and the bar diameter, respectively. The trend that larger diameter bars develop lower average bond strength than smaller diameter bars was confirmed in eccentric pull-out test, and mention to the inclusion of this effect on η_3 coefficient was done. Besides, some FRP bars gave relatively low bond strength when confinement was good, but had little splitting tendency, and thereby had a good bond, when confinement was only by concrete cover. Some other FRP reinforcements, with higher surface indentations and deformations, showed the opposite performance, because bond resistance was directly linked to splitting resistance.

Although pull-out tests have been widely accepted to study the bond behaviour of both steel and FRP rebars, a critical issue in the test set-up is that the stress conditions performed in pull-out tests differ from that occurring in the tension zone of flexural members, as in pull-out the concrete surrounding the bar is placed under longitudinal compression (Figure 2.16(a)), having an unaccountable favorable influence on the bond mechanism. Some attempts have been made in designing alternative tests that avoid the compression influence [33–35].

A specially designed test set-up was considered in [33], called Direct Tension Pull-out (DTP) test, where the anchorage was forced to occur in the presence of a uniform tensile stress field (Figure 2.16(b)). Thirty DTP square prisms having a total length of 250mm were considered, being the bar roughness and diameter, the size effect (expressed by the constant cover to bar diameter ratio) and the external confining pressure (exerted over the anchorage length by transverse externally bonded FRP sheets) the main variables studied. A constant embedment length of $5d_b$ was considered. Two types of FRP rebars, being the first type performed with sand coated and the second type with sand coated with helical lengthwise indentations, and three rebar diameters were considered.

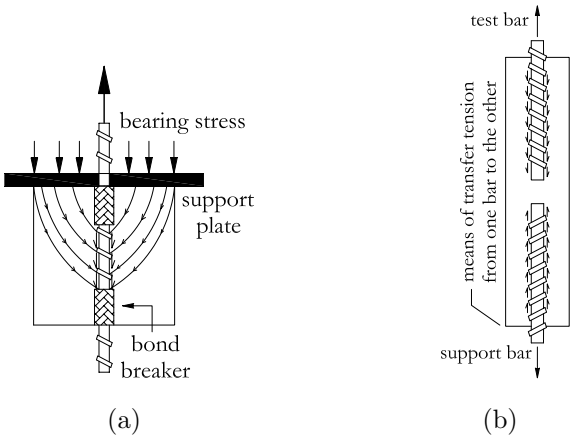

Figure 2.16: Test set-ups used in bond testing. Concrete is (a) in compression and (b) in tension.

Experimental results confirmed the unaccountable favorable influence of compression field in conventional pull-out tests, as local bond strength of GFRP bars anchored in DTP test was in the order of 6-10MPa, which is lower than the values reported in international literature that were obtained with conventional pull-out tests. Besides, an abrupt splitting mode of failure of the concrete cover was observed in all the cases where no extra confining pressure was provided, although the cover used was thick enough to promote a mix splitting/pullout failure mode (according to existing literature). In addition, the reported trend that higher bar diameter produce a lower bond strength was not confirmed for rebars with sand coated and different surface indentations, whose bond strength was similar irrespective of the rebar diameter.

As part of a wider research project on the bond between FRP reinforcement and concrete (rebars, sheets, laminates), results of traditional and modified pull-out tests are presented in [34]. The modified pull-out test was designed so that compression stresses on the concrete were avoided. The sketches of the test set up are shown in Figure 2.17.

Aramid, carbon and glass fiber-reinforced polymers (AFRP, CFRP and GFRP) externally sanded and spiral wound with fibers, GFRP ribbed, CFRP and GFRP fine sanded, CFRP and GFRP coarse sanded and traditional smooth and ribbed steel rebars were considered. Bond length of 5 rebar diameter was considered for the most of the specimens, but two different embedment lengths (5 and 7 rebar diameter)

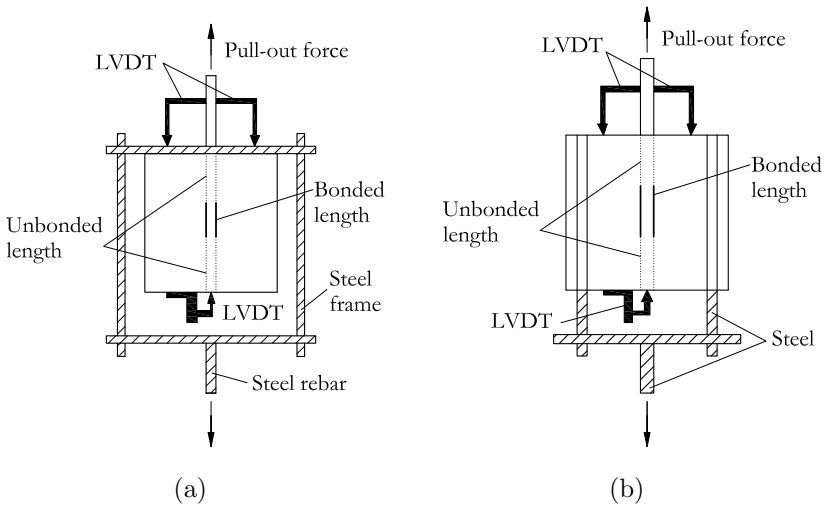

Figure 2.17: Test set up for (a) traditional and (b) modified pull-out test used in [34].

were considered for the first types of rebars. Four different concrete strengths were considered, ranging from 30 to 52MPa.
Experimental results showed that for deformed FRP rebars the contribution of mechanical interlocking is very efficient, performing threefold strength than that of sanded rebars. For both fine and coarse sanded FRP rebars the bond was attributed to chemical adhesion (given from the sand applied on the surface) and friction; therefore, a sudden drop of bond stress occurred after chemical bond was lost. Besides, the type of test had a different influence depending on the rebars investigated. The compression action on concrete, introduced in traditional pull-out test, was beneficial when steel an ribbed FRP rebars were used, because that action reduced possible concrete cracking. In contrast, the compression on the concrete gave a negative effect on the bond referring to sanded and spiral wound FRP rebars. The stress increase at the interface promoted the damage of the ribs, considering that in that case surface deformations were less effective in terms of mechanical interlocking with respect to the previous case.

An attempt to perform a modified beam test with great reduction of the compression stresses in the concrete core is presented in [35]. Seven bond tests were performed with GFRP bars (d_b=12.7mm, E_{FRP}=42GPa and average f_{fu}= 770MPa) and two more with steel reinforcing bars (for the sake of comparing bond properties).

Two different concrete grades were used, with average compressive strength values of 39MPa and 52MPa. However, within this concrete strength range, bond strength was dependent on the shear strength of the ribs of the FRP reinforcing bar rather than on the concrete strength, and therefore no influence was neither expected nor obtained. The main variable of this bond study was the embedment length, as four different values were considered (l_b=5d_b, 10d_b, 20d_b and 30d_b). The specimen scheme and the dimensions and scheme of the test set-up are shown in Figures 2.18 and 2.19 respectively. The test set-up allowed two bond tests on the two concrete elements to be conducted simultaneously.

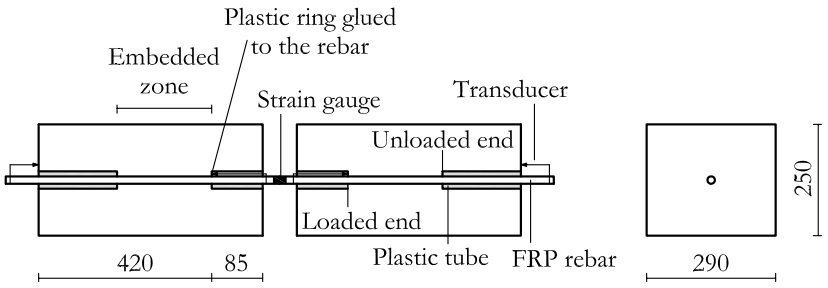

Figure 2.18: Specimen configuration used in [35] (units in mm).

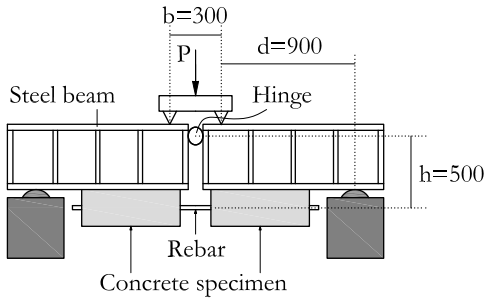

Figure 2.19: Test set-up for modified beam test in [35] (units in mm).

From experimental results, the authors concluded that an embedment length of 10d_b was approximately equal to the development length, as for shorter embedment lengths pullout failure took place whilst for larger embedment lengths bar failure in tension happened. When pull-out failure took place, damage was observed both on the ribs of the reinforcing bars and through the concrete. Reported results confirmed the trend that larger embedment lengths develop smaller bond strength and vice versa.

An innovative pull-out test was presented in [36] to investigate the top bar effect. The direct pull-out specimen consisted of a concrete wall (1200 x 760 x 400mm) with the GFRP bars placed at the top, bottom and middle through the wall, as shown in Figure 2.20. Top bar effect is defined as the ratio of ultimate bond strength reached in pulling out the bottom bar to that reached in pulling out the top bar. Due to the bleeding of water and air trapped beneath the top rebars, the concrete surrounding these bars was less consolidated than that of bottom bars.

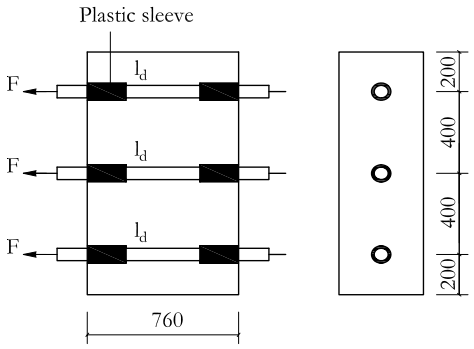

Figure 2.20: Pull-out specimens used in [36] (units in mm).

From experimental results on 18 pull-out tests, the author recommended a top bar effect factor of 1.3 to be used. However, a factor of 1.5 was recommended in [37] and 1.1 was recommended in [38]. Besides, experimental results on 64 beam tests on two types of FRP rebars, both of them made up with E-glass fibre and polyester resin (Figure 2.21), and d_b=12.7 and 19.2mm, were also presented. Type A rebar had a smooth surface which was deformed with an helical winding of the same kind of fibres. A thermosetting resin was applied as well as a coating of sand particles of a specific grain-size distribution. The geometry of the ribs was the same for all rebar sizes and the resulting rod surface was said to be spirally wound. In type B rebars the deformation was obtained by wrapping the rod thoroughly with a resin impregnated strand prior to entering in the heating die that polymerized the resin. The resulting rod surface was said to be deformed.

From the tests results the authors concluded that GFRP rebars showed lower bond strength values than steel rebars. Besides, bond strength of GFRP rebars was controlled by adhesion and friction, whilst the bearing component was the major source of the bond for steel rebars. Within GFRP rebars, type A rebar performed

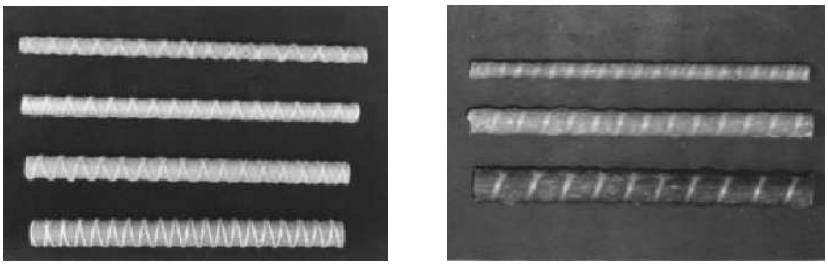

(a) (b)

Figure 2.21: Type A and B of GFRP rebars used in [36].

higher bond strength than type B. The decrease in bond strength due to an increase in rebar diameter or an increase in embedment length was explained as a consequence of the bleeding of water in concrete in the former, and the approach of the applied load to the tensile strength of the rebar in the latter.

2.3.5 Fibre reinforced concrete

Though the main research is focused in bond strength of FRP embedded in plain concrete, complementary research has been made in the bond behaviour when fibre reinforced concrete is considered.

A study on the pull-out bond-slip response of GFRP and CFRP reinforcing bars embedded in fibre reinforced concrete was performed in [39]. Three different reinforcing bars were considered. Type R1 and R2, with nominal diameters of 25.4 and 12.7mm respectively, consisted on GFRP rebars wrapped with helical fibre strand to create indentations along the rebars and sand particles added into the surface to enhance their bonding strength. Type R3 consisted on a 12.7mm CFRP rebar with very smooth surface. The resins used were vinylester and epoxy modified vinylester for GFRP and CFRP rebars, respectively. Commercially available polypropylene short fibres, with maximum length of 57mm, were used as concrete reinforcement in some specimens. The compression strength of concrete was 37 and 51MPa for FRC and plain concrete, respectively.
From experimental data on the bond behavior of 27 pull-out specimens, designed according to [40] and with embedment length of 5 and 10 rebar diameter, the authors

concluded that the addition of polypropylene fibres did not increase the ultimate bond strength but provided much more ductile bond behavior (in terms of larger slips for maximum bond strength) and changed failure mode from splitting to pull-out. Due to different surface treatments, different bond mechanisms were observed for GFRP and CFRP rebars. Bond strength decreased when embedment length increased for GFRP rebars whilst opposite behaviour was observed for CFRP rebars. Two peak bond values were observed for CFRP specimens. The first peak happened when maximum local chemical bond stress moved to free end, and the second peak value happened when friction force reached its peak.

Bond behaviour between non-corrosive FRP reinforcing bars and high-strength concrete when reinforcing fibers were added to make concrete less brittle was also studied in [41]. Bond specimens consisted on 150mm in diameter and 300mm in length cylinders. CFRP (9mm in diameter) and GFRP (13mm in diameter) rebars were considered, consisting the former of 70% carbon fibre and 30% vinylester resin and of 70% E-glass fibre and 30% vinylester resin the latter (Figure 2.22). Both types had surface ribs that were manufactured using PVA fiber braiding technology. Three different concrete mix proportions were considered with 20 or $40kg/m^3$ steel fibre, or 4.55 or $9.1kg/m^3$ synthetic fibre (Figure 2.23). The embedded length of the reinforcing bar was up to four times the bar diameter.

From experimental results it was concluded that the bonding of both CFRP and GFRP reinforcing bars increased significantly with the increase in concrete strength. Besides, concrete compressive strength increased slightly as more fiber was added to the mixture. Authors also concluded that bars with larger diameter produced a higher bond strength. However, this conclusion can not be taken as valid because fiber type effect and diameter effect were coupled in experimental results and their separate effects can not be distinguished from experimental data. The addition of fibres in concrete matrix enhanced the bond between the concrete matrix and reinforcing bar due to the bridging effect during the early micro-slip phase and concrete internal crack phase. Propagation of internal cracks was also prevented due to bridging effect. The highest bond strength improvement due to reinforcing fibre addition in concrete matrix was achieved with steel fibers.

Figure 2.22: FRP rebars used in [41].

(a) (b)

Figure 2.23: (a) Synthetic and (b) steel fibers used in [41].

2.3.6 Analytical studies

Bond between reinforcement and concrete can be analytically described by means of a constitutive bond stress-slip relationship that can be introduced in the solution of problems such as the calculation of the development length.

Generally, the evaluation of such constitutive law is performed with pull-out tests, that are normally characterized by short embedment lengths. Moreover, values of bond strength are obtained by assuming a constant distribution of bond stresses along the embedded zone. This procedure has been widely accepted when dealing with steel reinforcement, because slip values at the loaded and unloaded end are very similar and therefore the assumption of a constant distribution can be accepted. When FRP rebars are considered, the value of the slip for the loaded end differs from that of the unloaded end, meaning that the constant bond stress distribution assumption is inadequate. A possible solution to this situation is to reduce the embedment length of the FRP-concrete specimens, but the reduction in the embedment length can lead to a magnification of the local irregularities so

that the test results may have large scatter. This set of factors highlights that the assessment of the bond stress-slip law is not straightforward.

Some experimental programs have been combined with an analytical study on the bond stress-slip law. Every analytical study presented has been based on its own experimental data, being difficult to separate the experimental data report from the proposed analytical description of the bond-slip law. A brief review of some of this experimental/analytical research is presented next.

At the early stages of the study of bond behaviour of FRP materials, any analytical description of the bond-slip law was conducted by applying the well-known model for deformed steel rebars presented in [42] and known as B.E.P. model. The initial loading branch of B.E.P. model, for $0 \leq s \leq s_m$, is described as:

$$\frac{\tau}{\tau_{max}} = \left(\frac{s}{s_m}\right)^{\alpha} \tag{2.3}$$

where τ_{max} and s_m are the maximum bond stress and the corresponding slip, respectively, and α is a parameter to be calibrated. This loading branch was followed by a plateau $\tau = \tau_{max}$, for $s_m \leq s \leq s_2$, and by a linear decreasing branch starting from the point τ_{max}-s_2 and leading to the value of the residual bond-resistance, τ_{res} at a slip value s_3.

The first attempt in proposing a bond-slip law based on experimental results on FRP reinforcing bars was presented in [29]. After an experimental campaign on the possible influence of the confining pressure on the bond-behaviour of GFRP rebars, the author proposed two expressions to define the peak on the bond-slip law as a function of confinement as follows:

$$\frac{\tau_{max}}{f_t} = A + B\left(1 - e^{\frac{-C\sigma}{f_t}}\right) \tag{2.4}$$

$$\frac{s_m}{d_b} = D + E\frac{\sigma}{f_t} \tag{2.5}$$

where τ_{max} is the peak bond stress, s_m is the slip at the peak bond stress, σ is the confining axisymmetric radial pressure, f_t is the tensile strength, d_b is the nomi-

nal bar diameter and A, B, C, D and E are non-dimensional empirical constants. Afterwards, author proposed to describe the complete normalized bond-slip law as:

$$\frac{\tau}{\tau_{max}} = \frac{F\left(\frac{s}{s_m}\right) + (G-1)\left(\frac{s}{s_m}\right)^2}{1 + (F-2)\left(\frac{s}{s_m}\right) + G\left(\frac{s}{s_m}\right)^2} \tag{2.6}$$

where F and G are nondimensional empirical constant to be adjusted for each bar type.

An extension of the ascending branch of the B.E.P. model to its use in FRP reinforcement was proposed in [43]. The so called C.M.R. model proposed is defined by the following expression:

$$\frac{\tau}{\tau_{max}} = \left(1 - e^{\frac{-s}{s_r}}\right)^{\beta} \tag{2.7}$$

where s_r and β are parameters to be calibrated based on curve-fitting of experimental data. Authors denoted that the new C.M.R. model was based on B.E.P. model and not on Malvar model because the latter does not accurately describe the physical phenomenon at the beginning of the test. In other words, if the initial tangent of both models was compared (i.e. for s=0), B.E.P. initial tangent becomes infinity (which would represent the adhesion bond mechanism) whilst Malvar model initial tangent becomes $F\tau_m/s_m$. Experimental data was used to calibrate both B.E.P. and C.M.R. models and good accuracy was found for the two models. However, although the B.E.P. model describes the entire bond-slip curve, better predictions on the ascending branch were obtained with the C.M.R. model.

By comparing experimental bond-slip curves of FRP rebars and the analytical ones obtained by applying the original B.E.P. model (Equation 2.3), no experimental plateau was observed in [44]. Therefore, authors suggested not to consider it and modify the descending branch. The model that resulted from these changes is known as Double Branch Model (D.B.M) and can be expressed as shown next:

$$\tau = \tau_{max}\left(\frac{s}{s_m}\right)^{\alpha} \qquad\qquad s \leq s_m \tag{2.8}$$

$$\tau = \tau_{max}\left[1 - \frac{p\,(s - s_m)}{s_m}\right] \qquad s_m \leq s \leq s_3 \tag{2.9}$$

$$\tau = \tau_{res} \qquad s > s_3 \tag{2.10}$$

With the aim of assessing their reliability to simulate the experimental results, the main parameters of the D.B.M. (except α) and the C.M.R. model (Equations 2.8-2.10 and 2.7, respectively) were calibrated by the least-square error method, while parameter α of the D.B.M. model was evaluated by equating the area underneath the ascending branch of the analytical bonds-lip curve. Parameters of the Malvar law (Equation 2.6) were determined by curve-fitting. Results were presented with reference to the rebar surface in spite of the rebar diameter and plotted analytical curves were obtained by using the coefficients calibrated to its experimental counterpart instead of using the mean values reported. No specific formulation for different rebar surfaces or rebar diameters was presented. Because of the great importance of the ascending branch of the bond-slip law at serviceability conditions, the C.M.R. model was proven to lead to the best simulations.

A new analytical expression for the bond-slip law was proposed in [45]. The new expression, named m.B.E.P. model, was obtained by multiplication of B.E.P. model by a linear function assuming a value of 1 at s=0 and a value of 0 at a certain $\overline{s}$. The final expression that defines the m.B.E.P. model reads:

$$\tau = Cs^{\alpha}\left(1 - \frac{s}{\bar{s}}\right) \tag{2.11}$$

where C=τ_{max}/s_m^{α} and α and $\bar{s}$ are adjustable parameters. The presentation of the m.B.E.P. model [45] was complemented with the proposal of a numerical method to calibrate parameters of a given local bond-slip relationship by a computational minimization of the difference between the experimental and the numerically simulated pull-out test results. The method involved the slip distribution throughout the embedment length, corresponding to a certain pull-out force, as this important characteristic is related to the substantial difference between the loaded and unloaded end slips [22, 23, 46] and to the observed dependence of the average bond strength on the embedment length, which results from the nonlinear distribution of the bond

stress along the embedded portion of the bar [14, 23, 46]. The described method needed for each specimen a quite long computation time, owing to the necessity of solving a great number of different equations. Besides, authors did not define any tendency on the rebar diameter for the parameters of the local bond stress-slip relationship, meaning that new calibrations need to be done if different diameters than those considered in the study are analyzed.

After the proposal of a bond-slip law for the entire curve presented in [29], a new attempt to fit a model only to the ascending branch of the bond-slip law response was made in [30]. The expression was derived in two steps with the help of experimental data on CFRP rebars presented in the same publication [30]. First, the peak on the bond-slip curve was defined as a function of confinement with the following equations:

$$\frac{\tau_{max}}{f_t} = A + B\frac{\sigma}{f_t} \tag{2.12}$$

$$\frac{s_m}{d_b} = C + D\frac{\sigma}{f_t} \tag{2.13}$$

where A, B, C and D, are nondimensional empirical constant to be calibrated for each rebar. Second, the authors proposed a new relation for the ascending branch of the bond-slip law, that was named as modified C.M.R. model (M.C.M.R. model), and can be expressed as:

$$\frac{\tau}{\tau_{max}} = \left(1 - e^{\frac{-s\gamma}{s_m}}\right)^{\beta} \tag{2.14}$$

The difference between the C.M.R. model and the M.C.M.R. model is the replacement of $s_r = s_m/\gamma$. The experimental data presented in [30] was used and, for each bar type, the A, B, C and D constants were evaluated by minimizing the difference between measured and predicted bond stress (least square fit), keeping in mind that the proposed empirical formulas were limited to the ranges of pressures tested. The same procedure was used to evaluate the α parameter of the B.P.E. model [42] and the β and γ parameters of the M.C.M.R. model. This analytical work was then used to further develop and calibrate a different and more complete bond model [31] that incorporated both σ (the confining radial pressure) and the

interface dilation (representing the radial deformation).

The previously presented analytical expressions of the bond-slip law of FRP rebars have been widely considered in the literature to assess their reliability to simulate the experimental results available in the literature [19, 26, 29, 30, 34, 35, 43–45]. For instance, the experimental program developed in [26] was complemented with the calibration of the B.E.P. bond-slip analytical model [42]. The unknown parameters of the model were calibrated by best fitting for both machined and sanded CFRP rods. Calibration was done in a individually manner and no definition on the dependencies of these parameters was set. Moreover, three theoretical approaches were considered in [34] and bond stress-slip relationships were calibrated on the basis of the experimental results obtained. The analytical expressions of the theoretical approaches corresponded to Equations 2.3, 2.7 and 2.11, which describe the B.E.P. model [42], the C.M.R. model [43] and the m.B.E.P. model [45], respectively. A first calibration was made for each type of rebar analyzed, collecting data referred to both pull-out and modified pull-out tests, and with the aim of studying the influence of the kind of test. A second calibration was done to evaluate the influence of rebar deformability. Finally, all curves referring to the same kinds of rebars were calibrated. Results confirmed the relevant influence of the surface treatment on bond stress-slip law not only in terms of typology (ribbed, sanded and spiral wound) but also in terms of specific properties within the same typology. Although big efforts in calibrating the existing analytical expressions have been made, the lack of rebar surface or rebar diameter consideration is presented as the main drawback of the works already mentioned; improvement of the fitting process means the necessity on determnine how the rebar diameter and surface affect not only the maximum bond strength but also the different parameters included in the bond-slip law.

Alternatively, some authors have studied the dependencies between the bond strength of the FRP bars and the compressive strength of the surrounding concrete [24, 36, 47].

An extensive experimental program on pull-out test on straight FRP reinforcing bars was conducted in [47]. In the program 151 pull-out tests were performed and

a wide number of variables was studied: steel and FRP (AFRP, GFRP and CFRP) rebars, with diameters of 6, 8, 10, 16 and 19mm, different surface improvements (sand coating, surface texture, helical wrapping with sand coating, deep dents or grooves, and deformations by resin (surface undulations, indentations or ribs)), different embedment lengths (5, 7 and 9 times the rebar diameter) and three different concrete mixes, with compressive strengths ranging from 29.7MPa to 60.4MPa. For the proposal of the new relationship between concrete compressive strength and developed bond strength, next assumptions were made:

- The average bond strength was normally distributed.
- The average bond strength was proportional to $\left(f_c^{'}\right)^{0.5}$.
- As for steel, the average bond strength of FRP rebars decreased as the reinforcing bar diameter increased.

As a result, the authors proposed Equation 2.15 and calibrated it with experimental data, where $\tau_{b,max}$ is the average bond strength, f_c' is the specified concrete compressive strength and d_b is the effective rebar diameter. This new expression verified the relationship proposed for GFRP by [48], differing only in the constant (14.7 versus their value of 14.25).

$$\tau_{b,max} = 14.7\frac{\sqrt{f_c'}}{d_b} \tag{2.15}$$

Based on the relationship between concrete compressive strength and bond strength proposed in ACI design code (Equation 2.16), and considering that the conclusions of [11] and [47] (Equation 2.15) were based on the bond strength of FRP bars tested in the concrete with compressive strengths lower than 60MPa, two alternative equations for the evaluation of bond strength for a steel and a FRP bar, (Equations 2.17 and 2.18, respectively), embedded in a concrete with a compressive strength up to 90MPa were proposed in [24]. No dependence of bond strength on rebar diameter is seen as a drawback of the equations proposed.

$$\tau_{b,max} = 20.23\frac{\sqrt{f_c'}}{d_b} \tag{2.16}$$

$$\tau_{b,max} = 4.1\left(f_c'\right)^{0.5} \tag{2.17}$$

$$\tau_{b,max} = 3.3\,(f'_c)^{0.3} \tag{2.18}$$

A new proposal for the evaluation of the bond strength of FRP rebars was derived in [36]. The proposal was derived from a previous study on how to adapt the development length equation proposed for steel-reinforced concrete presented in ACI [8], and shown in Equation 2.19, to FRP reinforcement. Experimental data was used to find the value of K constant. Afterward, concrete compressive strength and FRP bond strength were related as shown in Equation 2.20

$$l_{db} = \frac{K A_b f_{fu}}{\sqrt{f'_c}} \tag{2.19}$$

$$\tau_{max} = 4.97 \frac{\sqrt{f'_c}}{d_b} \tag{2.20}$$

2.3.7 Numerical studies

In the empirical approaches described above, the constants that must be determined to calibrate the proposed models are valid and useful to describe the bond behaviour of the specific tests used for calibration. However, extension of these constants to predictions with different testing conditions is not possible. Therefore, efforts have been made to develop numerical models that provide higher flexibility in incorporating the very diverse bond mechanisms that exist for different FRP rebar surface configurations.

A complete up-to-date review on the numerical works dealing with the bond behaviour of FRP rebars was presented in [31]. The models were classified in three categories: a) *member scale*, where bond behaviour is characterized by a bond-slip law and each reinforcing element is treated as a one-dimensional bar element; b) *rib scale* where the complex shape of the bar surface should be discretized with finite elements, and c) *bar scale* where the bar surface structure is not explicity modeled and the effects of the mechanical interaction are characterized indirectly using an interface description. A *member scale* approach is not useful for the study of local bond-slip behaviour at an arbitrary point in the structure. Likewise, *rib scale* models are normally limited to qualitative evaluations of the active mechanisms of bond

because of the simplifying assumptions. Therefore, *bar scale* models were presented to be the most effective to study the bond mechanisms.

To give some examples of the different categories previously presented, some numerical studies are presented next. An example of *rib scale* model can be found in [49], where a commercial finite element program was used to create a two-dimensional, axisymmetric, non-linear model of a FRP rod/concrete specimen containing a strain probe (Figure 2.24). The model was created with four-noded elements. The contact pressure, produced by the initial radial interference, and Coulomb friction were modeled by two-dimensional interface elements, whilst chemical adhesion was modeled by nonlinear spring elements bridging all adjacent nodes of concrete and FRP within the embedment length.

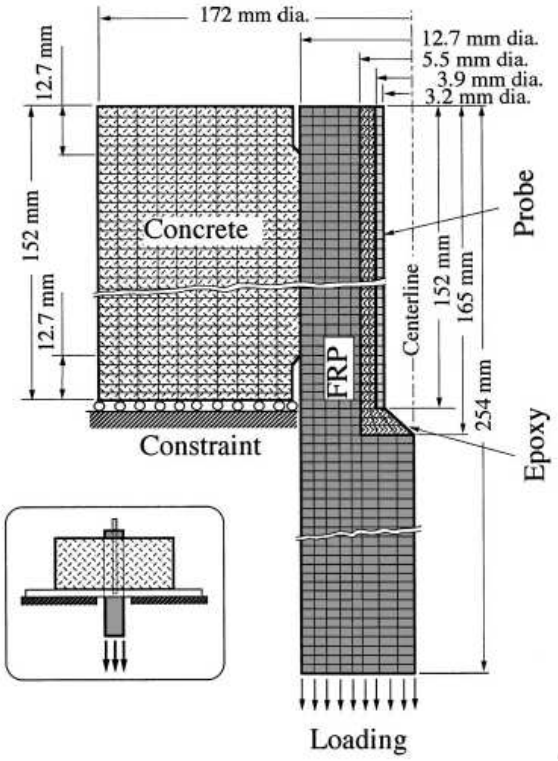

Figure 2.24: Two-dimmensional axisymmetric FEM of smooth rod [49].

The bond controlling parameters, identified by direct pull-out test data, were rigorously determined for smooth rods and the finite element predictions of the dependence of slip and longitudinal and hoop strain distribution in the embedment

length matched the experimental data. By conducting parametric studies, transverse stiffness of the smooth rods was identified as the most important bond controlling rod property. Friction caused by radial contact pressure and chemical adhesion were also found to be operative bond mechanisms. For the lugged rods, the experimentally observed bond mechanisms of mechanical interlock was simulated in a separate finite element model, which incorporated features of the smooth rod bond model. Parametric studies showed that the shear strength of the lugs was the single most important property controlling the bond of FRP rods tested, while moiré interferometry indicated that both shear and rotation of the lugs could affect bond stiffness.

A more recent example of *bar scale* model can be found in [50]. The FRP-concrete cube was modelled by using two-dimensional elements. Concrete and FRP rebar were modelled with 4-noded plane elements and 2-noded square elements, respectively. The bond interaction between the two materials was modelled with springs elements, whose characteristic input data were the spring extension and the corresponding forces. Experimental data of pull-out test in short embedment length (l_b=2d_b and 4d_b) was used to calibrate the spring characteristics. Thereafter, larger embedment lengths were modelled and the trend of bond strength decreasing with increasing embedment length was analytically confirmed. However, authors found that the rate of bond decrease was much faster in smaller embedment lengths whereas for larger embedment lengths the bond strength appeared to be leveled. The model was thereafter extended with the incorporation of the splitting behaviour to study the flexural behaviour.

Based on the one-dimensional geometry of the bar and considering the interface surface properties, a numerical model was presented in [51]. The system included concrete continuum elements, bar truss elements and bond elements, and any arbitrary bond-slip law could be implemented. Authors highlighted that results from any FEM model that assumes perfect bond are highly dependent on mesh size, and therefore bond models were presented as an efficient tool because they reduce the effect of mesh size.

Several cohesive-zone models have been proposed and studied in the last years, because of their flexibility to simulate the gradual process in which the separation of an incipient crack is constrained by cohesive stresses. Developed in the framework of damage mechanics and of the plasticity theory, these models offer a wide range of possible applications. A key aspect for engineering applications of the cohesive-zone models is represented by the combination of the debonding process with friction. In this sense, the model presented in [52] neglected friction as long as the interface damage was not complete and introduced a friction term only when complete decohesion was attained. On the other side, a friction term was introduced from the very beginning in the model presented in [53]. In a mid-point between these two extreme models, two uncoupled laws were used that represent the normal and tangential stresses in [54]. A condition of the tangential stress to be lower than the modulus of the normal stress times the friction coefficient was introduced. As an alternative to this last model, a representative element area was introduced in [55], which could be descomposed into an undamaged part and a completely damaged part. The idea of the study was to introduce a friction law only on the damaged part of the representative element area.

2.4 Bond influence on cracking behaviour of RC tensile members

The bond between the reinforcement and the surrounding concrete is commonly described through the relationship between the local bond stress and the relative slip of the bar. Although this bond-slip law is usually obtained in pull-out tests, the bond development of real reinforced concrete structures is not accurately described because of the compressive stresses of the concrete surrounding the reinforcing bar appearing in pull-out specimens.

The interaction between the reinforcing bar and the surrounding concrete is the central problem which affects the behaviour of the composite element. It governs the stress distribution along both the concrete and the reinforcing bar, and allows concrete to carry tension between cracks, thus providing additional stiffness to the overall structure response of reinforced concrete elements. This phenomenon

is known as *tension stiffening* and is expected to happen both in the tension zone of reinforced concrete elements subjected to bending and in reinforced concrete ties in pure tension. In this sense, although the former are the most probable elements to be found in structures, the latter are thought to better represent the bond behaviour, because a reinforced concrete element that is subjected to axial loading is one of the most simple problems which incorporates several basic characteristics of reinforced concrete without coupling bending singularities.

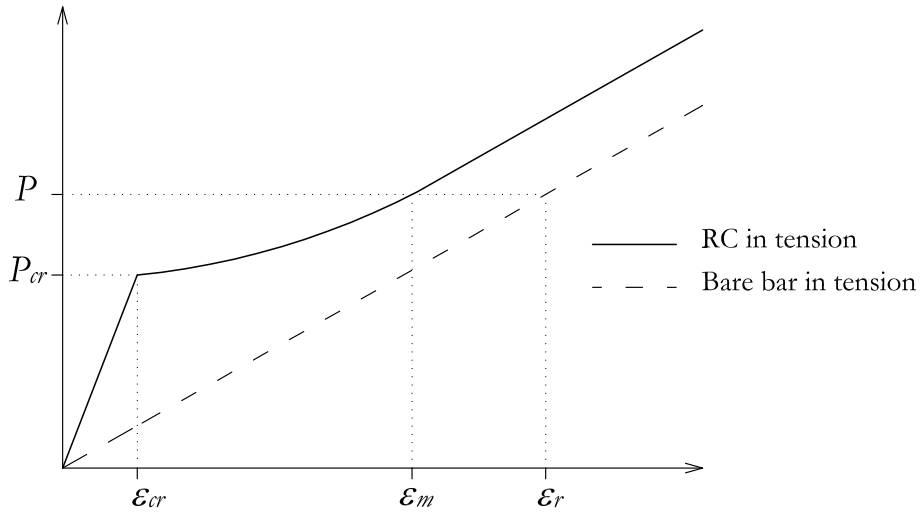

Figure 2.25: Applied tensile force vs. strain of bare bar and RC in tension.

Before cracking, stresses and strains in an RC element in tension are uniform along the length of the member. Forces equilibrium and compatibility of strains are linked together by assuming linear elastic material behaviour for both the concrete and the reinforcement. Therefore, the applied load is shared between the concrete and the reinforcement in relation to their respective rigidities (see Figure 2.25). Once the concrete cracks, the reinforcing bar experiences a jump in stress at the crack locations, and the distribution of stresses and strains is no longer uniform along the member length. The reinforcing material is assumed to carry all of the tension at the crack locations, whilst both the concrete and the reinforcing material share the tensile force between the cracks. A proper way to account for the variation in force and deformation values along the member length is to represent the member response with average or smeared stresses and strains. Therefore, for a certain applied

load P, whilst a bare bar would record a strain of ϵ_r (according to the stress-strain behaviour of the bar) the overall response of the bar embedded in concrete is equal only to ϵ_m , which is less than ϵ_r (see Figure 2.25). In other words, at the applied load P, it is only at crack sections that the bar stretches to the strain ϵ_r, and in all other sections the bar shares forces with the concrete, making the overall response of the RC element be equal to ϵ_m.

Similar to the case of pull-out test, the bond influence on the cracking response of RC members has been more widely studied for steel reinforcement than for FRP reinforcement. Additionally, although this bond influence is encountered when the reinforced concrete is under tension, the major part of the available work is based on flexural elements. Therefore, little literature centered on FRP RC tension ties is available and a complete review on both steel and RC reinforced members is presented next.

Existing models that study the cracking behaviour of reinforced concrete structures can be classified in three groups. The first group encloses the models that evaluate the deformability of the structure by an elastic analysis, where an effective cross-sectional area is determined as a combination of the gross area and the cracked area [6, 56].

The second group includes models that modify the constitutive equation of either the reinforcing material or the concrete. In the first case, known as the *tension stiffening strain* approach [62], the model uses a modified relationship for the stress-strain response of the embedded reinforcing material and concrete is described as a brittle material [5, 63, 64]. In the second case, known as the *load sharing* approach [62], reinforcement is supposed to behave as an elastic material and the extra stiffness of the RC member is included in concrete tensile post-cracking response. This *load sharing* approach was first introduced by Considère [65]. Based on this concept, several stress-strain curves for concrete in tension have been proposed for the study of steel reinforced concrete. As an example, a stepped stress-strain curve was proposed in [57], a gradual unloading curve was proposed in [58] and a discontinuous unloading curve was proposed in [59]. These works were the first notable

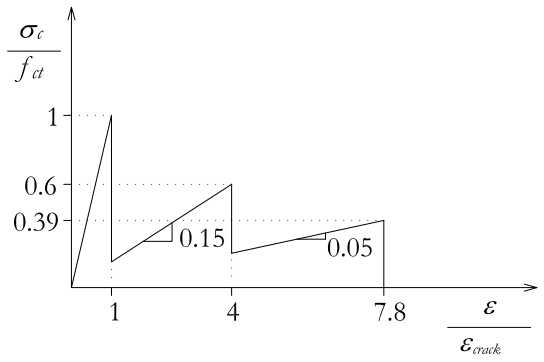

(a) Stepped curve proposed in [57]

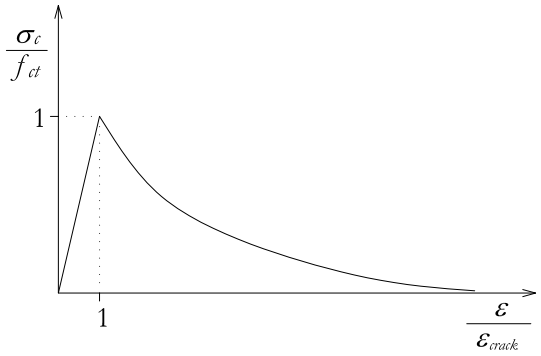

(b) Gradual curve proposed in [58]

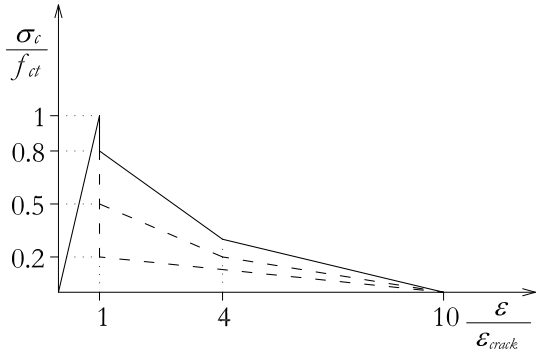

(c) Discontinuous curve proposed in [59]

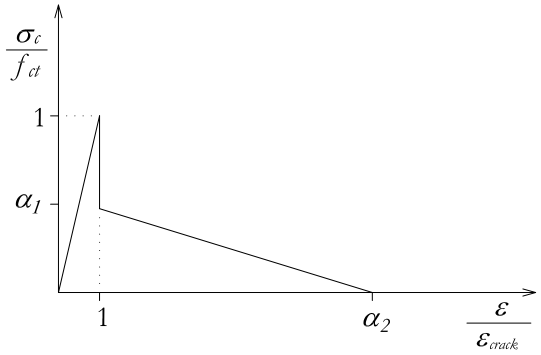

(d) Discontinuous curve proposed in [60, 61]

Figure 2.26: Modelling of concrete tensile stress-slip curves.

attempts to characterize the post-cracking behaviour of reinforced concrete through a concrete modified stress-strain relationship. Although being easy to implement and readily applied to analyze full-scale structures, they were said to oversimplify the *tension stiffening* effect because of the lack of consideration to differences in materials' properties and reinforcement ratios [66]. More recent works have proposed similar stress-strain curves for concrete in tension where the reinforcement ratio was included [60, 66].

Further works have been proposed to consider the different characteristics of reinforced concrete members. As an example, an average post-cracking tensile stress in concrete was expressed in [67] by the so-called *tension stiffening factor*, λ, defined as follows:

$$\lambda = \xi \left(1 - \eta\zeta\right)^{1/2} \tag{2.21}$$

The proposed factor was defined to be a function of three parameters (ξ, η and ζ) that were related to the maximum tensile stress in concrete, $\sigma_{c,max}$, the transfer length, l_t, the average crack spacing, s_{rm}, and the distribution of concrete stress. More recently, an exponential decay curve was proposed in [66] to describe the post-cracking range of the tensile stress-strain law of concrete:

$$\sigma_c = f_{ct} e^{-\alpha\left(\frac{\epsilon}{\epsilon_{cr}}\right)} \tag{2.22}$$

where α is the exponential decay parameter, f_{ct} is the concrete tensile strength and ϵ_{cr} is the corresponding strain. The exponential decay parameter, α, was defined as a function of the reinforcement ratio, ρ, and the steel-to-concrete modular ratio, n. Taking as a basis the CEB tension-stiffening model, Equation 2.22 was adjusted to each curve and adjusted α values were used to derive an expression that relates the exponential decay parameter and the value of $n\rho$.

In the last years, some studies were centered at determining the influence of the shrinkage deformation generated while curing on the behaviour of RC ties [61, 62, 68–70]. A generalized conclusion of the existence of an initial shortening of the member and a lower cracking load (since concrete is under an initial tensile load) has been

recognized. Kaklauskas and co-workers [61, 69, 70] state that the concrete post-cracking tensile behaviour is dependent on the reinforcement ratio, even when the effects of shrinkage deformation are included. In this sense, a methodology for determining the stress-strain relationship for concrete from experimental results on short term flexural tests of RC members has been proposed in [61]. However, Bischoff and co-workers [62, 68, 71] state that, as long as the shrinkage effects are included, reinforcement ratio plays no role on the tension stiffening effect. Based on this statement, a reinforcement ratio-free concrete post-cracking constitutive equation was proposed in [71] for its application to steel RC ties:

$$\frac{\sigma_c}{f_{ct}} = e^{-800(\epsilon_m - \epsilon_{cr})} \tag{2.23}$$

where σ_c is the concrete average tensile stress, f_{ct} is the concrete tensile strength and ϵ_{cr} is the concrete strain at cracking. Equation 2.23 was extended in [68] to FRP RC ties as:

$$\frac{\sigma_c}{f_{ct}} = e^{-1100(\epsilon_m - \epsilon_{cr})\frac{E_{FRP}}{200}} \tag{2.24}$$

where $\frac{E_{FRP}}{200}$ is a factor that normalizes the tie response respect the modulus of elasticity of steel.

All these models that define a constitutive behaviour of concrete capable to consider the contribution of concrete in tension between cracks [60, 61, 61, 62, 66–69, 71–73] appear to be an easy to implement and useful tool to study the cracking behaviour of RC members.

Finally, the third group of models that study the cracking behaviour of RC tensile members encompasses the models that take into account the natural/stand-alone behaviour of the materials (steel, FRP and concrete) and include the modelling of their interaction. In these models the member deformability is evaluated by a non-linear analysis using a specific bond-slip law. Within this third group, two different subgroups can be found. The former comprises those models that solve the system of differential equations that arise from the analytical study of the problem [67, 74–79]. The second subgroup includes those models that use a numerical procedure

(i.e. finite difference methods and/or finite element methods) to solve the system of differential equations [80–84].

2.4.1 Experimental studies

The study of the interaction between reinforcement and concrete is essential for predicting the deformations characteristics of reinforced concrete. The study of this interaction becomes more important for predictions at service loads, where serviceability limit states govern the design of RC flexural elements. Although existing code formulations for steel RC structures give good predictions, their "direct" adaptation to FRP reinforcement has not been successful in all cases. The lack of accuracy of some of the existing methods has brought researchers to perform experimental programs to understand how the differences in reinforcing material properties can affect the characteristics in cracking (i.e. crack spacing, crack width and deflections) of FRP RC flexural elements, and how *tension stiffening* effect, that results from the bond interaction of reinforcement and concrete, should be accounted for in design equations. However, little research has been focused on the study of FRP RC tensile elements, where the fundamentals that govern RC characteristics are more naturally represented.

First results of an experimental program on FRP RC tensile members can be found in [85, 86]. Ordinary concrete, with mean compressive strength of $f_c^{'} \simeq 47$MPa was used, and CFRP rebars with a modulus of elasticity of $E_{FRP} \simeq 110$GPa and a rupture tensile strength of $f_{fu} \simeq 2400$MPa were considered as internal reinforcement. The experimental investigation was carried out on cylindrical specimens varying the concrete cover thickness. Measurement of the elongation of the rebar embedded in concrete and of the concrete itself was possible due to the use of LVDTs. Moreover, strain gauges were glued on the rebar surface (before casting the specimen) and on the concrete surface to measure both the evolution of strain in the reinforcement and the possible load eccentricity. According to presented results, there exists a threshold value of concrete cover over reinforcement diameter, c/d_b=3, over which little further benefit from the bond interaction between reinforcement and concrete is obtained.

Based on the experimental study of the effect of shrinkage deformation on the cracking behaviour of SRC ties presented in [62], an experimental program on FRP RC ties was presented in [68]. The average concrete compressive strength was 48.8MPa and GFRP rebars with a modulus of elasticity of $E_{FRP} \simeq 41$GPa were considered. One reinforcing bar was centered at the square concrete cross section of each tie and three different reinforcement ratios were obtained. Experimental results were analyzed and a general concrete tensile post-cracking stress-strain relationship was proposed for its application to any reinforcing material (see Equation 2.24).

A parallel in time investigation was conducted in [87, 88] where the influence of different reinforcement ratios, ρ, concrete compressive strength, $f_c^{'}$, and bar diameter, d_b, on the cracking behaviour of FRP RC ties was studied. In this program, the composite strain of the reinforced concrete element was computed with the help of the measurements on the bar slips at both sides of the specimen, the concrete deformation and the elastic elongation of the reinforcement. According to experimental results, the reduction of reinforcement ratio and the increase of concrete grade derived in an increase of the additional stiffness observed at the post-cracking stage of RC tensile members, and no influence on the rebar diameter was found when results for equal reinforcement ratio were considered.

These studies give interesting information on the cracking behaviour of FRP RC tensile members and their average member strain. However, additional valuable information on the reinforcement strain distribution can be found in [89, 90] for steel RC ties and [87] for FRP RC ties.

A special procedure for fixing strain gauges at very close spacings along the length of the reinforcing rebars was used in [89, 90] with the aim at leading to a much clearer idea of the development of the interactions between steel and concrete. Reinforcement strain gauging was proved to be valid and the rebar strain distribution was plotted at different load levels. From experimental results, a close approximation to a linear strain distribution of strains between two cracks was found irrespective of the applied load. Based in this linearity of the reinforcement strain distribution,

equations for the prediction of both the deformation and the crack width in axially RC ties in tension were proposed. However, these equations were dependent on the distance needed for the reinforcement strain distribution to recover the composite action (i.e. the proposed equations were dependent on the transfer length, l_t, whose computation is not straightforward).

A special internally gauged FRP reinforcing rebar was used in [87] to measure the strain profile of the reinforcement along the bar during the complete cracking process. Additional to the internal gauging, three pre-cracks equally spaced were induced to assure three transverse cracks to appear at exact locations where reinforcing strain measurement was possible. Based on the reinforcement strain distribution, and neglecting the concrete strain, the local slip was determined through the integration of reinforcement strain between the point with zero slip (i.e. the midway section between two existing cracks) and the point where local slip is desired:

$$\Delta s = \int_0^x (\epsilon_f(x))\, dx \tag{2.25}$$

where $\epsilon_f(x)$ is the reinforcement strain distribution along the x-axis (with origin in the midway section between two cracks). Similarly, the local bond stress was defined as the force transferred from the reinforcing bar to concrete per unit surface area and was described to be proportional to the slope of the reinforcement strain distribution as follows:

$$\tau = \frac{d_b E_{FRP}}{4} \frac{d\epsilon_f(x)}{dx} dx \tag{2.26}$$

Based on Equation 2.26, the bond stress profile along the RC tie was computed at different load levels. The comparison between bond stress profile derived from FRP RC ties and that derived from steel RC ties (available in [91]) depicted that differences exist in the distribution of the bond forces (see Figure 2.27). For the case of FRP RC ties, as far as load was increased, a loose of the bond stresses close to the crack section accompanied with a shift of the peak bond stress away from the cracked section was obtained.

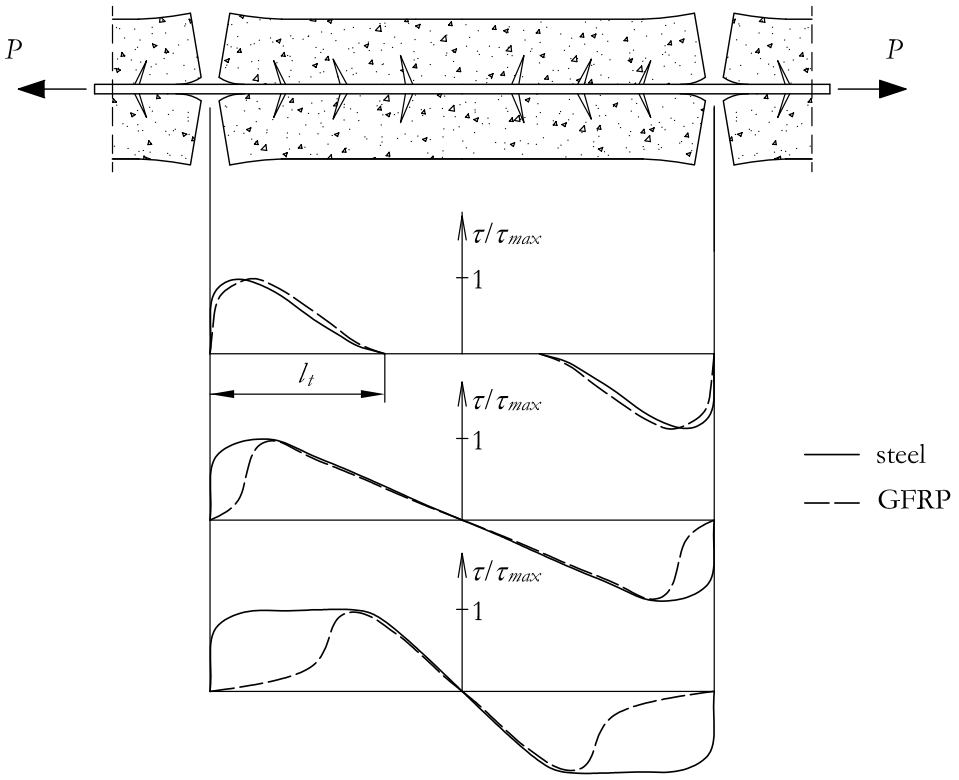

Figure 2.27: Assumed bond stress distribution for steel and GFRP reinforcement (after [87]).

Moreover, based on the statement of local bond-slip relationship to be dependent on the distance from the cracked section, the experimental reinforcement strain profiles were used to derive a bond stress-slip-strain relationship for GFRP reinforcement.

The limited amount of experimental programs centered on the behaviour of FRP RC tensile ties is partially understood if one considers that there are some aspects on the behaviour of steel RC tensile elements that have not been yet accurately studied. As an example, recent publications on concrete cover influence on both splitting cracking and crack width predictions at the concrete surface for traditional reinforcement can be found in [63, 92, 93].

The formation of splitting cracks during the cracking process is dependent on two factors: the value of the rings of tensile stresses developed in the concrete and

the amount of confinement. The rings of tensile stresses that develop in concrete appear in order to balance the radial component of the bond behaviour, which is enhanced by the bearing forces induced by bar surface deformations. Besides, if enough confinement is provided, the tensile hoop at concrete will not exceed concrete tensile strength and no splitting cracks will appear. On the contrary, if low confinement is provided, the bond stress will not reach the maximum bond strength and longitudinal cracks will appear.

With this in mind, rebar size and concrete strength were believed to be the key parameters in determining the splitting tendency of a RC tie in [92]. The experimental program was conducted on steel RC tie with reinforcement rebar size ranging from 10 to 30mm, and two concrete grades ($f_c^{'}$=34.9 and 90MPa). Within the two concrete grades, the increase in rebar size was associated with an increase in splitting cracks in final crack pattern. In the extreme cases, when rebar size 10 was considered only longitudinal cracks appeared and when rebar size 30 was considered only splitting cracks appeared. Besides, the beneficial influence of high-strength concrete on the tension stiffening effect is reduced with the increase in bar diameter. With the help of experimental results, and based on the average concrete tensile stress-strain relationship proposed in [94], a new coefficient that accounts for the detrimental effects of splitting crack on the cracking behaviour of RC tensile members was proposed, and splitting cracks were said to be only significant when $c/d_b \leq$2.5.

Based on the work presented in [92], the study was extended to six concrete cover to bar diameter ratios, c/d_b, and three concrete grades ($f_c^{'}$=25, 60 and 80MPa) in [63]. Registers on the load level causing first transverse and splitting cracks were taken for the 18 steel RC ties. The results indicated that high-strength concrete needed thicker cover to prevent splitting cracks to appear before transverse cracks. Therefore, the criterion of c/d_b=2.5, proposed in [92], was not applicable to high-strength concrete. Moreover, the formation of splitting cracks was not affected by concrete tensile strength but affected by the thickness of the concrete cover, as load causing first splitting cracks did not vary with the concrete grade but showed an increase tendency with increasing the cover thickness.

2.4.2 Numerical studies

Most of the existing numerical work on the study of the bond behaviour of RC elements is focused in solving models that take into account the stand-alone behaviour of concrete and reinforcing material and include the modelling of their interaction through a non-linear analysis using a specific bond-slip law. The solution can be found either by solving the differential equation that represents the bond problem [67, 74–79] or by using numerical procedures [80–84]. Whichever the approach selected, the differential equation that represents the bond problem of an RC member is shown next:

$$\frac{d^2 s(x)}{dx^2} = \frac{\tau(x) p_r}{A_r E_r} (1 + n\rho) \tag{2.27}$$

where p_r is the perimeter of the bar, A_r and E_r are the cross sectional area and the elastic modulus of reinforcement, respectively, n is the modular ratio, ρ is the reinforcement ratio and $s(x)$ and $\tau(x)$ are the slip and the bond stress along the x-axis. These two last unknowns are related through the bond-slip relationship.

The first attempts to model the post-cracking behaviour of RC elements were based on studying the tension stiffening behaviour through the solution of the characteristic equation (Equation 2.27). However, the solution of the differential equation is possible if proper basic assumptions are considered and boundary conditions are declared. In the following, the basic assumptions are presented and some of these earlier works are summarized.

Basic assumptions in the solution of the differential bond equation (Equation 2.27) are:

- The concrete participates in resisting the load, except at the cracks.
- Reinforcing material and concrete have elastic constitutive equations.
- Only transverse cracks appear in the cracking process.
- Due to the differences in strains, slipping arises between the rebar and concrete.

- Due to symmetry conditions, the bond stress reaches zero at a point halfway between two existing cracks.

- The crack width at the surface of a rebar is equal to the difference between the elongations of the rebar and concrete (i.e. the sum of slips from both sides).

Three idealized forms of the bond-slip relationship (linear, bilinear and constant bond stress) were considered in [74] to solve the differential equation. For the case of a linear bond-slip relationship, and based on the equilibrium conditions and compatibility conditions, the *tension stiffening* effect (expressed as the effective concrete tensile stress-strain curve) was found to be a function of the so-called *area parameter*, $n\rho$. For the case of bilinear relationship (which is aimed at being more realistic, with a first linear stage followed by a constant second stage with $\tau = f_m$), the dependence is found to be related to the *area parameter*, $n\rho$, and the *bond parameter*, f. The latter was defined as the ratio of the concrete cracking force ($A_c f_{ct}$) and the bond force ($k^{-1} p_r f_m$) transferred at the steel-concrete interface over the characteristic length, k^{-1}.

The need of three experimental points of the reinforcement strain curve, which is not always affordable, is seen as a drawback of the work presented in [74]. Moreover, their findings were based on the assumption that reinforcement and concrete strains have the same value at the central portion of the RC member length. As pointed in [75], this assumption of equal strains for both concrete and reinforcement in the central portion of the RC member is only applicable if we have a comparatively lightly loaded member (CLLM), i.e. if the applied load is low enough and/or the member length is large enough. For the case of higher values of applied load and/or for lower RC member length, the reinforcement strain will be higher than the concrete strain everywhere in the RC member, attaining its minimum value at mid-span (x=$L/2$). For this second situation the RC member is called to be a comparatively heavily loaded member (CHLM). As two possible physical cases could be distinguished, two analytical solutions were found when the B.E.P. bond-slip model [42] was considered: a closed form solution for the CLLM and by series of functions for the CHLM. Besides, for CLLM members the primary crack could occur at any section located in the aforementioned central portion, whilst CHLM members could develop primary

crack only at the symmetry section. The limit condition between CLLM and CHLM member was expressed either regarding to concrete and an intermediate section or regarding to reinforcement and the load end.

An step by step study on the solution to the equilibrium differential equation of a steel RC member was conducted in [76–78]. As a first step, an exact solution to the equilibrium differential equation for each zone of a piecewise linear bond stress-lip relationship was presented in [78]. In this study, only steel and interface properties were taken into account, since concrete stiffness was idealized to be very high. Real concrete properties were considered in a later study [77], where the equilibrium equations were presented as relationships between the axial forces and the corresponding axial displacements, and the stiffness matrix incorporated parameters of the reinforcing steel, the surrounding concrete and the bond-slip law. The steel-RC member response was obtained only for the uncracked stage. The formulation was thereafter extended to the crack stage in [76], assuming that the concrete is an homogeneous material, and therefore having crack formation at the mid-section of the member and sub-sequent submembers. The new model covered the entire range of loading until rebar yielding, and determined the sequence of appearance, location, size and growth of cracks.

Substituting a local bond stress-slip relationship into Equation 2.27 is one way to solve the equation. However there is no bond stress slip relationship that uniquely represents local bond stress-slip at all points along the section, and therefore exact solution of the equation is not presented to be valid for all the cases. In this framework, the differential equation should be solved anytime a new bond-slip law is considered. Therefore, models that use a numerical procedure to solve the bond differential equation are becoming more popular.

A mathematical model was proposed in [81] for obtaining mean moment-curvature relationship for a cracked beam. The beam was modelled as a group of block portions mutually independent limited by cracks that start forming when the cracking moment M_{cr} was attained. The characteristic cracking steps were described with the stress and strains states setting the change from one phase of the cracking phe-

nomenon to the next one. These three possible phases are: *incipient cracking* (i.e. the concrete tensile strength is reached at midway section between cracks), *crack formation* (i.e. a crack forms at midway section and two new blocks are formed, whose maximum concrete tensile stress is unknown) and *transient state* (i.e. load can be further increased until maximum concrete tensile stress in existing blocks reaches concrete tensile strength). Whenever this third state was achieved, the loading procedure stopped when stress state reached that of the incipient cracking phase. Once the characteristics stages of cracking were defined, a mathematical model was proposed that considers infinitesimal elements of length dx. By using finite difference method, the system of differential equations that derives from i) equilibrium of axial forces, ii) equilibrium of moments of the forces, iii) slip equilibrium and iv) sections remaining plane (i.e. strain compatibility) could be solved and the unknowns at the end of each infinitesimal element could be determined (i.e. variation in depth of neutral axis, variation in concrete stress in tension, variation in concrete stress in compression (or in steel stress in tension) and variation in the slip). The proposed mathematical model was proven to be valid to predict the moment-curvature relationship of RC beams, which was presented in a stepped form delimited by the characteristic points belonging to the changes in cracking phases.

This same numerical procedure was used for the load-deflection analysis of concrete elements reinforced with FRP rebars in [82, 95]. The Double Branch Model (D.B.M.) bond-slip law (Equations 2.8-2.10) was considered to model the interaction between the two materials. The possible phases of the cracking phenomenon presented in [81] were said to represent the two limiting configurations of the problem (corresponding to the maximum and minimum crack spacing). Therefore, instead of using an stepped moment-curvature relationship, a range of possible cracking responses was presented. To validate the numerical procedure, experimental results were compared to numerical predictions and code provisions, with experimental moment-curvature relationship falling in the numerical range proposed. Similarly, the same solving procedure and maximum and minimum crack spacing approach was used in [96], using the B.E.P. model bond-slip law presented in [42] (Equation 2.3). The model was thereafter used to predict both the crack width and crack spacing in FRP RC beams, and the trend of crack width decreasing with an increase

in bond strength or reinforcement ratio and a decrease in concrete cover was found.

The use of so-called *block models* (i.e. models that model the cracking behaviour of RC beams through a succession of blocks divided by flexural cracks) was also considered in [80] to analyze whether the use of local and average results on the moment-curvature relationship of RC flexural elements would yield to significance differences. However, the numerical solution of the *multiple shooting method* was chosen, and two supporting sections where zero slip occurs were introduced. The position of such sections was shifted by trial and error until all of the boundary conditions were satisfied in the integration. Numerical results showed that little differences between local and average results were found if the case of the constant bending moment is considered. However, in RC beams subjected to variable bending moment, an average evaluation did not appear to be accurate. The study progressed analyzing how the random nature of the cracking phenomenon of an RC beam subjected to constant bending moment could affect the predicted moment-curvature relationship. Because of the little differences encountered when different final crack patterns were considered, the authors decided to avoid pursuing a probabilistic approach and pointed out that, all the possible solutions could be included in the range delimited by the curves of maximum and minimum deformability, which corresponded to the maximum and minimum crack spacing stated in [95].

Until now the review of the existing numerical works was centered on either works that found the solution of the system of differential equation or works that solved the problem within a *block model* approach. However, other numerical works have been presented. Some of these existing numerical works are presented next.

The proposed *tension stiffening* model presented in [66] (Equation 2.22) was used to represent the post-cracking concrete tensile stress-strain behaviour in a nonlinear finite element model, which was implemented in a computational program called ANALEST. The reinforcing steel was assumed as an elasto-plastic material, modeled by a bilinear stress-strain curve. Comparison between FE analysis and experimental results (selected from existing literature) showed very good agreement in terms of load-displacement curves. Similarly, the *tension stiffening* model presented in [67]

was also implemented and compared to experimental average concrete stress-strain relationships available in the literature.

A three-dimensional constitutive model which simulates the behaviour of concrete under multiaxial stress conditions was presented in [97]. In the model, the behaviour of concrete was modeled using an equivalent uniaxial stress-strain curve combined with a compression scalar damage parameter. The model was modified in [98] to integrate variable tension stiffening factors defined as a function of the member strain (i.e. the reinforcing bar-concrete interaction was implicity simulated). The modifications allowed the constitutive model to be implemented as a user-defined subroutine, at Gauss integration point level, into finite element software. The goodness of the model was proven in [99].

Alternatively, a solution algorithm to determine the load-elongation relationship of RC tensile members was presented in [100]. To this end, the strain distribution of concrete within the zone where bond forces are being transferred, was defined with a polynomial function that satisfied the boundary conditions at the crack face and at the inner end of the transfer length. These boundary conditions can be defined as ϵ_c=0 at the crack face and $\epsilon_c = \frac{P}{E_c A_c(1+n\rho)}$ at the inner end of the transfer length. Therefore, the concrete stress distribution between two existing cracks was completely defined with the polynomial function being valid between the cracked section and the section where transfer length is achieved, and $\epsilon_c = \frac{P}{E_c A_c(1+n\rho)}$ in the central portion between the two sections where transfer length has been achieved. Besides, the transfer length, l_t, was determined by the relationship proposed in [101] and shown next:

$$l_t = K_p \frac{P_c}{p_r} \tag{2.28}$$

where P_c is the transfer load equal to $P_c = P/(1 + n\rho)$, p_r is the perimeter of the reinforcing bar and K_p is a constant to be determined from pull-out tests.

The assumed polynomial order of the concrete strain distribution, defined in [100], could be determined if a balance in strain energy components was set out. Moreover,

authors considered the concrete tensile strength to change according to the loading history and used the proposal presented in [91]. The solution algorithm starts computing the required transfer length (Equation 2.28) and it follows by determining the polynomial order through the energy balance. Once the strain distribution of both concrete and reinforcement are known, the possibility for further crack formation is checked and elongation and member forces are computed. Finally, load is further increased and the sequence is repeated until reinforcement yielding. Although being a simple model, when compared to classical approaches where repeated complex integrations are needed, the final strain distribution of concrete and reinforcement can be plotted as they are a direct result of the algorithm. However, although the load-deformation relationships derived with this algorithm are in good agreement with experimental results, no comparison of the predicted strain distribution with experimental data has been performed. Therefore, the bases where the numerical algorithm relies on have not been validated.

Whichever the procedure chosen to numerically study the transmission of bond forces and the cracking behaviour of RC tensile and flexural members, a bond-slip law needs to be assumed, which is supposed to be valid for the whole loading procedure. However, the need of using two bond functions was stated in [102], where a distinction between the bond acting in the initiation of cracks and the bond acting to their stable propagation was proposed. The proposed bond equations were used to compute an expression for the average stiffness of the RC member immediately after cracking. However, this average stiffness was found to be lower than that proposed in EC-2 [9].

2.4.3 Analytical studies

In code predictions, there are two main approaches that deal with the post-cracking behaviour of steel RC members: 1) the EC-2 [4] and MC90 [5] approach, that proposes a method to calculate the average strain in the reinforcement for a given load after concrete cracking (i.e. the models use a modified relationship for the stress-strain response of the embedded reinforcing material); 2) the ACI model [6] that proposes an effective cross sectional area in an analogous approach to that of the effective moment of inertia proposed for flexural elements. In the following, the

three code formulations are presented.

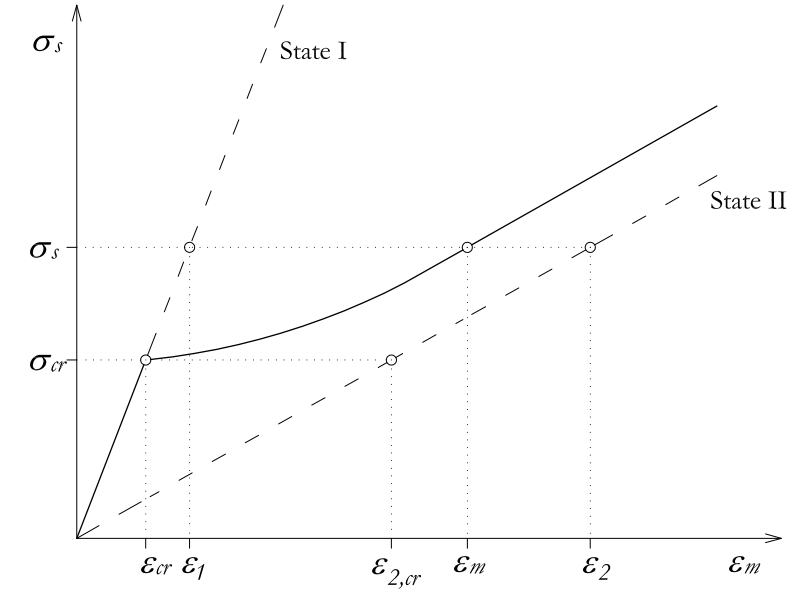

(a) EC-2 [4]

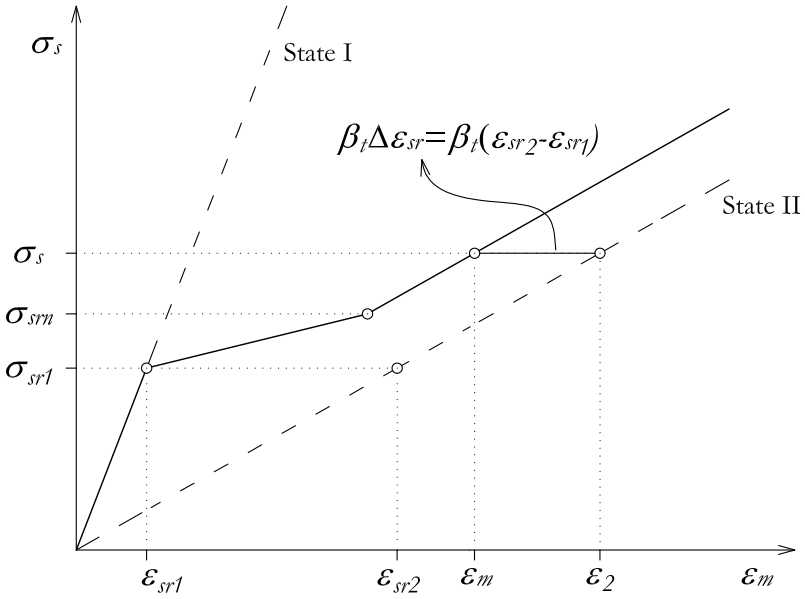

(b) MC90 [5]

Figure 2.28: Modified stress-strain relationship of embedded reinforcement.

Proposal of EC2

EC2-92 [4] proposes a method to calculate the average strain in the steel reinforcement interpolating between the strains calculated for uncracked (ϵ_1) and fully cracked (ϵ_2) sections:

$$\epsilon_m = \epsilon_1 \left(\frac{\sigma_{cr}}{\sigma_s}\right)^2 + \epsilon_2 \left[1 - \beta_1\beta_2 \left(\frac{\sigma_{cr}}{\sigma_s}\right)^2\right] \tag{2.29}$$

where β_1 stands for the bond characteristics of the internal reinforcing steel bars (1 for ribbed and 0.5 for smooth bars), β_2 considers the loading type (1 for first loading and 0.5 for repeated or sustained loading), σ_{cr} is the tensile stress in the steel reinforcing bar at cracked section when the first crack occurs (σ_{cr}=P_{crack}/A_s), σ_s is the stress in the steel bar at the cracked section at the actual load, and ϵ_1 and ϵ_2 are the strain calculated for the uncracked and fully cracked section (see Figure 2.28(a)). Although Equation 2.29 has been proposed only for steel RC structures, predictions on FRP RC structures can be computed if an adequate value for the bond quality coefficient (β_1) is assumed.

Proposal of MC90

Similar to EC2-92, a modified stress-train relationship of embedded reinforcement is proposed in MC90 [5] to account for the additional stiffness that derives in RC members from reinforcement and concrete interaction (see Figure 2.28(b)). At the linear elastic phase, the model proposes the member stiffness to be equal to the combination of both materials' stiffness. Beyond the cracking load, and during the whole crack formation phase, the strain in reinforcing bar can be calculated as follows:

$$\epsilon_m = \epsilon_2 - \frac{\beta_t\left(\sigma_s - \sigma_{sr1}\right) + \left(\sigma_{srn} - \sigma_s\right)}{\left(\sigma_{srn} - \sigma_{sr1}\right)}\left(\epsilon_{sr2} - \epsilon_{sr1}\right) \tag{2.30}$$

where ϵ_{sr1} and ϵ_{sr2} are the steel strains for uncracked and cracked section respectively, when first crack has formed, σ_{sr1} and σ_{srn} are the steel stress in the crack, when first and last crack has formed, respectively, and β_t is a factor for steel strain along the transmission length reading 0.4 for pure tension. Once the crack formation

phase ends and the stabilized cracking has been attained, the strain in reinforcing bar can be calculated as follows:

$$\epsilon_m = \epsilon_2 - \beta_t \left(\epsilon_{sr2} - \epsilon_{sr1}\right) \tag{2.31}$$

For normal cases, the steel stress at the last crack may be taken as σ_{srn}=1.3σ_{sr1}.

Proposal of ACI 224-92

Similar to the approach applied on the calculation of deflections on flexural members, ACI 224.2R-92 [6] proposes to study the tensile behaviour of steel RC elements with an analogous approach to that of the effective moment of inertia in ACI 318-05 [103]. Based on Branson's expression [56], ACI 224 proposes an expression for the effective cross-sectional area (A_e) that varies gradually from the gross sectional area (A_g) to the cracked cross sectional area (A_{cr}), as loading of the member increases beyond the cracking point:

$$A_e = A_g \left(\frac{P_{crack}}{P}\right)^3 + A_{cr}\left[1 - \left(\frac{P_{crack}}{P}\right)^3\right] \leq A_g \tag{2.32}$$

Consistently with ACI approach, once the cross-sectional area has been computed, the deformability of the member can be evaluated by an elastic analysis, where ϵ_m=$\frac{P}{E_c A_e}$. Although experimental results have demonstrated that predictions with [6] clearly overpredict the extra-stiffness found at cracking stage for the case of FRP RC members [87, 88, 104], no mention has been done on how to consider the differences in reinforcing materials when the tensile behaviour of FRP RC ties is studied. In this sense, some authors have indicated that Branson's model provides excessive amounts of tension stiffening for FRP beams [105]. The tension stiffening component in Branson's model has been proved to increase unrealistically as the gross-to-cracked moment of inertia ratio, I_g/I_{cr}, increases, which is typical with FRP reinforcement. This problem has been often attributed to FRP RC having less tension stiffening [106]. However, Bischoff observed comparable amounts of tension stiffening when this effect is measured relative to the concrete contribution [68]. Several approaches have been considered to increase the predicted deflections in FRP RC beams [107]. An attempt to soften member response consisted in increasing the cubic power in Branson's original equation to a higher value. However,

this approach was found to underpredict deflections also at lower load levels and therefore it has not been further considered. Alternatively, the member response could also be softened by multiplying the gross moment of inertia with a corrective factor. This approach was followed in ACI 440.1R-03 [108], and β_d=0.5[$\frac{E_{FRP}}{E_{steel}}$ + 1] was introduced to account for the differences in reinforcement characteristics. More recently, ACI 440.1R-06 [106] recommended using β_d=0.2($\frac{\rho}{\rho_b}$), where ρ_b stands for the balanced reinforcement ratio.

Based on ACI 440 adaptation, some authors dealing with the study of the tensile behaviour of FRP RC elements have introduced the coefficient proposed in ACI 440.1R-03 [108] into the effective cross-sectional area formula, instead of using the one proposed in the current version because of being impossible to compute the value of ρ_b. The final expression for the effective cross-sectional area (A_e) reads:

$$A_e = A_g \beta_d \left(\frac{P_{crack}}{P}\right)^3 + A_{cr}\left[1 - \left(\frac{P_{crack}}{P}\right)^3\right] \leq A_g \tag{2.33}$$

2.5 Literature review summary

2.5.1 Bond of FRP bars

As reported in previous sections, many experimental studies have been conducted in order to investigate bond between FRP rebars and concrete; such studies have been aimed either at understanding the resisting mechanism activated in pullout tests and at determining the bond stress-slip constitutive laws. Comparisons of bond strength and deformability between steel and FRP rods have also been carried out.

This section reports a summary of the state-of-the-art research on the bond behaviour of FRP rebars. Bond mechanisms were analyzed in order to understand how the different types of FRP reinforcements interact with concrete. A comparison between FRP and steel reinforcements was performed and different bond tests were examined.

The effect of factors such as surface treatment and characteristics, concrete com-

pressive strength, confinement pressure, bar diameter and embedment length on the bond behaviour was also discussed.

Surface treatment

The differences in the manufacturing of the outer surfaces and the material differences in longitudinal and transversal directions makes bond performance of FRP differ from that of steel.

A friction-resistance bond mechanism was defined for smooth bars in [12], as no mechanical interlocking or bearing resistance could be developed. The influence of the smoothness of the outer surface on the bond behaviour or FRP bars was confirmed by several researchers [13, 15, 24, 34], who coincide in defining a chemical adhesion bond when sand-coated FRP rebars are considered, resulting in large increments of bond strength with brittle bond failure.

Different bond mechanisms have been found when talking about deformed FRP rebars. Mechanical interlocking (also known as bearing) resistance was set as the main component of bond for ribbed and indented rebars [12, 24, 34]. A friction-resistance bond mechanism was defined for strand-shaped FRP bars in [12], whilst adhesion and friction were defined as the primary component of bond when both FRP bars with spiral indentation [14] and FRP bars with smooth surface with fibre helical winding [15] were considered.

As a result of the differences in the bond mechanisms activated for each surface treatment, differences in the bond stress-slip relationship can be found. As reported in [24], bond stress of the steel and sand coated GFRP bars dropped after attaining the maximum bond stress, whilst bars with helical wrapping and sand-coating exhibited a gradual reduction of bond. Moreover, the contribution of mechanical interlocking for deformed FRP bars was very efficient, performing threefold strength than that of sanded bars [34].

Bond strength

Several authors [14, 15, 20, 22, 23, 26, 29, 32, 36, 47] reported that, for the same test conditions, the average nominal bond stress at failure was greater for the steel rebars than for the FRP rebars; as an example, the GFRP rebars considered in [22], with sand coating and helical winding the same type of GFRP fibres, performed bond strength values equal to 62-84% that of steel. For the sand coated CFRP rebars considered in [26], with three different grain sizes, bond strength values ranged from 50 to 63% that of steel, depending on the concrete strength and grain size. The reduction of grain size was accompanied with the decrease in the ultimate bond strength, as smoother surfaces were provided.

As reported in [14, 28] the slip of the rebars relative to the concrete surface was greater for FRP rebars than for the steel rebars.

-Influence of rebar diameter. The effect of bar diameter on bond resistance has been widely studied. The trend that larger rebar diameters develop less average bond strength has been confirmed by results presented in [11, 17, 18, 36, 47]. This effect can be explained to be a consequence of the non-uniform distribution of stresses along the bar and the higher diameter reduction caused by the Poisson effect. Some authors agree in defining a third play of the "shear lag effect" only for the case of FRP rebars.

-Influence of embedment length. The influence of embedment length on the bond strength developed has also been studied [11, 17, 20, 26, 35, 36, 47], finding that lower embedment lengths performed higher bond strengths. This effect was explained to be a consequence of the non-uniform distribution of the shear stress along the embedment length.

-Influence of confinement pressure. The more the confinement provided, the more difficult for the cracks to progress through the concrete to the specimen surface, meaning that splitting failure is less likely to occur. Similarly, the increase in confinement pressure results in the development of greater bond strength values, as long as proper rebar's bond improvement properties are assured [29] and enough surface roughness is provided [30].

-Influence of fibre and resin type. No clear evidences of the fibre type influence on bond strength have been deducted, but epoxy resin specimens developed larger bond strength than those where vinyl ester resin was considered. Bond strength of FRP is therefore controlled by resin type, rather than fibre type [20, 23].

-Influence of concrete strength. Bond strength is likely governed by the compressive strength of concrete when steel reinforcement is considered, whereas bond strength value of FRP reinforcement depends on the relative shear strengths of concrete-resin and resin-fibre interfaces, as bond failure mode is affected by the concrete strength [11, 17, 24].
There exists a concrete compressive strength value beyond which failure takes places at the concrete matrix interface, being bond strength mainly controlled by the shear strength of concrete. For higher compressive strengths, failure mode changes and happens at the surface of the FRP rebars. In this case, bond strength is influenced by the interlaminar shear strength just below the resin rich surface layer of the bar [11, 17, 18, 20, 22, 23, 26, 32]. This change in failure interface depends on the properties of both materials (concrete and FRP rebars) and no fixed concrete compressive strength value can be established.

-Influence of lug width. According to the reported influence of the shear strength of concrete-resin and resin-fibre interfaces in bond failure mode, this bond failure is influenced by the rebar deformations lug width [20, 26]. The increase in lug width makes failure mode change from lug shearing to concrete shearing [20, 26]. Again, no fixed lug width can be deducted to set the change in failure mode, as this depends on relative rebar and concrete properties.

Fibre reinforced concrete

Main research has been focused in bond strength of FRP embedded in plain concrete, but complemental research [39, 41] has been performed in the bond behaviour when fibre reinforced concrete is considered. The combination of FRP (with brittle failure) and fibres may eliminate the problems related to corrosion of steel reinforcement while providing requisite strength, stiffness and desired ductility, which are shortcomings of the plain concrete and FRP reinforcement system.

Results from the study conducted in [39] permitted the author to conclude that the addition of polypropylene fibres, in a 0.5% volume fraction, permitted the increase in concrete compressive strength from 37 to 51MPa, but did not increase the ultimate bond strength; the addition of fibres provided much more ductile bond behaviour (in terms of larger slips for maximum bond strength). Tests performed in [41] considered synthetic and steel fibres as concrete reinforcing material. The compressive strength increased slightly as more fibre was added to the mixture and therefore, the increase in concrete compressive strength derived in an increase in the bond strength. The effect of the fibres on the ductility of the specimens was not studied.

Kind of test

The stress conditions developed in the concrete specimen during pull-out tests are rarely encountered in practice, as the compression reaction acting on the concrete surface at the loaded end eliminates transverse tension cracking that, generally, has and adverse effect on the bond stress. With the aim at reducing or removing this compression action on the concrete, different type of bond tests have been introduced.

The "Direct Tension Pull-out Test" (DTP test), presented in [33], forced the anchorage to occur in the presence of a uniform tensile stress field. As no additional compressive strength was provided, transverse tension cracking could not be eliminated, and therefore local bond strength was lower than that of conventional pull-out tests.

Compression stresses on the concrete were also avoided in "Modified Pull-out Test", presented in [34]. The lack of the compressive action affected bearing resistance and reduced bond strength value of ribbed and steel rebars. For cases where surface deformations were less effective in terms of mechanical interlocking (externally sanded and spiral wound with fibres rebars), the removal of the compressive action helped the surface of being damaged and allowed the performance of higher bond strengths. For sanded rebars, no difference in bond strength was performed.

A third modification of bond test was proposed in [35], consisting on a modification of the standard beam test. The new test proposal provided a great reduction of the compression stresses in the concrete core (better reproducing the actual behaviour of reinforcing bars embedded in the tensile portion of beams) and allowed two bond tests to be conducted simultaneously. No comparison between bond strength values obtained with this new test and those obtained in traditional pull-out test was made.

The "Direct Pull-out test" was used to investigate the top bar effect [36], defined as the ratio of ultimate bond strength reached in pulling out the bottom bar to that reached in pulling out the top bar of a Direct Pull-out specimen. The specimen consisted in a concrete wall with FRP bars placed at the top, bottom and middle through the wall.

Finally, pull-out test with eccentric placement of the bar was proposed to obtain the concrete cover splitting resistance along the bar in [18]. The cover splitting tendency along the bar was lower for the FRP bar than for steel bar (i.e. the pressure from the FRP bar cracked the concrete cover at a higher load than what was the case for steel bars).

2.5.2 Bond influence on cracking behaviour of RC tie

The bond influence on the cracking response of RC members has been more widely studied for steel reinforcement than for FRP reinforcement. Although this bond influence is encountered when the reinforced concrete is under tension, the major part of the available work is based on flexural elements. Therefore, little literature centered on FRP RC tension ties is available.

Three different approaches on the evaluation of the deformability and cracking behaviour of reinforced concrete structures can be distinguished:

- Models which determine an effective cross-sectional area as a combination of the gross area and the cracked area. The deformability is therefore evaluated

by an elastic analysis of the structure [6, 56].

- Models that modify the constitutive equation of one of the two materials. In the *tension stiffening strain* approach, a modified relationship for the stress-strain response of the embedded material is proposed and concrete is described as a brittle material [4, 5, 63, 64]. In the *load sharing* approach, reinforcement is supposed to behave as an elastic material and the extra stiffness of the RC member is included in concrete tensile post-cracking response [57–60, 65, 66].

- Models which perform a non-linear analysis and include the modeling of the materials interaction through a specific bond-slip law. In these models, the non-linear analysis can be performed with numerical procedures (i.e. finite difference methods and/or finite element methods) [72, 80–84, 95, 96] or solving the system of differential equations that describe the bond problem [67, 74–79].

Little experimental research has been conducted in FRP RC ties. In the experimental program presented in [85, 86] the authors stated that for values of concrete cover over reinforcement diameter larger than 3, little further benefit from the bond interaction was obtained. According to the results presented in [87, 88], the reduction of reinforcement ratio and the increase of concrete grade derived in an increase of the tension stiffness effect in RC tensile members. However, according to the results presented in [68], the tension stiffening effect was presented to be only dependent on the modulus of elasticity of the materials, as long as the shrinkage effects are included in the analysis.

Chapter 3

Pull-out test experimental methodology

An experimental series of pull-out tests was performed to investigate the bond behaviour of FRP in concrete structures. In this chapter the choice of the study parameters, the mechanical properties of the materials used, the specimen preparation, the experimental set up and the testing procedure are presented.

3.1 Introduction

Pull-out tests are used commonly in the assessment of bond performance of steel reinforcing bars and concrete. Although the stress conditions developed in the concrete specimen during pull-out tests are rarely encountered in practice and the bond values developed under those tests differ substantially from those developed in reinforced concrete elements for most practical conditions, pull-out tests have been widely adopted because they offer an economical and simple solution for the evaluation of the bond performance of reinforcing bars.

New bond tests have been introduced with the aim at reducing or even removing the compression action of the concrete taking place in traditional pull-out test [33–35], but little research has been conducted under this bond tests and therefore little experimental database is available for comparison purposes. The complexity of these alternative tests added to the lack of experimental database and test standardiza-

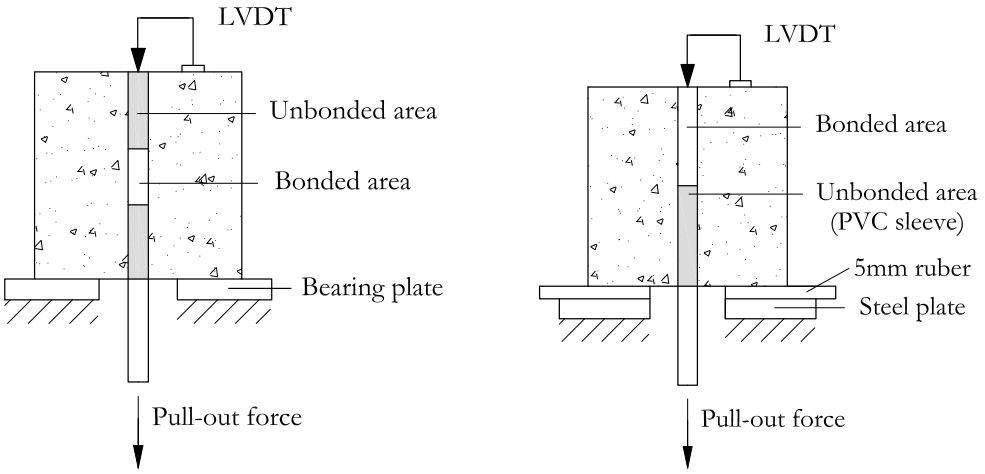

(a) Rehm [109] (b) RILEM/CEB/FIB [110]

Figure 3.1: Pull-out tests arrangements.

tion made the author to choose the traditional pull-out test to be performed in the experimental program.

The main aim of a bond test is to characterize the behaviour of the interface between rebars and concrete. Currently, this is usually made obtaining a bond stress-slip relationship at the loaded and free ends of FRP bars subjected to a pull-out load. A careful evaluation of the pull-out arrangement used for steel bars by previous researchers was conducted in order to find the most appropriate set-up. One of the first set-up was proposed by [109], shown in Figure 3.1(a), and has been used for years with minor changes in order to eliminate its weak points. Its weaknesses are not only related to the additional resistance produced by the wedging action of the undamaged bar, but also to the friction developed between the specimen and the bearing plate, that provides additional confinement and can assist the development of the arch-effect in the center of the specimen. Therefore, the RILEM/CEB/FIB [110] standard pull-out, shown in Figure 3.1(b), introduced a rubber between the concrete and the bearing plate to minimize the friction effects and moved the bonded length of the bar. For this testing series the RILEM/CEB/FIB [110] pull-out test arrangement was adopted.

3.2 Study parameters

The selection of primary variable for this experimental study was based on existing experience of bond behaviour of steel and FRP bars in concrete. There are some parameters affecting bond behaviour of FRP rebars that have been widely studied, having the research community therefore enough knowledge on their influences; some of these parameters are the rebar diameter, the embedment length, the resin type and the effect of the confinement pressure. In this study, additional factors that need further research to better understand their final influence on bond behaviour are considered. The factors examined in this experimental program are given next:

- Bar surface treatment and characteristics.
- Type of bar fibre.
- Concrete strength.
- Diameter of the bar.

A proper evaluation of the influence of these parameters on the bond behaviour is necessary to the understanding of Fiber Reinforced Polymer Reinforced Concrete Structures (FRPRCS). Although the influence of rebar diameter has been already described, the author decided to consider it to enlarge the personal database for future work necessities, for instance in the development of bond-slip models.

3.3 Materials

3.3.1 Concrete

In order to examine the influence of concrete strength on the bond development of FRP bars, two different concrete strengths, C1 and C2, were used. The concrete used for the pull-out specimens was prepared in the laboratory and its composition is given in Tables 3.1 and 3.2 . Due to capacity limitations, more than one casting was made for each batch of concrete. For each batch of concrete mix, two standard control samples (300x150mm cylinders) were cast and cured under the same conditions as the specimens. The control samples were tested in direct compression

to determine the concrete strength in compression. The C1 and C2 concrete mixes had compressive strength mean values of 28.63MPa (VC=6.12%) and 52.19MPa (CV=6.62%) respectively.

Component	Quantity
Water	200
Cement 42.5	325
Fine aggregate	875
Coarse aggregate	878
Polyfunctional additive Rheobuild 570	2.6

Table 3.1: C1 concrete composition in kg/m^3.

Component	Quantity
Water	171.5
Cement 52.5	380
Fine aggregate	843
Coarse aggregate	943
Superplasticizer Glenium ACE 325	4.6

Table 3.2: C2 concrete composition in kg/m^3.

3.3.2 FRP materials

GFRP, CFRP and steel bars acquired from five different firms were used in this study. The surface treatments and characteristics of the rebars used are shown in Figure 3.2 and detailed in Table 3.3.

Firm A provided CFRP (R1) and GFRP (R2) rebars, both with a sand-coated surface. Firm B provided CFRP rebars with a textured surface (R3) and GFRP rebars with a helical wrapping surface and some sand coating (R4). Firm C supplied GFRP rebars with a grooved surface (R5). Firm D provided rebars (R6) similar to

R4: GFRP rebars with a helical wrapping on the surface but no sand coating. Finally, steel rebars (R7) were used for comparison purposes. The nominal diameters of the rebars were 8, 12, 16 and 19mm, and #3, #4, #5 and #6, where # indicates eighths of an inch.

Normalised tests were conducted to determine the cross-sectional areas of the rebars, according to ACI 440.R3-04 [111] and CSA S806-02 [25]. The rebar surface treatment, their mechanical properties (tensile strength, f_{fu}, and Young Modulus, E_r), and their geometrical properties (nominal bar diameter, d_n, and experimental bar diameter, d_b) are summarised in Table 3.3.

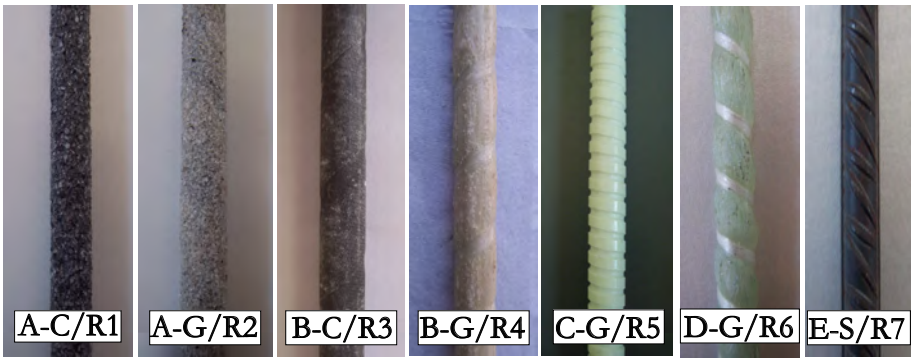

Figure 3.2: Surface deformations and characteristics of rebars (R1-R7).

3.4 Specimen preparation

3.4.1 Bar preparation

FRP reinforcing bars have low transverse strength. To avoid fibre damage and prevent fibre failure at the gripping zone, the rebars can not be tested in tension using the same gripping systems that are used for steel rebars. In this initial conditioning, the FRP bars were cut in 574mm length. On one of the two ends, the one acting as loaded end during the test, a special protection system was adapted to allow the application of the load and its transmission to the final specimen without involving any damage to the bar. On the other end, the one acting as the unloaded end, the bars were properly marked so that the embedment length, $l_b = 5d_b$, would lie in the

final of the concrete cube (Figure 3.3). Non-contact (debonded) areas between bar and concrete outside the embedment length were created with plastic pipes.

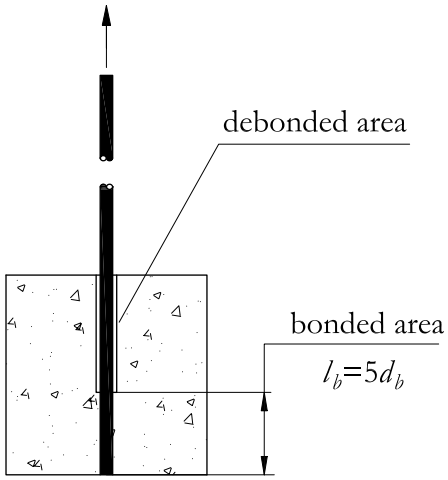

Figure 3.3: Pull-out specimen.

3.4.2 Mould preparation, casting and curing procedure

The moulds used for casting the 200mm side concrete cubes were made of metal. The bars were positioned vertical in the moulds, lying in the middle of the future specimens; concrete was placed in two layers and each layer was vibrated by the means of hammer vibrators, with special consideration in order not to disturb the verticality of the bar (Figure 3.4(a)). Compacting and leveling was imposed on the specimen surface to eliminate voids and minimize geometric irregularities (Figure 3.4(b)). Before each casting, the inside of the mould was coated with a thin film of oil to make easier the demoulding of concrete cubes.

After moulding, specimens were transferred to the curing room for 24h. Thereafter, the concrete cubes were demoulded, marked and transferred again in the curing room with a temperature of 20±2°C and a humidity of about 95%.

3.5 Experimental set-up and testing procedure

The pull-out test arrangement used is shown in Figure 3.5. The concrete cube with the embedded FRP bar was placed in a steel frame that was positioned in the

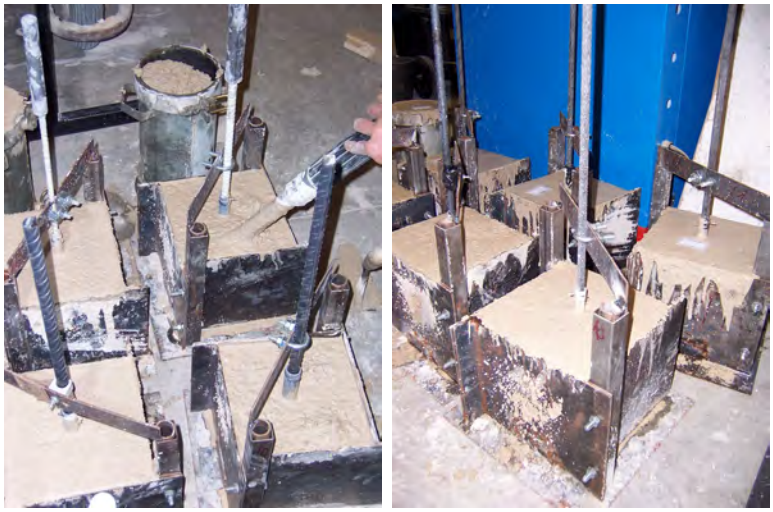

(a) (b)

Figure 3.4: (a) Vibration of concrete with hammer vibrators and (b) final specimen.

testing machine. Two steel plates 25mm thick were connected at the four edges with four 20mm diameter rods. The top plate had a 30mm diameter hole in its center allowing the FRP bar to pass through. Three additional holes were also mechanized in a triangular arrangement around the main hole, allowing the three LVDTs, located at the loaded end of the specimen, to touch the top surface of the concrete cube. The bottom end of the frame was secured on the testing machine, providing the reaction to the pull-out load imposed to the specimen.

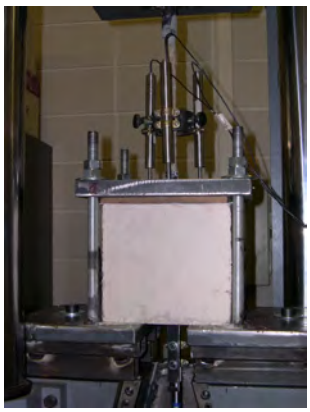

Figure 3.5: Pull-out test arrangement.

Between the concrete block and the bearing steel plate, a 5mm thick wooden plate was introduced to secure the contact between the top surface of the concrete

block and the steel bearing plate. Accidental bending on the bar during loading produced by the small irregularities at the top surface of the cube were avoided.

The slips of the bar at the loaded and unloaded ends were measured with three and one LVDTs, respectively. The latter was attached on an aluminium frame that was then screwed on the concrete cube, as shown in Figure 3.6. A specially manufactured mounting ring was used to held the top three LVDTs attached to the FRP bar by means of three bottom screws, as shown in Figure 3.7.

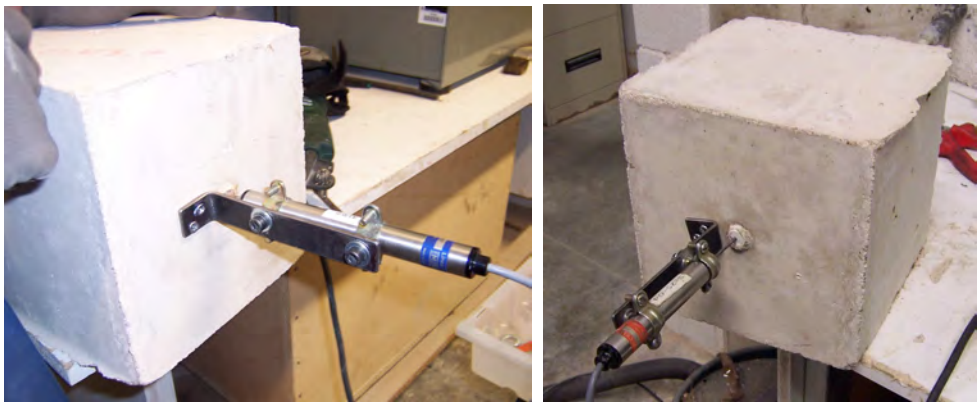

(a) (b)

Figure 3.6: LVDT at the bottom face of the cube.

Figure 3.7: LVDTs at the top face of the cube.

The specimen was positioned in a servo hydraulic universal testing machine with

a load capacity of 600kN. The distance between the mounting ring and the concrete surface was then measured. This distance was used in the calculation of the elongation of the bar due to pull-out load, which had to be subtracted from the slip measurements, as will be explained later. The pull-out load was applied to the specimen at a rate of 0.02mm/s and the experimental data from the four LVDTs and the load cell were recorded every 2 seconds. The tests were performed in displacement control mode to obtain the post peak behaviour. Output data from the hydraulic machine and the LVDTs were recorded using an automatic data acquisition system.

When the test was ended, the experimental data was saved and the specimen was removed for further examination of the mode of bond failure of the FRP rebar.

The experimental program began with R1, R2, R3 and R4 rebars in C2 concrete. Three nominally identical specimens for each configuration were tested. Since there was only a small discrepancy between the results of the nominally identical specimens, the experimental program was continued testing two nominally identical specimens for the rest of tests with C2 concrete and for all the tests with C1 concrete. In total, 88 specimens were tested.

3.6 Analysis of measurements

Data recorded during the tests were used to reproduce the average bond stress-slip relationship for each specimen. The average bond stress at any stage in the test was the recorded pullout load on the bar divided by the nominal surface area of the embedment length of the bar, as shown in Equation 3.1, where τ_{av} is the average bond stress (MPa), P is the tensile load (N), d_b is the rebar diameter and l_b is the embedment length (mm)[111].

$$\tau_{av} = \frac{P}{\pi d_b l_b} \tag{3.1}$$

The unloaded end slip was directly obtained from the bottom LVDT. However, the three top LVDTs measured not only the slip of the rebar relative to concrete but also the elastic elongation of the portion of the bar from the transducer support point

to the level of the bonded bar. Therefore, the loaded end slip s_{le} was obtained as the difference of the average measured slip s_t and the slip correction s_c (Equation 3.2). The slip correction s_c represents the elongation of the rebar between the actual loaded end of the embedment length and the attachment point of the LVDTs, and could be computed using Equation 3.3, where L is the length between the top surface of bonded length and the average point of attachment of the LVDTs on the rebar, E_r is the modulus of elasticity of the rebar and A_r is the effective cross-sectional area.

$$s_{le} = s_t - s_c \tag{3.2}$$

$$s_c = \frac{PL}{E_r A_r} \tag{3.3}$$

Rebar[a]	Resin[b]	d_n[c]		d_b [d]	Surface treatment[e]	f_{fu}[f]	E_r[f]
		(mm)	(in)	(mm)		(MPa)	(GPa)
A-C/R1	V		#3	10.65	SC	1596	120
			#4	13.43	SC	1899	144
A-G/R2	V		#3	10.22	SC	778	45
			#4	14.13	SC	782	46
			#5	16.44	SC	803	46
			#6	19.55	SC	612	42
B-C/R3	E		#3	9.05	ST	2068	124
			#4	12.53	ST	2068	124
B-G/R4	V		#3	9.28	HW,SC	760	40.8
			#4	13.73	HW,SC	690	40.8
			#5	16.11	HW,SC	655	40.8
			#6	19.14	HW,SC	620	40.8
C-G/R5	UV	8		8.55	GR	1000	60
		12		13.72	GR	1000	60
		16		17.25	GR	1000	60
D-G/R6	P	8		7.07	HW	689	46
		12		12.35	HW	689	46
		16		17.36	HW	689	46
		19		21.25	HW	689	46
E-S/R7	-	10		10	-	550	200
		12		12	-	550	200
		16		16	-	550	200
		20		20	-	550	200

[a] G=glass; C=carbon and S=steel.

[b] V=vynilester; E=epoxy; UV=urethane vynilester and P=polyester.

[c] Bar size numbers (in.) are based on the number of eighths of an inch.

[d] According to ACI 440.3R-04 (for FRP bars) and standardised (for steel rebars).

[e] SC=sand coating; ST=surface texture; HW=helical wrapping and GR=grooves.

[f] From manufacturers specifications.

Table 3.3: Geometrical and mechanical properties of the rebars.

Chapter 4

Pull-out test experimental results

The experimental results from the pullout tests described in the previous chapter are presented in the following. From the experimental data, an examination of the mode of bond failure of the reinforcing bars and of the various parameters that influence bond development has been performed.

4.1 Introduction

In this study, 88 pull-out specimens were tested to analyze bond behaviour. The analysis was performed in relation to different types of FRP rebars, as well as steel rebars, and various influencing parameters (surface treatment, types of fibres, rebar diameter, concrete strength). The influence of rebar fibre type on the interface stiffness was also analyzed.

The experimental results obtained from the bond tests, as well as the mode of failure, are given in Tables 4.1 and 4.2, for C1 concrete and in Tables 4.3-4.6, for C2 concrete. In these tables, f'_c is the concrete compressive strength of the control samples taken from eacht batch, τ_{max} is the bond strength, and $s_{m,le}$ and $s_{m,ue}$ are the slip values at the bond strength for the loaded and the unloaded ends, respectively. The mean values of the bond strength and the corresponding slips of nominally identical specimens are also reported. A normalised bond strength (τ^*_{max}), that accounts for the effect of the concrete strength, is defined by

$$\tau^*_{max} = \frac{\tau_{max}}{\sqrt{f'_c}} \tag{4.1}$$

Since a large variety of FRP bars were tested a single code notation that represented the parameters of each specimen was difficult to be applied. Therefore, a general code notation defined in Figure 4.1 was used, describing the specimen features of any specimen.

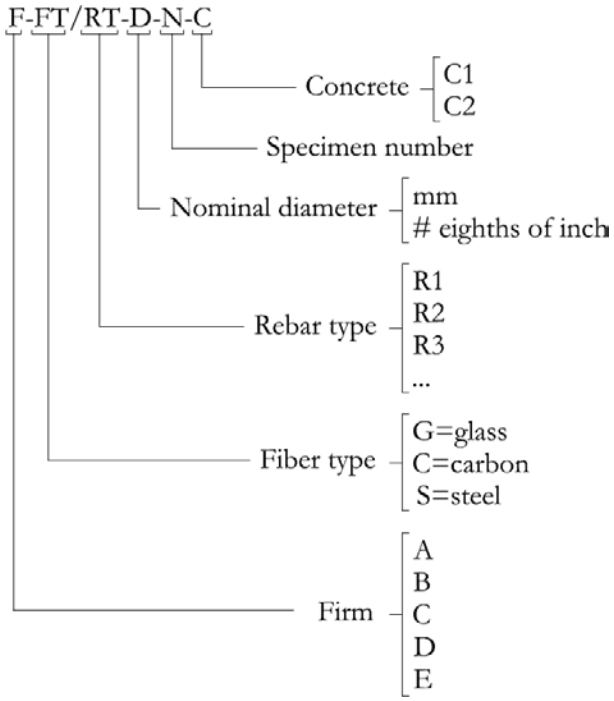

Figure 4.1: Specimen identification description.

For each test, the bond stress-slip curves were depicted both at the loaded and unloaded end of the bar. These graphs will facilitate comparison among the tests and are presented for most of the tests in Appendix A. In some of the tests it was not possible to measure the unloaded end slip of the bar due to some LVDT problems. In these cases, the authors decided to proceed with the testing procedure without the bottom transducer, instead of stopping the test and start again, since it was assumed that the bond capacity of the bar might be influenced if a second load cycle was imposed to the bar.

Specimen[a]		f'_c (MPa)	P_{max} (kN)	τ_{max} (MPa)	$s^b_{m,le}$ (mm)	$s^b_{m,ue}$ (mm)	τ^*_{max} (MPa$^{0.5}$)	Failure Mode[c]
A-C/R1-#3	1-C1	27.80	30.471	17.113	1.169	0.375	3.246	PO
	2-C1	27.80	28.082	15.771	1.132	0.365	2.991	PO
	mean			16.442	1.151	0.370		
A-C/R1-#4	1-C1	29.34	36.444	12.865	0.699	0.145	2.375	PO
	2-C1	26.50	40.028	14.131	0.732	0.171	2.745	PO
	mean			13.498	0.716	0.158		
A-G/R2-#4	1-C1	26.70	34.652	11.057	1.932	0.242	2.140	PO
	2-C1	26.70	35.548	11.343	2.051	0.260	2.195	PO
	mean			11.200	1.992	0.251		
A-G/R2-#5	1-C1	28.30	51.676	12.169	1.208	0.197	2.288	PO
	2-C1	26.70	51.078	12.029	1.283	0.208	2.328	PO
	mean			12.099	1.246	0.203		
B-C/R3-#3	1-C1	26.50	11.954	9.302	0.518	0.053	1.807	PO
	2-C1	31.30	21.810	16.972	0.469	0.044	3.034	PO
	mean			13.137	0.494	0.049		
B-C/R3-#4	1-C1	30.70	14.940	6.062	0.439	0.167	1.094	PO
	2-C1	31.30	20.615	8.365	0.372	0.157	1.495	PO
	mean			7.214	0.406	0.162		
B-G/R4-#4	1-C1	30.00	29.276	9.888	7.114	5.028	1.805	PO
	2-C1	28.30	28.978	9.787	5.961	4.189	1.840	PO
	mean			9.838	6.538	4.609		
B-G/R4-#5	1-C1	30.00	42.716	10.477	3.608	1.907	1.913	PO
	2-C1	28.30	49.884	12.235	7.104	4.947	2.300	PO
	mean			11.356	5.356	3.427		

[a] Specimen identification according to Figure 4.1.

[b] -, Not measured (blocked LVDT).

[c] PO=pull-out.

Table 4.1: Experimental results for specimens with R1, R2, R3 and R4 rebars in C1 concrete.

Specimen[a]		f'_c (MPa)	P_{max} (kN)	τ_{max} (MPa)	$s^b_{m,le}$ (mm)	$s^b_{m,ue}$ (mm)	τ^*_{max} (MPa$^{0.5}$)	Failure Mode[c]
C-G/R5-8	1-C1	29.66	14.642	12.754	1.350	0.271	2.342	PO
	2-C1	29.66	14.044	12.234	1.337	0.352	2.246	PO
	mean			12.494	1.344	0.312		
C-G/R5-12	1-C1	27.16	26.887	9.089	1.093	0.242	1.744	PO
	2-C1	29.34	25.095	8.484	1.181	0.290	1.566	PO
	mean			8.787	1.137	0.266		
C-G/R5-16	1-C1	26.67	54.662	11.698	1.284	0.327	2.265	PO
	2-C1	27.16	46.001	9.844	1.402	0.334	1.889	PO
	mean			10.771	1.343	0.331		
D-G/R6-8	1-C1	29.34	15.239	19.420	-	-	3.585	PO
	2-C1	29.34	11.655	14.853	5.055	3.345	2.742	PO
	mean			17.137	5.055	3.345		
D-G/R6-12	1-C1	30.00	37.937	15.832	6.146	2.631	2.891	PO
	2-C1	29.34	41.820	17.453	7.988	4.088	3.222	PO
	mean			16.643	7.067	3.360		
E-S/R7-12	1-C1	26.50	28.380	12.547	1.249	0.974	2.437	PO
	2-C1	30.70	35.249	15.584	2.620	2.085	2.813	PO
	mean			14.066	1.935	1.530		
E-S/R7-16	1-C1	27.16	53.468	13.296	1.569	1.349	2.551	PO
	2-C1	29.66	68.998	17.159	1.674	1.312	3.151	PO
	mean			15.228	1.622	1.331		

[a] Specimen identification according to Figure 4.1.

[b] -, Not measured (blocked LVDT).

[c] PO=pull-out.

Table 4.2: Experimental results for specimens with R5, R6 and R7 rebars in C1 concrete.

Specimen[a]		f'_c (MPa)	P_{max} (kN)	τ_{max} (MPa)	$s^b_{m,le}$ (mm)	$s^b_{m,ue}$ (mm)	τ^*_{max} (MPa$^{0.5}$)	Failure Mode[c]
A-C/R1-#3	1-C2	54.93	43.313	24.325	1.273	0.128	3.282	P
	2-C2	54.93	53.169	27.860	1.594	0.194	4.029	P
	3-C2	54.93	46.599	26.170	1.509	0.216	3.531	P
	mean			26.118	1.459	0.179		
A-C/R1-#4	1-C2	54.93	58.545	20.667	0.764	0.100	2.789	P
	2-C2	54.93	55.260	19.508	0.755	0.053	2.632	P
	3-C2	54.93	55.558	19.613	1.197	-	2.646	P
	mean			19.929	0.905	0.076		
A-G/R2-#3	1-C2	53.54	25.394	15.466	-	-	2.114	P
	2-C2	53.11	28.658	17.454	1.979	0.079	2.395	P
	3-C2	53.11	26.290	16.011	1.931	0.040	2.197	P
	mean			16.130	1.955	0.060		
A-G/R2-#4	1-C2	53.11	52.572	16.775	1.883	0.122	2.302	P
	2-C2	53.11	48.391	15.441	2.054	0.059	2.119	P
	3-C2	53.54	47.196	15.060	1.791	0.057	2.058	P
	mean			15.759	1.909	0.079		
A-G/R2-#5	1-C2	53.11	94.086	22.156	3.111	0.294	3.040	P
	2-C2	53.11	91.696	21.594	1.913	0.242	2.963	P
	3-C2	53.54	96.176	22.649	2.401	-	3.095	P
	mean			22.133	2.475	0.268		
A-G/R2-#6	1-C2	53.11	95.878	15.978	2.045	-	2.193	P
	2-C2	53.54	90.502	15.082	1.254	0.061	2.061	P
	3-C2	53.11	88.411	14.734	1.300	0.055	2.022	P
	mean			15.265	1.533	0.058		

[a] Specimen identification according to Figure 4.1.

[b] -, Not measured (blocked LVDT).

[c] P=peeling off.

Table 4.3: Experimental results for specimens with R1 and R2 rebars in C2 concrete.

Specimen[a]		f'_c (MPa)	P_{max} (kN)	τ_{max} (MPa)	$s^b_{m,le}$ (mm)	$s^b_{m,ue}$ (mm)	τ^*_{max} (MPa$^{0.5}$)	Failure Mode[c]
B-C/R3-#3	1-C2	54.93	19.420	13.485	0.646	0.123	2.039	PO
	2-C2	54.93	17.031	13.021	0.503	0.119	1.788	PO
	3-C2	54.93	11.954	9.070	0.457	0.171	1.255	PO
	mean			11.859	0.535	0.138		
B-C/R3-#4	1-C2	54.93	28.679	11.637	0.715	0.083	1.570	PO
	2-C2	54.93	28.978	9.940	0.616	0.178	1.586	PO
	3-C2	54.93	32.263	9.334	0.583	0.189	1.766	PO
	mean			10.304	0.638	0.150		
B-G/R4-#3	1-C2	49.55	31.068	22.987	2.398	0.230	3.266	PO
	2-C2	53.65	29.276	21.661	2.333	-	2.957	PO
	3-C2	53.65	28.082	20.777	2.699	0.297	2.837	PO
	mean			21.808	2.477	0.264		
B-G/R4-#4	1-C2	49.55	45.404	15.336	2.261	0.547	2.179	PO
	2-C2	53.65	51.377	17.353	2.532	0.522	2.269	PO
	3-C2	49.55	54.065	18.261	2.128	0.283	2.594	PO
	mean			16.983	2.307	0.451		
B-G/R4-#5	1-C2	49.55	73.179	17.948	3.888	4.833	2.550	PO
	2-C2	49.55	68.699	16.850	7.454	5.709	2.394	PO
	3-C2	49.55	70.491	17.289	7.738	5.690	2.456	PO
	mean			17.362	6.360	5.411		
B-G/R4-#6	1-C2	53.65	82.438	14.323	5.087	3.403	1.955	PO
	2-C2	53.65	83.931	14.582	5.440	3.733	1.991	PO
	3-C2	53.65	86.619	15.049	4.433	3.558	2.055	PO
	mean			14.651	4.987	3.565		

[a] Specimen identification according to Figure 4.1.

[b] -, Not measured (blocked LVDT).

[c] PO=pull-out.

Table 4.4: Experimental results for specimens with R3 and R4 rebars in C2 concrete.

Specimen[a]		f'_c (MPa)	P_{max} (kN)	τ_{max} (MPa)	$s^b_{m,le}$ (mm)	$s^b_{m,ue}$ (mm)	τ^*_{max} (MPa$^{0.5}$)	Failure Mode[c]
C-G/R5-8	1-C2	50.50	18.823	16.396	1.613	0.262	2.307	PO
	2-C2	56.30	20.316	17.697	1.851	0.206	2.359	PO
	mean			17.047	1.732	0.234		
C-G/R5-12	1-C2	50.50	43.015	14.541	1.452	0.148	2.046	PO
	2-C2	56.30	46.599	15.753	1.391	0.261	2.099	PO
	mean			15.147	1.422	0.205		
C-G/R5-16	1-C2	58.20	72.283	15.468	1.128	0.261	2.028	PO
	2-C2	56.30	73.179	15.660	1.198	0.345	2.087	PO
	mean			15.564	1.163	0.303		
D-G/R6-8	1-C2	47.89	23.285	29.673	8.266	3.385	4.288	PO
	2-C2	46.15	20.598	26.250	7.140	2.738	3.864	PO
	mean			27.962	7.703	3.062		
D-G/R6-12	1-C2	47.89	59.106	24.667	9.219	4.067	3.564	PO
	2-C2	47.89	65.076	27.158	8.617	2.881	3.924	PO
	mean			25.913	8.918	3.474		
D-G/R6-16	1-C2	46.15	92.538	19.553	9.262	5.577	2.878	S
	2-C2	47.89	102.389	21.634	6.689	3.068	3.126	S
	mean			20.594	7.976	4.323		
D-G/R6-19	1-C2	46.15	121.729	17.164	5.497	2.710	2.527	S
	2-C2	46.15	113.200	15.953	5.429	3.539	2.348	S
	mean			16.559	5.463	3.125		

[a] Specimen identification according to Figure 4.1.

[b] -, Not measured (blocked LVDT).

[c] PO=pull-out and S=splitting.

Table 4.5: Experimental results for specimens with R5 and R6 rebars in C2 concrete.

The most important observations of the experimental series are presented next, including an examination of the parameters affecting the bond development of FRP bars to concrete.

Specimen[a]		f'_c (MPa)	P_{max} (kN)	τ_{max} (MPa)	$s^b_{m,le}$ (mm)	$s^b_{m,ue}$ (mm)	τ^*_{max} (MPa$^{0.5}$)	Failure Mode[c]
E-S/R7-10	1-C2	49.54	46.897	29.856	5.784	0.783	4.242	Y
	2-C2	49.99	44.508	28.335	9.510	0.285	4.008	Y
	mean			29.096	7.647	0.534		
E-S/R7-12	1-C2	49.99	65.713	29.052	5.913	0.803	4.109	Y
	2-C2	49.99	65.414	28.920	8.544	1.381	4.090	Y
	mean			28.986	7.229	1.092		
E-S/R7-16	1-C2	58.20	109.019	27.111	1.633	1.228	3.554	PO
	2-C2	50.50	102.150	25.403	-	1.189	3.575	PO
	mean			26.257	1.633	1.209		
E-S/R7-20	1-C2	49.46	140.378	22.342	0.712	0.210	3.177	S
	2-C2	49.54	91.995	14.642	0.332	0.098	2.080	S
	mean			18.492	0.522	0.210		

[a] Specimen identification according to Figure 4.1.

[b] -, Not measured (blocked LVDT).

[c] PO=pull-out; S=splitting and Y=bar yielding.

Table 4.6: Experimental results for specimens with R7 rebars in C2 concrete.

4.2 Bond stress-slip relationship

The global behaviour of the bond stress-slip relationship is characterised by an initial increase in the bond stress with little slippage, followed by softening once the maximum bond stress is attained. Up to the failure, bond can be attributed to bearing (for deformed or indented bars), adhesion and friction between the rebar and concrete. Once the adhesive bond fails, different behaviours are obtained for different surface treatments.

Representative specimen curves for each tested diameter are shown in Figures 4.2, 4.3, 4.5, 4.7, 4.8, 4.11 and 4.12 to illustrate the bond stress-slip relationship obtained for the different specimens.

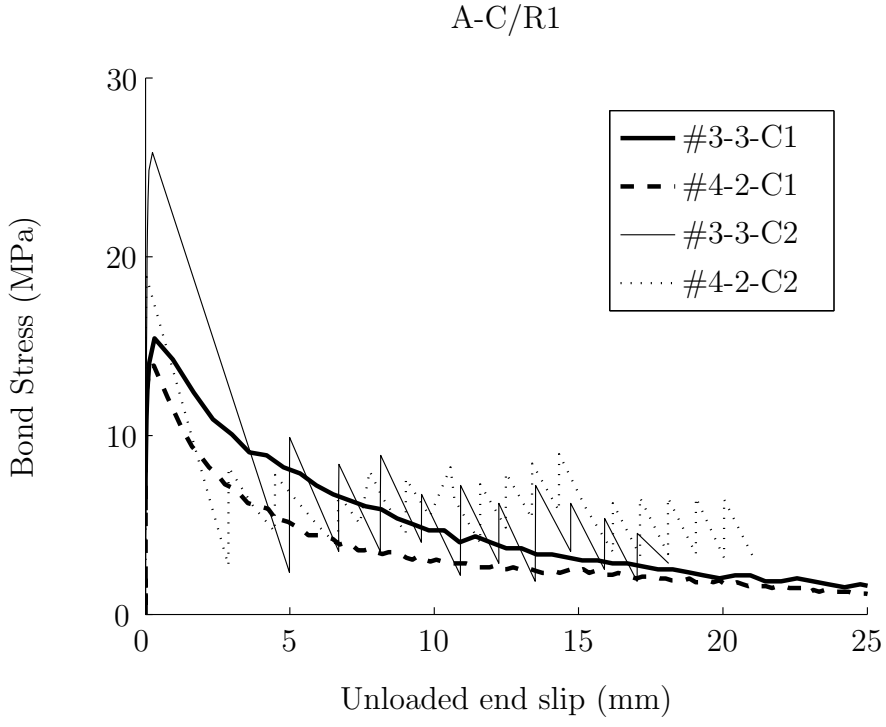

(a)

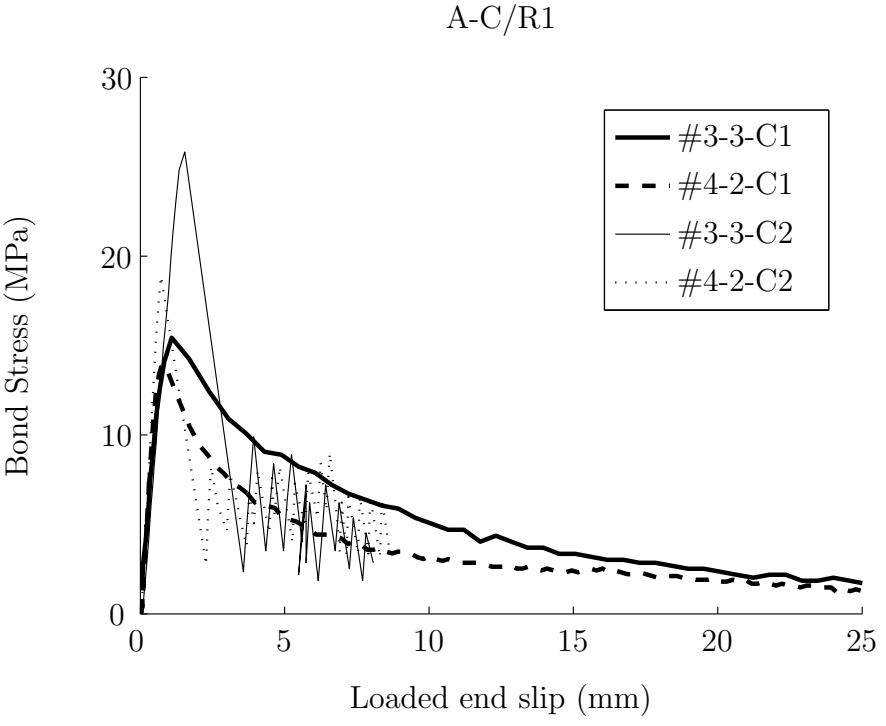

(b)

Figure 4.2: Representative bond-slip curves for R1 rebars for the (a) unloaded and (b) loaded end.

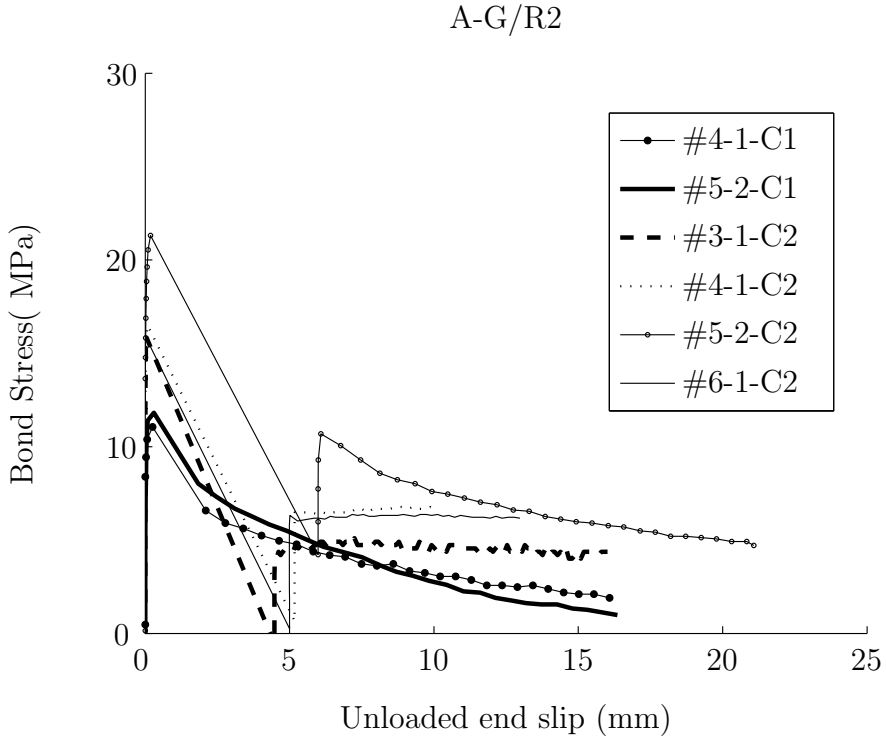

(a)

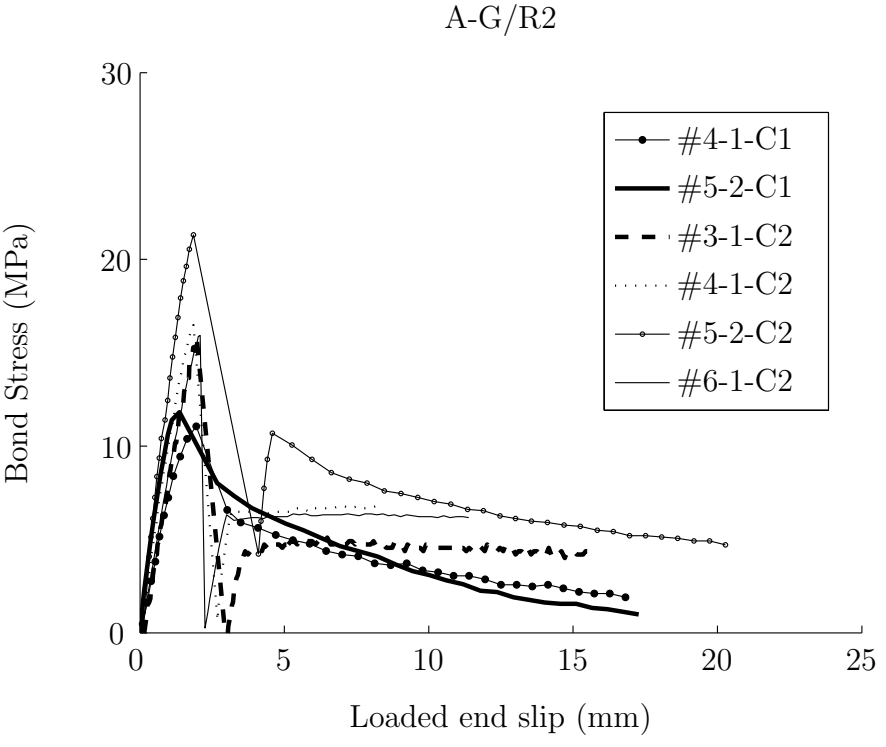

(b)

Figure 4.3: Representative bond-slip curves for R2 rebars for the (a) unloaded and (b) loaded end.

For non-deformed or non-indented bars (R1, R2, and R3), the load transfer is provided by friction and strongly depends on the transverse pressure; later on the friction diminishes as the rebar is pulled further out and the contact surface is damaged. For sand-coated rebars (R1 and R2), Figures 4.2 and 4.3, an initial good bond performance with high bond strength, almost linear behaviour and a relatively small unloaded end slip at the ascending branch of the stress-slip curve is observed. Sanding leads to an increase in the chemical bond, as reported in [22, 23]. Once the bond strength is reached, the sand coating surface debonds from the rebar, and an abrupt decay is observed due tot the dynamic effects that occur. This phenomenon is observed regardless of the concrete strength; however, for the lower concrete strength (C1) the softening decay is smoother. When using C1 concrete, pull-out of the sand from the resin layer takes place, but for higher concrete strength (C2), a sudden debonding of the whole sand coating layer is observed (see Figure 4.4). The dynamic effects taking place during the test, when the sand-coated layer debonds, explain the unloading and reloading paths observed in Figures 4.2 and 4.3 after the maximum bond stress.

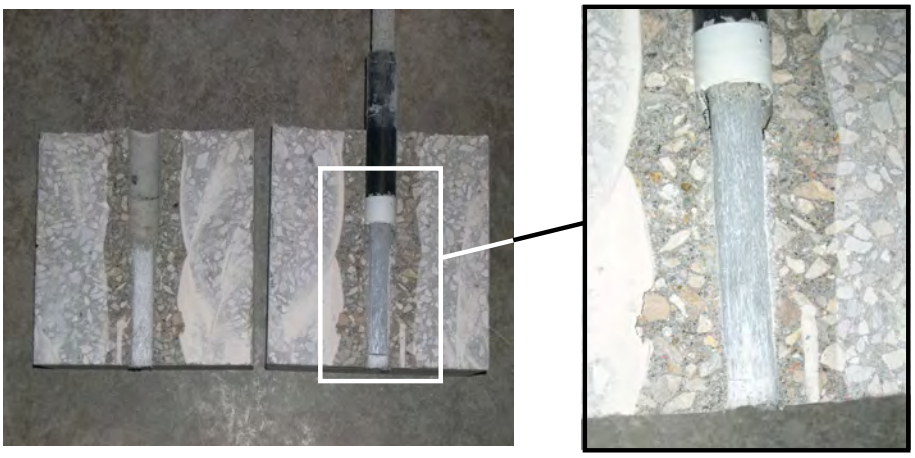

Figure 4.4: Peeling off failure mode of A-C/R2-C2 specimen.

CFRP rebars with surface texture (R3) presented a very smooth surface. Consequently, as with R1 and R2 rebars, bond strength is based primarily on chemical adhesion and friction force, and low mechanical bearing forces are expected. However, the behaviour of R3 rebars differs from the behaviour of R1 and R2 rebars. A

first peak at a very small unloaded end slip is obtained when the chemical adhesion is lost (see Figure 4.5). The debonding of the sand coating observed in R1 and R2 rebars does not take place in R3 rebars and, therefore, after the initial peak, the friction between rebar and concrete increases the maximum bond stress in high strength concrete (C2) and gives a smooth softening decay in the low strength concrete (C1), similar to the behaviour reported in [39]. However, because of its smoother surface, the R3 rebar bond strength is smaller than the R1 rebar bond strength, with the difference being even larger in C2 concrete.

Therefore, it can be concluded that for non-deformed/indented rebars (R1, R2, and R3), the rebar surface plays a very important role in the bond strength and this importance increases with the concrete strength. Moreover, it should be noted that the failure mode of the rebars is always located at the interface between the concrete and the rebar of by internal debonding of the rebar itself.

For deformed and indented rebars (R4, R5, and R6), the crushed concrete sticking to the front of the lugs exerts a wedging action; as a consequence, the surrounding concrete exerts a confinement action on the rebar. Depending on the confinement, pull-out or splitting failure occurs. Therefore, the geometry of the rebar is vey important for the stress-slip response. The influence of the rebar geometry was analysed by looking at two geometric ratios: a_s and CLR (see Figure 4.6). The first, a_s, defined as the ratio of the projected rib area normal to the axis to the centre-to-centre rib spacing (Equation 4.2), is computed for deformed and indented rebars and is presented in Tables 4.7 and 4.8. The second, the CLR ratio, is computed for the R5 rebars (see Table 4.8) because of the difference in surface geometry between R5 rebars and R4 and R6 rebars. The CLR ratio was first presented in [26] to analyse the influence of the lug geometry of indented rebars on bond behaviour and bond strength. It is defined as the ratio between the concrete lug width, w_c, and the sum of the widths of the concrete lug and FRP rebar lug, $w_c + w_f$ (Equation 4.3) .

$$a_s = \frac{A_r}{r_s} \tag{4.2}$$

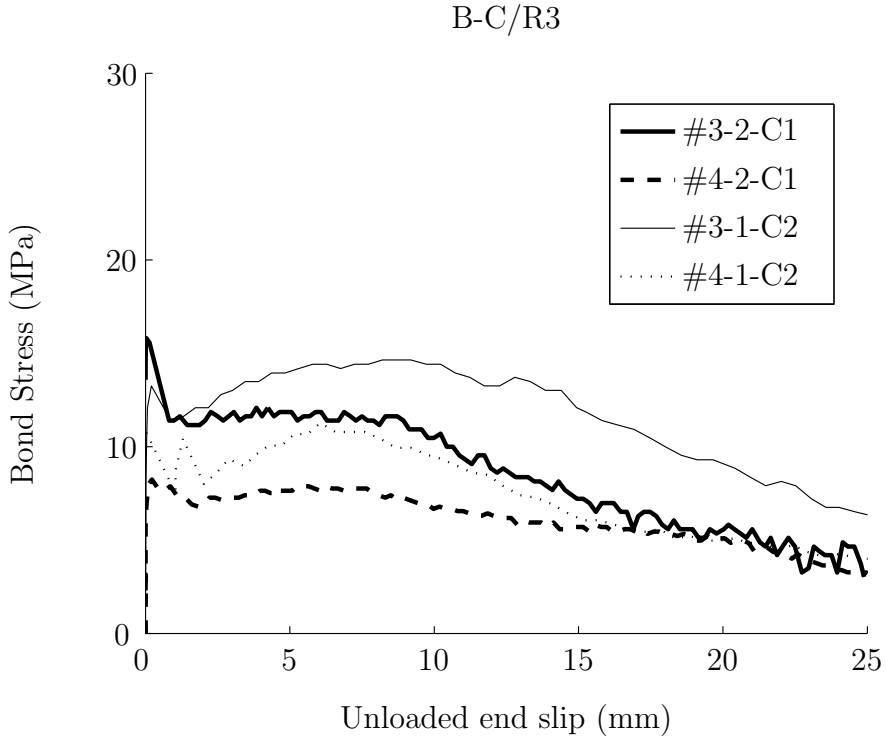

(a)

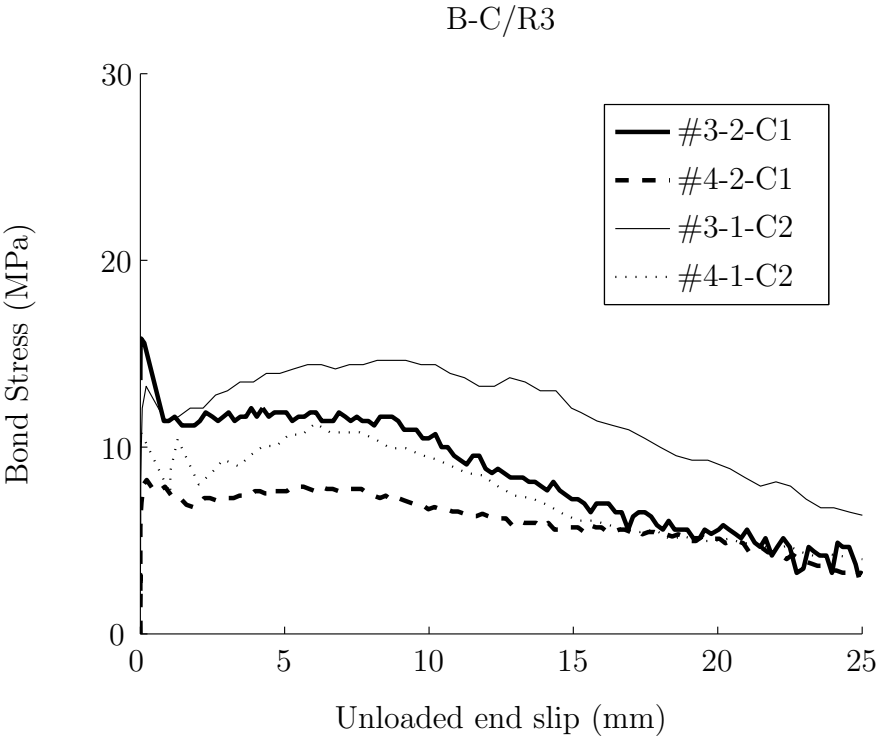

(b)

Figure 4.5: Representative bond-slip curves for R3 rebars for the (a) unloaded and (b) loaded end.

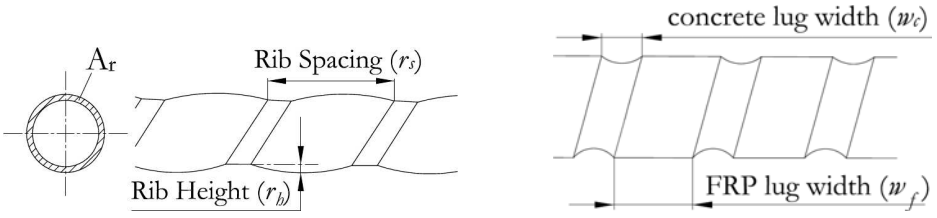

(a) (b)

Figure 4.6: Definition of (a) the area to space ratio, a_s, and (b) the concrete lug ratio, CLR.

$$CLR = \frac{w_c}{w_c + w_f} \tag{4.3}$$

Rebar	$d_b(mm)^a$	Surface characteristics		
		$r_s(mm)$	$r_h(mm)$	$a_s(mm)$
B-G/R4	9.28	22.75	0.47	0.633
	13.73	21.66	0.47	0.968
	16.11	19.60	0.47	1.249
	19.14	17.35	0.47	1.669
D-G/R6	7.07	18.39	1.38	1.992
	12.35	16.02	1.09	2.873
	17.36	16.13	0.84	2.978
	21.25	16.42	1.03	4.391

[a] According to ACI 440.3R-04

Table 4.7: Geometrical characteristic of R4 and R6 rebars.

GFRP rebars with helical wrapping and some sand-coating (R4) presented a surface with a constant rib height but a rib spacing that decreases with the rebar diamter. The shape of the bond stress-slip curves obtained for the higher concrete strength, C2, changes with the rebar diameter, as shown in Figure 4.7. For smaller diameters the rib spacing increases, therefore the area to space ratio, a_s, decreases. For smaller values of a_s, bearing resistance decreases, producing a more abrupt decay in bond stress after the peak. For larger values of a_s, larger bearing resistance

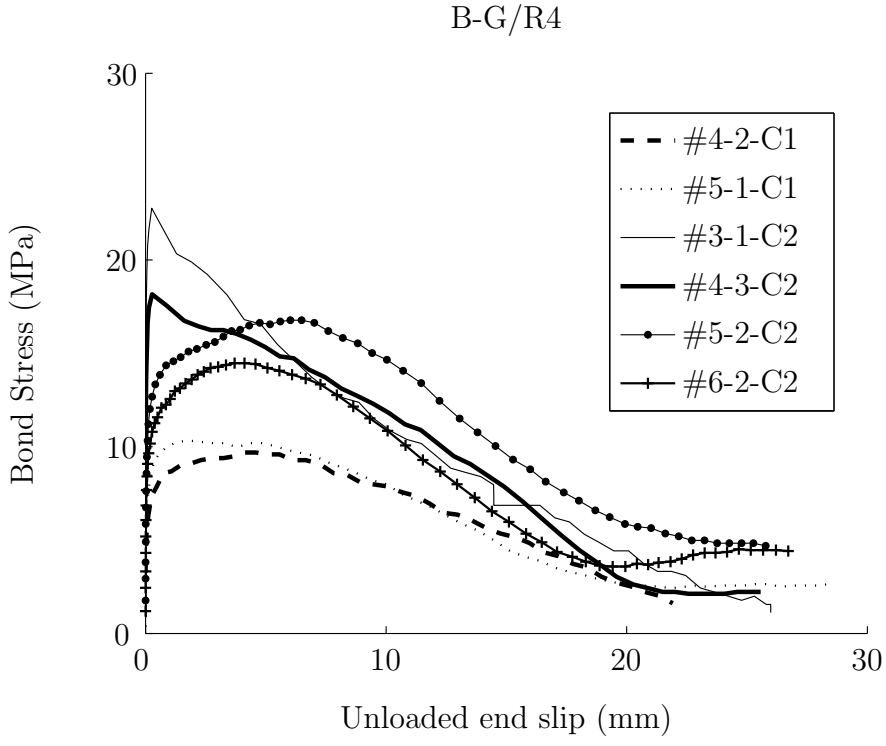

(a)

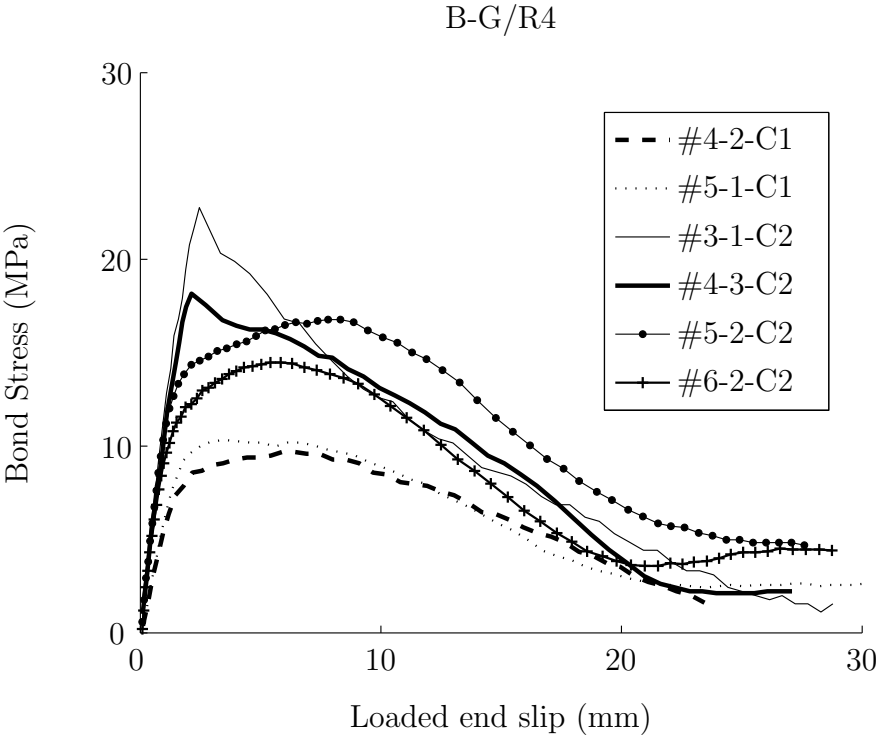

(b)

Figure 4.7: Representative bond-slip curves for R4 rebars for the (a) unloaded and (b) loaded end.

Rebar	$d_b(mm)^a$	Surface characteristics			
		$r_s(mm)$	$r_h(mm)$	CLR	$a_s(mm)$
C-G/R5	8.55	5.40	3.60	0.400	1.250
	13.72	5.32	3.68	0.409	3.260
	17.25	4.75	4.25	0.472	5.969

[a] According to ACI 440.3R-04

Table 4.8: Geometrical characteristic of R5 rebars.

develops after the point where the chemical adhesion is lost, increasing the bond strength. This explains the difference in the bond stress-slip curve obtained when using smaller diameters (#3 and #4 compared to #5 and #6). For smaller diameters, the unloaded end slip at the maximum bond-stress is significantly smaller than it is for larger diameters. The concrete strength has an important influence on the bearing resistance, which decreases with decreasing concrete strength. Therefore, a smaller influence of rib spacing and a_s in the bond-slip curve is expected when using C1 concrete, as it can be observed in Figure 4.7. The differences observed between the bond-slip curves of #4 and #5 rebars in C2 concrete are not observed in C1 concrete.

The experimental results obtained using the specimens with grooved rebars (R5) present an almost linear behaviour until bond strength is reached, with a very small unloaded end slip. Once the bond strength is reached, however, a softening behaviour, followed by an additional undulation of the curve is observed (Figure 4.8). This undulation is related to the re-engaged mechanical interlock after the shearing off of the rib or the concrete lug (see Figure 4.9), as the period of oscillations corresponds approximately to the deformation spacing of the rebar ($w_c + w_f$ in Table 4.8). A similar undulating behaviour has also been reported for steel bars as indicated in MC-90 [5]. When using C2 concrete, the shearing off of the ribs is more pronounced and the observed undulations diminish compared to specimens in C1 concrete. A similar undulating behaviour is observed for R4 and R6 rebars.

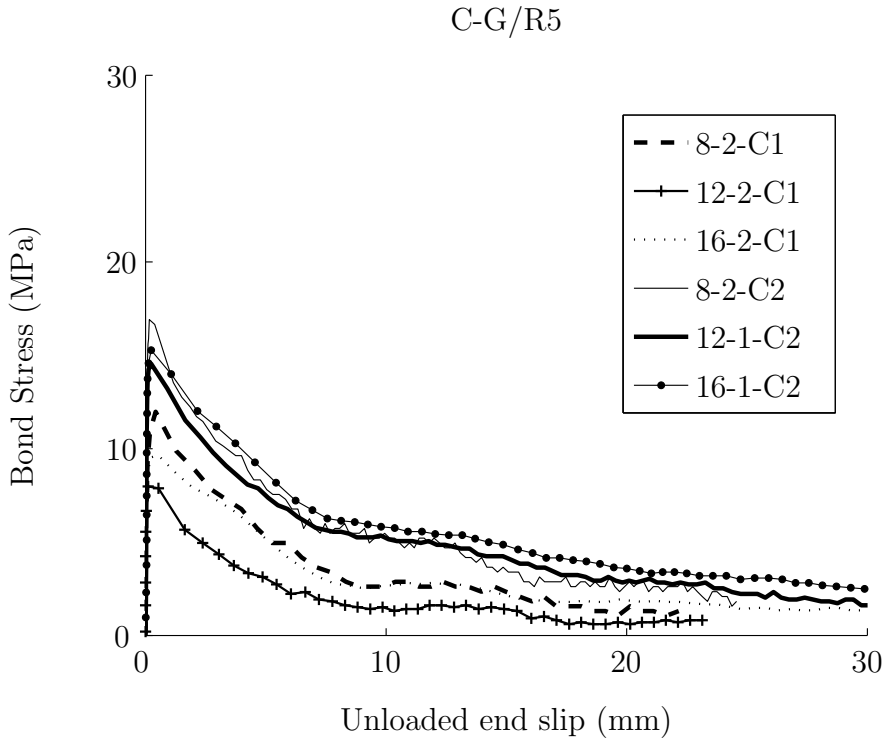

(a)

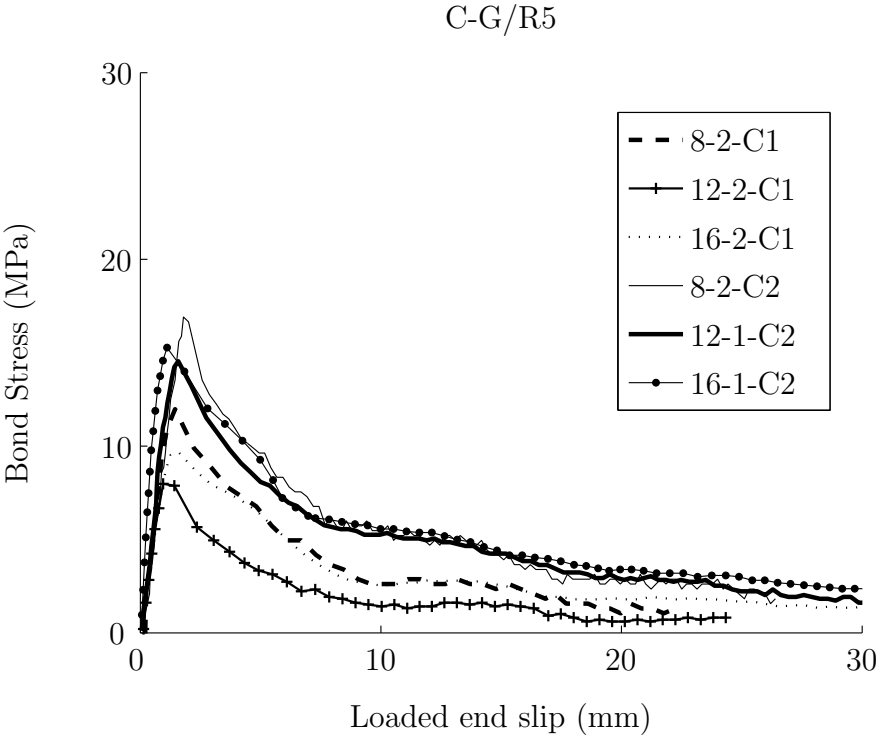

(b)

Figure 4.8: Representative bond-slip curves for R5 rebars for the (a) unloaded and (b) loaded end.

The R5 rebars presented a constant rib height of about 5% of the diameter, which is considered to be sufficient to provide adequate bond behaviour to concrete [11, 17, 29, 30]. Also, the spacing between ribs in R5 rebars is considerably smaller than in R4 and R6 rebars. Therefore, for R5 rebars, the wedging action resulting from the crushed concrete sticking to the front of the ribs is less pronounced than it is for R4 and R6 rebars. This may explain why the bond-slip behaviour of the R5 rebars is more similar to the sand-coated R2 rebars than it is to the R4 and R6 rebars with helical wrapping. Furthermore, the influence of the *concrete lug ratio*, *CLR*, has to be considered in order to compare the bond-slip curves obtained for different diameters. R5 rebars presented a constant *CLR* value of ≈ 0.4 for 8 and 12mm diameter rebars, increasing to 0.47 for a diameter of 16mm. Due to this increase in the *CLR* value, the tendency of larger diameter rebars to develop lower bond strengths is not quite followed by R5 rebars (see Tables 4.1- 4.6 and Figure 4.8). An increase in the *CLR* increases the bond strength, as reported by Al-Mahmnoud et al. [26] for rebars with a grooved surface. However, it is observed that the *CLR* does not have any effect on the initial stiffness of the bond-slip curve.

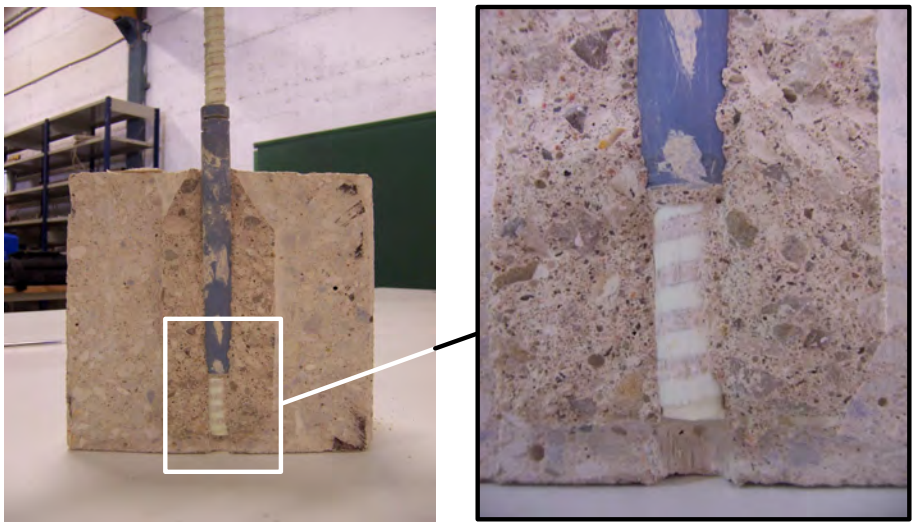

Figure 4.9: Shearing off of the concrete lug failure mode of C-G/R5-C1 specimen.

GFRP rebars with deeply-marked helical wrapping (R6) presented a surface with a variable rib height and spacing for the different rebar diameters, with a_s increasing with the rebar diameter. It should be noted that a_s is much larger in the R6 rebars

than it is for the rest of the rebars. The shape of the bond stress-slip curves obtained for R6 rebars (shown in Figure 4.11) is significantly different from the others, except for R4 rebars with large diameters (smaller rib spacing). The ascending branch of the curve is clearly non-linear and the slips corresponding to the bond strength are higher than they are for the other rebars. Moreover, for larger diameter R6 rebars (16 and 19mm), the specimens failed by splitting, indicating that the higher a_s increases the radial stresses on the specimen (see Figure 4.10).

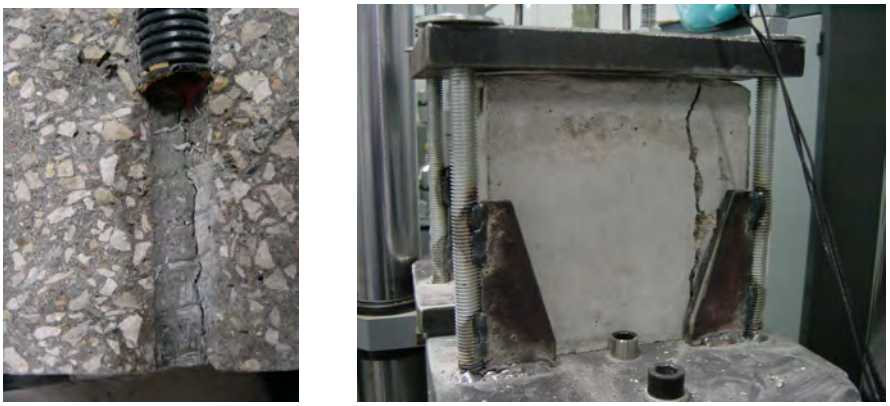

(a) (b)

Figure 4.10: Splitting failure mode of D-G/R6-C2; (a) splitting crack starting at the bond interface and (b) splitting crack visible at the outer face of pull-out specimen.

For comparison purposes, pull-out tests with steel rebars were also performed (Figure 4.12). For steel rebars, only the unloaded end slip is usually reported in pull-out tests, since not much elongation is expected [110]. In this study, slip data were recorded for both the loaded and unloaded ends. For the tests performed with rebars with nominal diameters of 10 and 12mm using C2 concrete, the bond capacity was greater than the bar capacity and the steel rebars yielded (see the plateau obtained in curves in Figure 4.12(b) for C2 concrete). For larger diameters, as in the case of R6 rebars, splitting failure occurred. Moreover, the slips corresponding to the maximum strength are small, indicating that an almost linear behaviour is obtained in the ascending branch of the derived bond stress-slip curves. Higher bond strengths are obtained with smaller diameters.

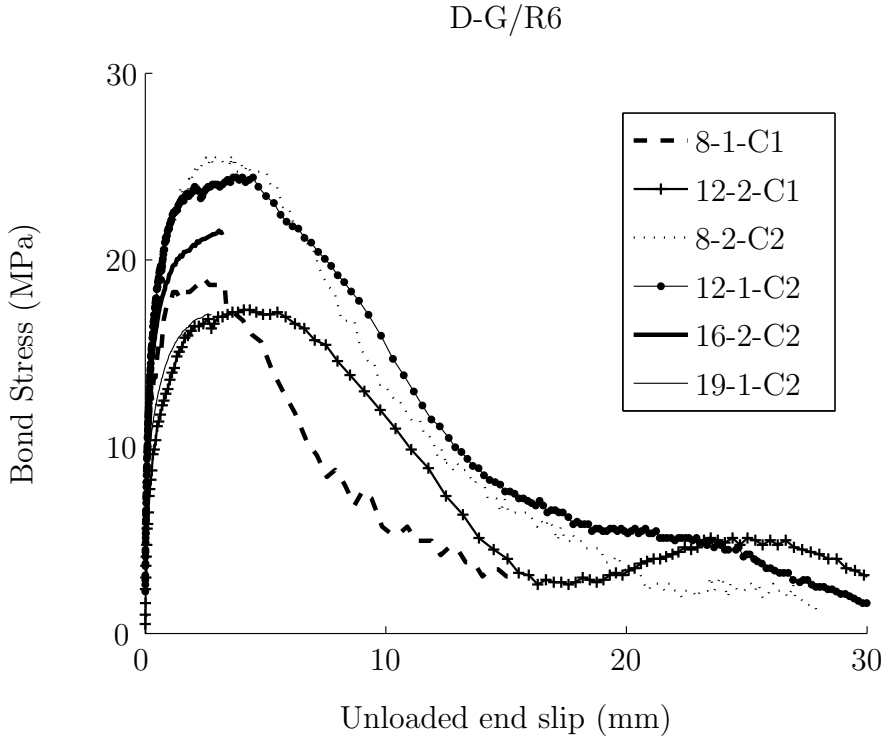

(a)

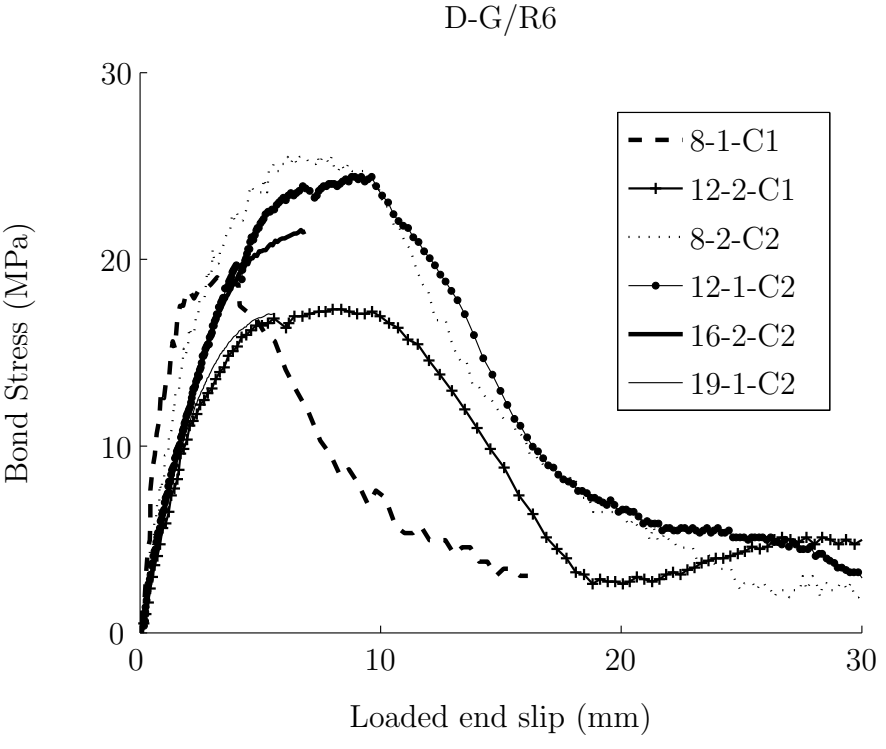

(b)

Figure 4.11: Representative bond-slip curves for R6 rebars for the (a) unloaded and (b) loaded end.

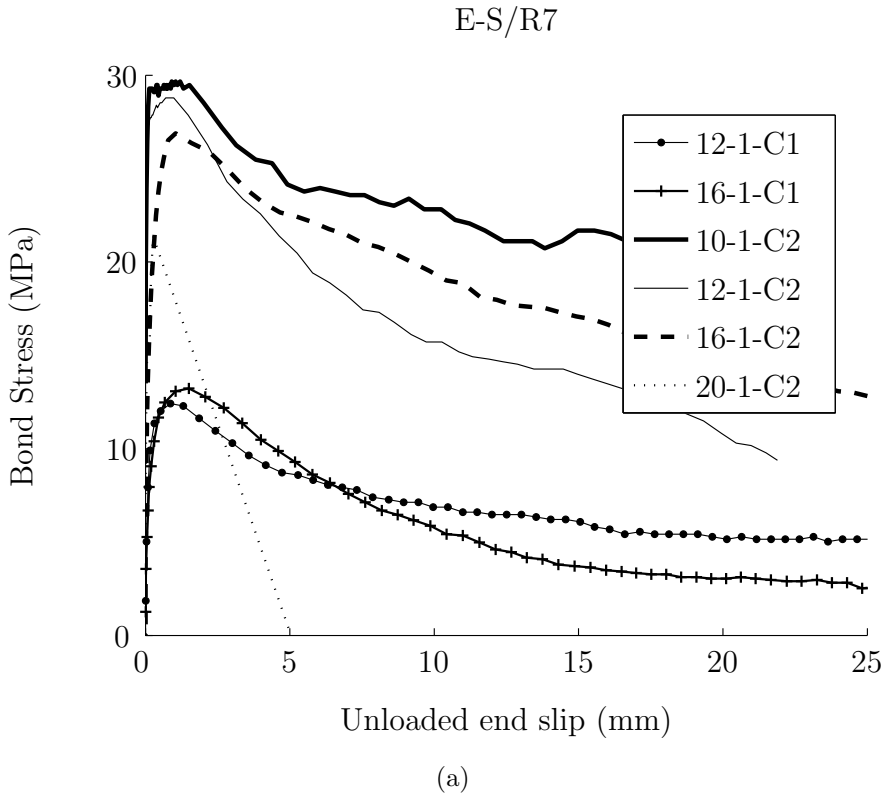

(a)

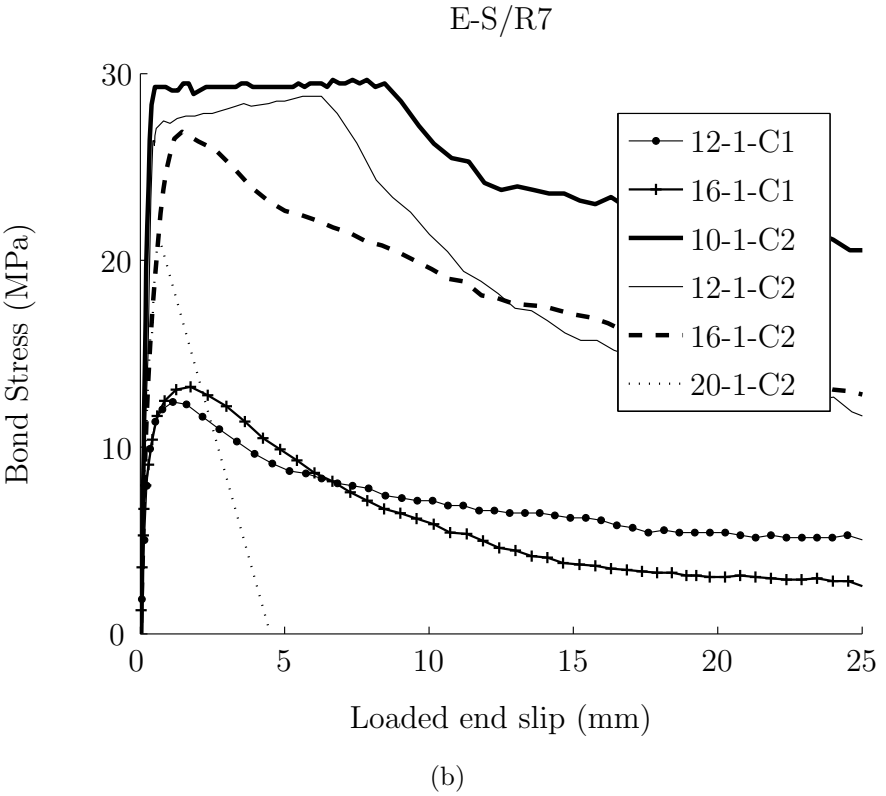

(b)

Figure 4.12: Representative bond-slip curves for R7 rebars for the (a) unloaded and (b) loaded end.

4.2.1 Initial stiffness

The influence of the different types of rebar and the rebar diameter on the initial stiffness of the bond-slip curve is analysed in this section. The ascending branches of bond stress versus loaded end slip curves for CFRP and GFRP sand-coated (R1 and R2) and steel (R7) rebars, in C1 and C2 concrete, are analysed. Specimens of similar nominal diameter have been selected in order to eliminate the effects of different rebar diameters.

GFRP bars are expected to develop greater slip values than CFRP bars under similar pull-out loads, since their elastic modulus is less than half that of CFRP bars. This is confirmed by the results shown in Figure 4.13. For lower traction forces, the slip of the steel rebars (R7) is negligible, regardless of the concrete used. However, for FRP rebars, as soon as traction is applied, the slip between the rebar and the concrete can be measured.

The ascending branches for the different GFRP rebars used in this experimental study are also plotted in Figure 4.14. Specimens of R5 rebars present the highest initial stiffness because they have the highest Young's modulus of all the GFRP rebars. However, for the rest of the GFRP rebars, a higher stiffness is obtained when using R2 rebars. R2 and R6 have a similar elastic modulus, while R4 has the smallest elastic modulus, according to manufacturer indications shown in Table 3.3. However, the experimentally measured Young modulus for R2, R4 and R6 rebars were 46.8, 39.3 and 39.1MPa, respectively. Therefore, the differences in the initial stiffness, observed in Figure 4.14, are attributed to the differences in the measured rebar stiffness.

The influence of the rebar diameter on the initial sitiffness is also analysed. As seen in Figures 4.2, 4.3, 4.5, 4.7, 4.8, 4.11 and 4.12, the initial stiffness is not mainly influenced by the rebar diameter. Only the 8mm diameter R6 rebars presented a different initial stiffness. This may be because of some geometric effect since, in the R6 rebars, the rib spacing and height varies with diameter, although without a defined pattern. However, further investigation is required to analyse this.

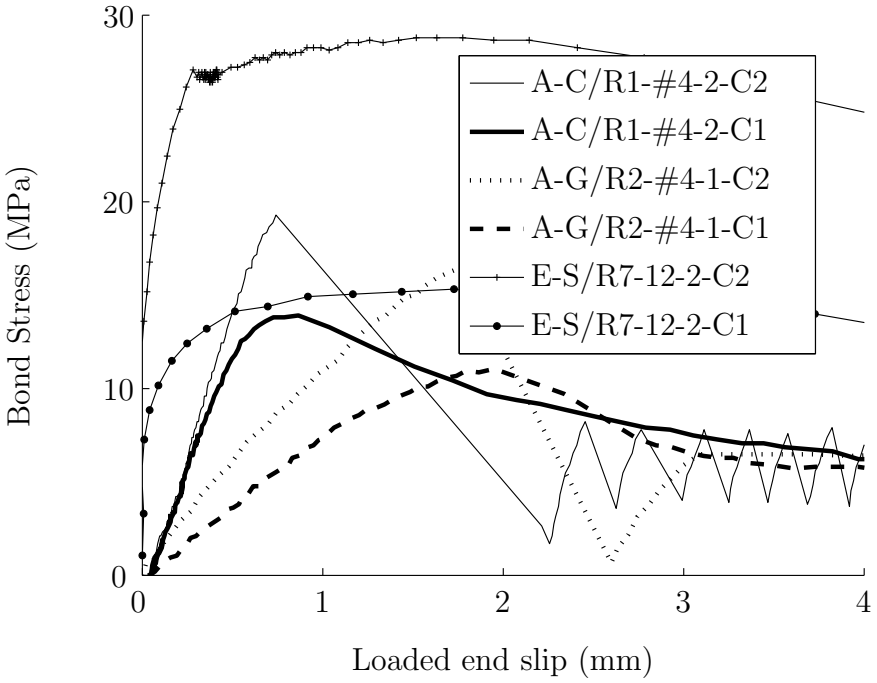

Figure 4.13: Comparison of the initial stiffness of the bond-slip curves (for the loaded end) of specimens with carbon (R1) and glass fibres (R2) and steel (R7) and two concrete grades.

Finally, it is worth mentioning that no influence of the concrete compressive strength on initial stiffness has been observed when using CFRP and steel rebars; in contrast, when using GFRP with lower Young Modulus values, the higher the concrete compressive strength, the higher the initial stiffness obtained (see Figures 4.7(b) and 4.13). This is because of the larger effect that a change in concrete compressive strength (and therefore in the Young Modulus of concrete) has on the response of a GFRP reinforced member; i.e. the similar Young Modulus values of the two materials (GFRP and concrete) increase the global response sensitivity to a change in the materials' properties. When a CFRP reinforced member is considered, the larger differences in the Young Modulus values of the materials diminish the effect of concrete compressive strength on the global response.

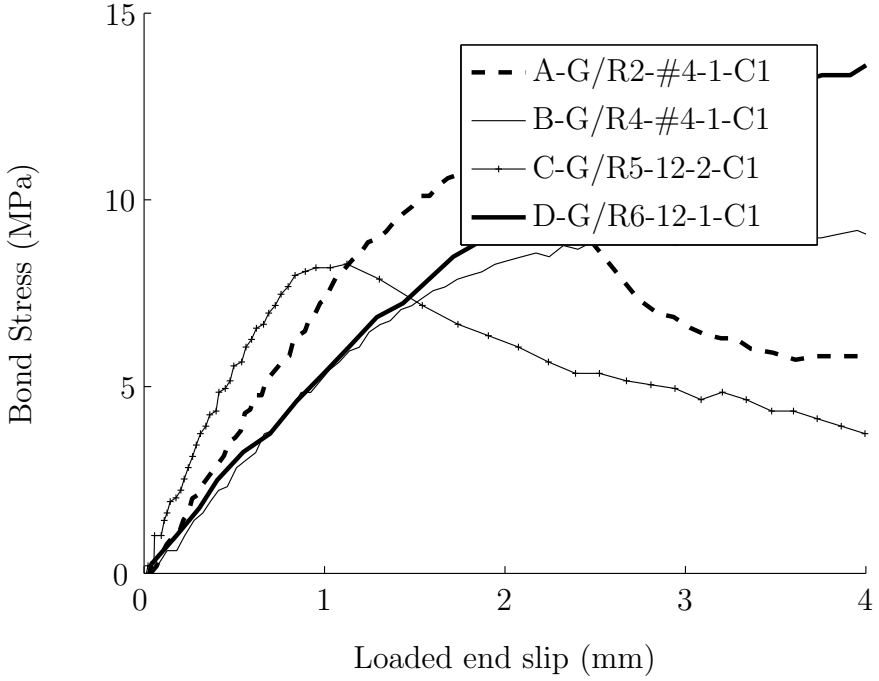

Figure 4.14: Comparison of the initial stiffness of the bond-slip curves (for the loaded end) of specimens with glass fibres but different surface treatment (rebars R2, R4, R5 and R6) and C1 concrete grade.

4.2.2 Effect of concrete strength on bond strength

The strength of the concrete affects the bond failure model of the rebar during pull-out (Tables 4.3-4.6). As indicated in [11, 18], for concrete with compressive strength approximately greater than 30MPa, the bond failure occurs at the surface of the FRP rebars. Consequently, the bond strength of FRP rebars does not depend greatly on the value of concrete strength, but rather on the rebar's properties. However, for lower compressive strength concretes (around 15MPa), the bond failure model changes and failure takes place at the concrete matrix interface.

This tendency has been confirmed by the tests carried out in this study. Although the concrete strengths were not low enough to produce failure that was caused exclusively by damage in the concrete, less damage in the bars and more in the concrete was detected for lower concrete strengths, and vice versa.

When using C1 concrete, all specimens failed in a pull-out mode with failure taking place in the concrete surface. In most cases, the change in concrete compressive strength did not involve a change in failure mode; nevertheless, a change in failure surface did take place, involving more damage on the rebar surfaces (Figure 4.15). A change in failure mode when using C2 concrete was obtained for sand coated rebars (R1 and R2), where debonding of the whole layer of he sand coating from the bar occurred (Figure 4.4). A change in failure mode when using C2 concrete was also observed for the larger diameters of R6 and R7 rebars. In those cases, concrete splitting, rather than a pull-out failure was observed (see Figure 4.10). Furthermore, yielding was observed for the small diameter R7 rebar tested in C2 concrete (see Figure 4.12(b)).

(a) (b)

Figure 4.15: Pull-out failure mode of (a) B-G/R4-C1 specimen with little damage on the rebar surface and some attached concrete and (b) B-G/R4-C2 specimen with damage concentrated on rebar surface.

The mean bond strengths obtained for the different rebars, as well as the maximum and minimum experimental values obtained, are shown in Figure 4.16. It can be seen that the higher the concrete strength, the higher the bond strength is. Although the increase in strength depends on the type of bar, variations of up to 2.1 are obtained (see Figure 4.17), indicating the effect of the concrete strength on the bond strength.

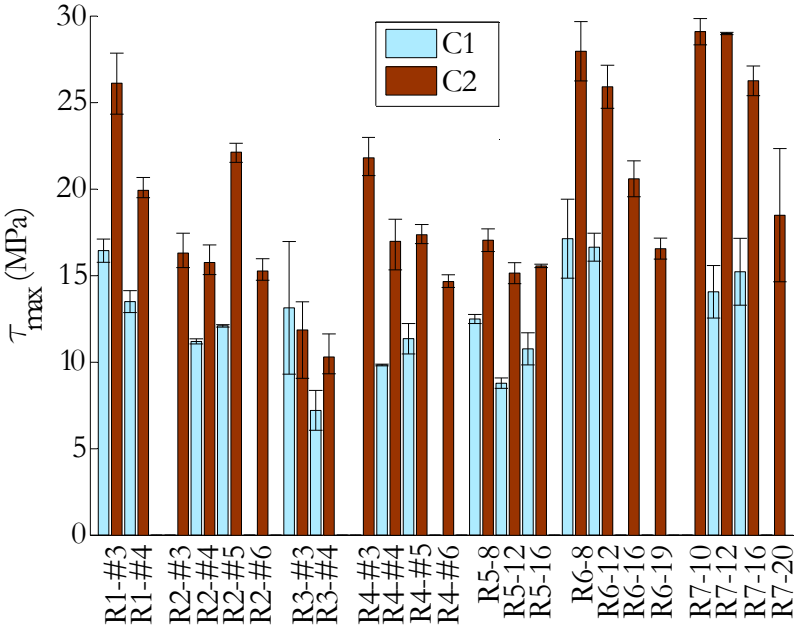

Figure 4.16: Bond strength for specimens in C1 and C2 concrete.

4.2.3 Effect of bar diameter on bond strength

Many references in the literature [11, 15, 17, 18, 23, 36, 44] have pointed out that larger bar diameters develop lower bond strengths. During the pull-out test, the peak bond stress moves gradually from the loaded end towards the unloaded end of the bar, while the bond stress value at the loaded end decreases considerably, having a nonlinear distribution of stresses along the bar. It has been suggested by some authors [11, 17] that this migration and nonlinear stress distribution would explain the bond strength's dependence on rebar diameter, since this nonlinear distribution is more evident in the case of the larger embedment lengths needed for larger diameters ($l_b = 5\,d_b$), which result in the lower average bond strength values obtained in these tests.

Moreover, the Poisson effect may also have an influence on this phenomenon because of the reduction in the bar diameter when an FRP bar is pulled under tension. This diameter reduction (in absolute value) increases with the bar size, which can lead to a reduction in the frictional and mechanical locking stresses. Further

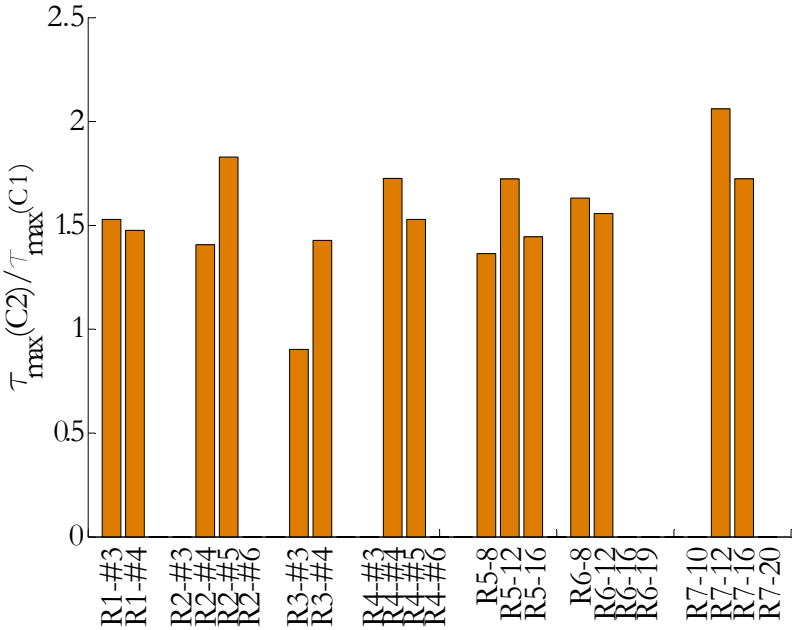

Figure 4.17: Increase in bond strength due to change in concrete compressive strength represented through the ratio $\tau_{max}(C2)/\tau_{max}(C1)$.

evidence of a relationship between diameter and bond strength can be found using the size effect concept [112]; for geometrically similar specimens, the larger the rebar diameter, the lower the bond strength. This is due to the brittle nature of the failure observed in the pull-out tests and the greater amount of elastic energy available when using larger diameters.

The dependence of bond strength on bar diameter can be observed in Figure 4.16. For the specimens in C2 concrete, a general trend of decreasing bond strength with increasing rebar diameters is observed. However, this tendency is not clear with the specimens in C1 concrete.

4.2.4 Effect of surface treatment on bond strength

The rebars used in this study (see Table 3.3 and Figure 3.2) are designed to improve the bond in different ways. Due to the importance of the rebar surface on bond behaviour, it is worth comparing the bond strengths obtained for the different rebars.

In the case of CFRP rebars (R1 and R3), the higher bond strengths are obtained with the sand coated rebars (R1), irrespective of the concrete strength. In both cases, rebar surface can be considered as non-deformed, with bond strength strongly dependent on the friction resistance provided by the surface treatment.

However, three out of four of the GFRP rebars considered in this study belong to the deformed/indented category. Therefore, the analysis of the influence of the surface treatment is carried out with respect to the surface geometry. The highest bond strength is obtained with R6 rebars and can be attributed to their highest a_s value. For the rest of GFRP rebars, with either non-deformed surface or deformed surface with low a_s value, lower bond strengths are obtained because there is little bearing resistance. The smaller rib spacing of R5 rebars results in a smaller wedging action of the crushed concrete in the C2 series, and therefore in bond strength values closer to those of R2 rather than those of R4 and R6 rebars.

The effect of surface treatment can also be analysed with regard to the concrete strength. Damage is expected to be found more in the concrete surface in C1 concrete tests, and more in the rebar surface for the C2 tests. The results show similar bond strength values for C1 concrete, regardless of the surface treatment, while higher differences in bond strength values are found for C2 concrete. Therefore, the surface treatment has a significant influence on bond strength in those cases where failure is not occurring in the concrete.

4.3 Concluding remarks

In this chapter, the interfacial bond behaviour between different kinds of carbon and glass FRP bars and two different concrete strengths has been analysed. Based on the results of this experimental study the following conclusions can be drawn.

Bond behaviour between FRP bars and concrete depends on many factors including concrete compressive strength, rebar diameter and surface treatment. An increase in bond strength and changes in failure model and failure surface are ob-

served when changing concrete compressive strength. The analysis of the influence of the surface treatment on bond behaviour confirms the existence of different bond mechanisms for different surface treatments. Furthermore, the influence of rebar surface treatment on bond strength is less important in the low concrete strength C1 series than in the high concrete strength C2 series (in which bond strength influence is more pronounced). For deformed or indented rebars the influence of the surface geometry is analysed using the a_s and CLR geometric ratios, obtaining higher bond strength for higher values of a_s. Similarly, an increase in the CLR ratio increases bond strength.

The experimental results confirm the tendency of rebars with larger diameters to have lower bond strength, especially in the case of C2 concrete. However, the initial stiffness is not mainly influenced by the rebar diameter. Nevertheless, changes in the initial stiffness due to a change in concrete compressive strength are observed for some specimens of GFRP rebars. The slip values obtained for GFRP are greater than those for CFRP bars. There is also a difference in the first loading branch between the bond-slip law of steel rebars compared to that of FRP rebars, since there is a high level of stiffness with no slip in the steel rebars, whereas the FRP rebars develop slip from the beginning.

Chapter 5

Experiments on GFRP RC ties

This chapter provides detailed data on the test design, specimens manufacturing, final testing and data analysis of GFRP RC ties. First, information regarding tensile tests performed on bare GFRP rebars is presented and details on specially strain gauged GFRP rebars are given. Then experimental methodology of GFRP RC ties is presented. The chapter continues with the presentation and analysis of experimental data. Finally, specific experimental data on notched ties is analyzed.

5.1 GFRP bars tensile tests

Before studying the behaviour of GFRP RC ties, it is necessary to determine the mechanical properties on GFRP reinforcing rebars. RC tension tests performed in this thesis were not tested in the same experimental campaign. Therefore, although the reinforcing bar diameter was equal for some tests, direct tensile tests on all the rebars were performed, to avoid possible miscalculation of mechanical and geometrical properties of rebars, coming from different manufacturing batches.

The GFRP reinforcing bars, named B-G/R4 in Chapter 4, were manufactured by Hughes Brothers Inc. and had a helical wrappping surface and some sand coating (see Figure 5.1). Three different rebar sizes were used in the tests: #4, #5 and #6, where # stands for eighths of an inch. Hereafter, the rebars will be referenced using their nominal diameter expressed in mm. This way, rebars identification 13, 16 and 19 refer to rebars having nominal diameter size equal to 12.7, 15.9 and 19.1mm.

Figure 5.1: GFRP rebars used in direct tensile tests.

The performance of tension tests on GFRP bars is different from that of steel, as any load applied perpendicular to fibre direction (through the gripping system) will cause damage. Therefore, care was taken to manufacture the gripping arrangement. The final solution consisted in a drilled-through steel housing that was bonded to the rebar with a bisphenol-A type epoxy resin (RFS 816) with an amine-based hardener (Epolam 2500). The epoxy system was poured into the housing and the bar was introduced from the top. Special care was taken to ensure the rebars to be in alignment with the housing (see Figure 5.2) so that no flexural load was introduced during the test. The gripping arrangement was left to cure for at least 24 hours prior to cast the arrangement on the other side of the bar. For all the tests, dimension on the total specimen length and gripping system length was kept constant to 900 and 250mm, respectively (see Figure 5.3). On the contrary, the inner and outer diameters of the steel housing were varied according to the rebar size. For 13mm rebars, inner and outer housing diameters were 20 and 32.5mm, respectively, whilst for 16 and 19mm rebars, inner and outer housing diameter were 23.5 and 36.5mm, respectively.

The bare bar tensile tests were performed using a servo-hydraulic testing machine with a capacity of 600kN. Displacement control was selected and load was applied to the bar at a rate of 0.08 mm/s until failure. Load was measured with the electronic load cell of the testing machine and displacement was captured with an axial extensometer with a gauge length of 100mm. The axial extensometer was removed from the rebar at a load level of $0.6P_{rupture}$ to avoid any damage, where

Figure 5.2: Detail of the rebar alignment with steel housing.

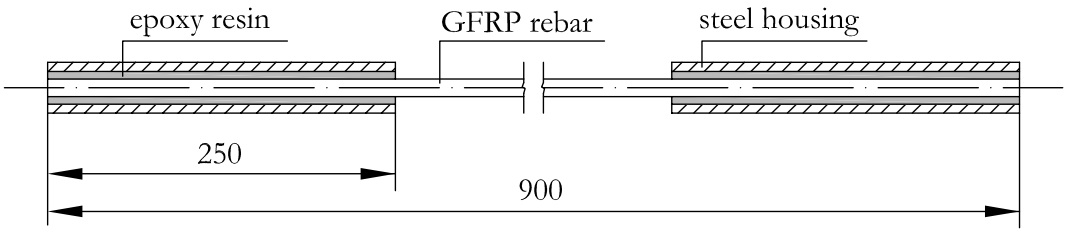

Figure 5.3: Sketch of rebar tensile test specimen (units in mm).

$P_{rupture}$ is the rebar rupture tensile load. Final rebar failure for the three diameters is shown in Figure 5.4.

Moreover, normalized tests were conducted to determine the cross-sectional areas of the rebars, according to ACI 440.3R-04 [111] and CSA S806-02 [25]. Mean values of mechanical properties obtained from uniaxial tension tests are shown in Table 5.1.

Rebar designation	Nominal diameter, d_n (mm)	Experimental diameter, d_b (mm)	Rupture tensile strength, f_{fu} (MPa)	Axial stiffness, $E_r A_r$ (kN)
13	12.7	13.73	770	5540
16	15.9	16.11	751	7900
19	19.1	19.14	637	11680
16-2	15.9	16.88	1030	9362

Table 5.1: GFRP rebars mechanical properties.

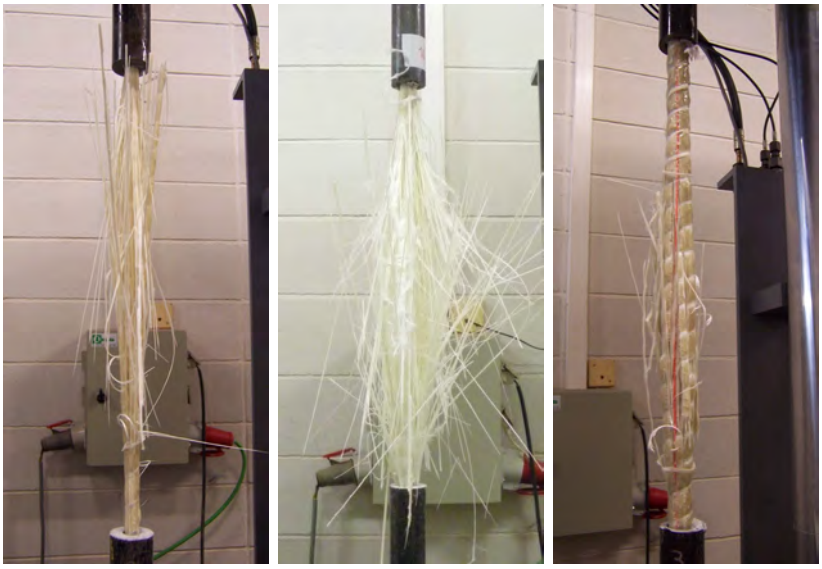

(a) (b) (c)

Figure 5.4: Tensile failure for (a) 13mm, (b) 16mm and (c) 19mm GFRP rebars used in the experimental program on reinforced concrete ties.

Additionally, two specially manufactured internally strain gauged rebars were used as internal reinforcement in two notched FRP RC ties, with the aim at obtaining the strain profile of the internal reinforcement during a direct tension test.

The aim of this thesis is to study the bond behaviour between FRP bars and concrete. Results on pull-out tests, presented in Chapter 4, show a clear influence of rebar surface treatment on bond behaviour. Therefore, the idea of attaching strain gauges on the rebar surface was ruled out to avoid any interference with the bond development. In contrast, specially manufactured internally strain gauged rebars were designed.

The technique explained in what follows was applied to rebars with original diameter of #5 and #6. This specially manufactured rebars will be referred to in the present chapter as rebars 16-N and 19-N. The original bars were cut in two halves and smoothed. On one half, strain gauges were placed every 50mm centres in the centre of half bar (see Figure 5.5). On the other half, a 6.5mm wide and 4mm deep groove was cut to accommodate the wiring of the strain gauges. Additional 5mm

diameter holes were drilled @100mm to allow the gauges' wiring to come out of the bar. After protecting the gauges from possible humidity (see Figure 5.6), the bar was closed, with the two halves glued together, to form a single round bar (see Figure 5.7).

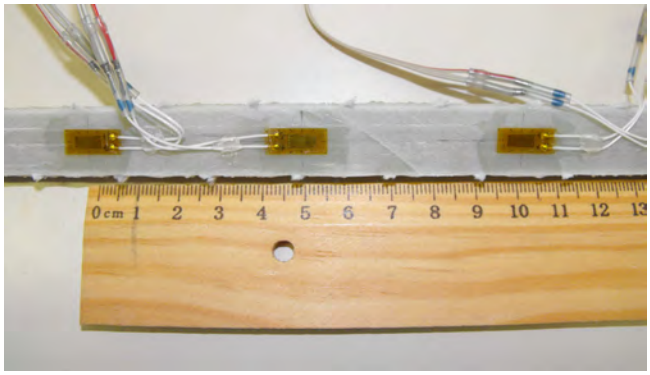

Figure 5.5: Strain gauges placed @50mm centres.

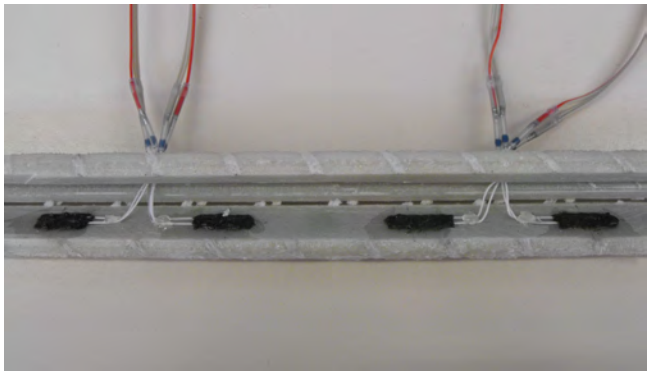

Figure 5.6: Two halves prepared to be glued together with protection on strain gauges and wires coming out through the drilled holes.

Similar to the procedure of "not-gauged" rebars, testing was conducted to determine both the geometrical and mechanical properties of internally strain gauged reinforcing bars. To this end, similar specimens to that previously presented were manufactured and ACI 440.3R-04 [111] and CSA S806-02 [25] standards were followed (see Figures 5.8 and 5.9). Mean values of mechanical properties obtained from uniaxial tension tests are shown in Table 5.2.

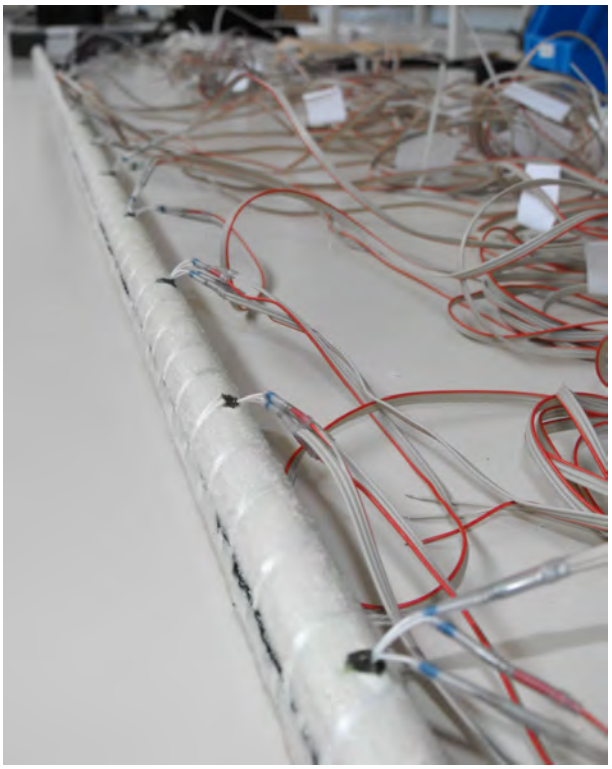

Figure 5.7: Internally strain gauged glued bar.

(a) (b)

Figure 5.8: Tensile sample to measure rebar mechanical properties; (a) Glued sample placed on testing machine with visible drilled holes and (b) final failure mode.

Figure 5.9: 200mm long samples to measure glued rebar geometrical properties.

Rebar designation	Nominal diameter, d_n (mm)	Experimental diameter, d_b (mm)	Rupture tensile strength, f_{fu} (MPa)	Axial stiffness, $E_r A_r$ (kN)
19-N	19.1	20.57	535	12750
16-N	15.9	18.24	917	10087

Table 5.2: Mechanical properties of internally gauged GFRP rebars.

5.2 GFRP RC tensile tests

In this section, the experimental methodology of direct tension tests, along with the instrumentation and testing set-up, are presented. Using the reinforcing bars analyzed in previous section as internal reinforcement, direct tension tests were performed to investigate the post-cracking response of reinforced concrete. The influence of the reinforcement ratio is studied.

5.2.1 Material properties

GFRP rebars previously tested in tension, as described in Section 5.1, were used as internal reinforcement for the reinforced concrete ties. Mechanical properties are presented in Tables 5.1 and 5.2.

Ready-mix concrete, with a maximum aggregate size of 20mm and a target compressive strength of 50MPa, was used to cast the specimens. Due to limited capacity

of the laboratory and with the aim of avoiding undesirable errors outcoming from testing inexpertence, the experimental campaign was conducted in three temporary spaced stages. The composition of the concrete is shown in Table 5.3.

Component	Units	C1 mix	C2 mix	C3 mix
Water	kg/m^3	160	160	160
Cement 42.5	kg/m^3	450	450	400
Fine aggregate	kg/m^3	775	775	825
Coarse 12 aggregate	kg/m^3	250	250	250
Coarse 20 aggregate	kg/m^3	700	700	700
Superplastizier Sika Viscocrete 5920	% cement weight	1.10	1	1
Superplastizier Sikament 90P	% cement weight	-	-	0.6
Superplastizier Sikament 290	% cement weight	072	0.6	-

Table 5.3: Composition of concrete.

Control cylinders, shown in Figure 5.10, having a nominal diameter of 150mn and height of 300mm, were match-cured and tested at the same time as the specimens. The compressive strength and modulus of elasticity were tested according to UNE-EN 12390-3 [113] and ASTM C469 [114] standards, respectively. The testing setup to determine the modulus of elasticity and the final compressive failure mode of one of the control samples are shown in Figure 5.11. Concrete mechanical properties are summarized in Table 5.4.

Concrete mix	Compressive strength, f_c (MPa)	Elasticity modulus, E_c (MPa)
C1	48.1	27315
C2	66.2	33275
C3	46.6	34514

Table 5.4: Concrete mechanical properties.

Figure 5.10: Concrete control samples used to obtain concrete mechanical properties.

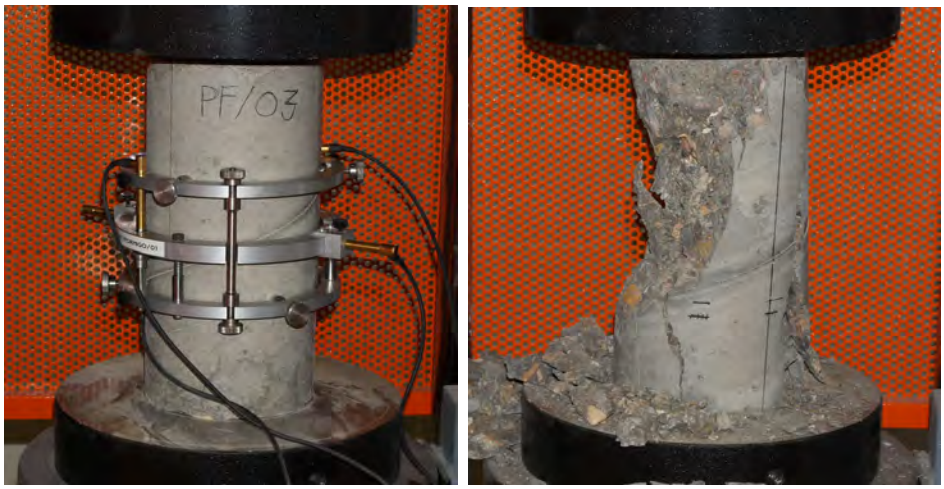

(a) (b)

Figure 5.11: Characterization of concrete; (a) test to determine the modulus of elasticity and (b) failure in compression of control sample.

5.2.2 Specimen preparation

Ties characteristics

All GFRP RC ties were 1300mm long, but bond between concrete and reinforcement was possible in the central 1200mm because a fifty milimetre de-bonded length was maintained on either side of all specimens. Three GFRP bar diameters and two concrete square section sizes were used. One reinforcing bar was placed in the

centre of the cross section and four different reinforcement ratios were obtained: 0.44, 0.68, 0.98 and 1.63%, as shown in Table 5.5.

Specimen	Concrete mix	Nominal diameter, d_n (mm)	Cross section size (mm)	Reinforcement ratio, ρ (%)
13-170	C1	12.7	170	0.44
16-170	C1	15.9	170	0.68
19-170	C2	19.1	170	0.98
16-110	C2	15.9	110	1.63
16-170-2	C3	15.9	170	0.68

Table 5.5: Geometric characteristics of the ties.

The experimental work on FRP RC ties was complemented with two additional tests, where specially gauged rebars (i.e. rebars 16-N and 19-N) were used as internal reinforcement. Concrete casting was performed with the same mould as previous ties, with a 170mm side square section, and therefore copies of two previously presented ties were obtained.

Specimen	Concrete mix	Nominal diameter, d_n (mm)	Cross section size (mm)	Reinforcement ratio, ρ (%)
19-170-N	C2	19.1	170	0.98
16-170-3N	C3	15.9	170	0.68

Table 5.6: Geometric characteristics of additional notched ties.

20mm deep pre-cracks were induced right around the perimeter of the tie, therefore ensuring the initiation of cracks at these specific locations. The pre-crack was created by placing a 4mm wide steel rectangular section in the mould prior to casting. The four lateral pieces of the steel rectangular section were screwed in a way so they could be unscrewed to facilitate the de-moulding process of the ties (see Figure 5.12). In one of the cases, only one notch was induced, thus dividing the 1200mm bonded length into two pieces, whereas for the second case three notches

were induced and four pieces were obtained. Therefore, the specimens identification of these ties end with "N" or "3N" postscript (see Table 5.6)

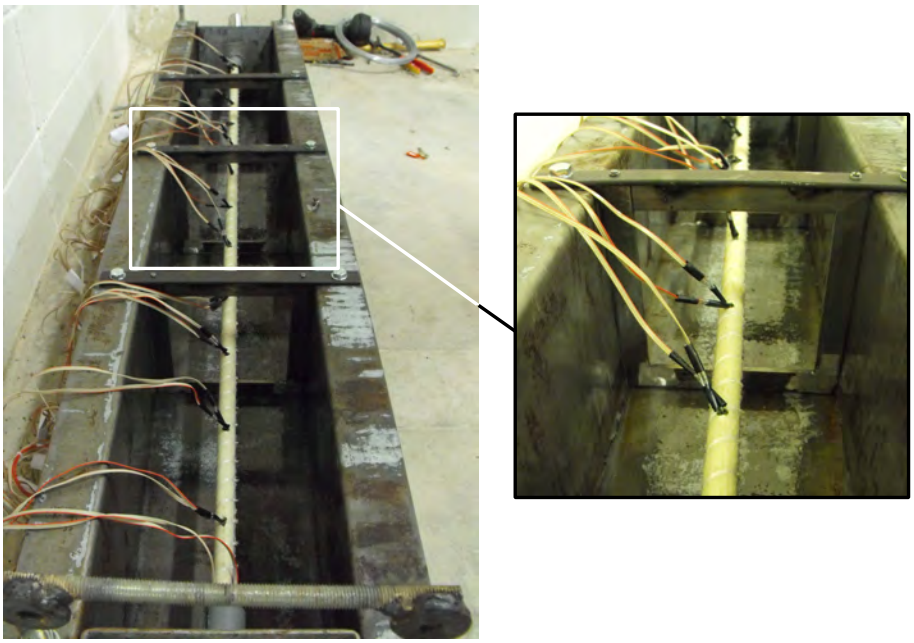

Figure 5.12: Detail on the steel rectangular frame used to create the pre-cracks in the ties.

Although gross geometrical properties of the ties were copied from two previously tested ties (i.e. same rebar size and same section size), the real reinforcement ratio should be defined according to the weakest section in the tie. Therefore, due to the pre-cracks induced around the perimeter of the ties, higher reinforcement ratios were obtained. The differences in reinforcement ratios are presented in Table 5.7.

Specimen	$\rho_{orig}(\%)$	$\rho_{real}(\%)$
19-170-N	0.98	1.70
16-170-3N	0.68	1.17

Table 5.7: Actual reinforcement ratios for notched ties.

Bar preparation

Before casting the concrete, GFRP reinforcing rebars needed to be prepared. Similarly to what was done for testing GFRP rebars in tension, a special anchoring device was needed to prevent any damage on the rebar during the loading of the RC tie. However, the drilled-through steel housing system used in the characterization of GFRP bars could not be used, because the connection system between the RC tie and the test actuator was done in a different way. The new gripping system consisted on drilled-through threaded-bars; the housing was drilled in two different diameters, so that a step inside the housing was obtained, and higher resistance for the bonding resin was possible. In Figure 5.13 and Table 5.8 the details on the gripping system are shown.

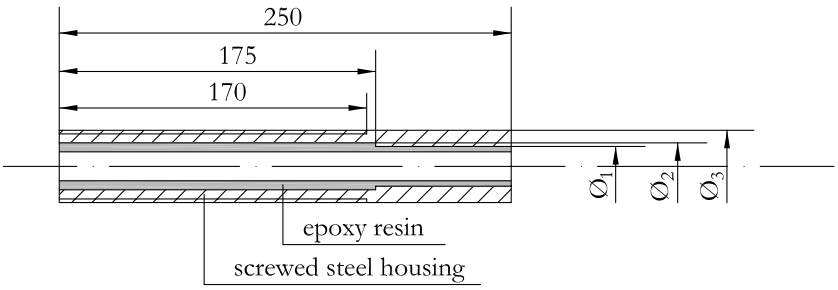

Figure 5.13: Anchoring device for RC tensile test (units in mm).

Rebar designation	Φ_1 (mm)	Φ_2 (mm)	Φ_3 (mm)
13	20	25	40
16	22	26	40
19	26	32	48

Table 5.8: Geometric characteristics of screwed gripping system.

The same epoxy based resin was used to connect the housing (i.e. the gripping system) to the reinforcing rebar. But before bonding the two parts, a plastic pipe was placed so that a 50mm unbonded length was possible at both ends of the final RC tie. Additionally, a plastic annulus was also introduced to allow the rebar being

completely aligned in the center of the future RC tie. This was done because both ends of the tie mould had a hole so that the tie could be demoulded even when the gripping system was already bonded to the reinforcing rebar (see Figure 5.14). Once the 50mm bond-breaker system and the aligning annulus where placed, the first gripping system could be bonded to the rebar. This was done vertically, with the resin being poured into the housing and the bar being inserted from the top (Figure 5.15). After 24 hours, the second gripping system was bonded to the other end of the bar, and the bar was left to cure for another 24 hours. Now the bar was prepared to be placed in the tie mould.

Figure 5.14: Detail of the plastic pipe bond-breaker and aligning annulus when reinforcing rebar already placed in the mould.

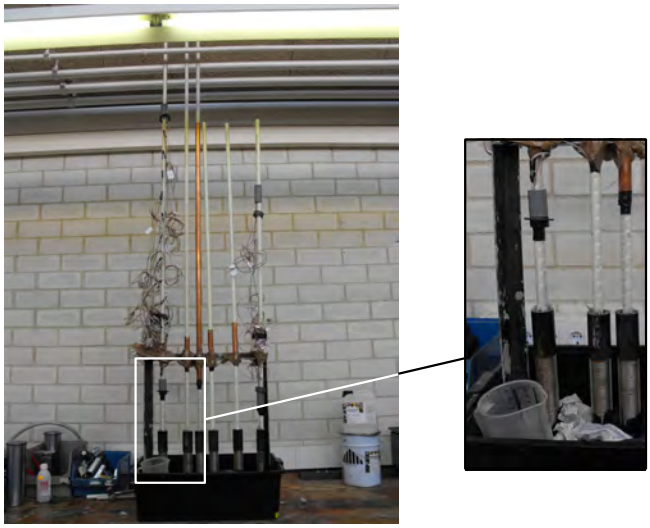

Figure 5.15: Bonding gripping system to GFRP reinforcing rebar.

Casting and curing procedure

The GFRP rebar was placed in the mould so that special care was taken to ensure the rebar remaining horizontal along the specimen length. Before casting, the external screw of the gripping system was protected to avoid concrete being poured on it. Concrete was cast in two layers and each layer was vibrated by the means of hammer vibrators. Compacting and leveling was imposed on the specimen surface to eliminate voids and minimize geometric irregularities (Figure 5.16). Similar to the casting of the pull-out test, a thin film of oil was used to coat the mould and make easier the demoulding of concrete ties.

(a) (b)

Figure 5.16: Casting sequence; (a) concrete being poured in two layers and (b) compacting an leveling to final surface.

Special care was taken to keep the RC ties in saturated humidity conditions while curing. After 24 hours the ties were demoulded and covered to keep humidity. The specimens were tested at the age of 28 days.

Although the study of shrinkage influence on the deformation behaviour of RC ties was not within the scope of this thesis, a register on the temperatures and humidity during the curing days was performed. The experimental ties were cast and cured at three temporally spaced stages, under different curing conditions. Therefore, humidity and temperature registers allowed to compute how these different environmental conditions could affect the experimental results on RC ties.

According to MC90 [5], total shrinkage strain $\epsilon_{cs}(t, t_s)$ can be computed from

$$\epsilon_{cs}(t, t_s) = \epsilon_{cso}\beta_s(t - t_s) \tag{5.1}$$

where ϵ_{cso} is the notional shrinkage coefficient computed according to Equation 5.2, $\beta_s(t, t_s)$ is the coefficient to describe the development of shrinkage with time computed according to Equation 5.5, t is the age of concrete (in days) and t_s is the age of concrete at the beginning of shrinkage (i.e. 15 days in the test).

$$\epsilon_{cso} = \epsilon_s(f_{cm})\beta_{RH} \tag{5.2}$$

For the computation of the notional shrinkage coefficient, $\epsilon_s(f_{cm})$ and β_{RH} can be computed from Equation 5.3 and 5.4, respectively. In Equation 5.3, β_{sc} is a coefficient depending on the type of cement and f_{cm} is the mean compressive strength of concrete at the age of 28 days; in Equation 5.4 $\beta_{sRH} = 1 - \left(\frac{RH}{100}\right)^3$, with RH being the relative humidity of the ambient atmosphere (%).

$$\epsilon_s(f_{cm}) = \left[160 + 10\beta_{sc}\left(9 - \frac{f_{cm}}{f_{cmo}}\right)\right] 10^{-6} \tag{5.3}$$

$$\begin{aligned} \beta_{RH} &= -1.55\beta_{sRH} && 40\% \leq RH \leq 99\% \\ \beta_{RH} &= 0.25 && RH \geq 99\% \end{aligned} \tag{5.4}$$

The development of shrinkage with time is given by

$$\beta_s(t, t_s) = \left[\frac{(t - t_s)/t_1}{350(h/h_o)^2 + (t - t_s)/t_1}\right]^{0.5} \tag{5.5}$$

where t_1 is 1 day, h_o is 100mm and h is the notional size of the cross-section, defined as $h = \frac{2A_c}{u}$, with A_c being the concrete cross-sectional area and u being the perimeter of that part of the cross section which is exposed to drying.

According to the formulation presented and the registers of humidity, Model Code 90 [5] predictions on shrinkage deformations are presented in Table 5.9.

Predictions confirmed that testing on RC members would be influenced by the shrinkage effects, although this influence would be small because of the small shrinkage strain at the age of 28 days.

Specimen	f_{cm} (MPa)	RH (%)	$\epsilon_{cs}(t, t_s)$ ($\mu\epsilon$)
13-170	48.1	60	-99
16-170	48.1	60	-99
16-110	66.2	45	-130
19-170	66.2	45	-87
19-170-N	66.2	45	-87
16-170-2	46.6	52	-111
16-170-3N	46.6	52	-111

Table 5.9: Predictions on shrinkage strains.

5.2.3 Experimental set-up and testing procedure

The tensile test arrangement used to perform the tensile tests on RC ties is shown in Figure 5.17. Specimens were stressed by applying the load at the ends of the protruding bars. The applied load was then partially transferred to the concrete by bond along the development length at the ends of the prisms. Load was applied by means of an hydraulic jack at the specimen's life end, and a rigid reaction structure was used to connect the specimen's dead end, as shown in Figure 5.17. The load was applied under displacement control and an automatic data acquisition system was used to collect the data. Load steps were not predefined, as the tests were stopped anytime a new crack appeared at the concrete surface; at each stop the evolution of cracks and strains was recorded. Crack widths were measured with an optical magnifier with an accuracy of 0.05mm. A linear variable differential transformer (LVDT) was used to measure the member deformation. Additionally, member strains were measured at the height of the reinforcement by means of a mechanical extensometer with a gauge length of 150mm between Demec points; both the LVDT and mechanical extensometer registers on deformations were measured over the 1200mm bonded length. Four concrete strain gauges were placed at each face of the ties at a distance of 100mm from the midspan section to control that the ties were loaded in pure tension.

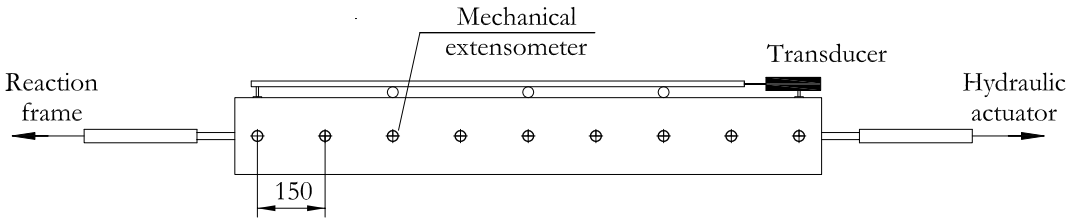

Figure 5.17: Sketch of GFRP RC tensile test setup (units in mm).

5.3 Experimental results and discussion on GFRP RC tensile tests

In this section the experimental results of the present study on GFRP RC tensile tests are summarized. Details on the tensile behaviour, along with results on cracking analysis, of concrete elements reinforced with GFRP rebars are given.

5.3.1 Tensile behaviour

Cracking resistance and deformation of RC members could be affected by the shrinkage deformation generated while curing [61, 62, 69, 70]. The reinforcement embedded in concrete provides restraints to concrete shrinkage, thus leading to compressive stresses appearing in reinforcement and respective tensile stresses appearing in concrete. Therefore, the two main effects on the final response of the RC tie are the initial shortening of the member and the lower cracking load (since concrete is under an initial tensile load, hereafter referred to as P_{add}). These two effects are clearly visible in the representation proposed by Bischoff [62] and shown in Figure 5.18.

Because of the small shrinkage strain values and early testing at the age of 28 days, little influence of shrinkage was expected. The estimated shrinkage strains, ϵ_{sh}, the initial shortening, $\epsilon_{m,i}$, and the additional load, P_{add}, that should be added to the measured load during testing are shown in Table 5.10.
Measured member responses of applied load, P, versus member strain, ϵ_m, are shown in Figures 5.19-5.25. Member strain has been computed as the continuously recorded member elongation, δ, measured with the LVDT over the bonded length, L (i.e. 1200mm).

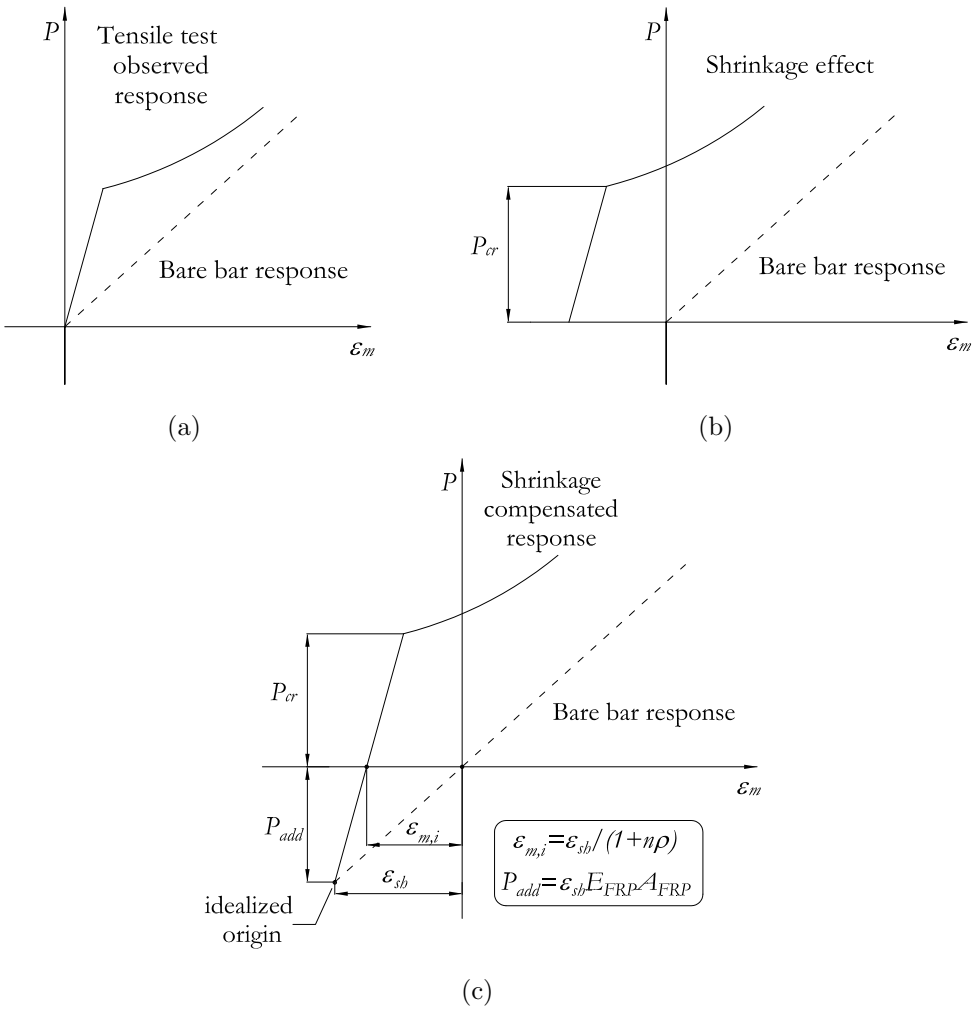

Figure 5.18: (a) Load-deformation diagram neglecting pre-loading displacement due to shrinkage; (b) shrinkage effect on load-deformation behaviour and (c) shrinkage compensated response and definition of the initial shortening, ϵ_{sh}, bare bar strain offset, $\epsilon_{m,i}$, and additional load, P_{add} (after Bischoff [62]).

The sum of the strain measurement with the mechanical extensometer between Demec points have also been used to represent the member strain. Good agreement is observed in Figures 5.19-5.25 for the two measurements in each tie.

Initial member shortening derived from shrinkage effects is taken into account in the representation of the member tensile behaviour by offsetting the bare bar response with the shortening value, $\epsilon_{m,i}$, presented in Table 5.10. Although being almost unperceptive, the highest initial shortening corresponds to specimen 16-110.

Specimen	ϵ_{sh} ($\mu\epsilon$)	$\epsilon_{m,i}$ ($\mu\epsilon$)	P_{add} (N)
13-170	-99	-98	499
16-170	-99	-98	782
16-110	-130	-127	1023
19-170	-87	-86	1017
19-170-N	-87	-86	1017
16-170-2	-111	-110	1058
16-170-3N	-111	-110	1058

Table 5.10: Member shortening and reduction in cracking load due to shrinkage deformation.

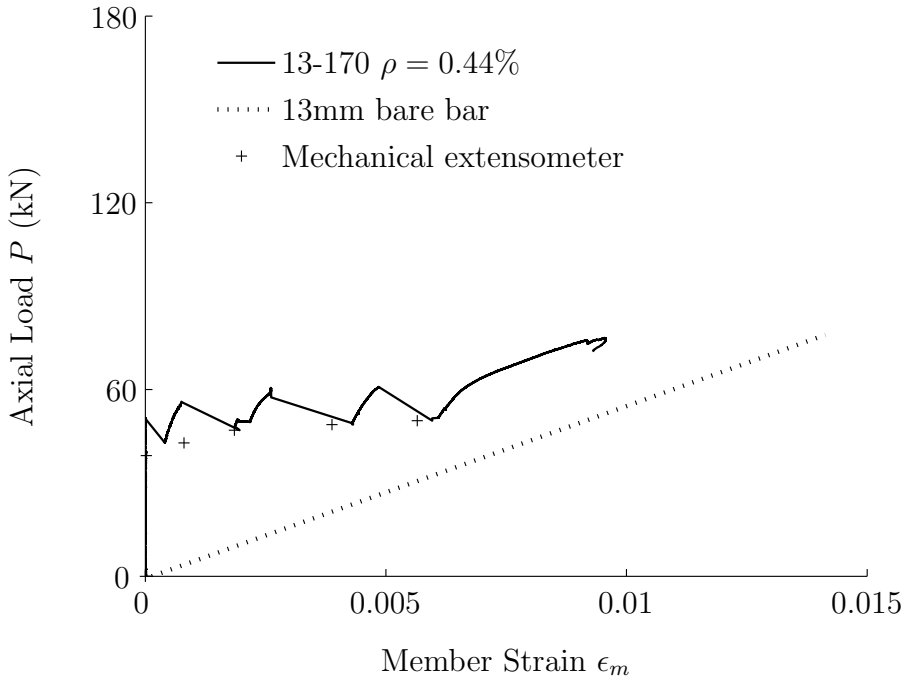

Figure 5.19: Experimental load-member strain response of specimen 13-170.

The initial lineal branch with a steep slope visible in the load-member strain relationship (Figures 5.19-5.25) corresponded to the uncracked condition of the ties. Once cracking load was achieved the first transversal crack appeared. From that

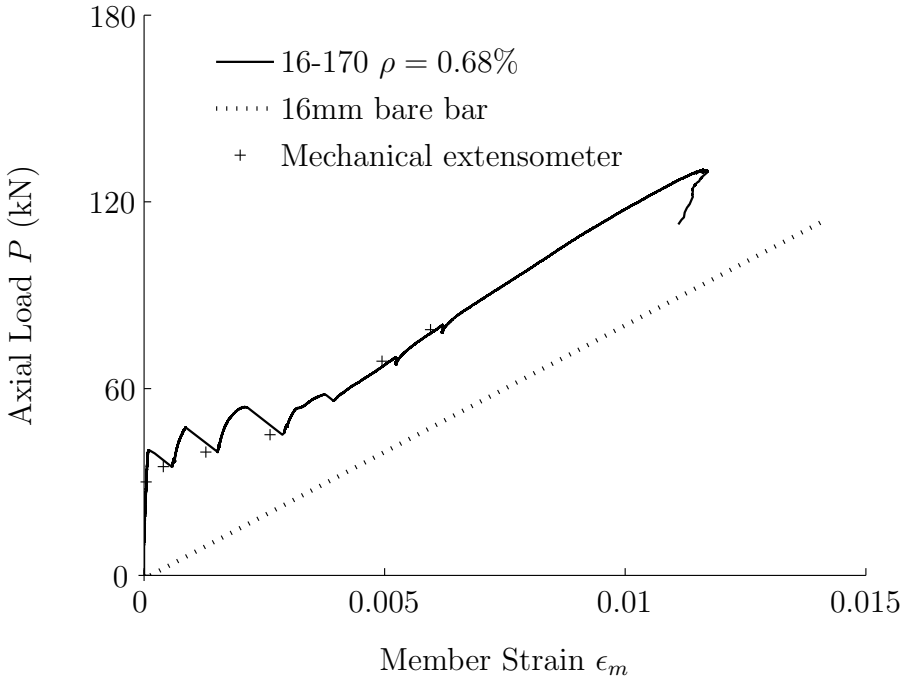

Figure 5.20: Experimental load-member strain response of specimen 16-170.

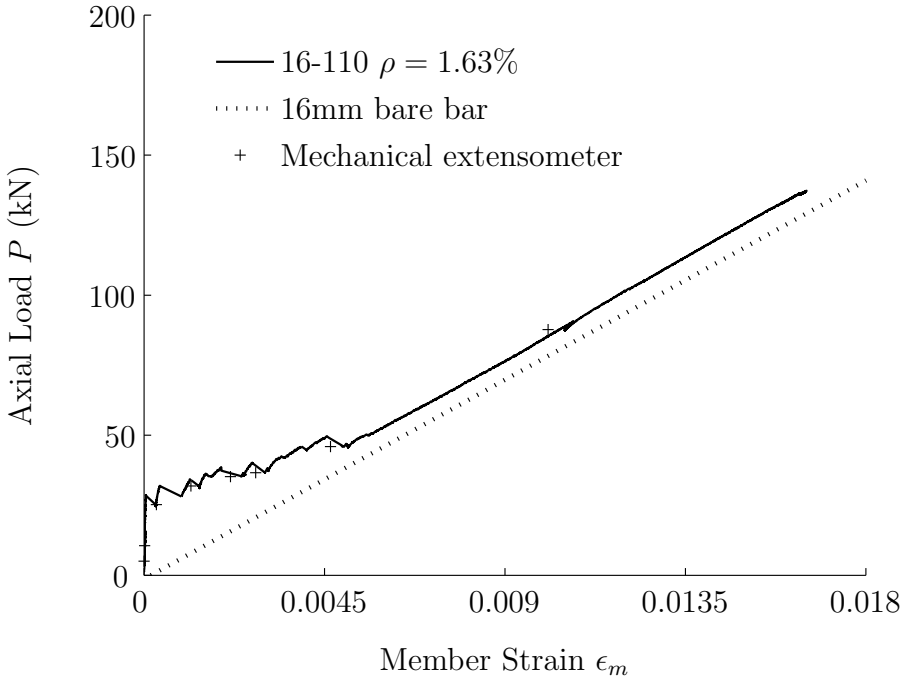

Figure 5.21: Experimental load-member strain response of specimen 16-110.

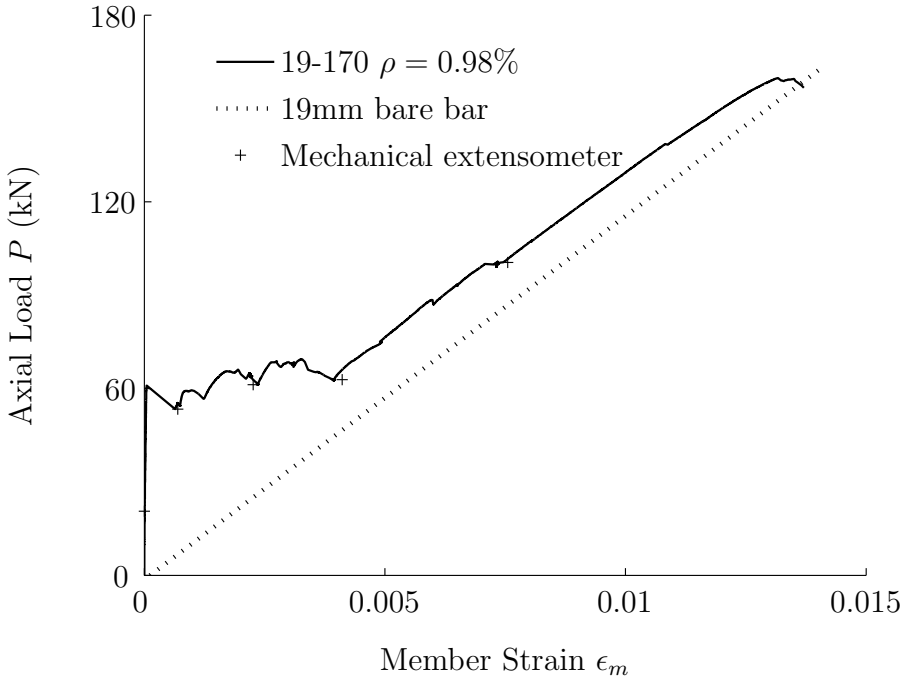

Figure 5.22: Experimental load-member strain response of specimen 19-170.

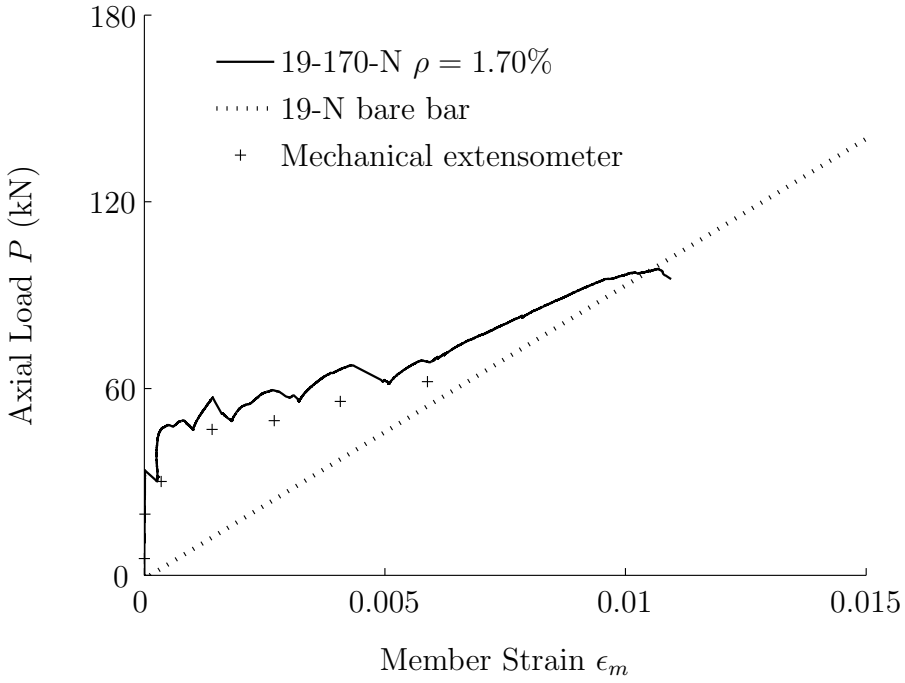

Figure 5.23: Experimental load-member strain response of specimen 19-170-N.

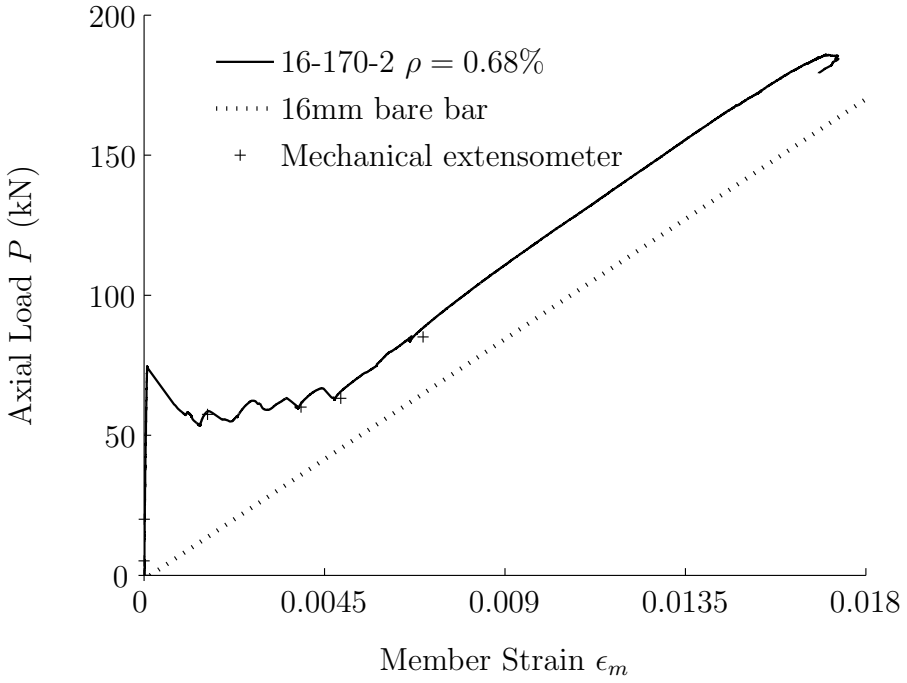

Figure 5.24: Experimental load-member strain response of specimen 16-170-2.

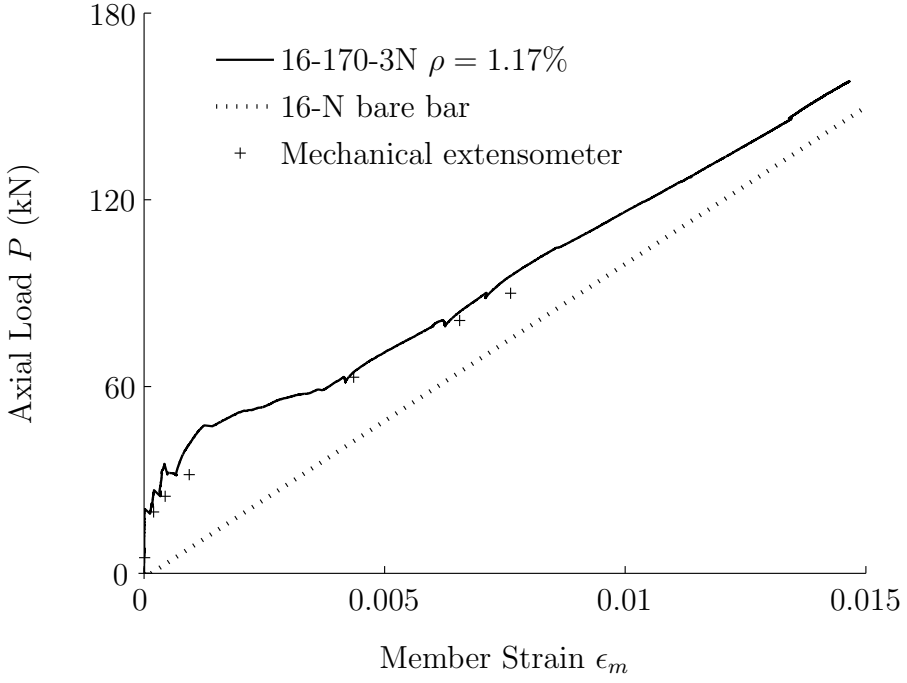

Figure 5.25: Experimental load-member strain response of specimen 16-170-3N.

moment, and due to the increments in the applied load, a progressive transverse cracking of the ties with $\rho = 0.44\%$, $\rho = 0.68\%$ and $\rho = 1.63\%$ was observed with more cracks appearing. However, for the tie with $\rho = 0.98\%$, as more load was applied beyond the cracking load, a combination of transverse and splitting cracking took place. The zigzag line observed in the crack formation phase is the result of the displacement control mode chosen to conduct the tests. Finally, once the cracking process stabilized, no more new cracks appeared and only the opening of the existing ones could be observed. The final crack patterns of the specimens are shown in Figure 5.26, with cracks numbered according to appearance order and crack spacing measurements taken at the height of the reinforcement.

Table 5.11 summarizes the results of tensile tests in terms of measured cracking load, P_{crack}, concrete tensile strength, f_{ct}, ultimate load, P_{ult}, reinforcement rupture tensile strength, $f_{fu,exp}$, and ultimate elongation, δ_{ult}. Although concrete compressive strength, $f_c^{'}$, and modulus of elasticity, E_c, were obtained with normalized characterization tests from control samples match-cured with reinforced concrete ties, concrete tensile strength, f_{ct}, was derived from experimental results on reinforced concrete ties.

Specimen	P_{crack} (kN)	f_{ct} (MPa)	P_{ult} (kN)	$f_{fu,exp}$ (MPa)	δ_{ult} (mm)	Failure mode[a]
13-170	50.6	1.75	76.6	517.2	11.46	TC
16-170	40.3	1.39	130.4	639.5	13.94	TC
16-110	28.4	2.34	137.3	673.4	19.83	TC
19-170	60.9	2.10	159.8	555.3	15.79	TC,SC
16-170-2	74.6	2.58	185.9	830.7	20.41	TC

[a] TC=transverse cracking and SC=splitting cracking.

Table 5.11: Measured cracking and ultimate loads, P_{crack} and P_{ult}, concrete tensile strength, f_{ct}, reinforcement ultimate tensile strength, $f_{fu,exp}$, ultimate deflection, δ_{ult}, and failure mode.

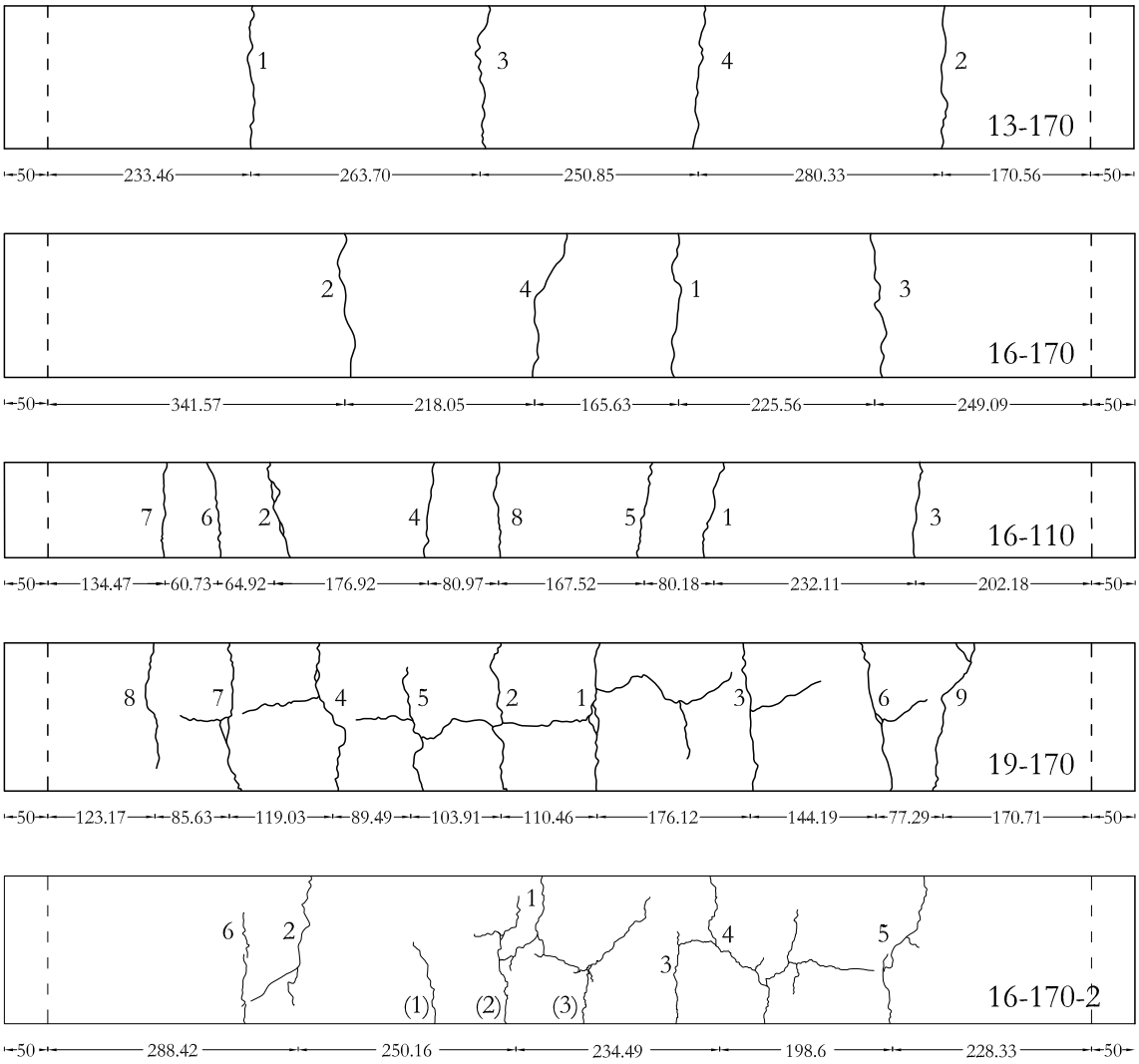

Figure 5.26: Final crack pattern for tested ties (units in mm).

5.3.2 Prediction of load vs. deformation response

The tension response of a RC member can be defined with three different regions (see Figure 5.27). In the pre-crack stage, also defined as uncracked elastic (State I), concrete and reinforcement are acting compositely and homogeneous concrete cross section can be supposed for analysis. At this stage, relatively low loads are applied and tensile stresses present in concrete are lower than the concrete tensile strength.

Once cracking takes place, strain and stresses at crack section are defined with the cracked elastic with no tension stiffening state (State II). At these crack sections,

specimen's stiffness is defined by reinforcement stiffness. However, in neighbouring sections a limited tensile force can be transferred from reinforcement to concrete by bond forces. At this regions, strains in concrete and reinforcement are not constant, and reinforcement average strain (ϵ_m) is lower than that of the bare reinforcement at a crack section ($\epsilon_2 = P/E_r A_r$). This difference in strain, $\Delta\epsilon_s = \epsilon_{s2} - \epsilon_{sm}$, is a measure of the *tension stiffening* effect. As long as load is increased, the member stiffness reduces, as more cracks appear and lower force transmission is possible. This second stage is also called as cracking stage.

When stabilized cracking is attained (i.e. post-cracking stage), no more new cracks can appear and the increase in member deformation is directly linked with the opening of existing cracks. Depending on the bond deterioration or the splitting cracks propagation, the overall specimen response tends to be parallel to the bare bar response.

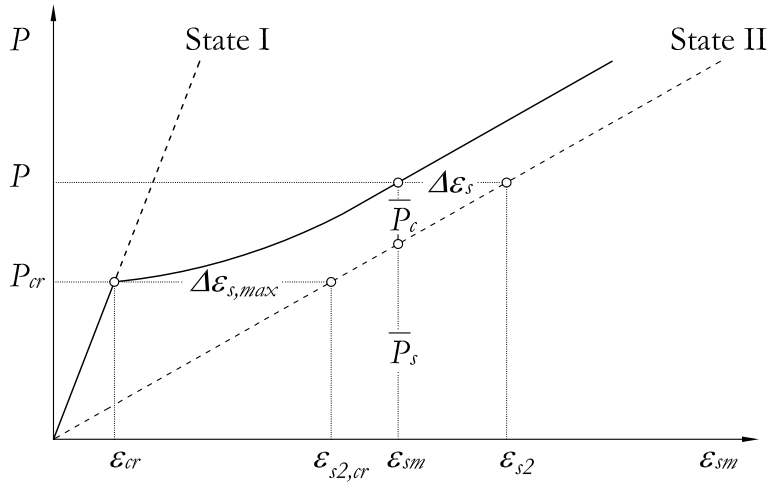

Figure 5.27: Representation of tension response and tension stiffening effect.

Proposal of EC2-92

EC2-92 [4] proposes a method to calculate the average strain in the steel reinforcement interpolating between the strains calculated for uncracked (ϵ_1) and fully cracked (ϵ_2) sections:

$$\epsilon_m = \epsilon_1 \left(\frac{\sigma_{cr}}{\sigma_s}\right)^2 + \epsilon_2 \left[1 - \beta_1 \beta_2 \left(\frac{\sigma_{cr}}{\sigma_s}\right)^2\right] \tag{5.6}$$

where β_1 stands for the bond characteristics of the internal reinforcing steel bars (1 for ribbed and 0.5 for smooth bars), β_2 considers the loading type (1 for first loading and 0.5 for repeated or sustained loading), σ_{cr} is the tensile stress in the steel reinforcing bar at cracked section when the first crack occurs (σ_{cr}=P_{crack}/A_s), σ_s is the stress in the steel bar at the cracked section at the actual load, and ϵ_1 and ϵ_2 are the strain calculated for the uncracked and fully cracked section.

Although Equation 5.6 has been proposed only for steel RC structures, predictions on FRP RC structures can be computed if an adequate value for the bond quality coefficient (β_1) is assumed.

Proposal of ACI 224-92

Similar to the approach applied on the calculation of deflections on flexural members, ACI 224.2R-92 [6] proposes to study the tensile behaviour of steel RC elements with an analogous approach to that of the effective moment of inertia in ACI 318-05 [103]. Based on Branson's expression [56], ACI 224 proposes an expression for the effective cross-sectional area (A_e) that varies gradually from the gross sectional area (A_g) to the cracked cross sectional area (A_{cr}), as loading of the member increases beyond the cracking point:

$$A_e = A_g \left(\frac{P_{crack}}{P}\right)^3 + A_{cr}\left[1 - \left(\frac{P_{crack}}{P}\right)^3\right] \leq A_g \tag{5.7}$$

In ACI 440.1R-03 [108], the code for FRP RC flexural elements, a reduction coefficient β_d was used to modify Branson's equation and adapt it to the FRP characteristics. However, no modification has been introduced in the code for tensile members. Therefore, based on ACI 440 adaptation, some authors have introduced this same coefficient to study the tensile behaviour of RC ties [88, 104], with the final expression for the effective cross-sectional area reading:

$$A_e = A_g\beta_d \left(\frac{P_{crack}}{P}\right)^3 + A_{cr}\left[1 - \left(\frac{P_{crack}}{P}\right)^3\right] \leq A_g \tag{5.8}$$

where β_d computes for the differences in reinforcement characteristics:

$$\beta_d = 0.5 \left[\frac{E_{FRP}}{E_{steel}} + 1 \right] \tag{5.9}$$

Consistently with ACI approach, once the cross-sectional area has been computed, the member average strain can be computed with:

$$\epsilon_m = \frac{P}{E_c A_e} \tag{5.10}$$

Proposal of MC90

Tension stiffening effect, responsible of increasing the RC tie post-cracking stiffness, is taken into account in MC90 [5] by the modified stress-strain relationship of embedded reinforcement described next:

- uncracked phase

$$\epsilon_m = \epsilon_1 \tag{5.11}$$

- crack formation phase

$$\epsilon_m = \epsilon_2 - \frac{\beta_t \left(\sigma_s - \sigma_{sr1}\right) + \left(\sigma_{srn} - \sigma_s\right)}{\left(\sigma_{srn} - \sigma_{sr1}\right)} \left(\epsilon_{sr2} - \epsilon_{sr1}\right) \tag{5.12}$$

- stabilized cracking

$$\epsilon_m = \epsilon_2 - \beta_t \left(\epsilon_{sr2} - \epsilon_{sr1}\right) \tag{5.13}$$

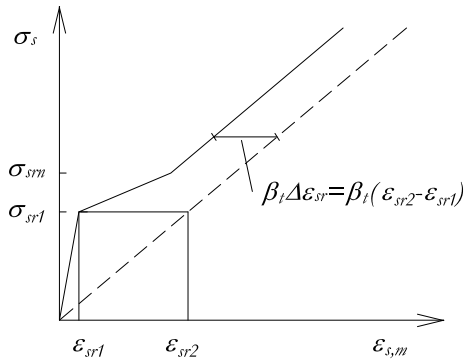

Figure 5.28: Simplified stress-strain relationship of embedded reinforcing steel proposed in MC90 [5].

where ϵ_{sr1} and ϵ_{sr2} are the steel strains for uncracked and cracked section respectively, when first crack has formed, σ_{sr1} and σ_{srn} are the steel strain in the crack,

when first and last crack has formed, respectively, and β_t is a factor for steel strain along the transmission length reading 0.4 for pure tension. For normal cases, the steel stress at the last crack may be taken as σ_{srn}=1.3σ_{sr1}.

The code draws a distinction between the cracking stage, the stabilized cracking stage and the post-yielding stage. However, the code is hereafter used to predict the response of GFRP RC ties, whose reinforcement has a brittle failure. Therefore, no mention is done to the post-yielding stage, neither in Figure 5.28 nor in Equations 5.11-5.13.

Comparison with experimental results

Evaluation of load vs. deformation for tensile members with EC2-92 [4], MC90 [5] and ACI proposal modified with β_d factor according to Equation 5.8 (hereafter referred to as ACI 224/440) is shown in Figures 5.29-5.35.

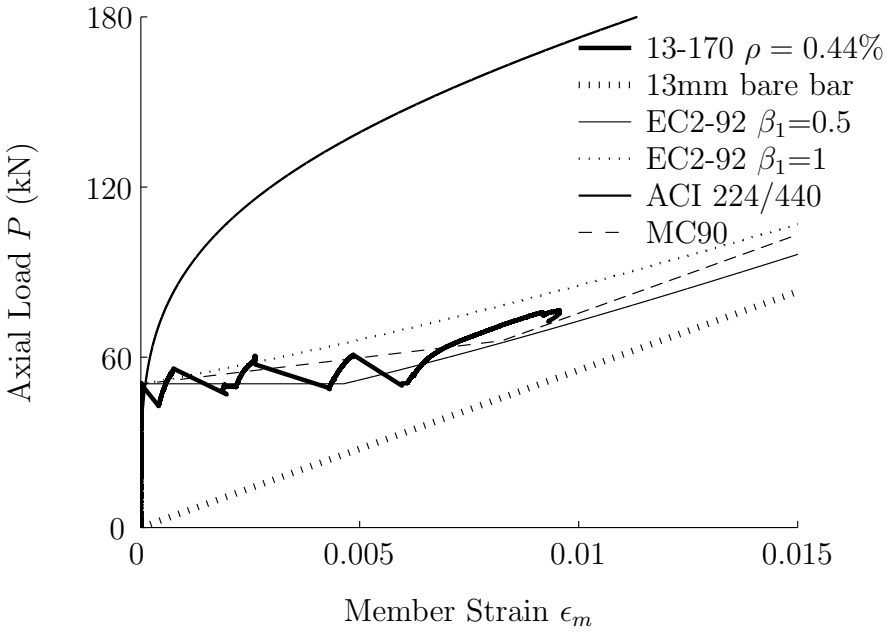

Figure 5.29: Comparison of 13-170 member response with EC2-92 [4], ACI 224/440 (Equation 5.8) and MC90 [5] theoretical predictions.

According to Equation 5.6, the differences in mechanical properties of FRP and

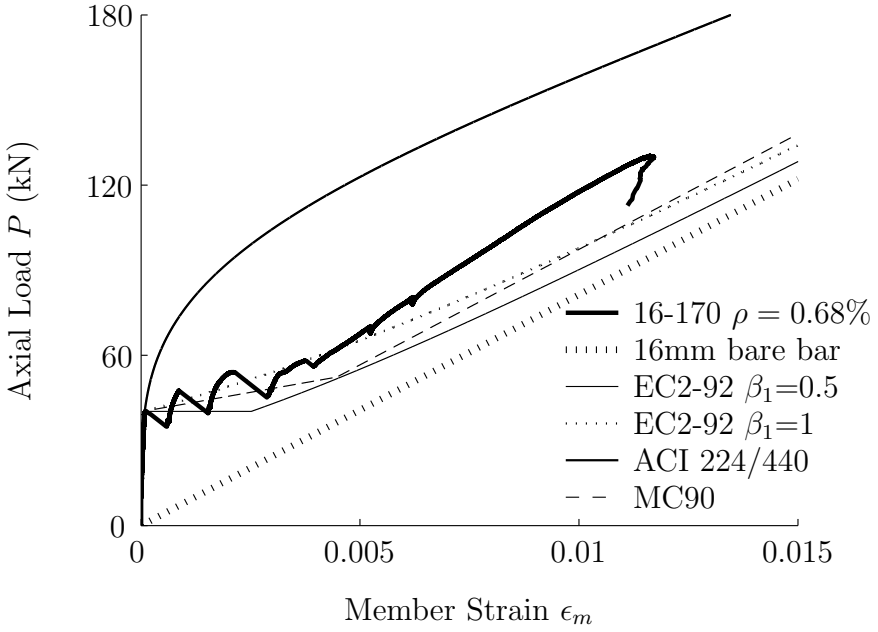

Figure 5.30: Comparison of 16-170 member response with EC2-92 [4], ACI 224/440 (Equation 5.8) and MC90 [5] theoretical predictions.

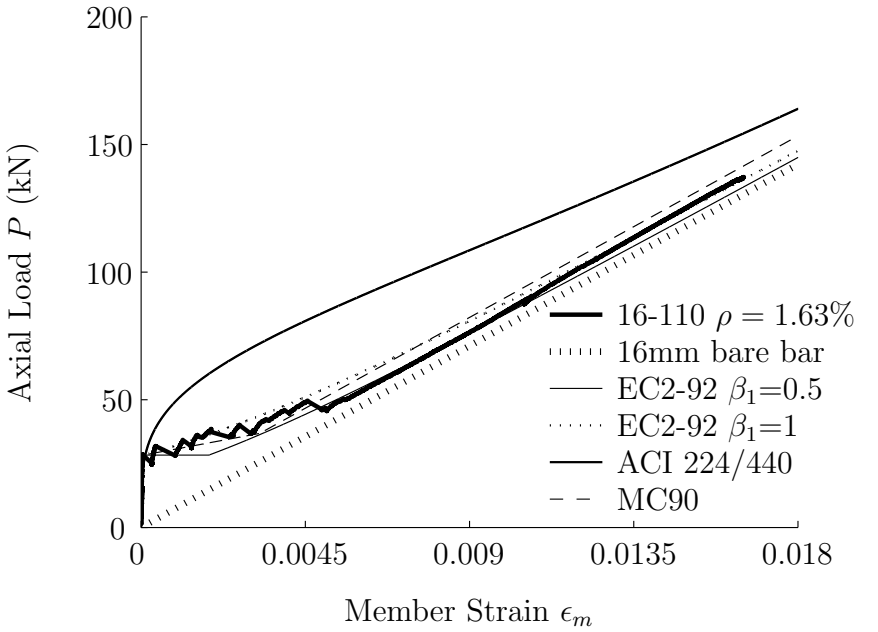

Figure 5.31: Comparison of 16-110 member response with EC2-92 [4], ACI 224/440 (Equation 5.8) and MC90 [5] theoretical predictions.

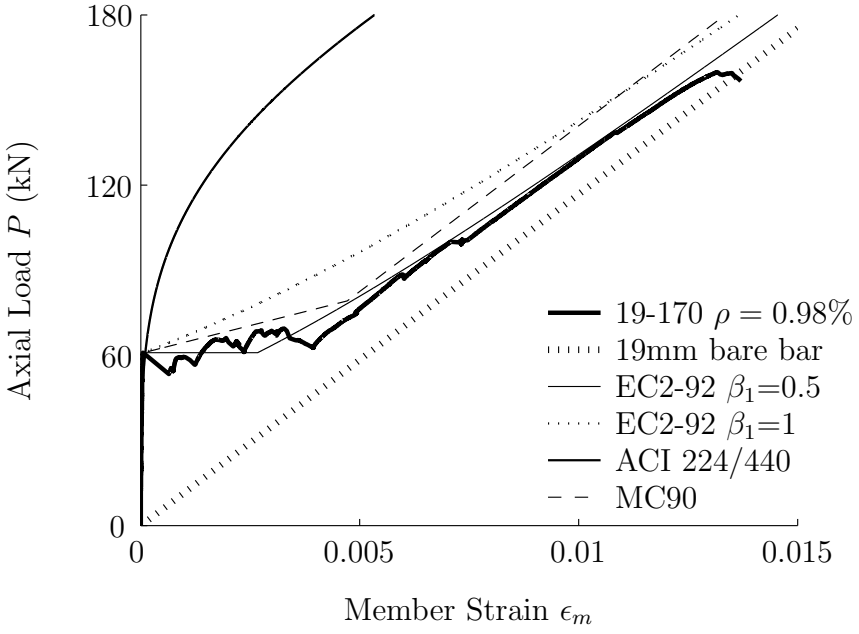

Figure 5.32: Comparison of 19-170 member response with EC2-92 [4], ACI 224/440 (Equation 5.8) and MC90 [5] theoretical predictions.

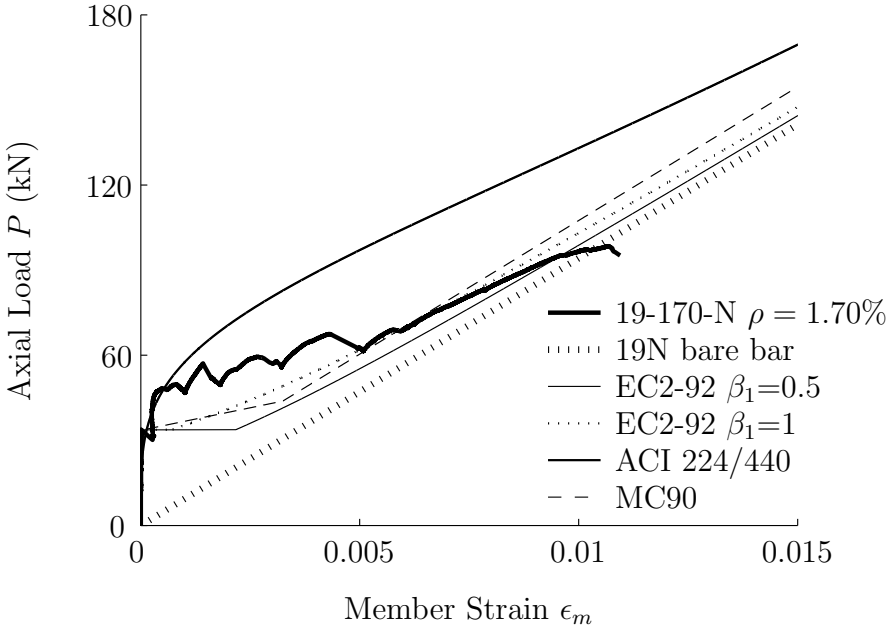

Figure 5.33: Comparison of 19-170-N member response with EC2-92 [4], ACI 224/440 (Equation 5.8) and MC90 [5] theoretical predictions.

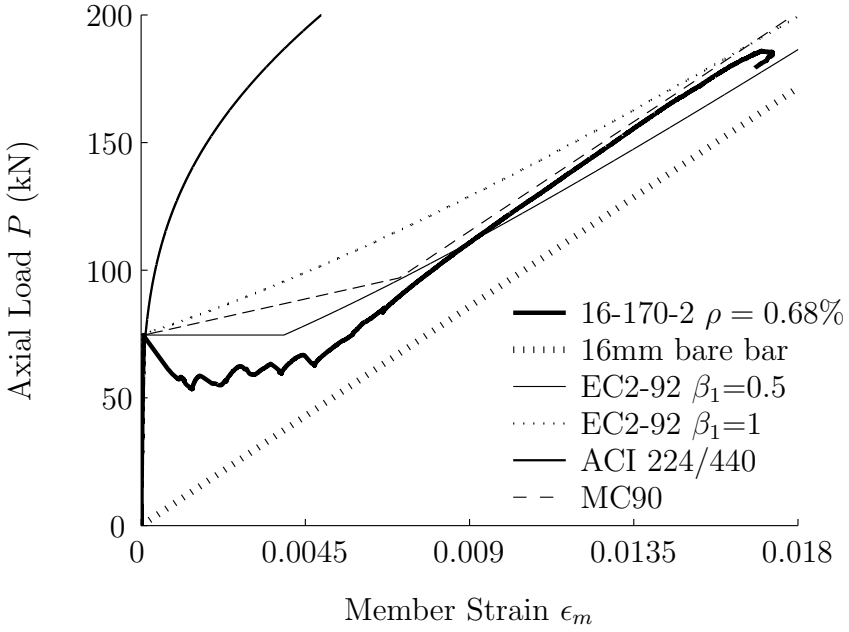

Figure 5.34: Comparison of 16-170-2 member response with EC2-92 [4], ACI 224/440 (Equation 5.8) and MC90 [5] theoretical predictions.

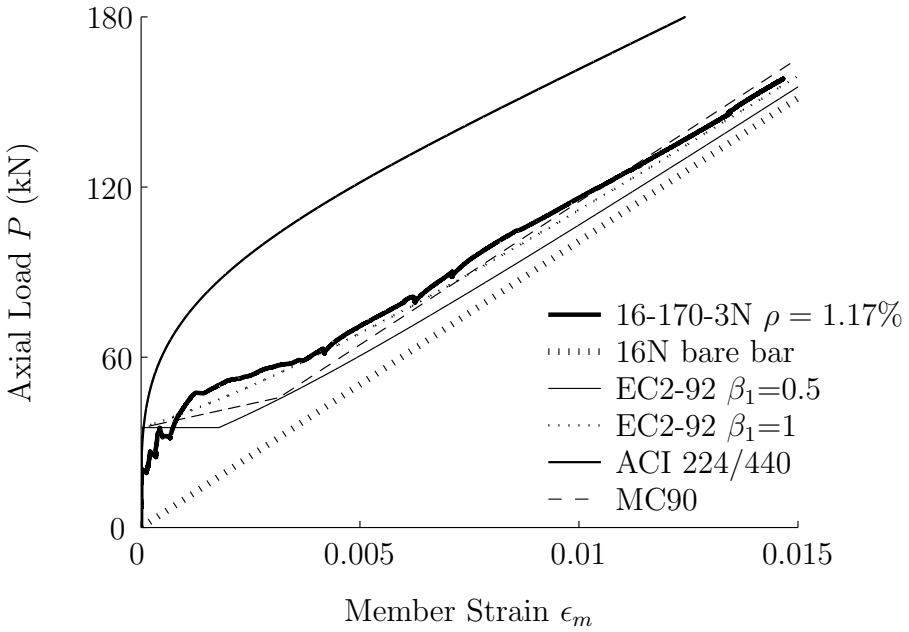

Figure 5.35: Comparison of 16-170-3N member response with EC2-92 [4], ACI 224/440 (Equation 5.8) and MC90 [5] theoretical predictions.

steel reinforcement can be account for in EC2-92 code with a proper assumption on the bond quality coefficient β_1. For instance, in the experimental program presented in [86] a global β_1 value very close to that proposed for smooth rebars (i.e. β_1=0.5) was found; however, authors reminded the necessity of analyzing a wider number of tests. In this section, with no specific data available for the rebar used, extreme values of β_1=0.5 and β_1=1 have been assumed in the verification of EC2-92 proposal. In the verification of ACI 224/440, the reduction coefficient β_d first presented in ACI 440.1R-03 [108] has been used.

The prediction of member deformation with ACI equation clearly underestimates the strain of the FRP RC specimen (see Figures 5.29-5.35), as was also reported in previous studies [86, 88]. This overestimation of the tension stiffening effect is directly linked with the underprediction of computed deflections for flexural elements observed by others in the past [115–119]. On the contrary, experimental responses fall between EC2-92 predictions and bond characteristics can be better studied. Better agreement with EC2-92 predictions using β_1=1 is visible for those cases where only transverse cracks took place; moreover, for those cases where both transverse and splitting cracks took place, with worst bond quality and rapid loss in tension stiffening effect, a better agreement is found with β_1=0.5.

5.3.3 Cracking behaviour

Cracks, arising from the limited tensile deformation capacity of concrete, have a direct influence on aesthetics, stress transfer and structure durability. Therefore, the study on the serviceability limit states is of great importance. Differences in surface configurations and mechanical properties do exists when traditional steel reinforcement is compared to FRP reinforcement. Therefore, differences in the cracking behaviour (such as crack pattern, crack width and crack spacing) are expected, and the analysis of cracking behaviour of FRP reinforced structures becomes important.

Crack formation and stabilized cracking phase

After an initial linear elastic behaviour of RC ties, and once the load causing first cracking, P_{crack}, is attained, cracks appear randomly due to non homogeneity of

concrete. At cracked sections, concrete stress drops to zero and strain compatibility is lost. Due to the action of bond forces, stress is transferred from reinforcement to concrete and at some distance the compatibility condition is recovered. The better the bond behaviour between the two materials is, the shorter the strain compatibility recovering distance needed. During this crack formation phase, new cracks will appear as long as load is increased, therefore reducing the average crack spacing. This behaviour remains valid until the cracking stabilization load, P_{sta}, is attained. From this point on, no more cracks can appear, and the average crack spacing remains constant. Any increase in load will derive in the opening of the existing cracks.

In Figure 5.36, the experimental values of the ratio of crack stabilization load to first cracking load, P_{sta}/P_{crack}, are presented. Contrary to MC90 proposal of a constant ratio equal to 1.3, a dependence on the reinforcement ratio is found. This divergence between code proposal for steel RC ties and experimental results of GFRP RC ties indicates the possible influence of some parameters, such as elastic modulus or bond characteristics, on the cracking phase. Experimental data presented in Figure 5.36 is also summarized in Table 5.12.

Specimen	First cracking load, P_{crack} (kN)	Crack stabilization load, P_{sta} (kN)	P_{sta}/P_{crack}	number of transverse cracks, n_c
$13-170$	50.6	60.8	1.20	4
$16-170$	40.3	58.1	1.44	4
$16-110$	28.4	49.7	1.75	8
$19-170$	60.9	100.8	1.65	9
$16-170-2$	74.6	85.0	1.14	6

Table 5.12: Experimental values of first cracking load, P_{crack}, crack stabilization load, P_{sta}, ratio of loads, P_{sta}/P_{crack}, and number of transverse cracks.

From experimental data it can be observed that different development of the crack formation phase occurred. In Figure 5.37, the increase in number of transverse cracks is presented as a function of the average strain in reinforcement (lectures from

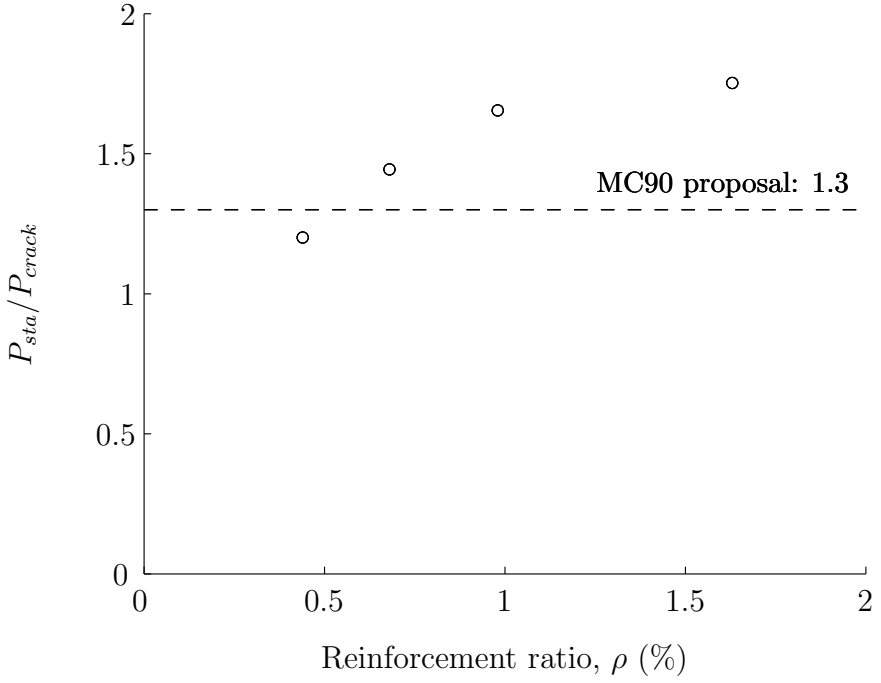

Figure 5.36: Ratio of crack stabilization to first cracking load.

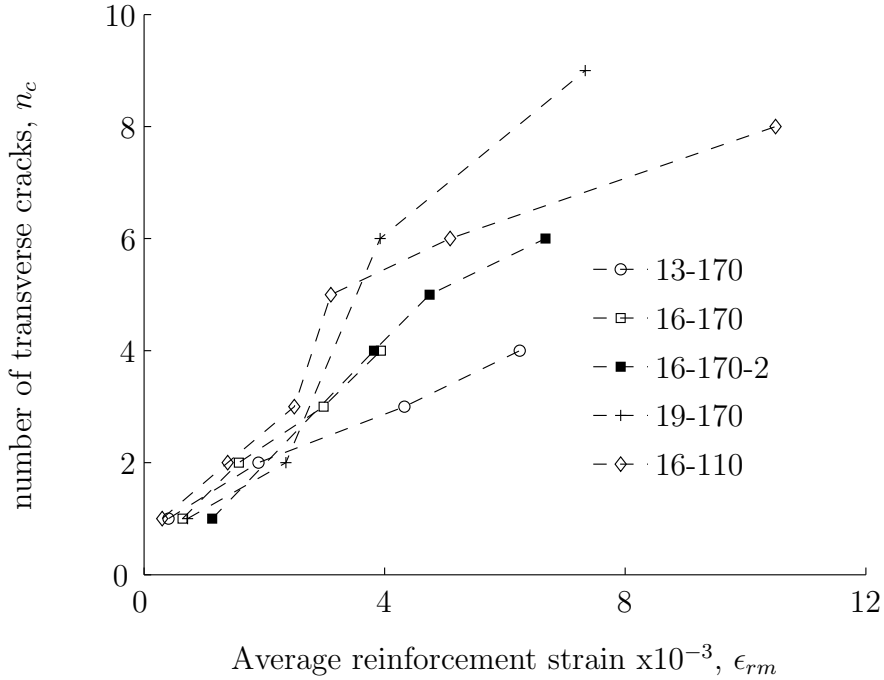

Figure 5.37: Number of transversal cracks as a function of average reinforcement strain.

$P - \epsilon_{rm}$ graphs). Results are presented up to the crack stabilization phase. Some differences arise in the strain level at which a fix number of cracks was formed, thus confirming the differences in the crack formation phase. Similarly, stabilization of crack pattern is attained at different average reinforcement strain, with no clear dependence on any geometrical or mechanical tie characteristic.

5.3.4 Crack spacing

In previous section, the transient behaviour between linear elastic (i.e. uncracked) and crack stabilized response was analyzed. The crack stabilization phase is attained when crack spacing between two existing cracks is not large enough to allow for a new crack to form. Therefore, a minimum crack spacing, s_{r0}, can be defined as the closest point to an existing crack at which concrete tensile strength has been reached. If Figure 5.38 is considered, a new crack can form if $s_r \geq 2s_{r0}$, whereas if $s_r < s_{r0}$ no more cracks can form. Therefore, crack spacing are expected to vary between $s_{r,min} = s_{r0}$ and $s_{r,max} = 2s_{r0}$, whilst average crack spacing could be defined as s_{rm}=1.5s_{r0}. According to these equalities, ratios of maximum to average and minimum to average crack spacing could be expressed as:

$$\frac{s_{r,max}}{s_{rm}} = 1.33 \tag{5.14}$$

$$\frac{s_{r,min}}{s_{rm}} = 0.67 \tag{5.15}$$

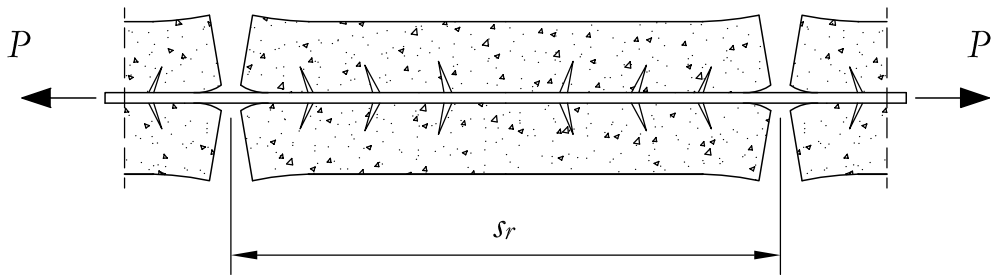

Figure 5.38: Sketch of cracked RC tie.

In Table 5.13 experimental results on crack spacing readings, measured at the height of the reinforcement once stabilized cracking was attained, are presented. Experimental average crack spacing is defined as the ratio of the distance between

the most external transverse cracks formed during the test to the quantity (n_c-1), where n_c is the number of transverse cracks.

Specimen	ρ (%)	$s_{r,max,exp}$ (mm)	$s_{r,min,exp}$ (mm)	$s_{rm,exp}$ (mm)
$13-170$	0.44	280.33	170.56	264.96
$16-170$	0.68	341.57	165.63	203.08
$16-110$	1.63	232.11	60.73	123.34
$19-170$	0.98	176.12	77.29	113.27
$16-170-2$	0.68	288.42	198.60	227.75

Table 5.13: Experimental values of maximum, $s_{r,max,exp}$, minimum, $s_{r,min,exp}$, and average, $s_{rm,exp}$, crack spacing at cracking stabilized phase.

In Figure 5.39 experimental values of the ratios $\frac{s_{r,max}}{s_{rm}}$ and $\frac{s_{r,min}}{s_{rm}}$, computed for each tie at crack stabilization phase, are shown. The ratios are presented versus average crack spacing. Although no trend line can be drawn, the mean value of the ratio is also presented with a dashed line. Good agreement for the ratio of minimum to average crack spacing is found, $\frac{s_{r,min}}{s_{rm}}$=0.70, but a slightly larger value of maximum to average crack spacing, $\frac{s_{r,max}}{s_{rm}}$=1.49, is observed. However, experimental values obtained in the tests fall between ranges of $\frac{s_{r,min}}{s_{rm}} \in [0.67, 0.77]$ and $\frac{s_{r,max}}{s_{rm}} \in [1.33, 1.54]$ proposed in previous studies on flexural members [120].

These same ratios are plotted in Figure 5.40 as a function of the reinforcement ratio. Whilst the ratio of maximum to average crack spacing increases with the reinforcement ratio, no defined pattern can be drawn for the minimum to average crack spacing ratio. Therefore, further analysis is done in Figures 5.41 and 5.42, where $s_{r,max}$, $s_{r,min}$ and s_{rm} are plotted vs. the reinforcement ratio. A decrease in crack spacing values with increasing reinforcement ratios is observed. Moreover, special attention has to be taken for the specimen with $\rho = 0.98\%$. In this case, lower crack spacings are observed, therefore indicating the possible effect of other parameters on cracking behaviour. The splitting cracks that appeared during the test may indicate the possible effect of concrete cover.

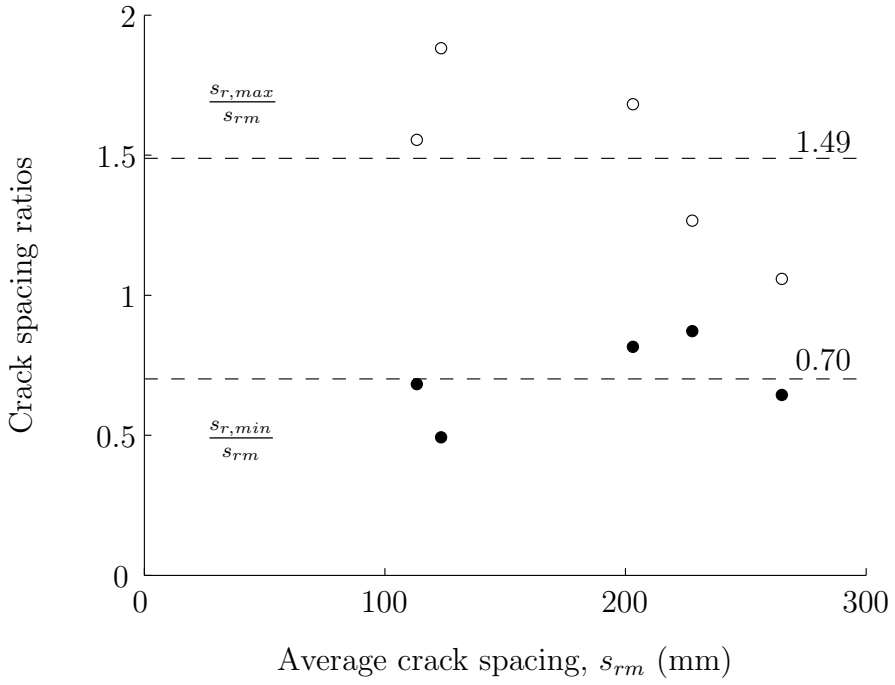

Figure 5.39: Ratios of maximum to average and minimum to average crack spacing vs. average crack spacing.

Based on least square error method, linear relationships for maximum, minimum and average crack spacing proposed in Figures 5.41 and 5.42 have been adjusted in Table 5.14.

Crack spacing (mm)	Linear relationship
$s_{r,max}$	$326.55 - 7.125{\cdot}10^3\rho$
$s_{r,min}$	$234.60 - 1.134{\cdot}10^4\rho$
s_{rm}	$291.54 - 1.191{\cdot}10^4\rho$

Table 5.14: Linear relationships proposed for maximum, minimum and average crack spacing.

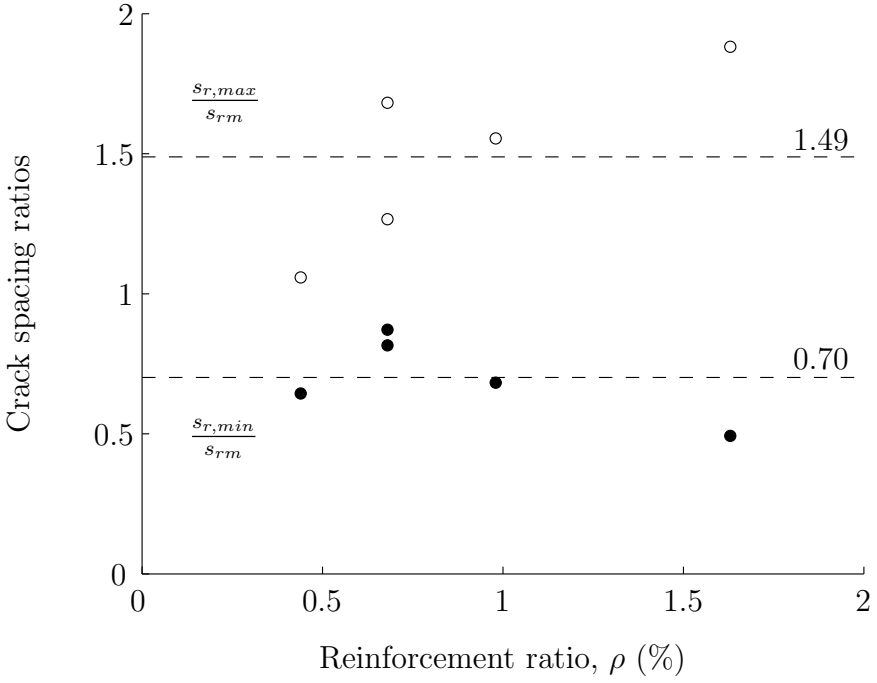

Figure 5.40: Ratios of maximum to average and minimum to average crack spacing vs. reinforcement ratio.

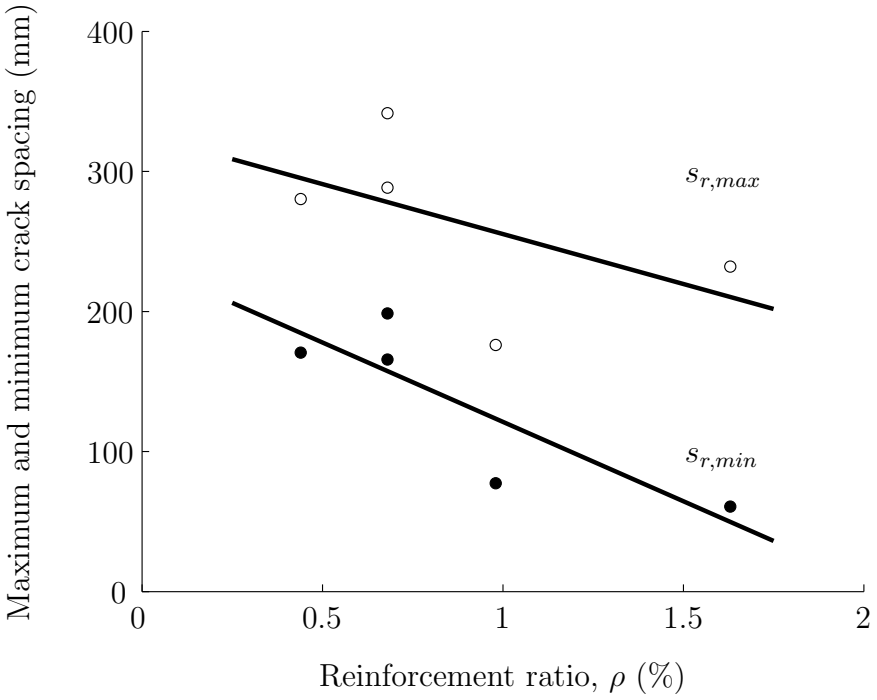

Figure 5.41: Maximum and minimum crack spacing vs. reinforcement ratio.

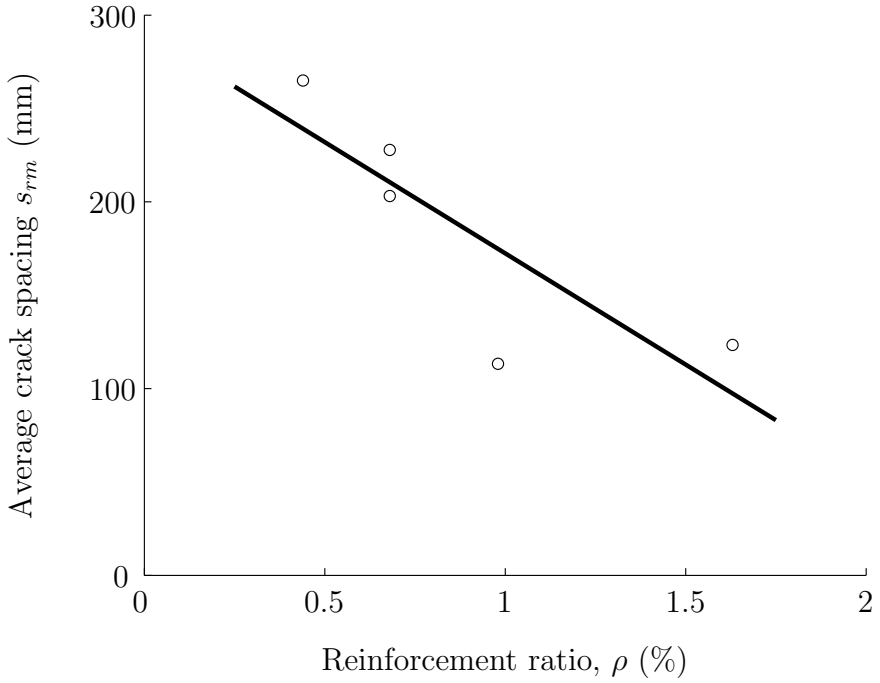

Figure 5.42: Average crack spacing vs. reinforcement ratio.

Proposal of EC2

EC2-92 [4] proposal for mean crack spacing predictions describes the influence of reinforcement size and reinforcement ratio as described next:

$$s_{rm} = 50 + 0.25 k_1 k_2 \frac{d_b}{\rho_{eff}} \tag{5.16}$$

where k_1 is the bond coefficient, reading 0.8 for ribbed and 1.6 for smooth steel bars, k_2 is the loading type coefficient, reading 0.5 for flexural and 1 for tensile loading, and ρ_{eff} is the ratio of internal reinforcement to the effective area of concrete in tension. However, no mention is done on the possible influence of other parameters, such as concrete cover or bar spacing.

In the last version of EC2-04 [9], the influence of concrete cover on maximum crack spacing is included explicitely:

$$s_{r,max} = 3.4c + 0.425 k_1 k_2 \frac{d_b}{\rho_{eff}} \tag{5.17}$$

Similar to Equation 5.6, the bond coefficient (k_1) adjustment may allow Equations 5.16 and 5.17 to be adapted to FRP RC structures.

Comparison with experimental results

EC-2 provisions for crack spacing are compared with experimental results in Table 5.15. Although good bond behaviour of FRP bars was considered in the provisions, k_1=0.8, a clear overestimation of crack spacing is visible through comparison of predicted and experimental results.

Specimen	Maximum crack spacing		Mean crack spacing	
	$s_{r,max,exp}(mm)$	$s^a_{r,max}/s_{r,max,exp}$	$s_{rm,exp}(mm)$	$s^b_{rm}/s_{rm,exp}$
13-170	280.33	4.19	264.96	2.21
16-170	341.57	3.04	203.08	2.49
19-170	176.12	5.17	113.27	3.83
16-110	232.11	2.09	123.34	1.96
16-170-2	288.42	3.47	227.75	2.13

[a] Estimated value according to EC2-04, Equation 5.17.

[b] Estimated value according to EC2-92, Equation 5.16.

Table 5.15: Maximum and mean crack spacing provisions.

Following the approach of EC-2, experimental mean crack spacing is presented in Figure 5.43 as a function of d_b/ρ_{eff}. Based on experimental results on average crack spacing and for the available d_b/ρ_{eff} values, a linear relationship is adjusted to describe their dependency:

$$s_{rm} = 27.13 + 0.073\frac{d_b}{\rho_{eff}} \tag{5.18}$$

The value of the origin ordinate of Equation 5.18 does not fit with any of the two proposals of EC-2 (Equations 5.16 and 5.17). Therefore, the role that concrete cover plays on the crack spacing of RC ties differs from that of RC flexural members, where usually smaller concrete covers are found.

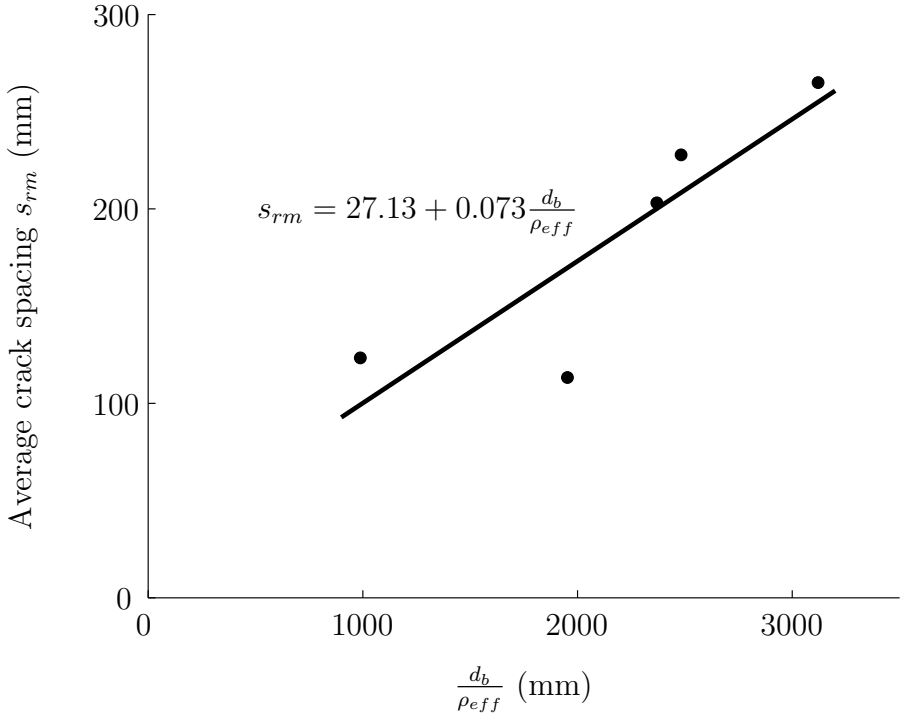

Figure 5.43: Average crack spacing vs. d_b/ρ_{eff}.

5.3.5 Crack width

The development of crack width prediction formulas has usually been based on analytical procedures that determine the concrete tensile distribution [121]. Some of the analytical investigations are coupled with experimental data, whilst other empirical relationships are totally based on large number of experimental tests.

In this section, crack width measurements taken at the height of the reinforcement are presented. In Table 5.16 maximum, minimum and average crack widths measured during the crack formation phase are reported. These measures were taken anytime a new crack appeared during the test, therefore the load level at measuring time and the number of cracks at that load are also reported. As all test were performed under displacement control, measurement loads reported in Table 5.16 are lower than loads causing cracking.

In Figure 5.44 maximum and minimum crack widths are plotted as a function of

ρ (%)	Measurement load P (kN)	n_c	$w_{max,exp}$ (mm)	$w_{m,exp}$ (mm)	$w_{min,exp}$ (mm)
0.44	42.8	1	1.00	1.00	1.00
	49.9	2	1.50	1.30	1.10
	52.4	3	2.10	1.67	1.00
	53.8	4	2.20	1.95	1.80
0.68[a]	36.809	1	0.20	0.20	0.20
	41.9	2	0.90	0.85	0.80
	48.3	3	1.10	1.07	1.00
	68.6	4	3.20	1.75	0.80
1.63	25.1	1	0.40	0.40	0.40
	31.7	2	0.80	0.75	0.70
	36.1	3	1.60	0.93	0.40
	37.8	5	1.10	0.64	0.20
	46.2	6	1.60	0.93	0.20
	87.7	8	3.00	1.51	0.30
0.98	54.9	1	0.80	0.80	0.80
	61.5	2	2.00	1.25	0.50
	62.8	6	1.70	0.82	0.30
	100.2	9	2.20	0.98	0.30
0.68[b]	57.5	1	1.50	1.50	1.50
	60.0	4	1.70	0.95	0.50
	63.2	5	1.70	1.08	0.50
	85.1	6	2.30	1.05	0.20

[a] Specimen $16-170$.

[b] Specimen $16-170-2$.

Table 5.16: Experimental values of maximum, $w_{max,exp}$, average, $w_{m,exp}$, and minimum, $w_{min,exp}$, crack width after each crack formation.

experimental average crack spacing. Although some scatter is found in experimental results, maximum and minimum crack opening can be defined as a linear function of average crack width.

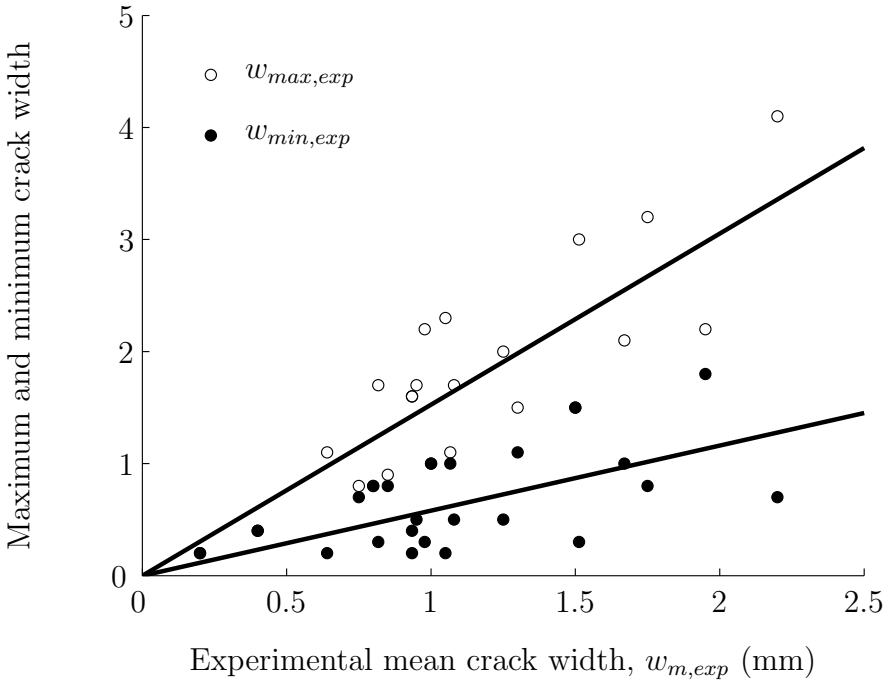

Figure 5.44: Maximum and minimum crack width vs. average crack width.

To further study crack width measurements, the ratio of maximum to average and minimum to average crack width are plotted in Figure 5.45 as a function of the reinforcement ratio. However, no clear tendencies on the effect of reinforcement ratio can be drawn. Individual effects of either bar diameter or reinforcement ratio on the crack width are difficult to be studied separately, due to the interdependency of the two variables. The following general trend can be derived from most of crack width predictive formula: the higher the bar diameter and the concrete cover are and the lower the reinforcement ratio is, the larger the crack width obtained. However, a combined action of these effects is present in the tests conducted in this thesis. Therefore, the decrease in crack width caused by using higher reinforcement ratios could be partially compensated by an increase in crack width caused by using larger bar diameters. Because of this ambiguity in experimental results, only the mean values are marked in Figure 5.45 with dashed horizontal lines.

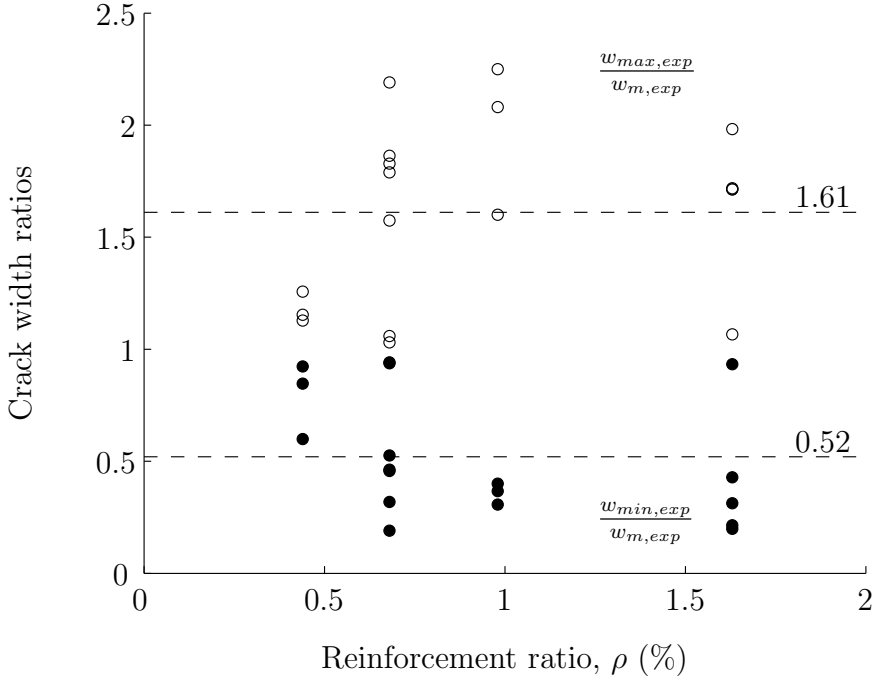

Figure 5.45: Ratios of maximum to average and minimum to average crack width.

Proposal of EC2

EC2-92 [4] proposal for characteristic crack width is derived from average crack width, through coefficient β_k. Therefore, the characteristic crack width is a function of the product of average crack spacing, s_{rm}, and average strain of reinforcement, ϵ_{sm}, and reads:

$$w_k = \beta_k s_{rm} \epsilon_{sm} \tag{5.19}$$

where s_{rm} is described through Equation 5.16 and ϵ_{sm} is defined as:

$$\epsilon_{sm} = \epsilon_2 \left[1 - \beta_1 \beta_2 \left(\frac{\sigma_{cr}}{\sigma_s} \right)^2 \right] \tag{5.20}$$

In its last version, EC2-04 [9], a different theoretical background is adopted and characteristic crack width is defined as the product of maximum crack spacing and the difference between the mean strain of steel and concrete between cracks:

$$w_k = s_{r,max} \left(\epsilon_{sm} - \epsilon_{cm} \right) \tag{5.21}$$

where $s_{r,max}$ is described through Equation 5.17 and the difference in materials strains between cracks is described as:

$$\epsilon_{sm} - \epsilon_{cm} = \epsilon_s - k_t \left[\frac{f_{ctm} A_{c,eff}}{E_s A_s} + \frac{f_{ctm}}{E_c} \right] \tag{5.22}$$

where f_{ctm} is the mean tensile strength of concrete and k_t is a factor depending on the duration of the load, reading 0.6 for short term loading and 0.4 for long term loading. Within this new provision, and contrary to provisions of EC2-92 [4], the reinforcing bar surface type is included in the calculation of the tension stiffening term $(\epsilon_{sm} - \epsilon_{cm})$, with a coefficient of 1 related with high bond bars.

Proposal of ACI 224

The american code for steel RC structures [6] proposes an empirical formula to directly evaluate the maximum crack width in fully cracked tensile members without evaluating crack spacing:

$$w_{max} = 0.0145 \sigma_s \sqrt[3]{d_c A} \times 10^{-3} \tag{5.23}$$

where σ_s is the stress in the steel reinforcement at the cracked section, d_c is the distance from center of bar to extreme tension fiber (i.e. concrete cover) and A is the area of concrete symmetric with reinforcing steel divided by number of reinforcing bars. A large variability in maximum crack width for tensile members is recognized in the code, and therefore variations of up to 30% are expected. Moreover, no extension of Equation 5.23 to FRP RC ties has been proposed.

Proposal of ACI 440

Contrary to the code for RC tensile members, predictive equations originally derived for steel RC beams have been extended to their use in FRP RC flexural members in [108]. In this code, an empirical formula is proposed to define the most probable maximum crack width:

$$w = 2.2 \alpha k_b \frac{\sigma_{FRP}}{E_{FRP}} \sqrt[3]{d_c A} \tag{5.24}$$

where α is the ratio of the distance from the neutral axis to extreme tension fiber to the distance from the neutral axis to the center of tensile reinforcement, σ_{FRP} is the stress in the FRP reinforcing bar at the cracked section, E_{FRP} is the modulus of elasticity of the reinforcing bar and k_b is a coefficient accounting for the degree of bond between FRP bar and surrounding concrete. This coefficient can be assumed to read 1 for bars having similar bond to steel rebars. However, according to [108] provisions, k_b can vary from 0.71 to 1.83, with a design value proposal of 1.2 for those cases where no data is available for a given bar.

Comparison with experimental results

Although experimental crack spacing is overestimated by EC2 provisions, a comparison between experimental and code provisions on characteristic crack width is performed in Figure 5.46.

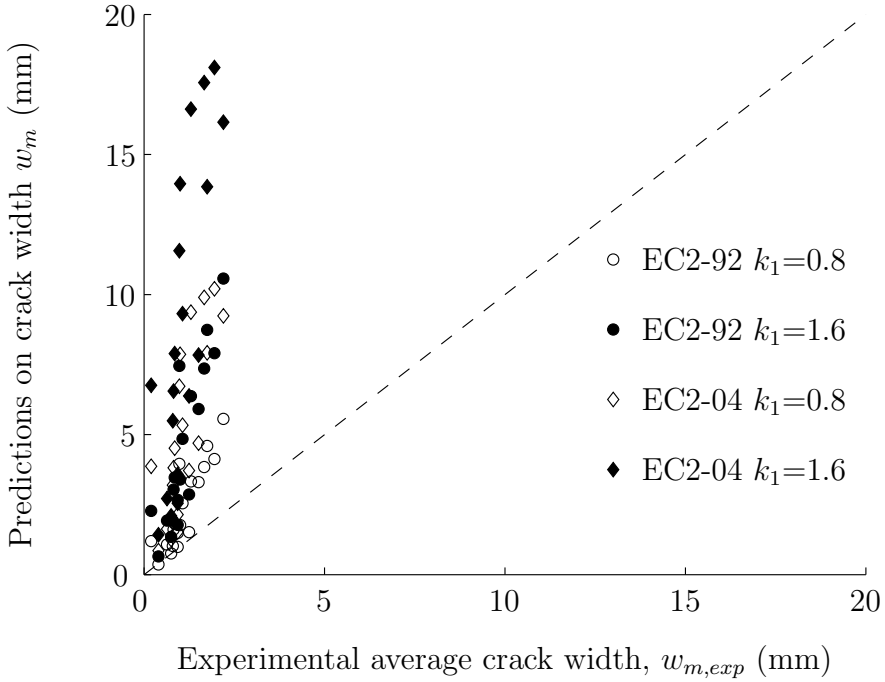

Figure 5.46: Comparison between experimental and EC-2 [4, 9] provisions of mean crack width using k_1 bond coefficient limits.

Both versions of EC2, the older one published in 1992 [4] and the modern one published in 2004 [9], define a dependence of crack width on crack spacing (see

Equations 5.19 and 5.21), and use k_1 bond coefficient to represent the bond strength level. In Figure 5.46 comparison between experimental crack width at different load levels and code provisions is presented for the two limiting values (i.e. for k_1=0.8 and k_1=1.6).

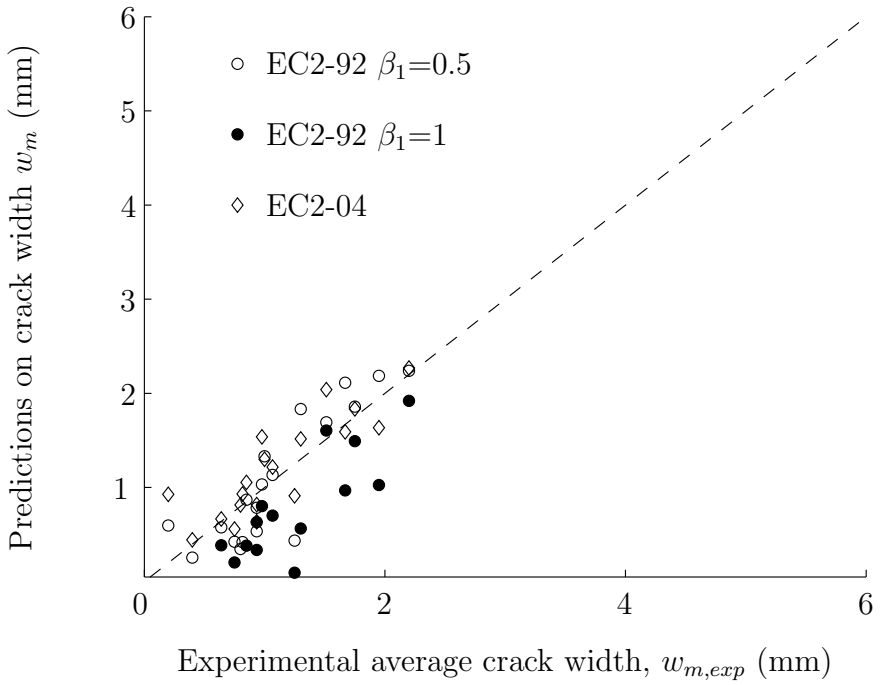

Figure 5.47: Comparison between experimental and EC-2 [4, 9] provisions of mean crack width, using proposed Equation 5.18.

Similar to the case of crack spacing predictions, a clear overestimation of crack width is visible, even when bond coefficient for high bond bars is considered (k_1=0.8). The goodness of EC2 crack width predictions relies on the effectiveness of the code to predict crack spacing. However, predictions on crack spacing have been proven to overestimate the experimental values. Therefore, a second comparison between new predictions and experimental readings is presented in Figure 5.47. In these new predictions, mean crack spacing has been computed with Equation 5.18 adjusted in Section 5.3.4. An improvement in code predictions has been obtained and therefore the crack width code formulas (Equations 5.19 and 5.21) are proven to be valid, although contingent on crack spacing provisions.

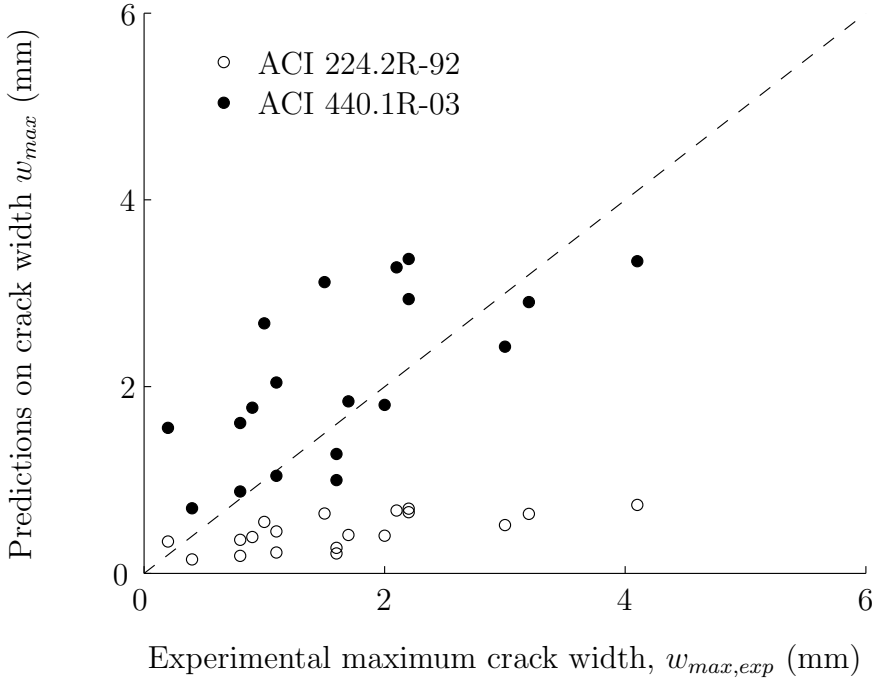

Figure 5.48: Comparison between experimental and ACI [6, 108] provisions of maximum crack width.

Experimental maximum crack width, $w_{max,exp}$, is compared with ACI provisions in Figure 5.48. The lack of a specific coefficient in ACI 224 [6] to account for the differences in bond behaviour of FRP RC ties compared to steel, leads to underestimations in the crack width provisions. However, although being developed for predicting crack width in flexural FRP RC members, accurate provisions of maximum crack width in GFRP RC ties are obtained with ACI 440 [108]. The better agreement obtained with provisions of flexural code instead of direct tensile code is attributed to the proper adaptation to FRP RC structures in the former case. Based on the assumption of crack width being proportional to the strain in the reinforcement rather than the stress, stated in [122], ACI 440 [108] introduces the elastic modulus of FRP reinforcement in the crack width prediction formula (Equation 5.24). Author's opinion is that a similar procedure is necessary to properly adapt the code for tensile members to its application to FRP reinforced ties, therefore accounting for the differences in mechanical properties of new reinforcing material.

5.3.6 Concrete post-cracking response

In section 5.3.2 the study of the tension stiffening effect has been performed trough the *tension stiffening strain* approach. Within this approach the tensile contribution of concrete is computed for through a modified relationship for the stress-strain response of the embedded reinforcing rebar. No post-cracking tensile strength is accounted for the concrete in tension. An alternative approach is the so called *load sharing* approach, where a post-cracking stress-strain response of concrete in tension is obtained, whilst no additional stiffness is attributed to the reinforcing material.

In this section, experimental data is used to derive the post-cracking stress-strain response of concrete (i.e. proceeding with the *load sharing* approach). To this end, the average load carried by the cracked concrete can be derived from the measured member response by substracting the bare bar response. This average tension force in the concrete can not be considered as a material property because it depends on both the concrete tensile strength, f_{ct}, and the area of concrete affected by the reinforcement. Therefore, the load is normalized with maximum concrete tensile load, which corresponds to the force carried by the concrete at first cracking.

In Figures 5.49-5.51 the normalized post-cracking stress-strain responses derived from experimental tests are shown. Responses are grouped according to the concrete batch they belong to (i.e. C1, C2 and C3).

Although different reinforcement ratios are studied, little differences are found in the post-cracking stress-strain relationship. These results seem to confirm the statement of Bischoff [68], who indicated that the tension stiffening effect is related to the average strain in reinforcement and the modulus of elasticity of the reinforcing rebar. However, more experimental work would be needed to analyze the possible influences of these and other mechanical and geometrical variables.

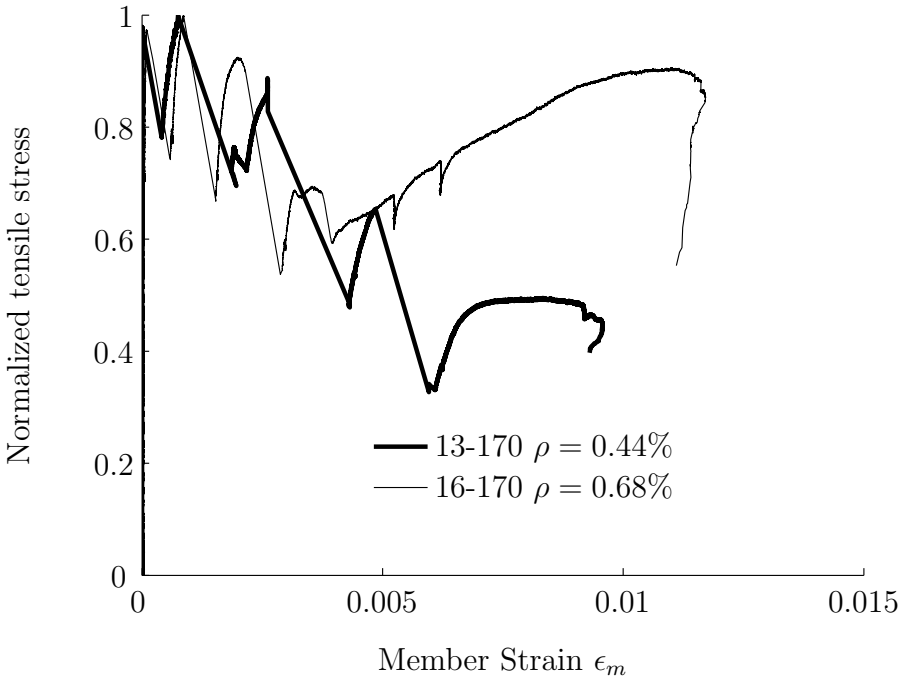

Figure 5.49: Normalized concrete post-cracking stress-strain response in C1 series.

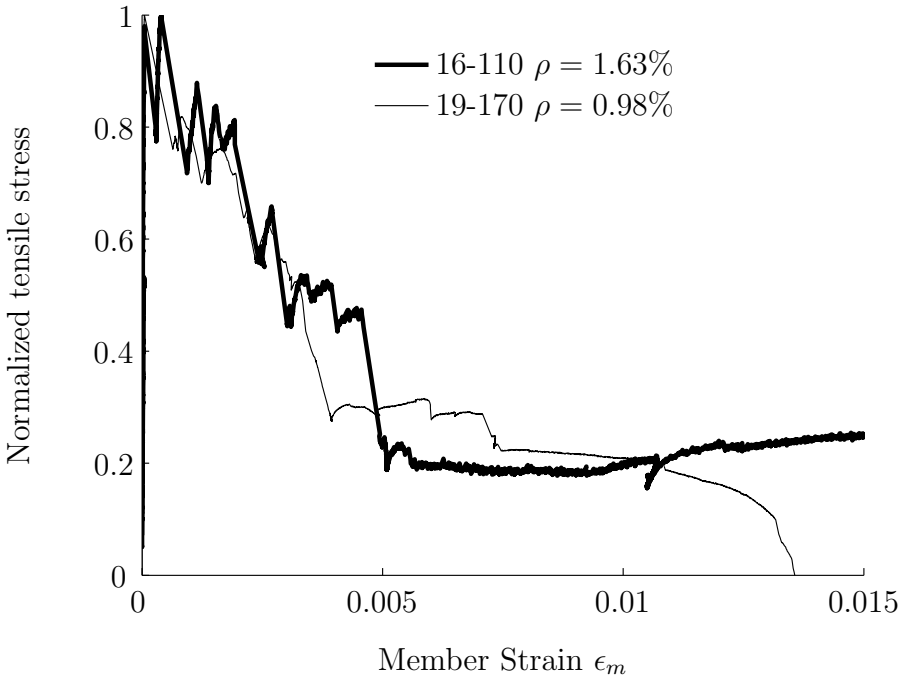

Figure 5.50: Normalized concrete post-cracking stress-strain response in C2 series.

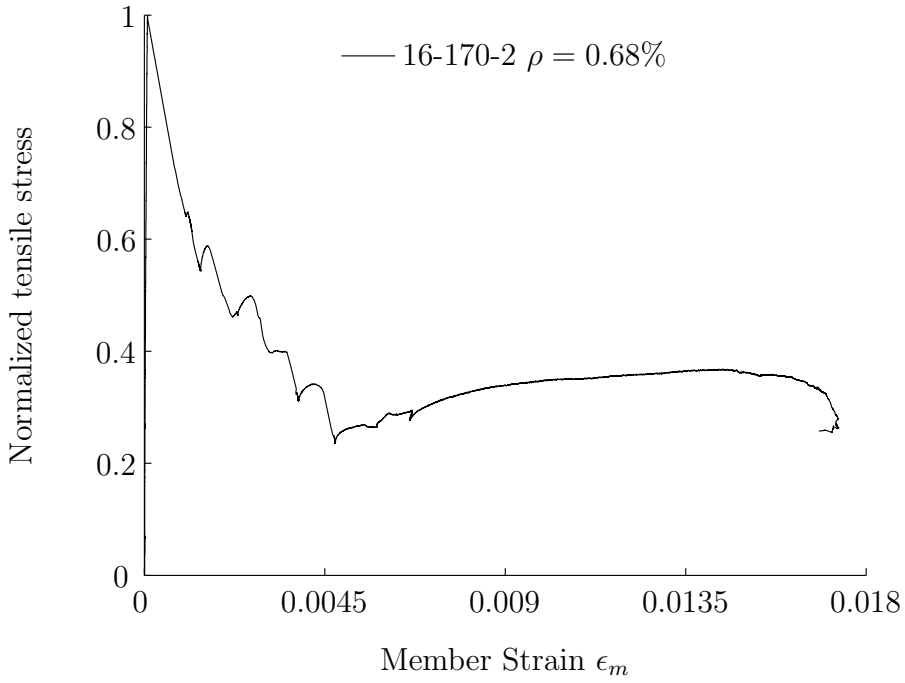

Figure 5.51: Normalized concrete post-cracking stress-strain response in C3 series.

5.4 Additional notched tests

The experimental work on FRP RC ties was complemented with two additional tests. These tests were specially designed with internal strain gauging with the aim at obtaining the strain profile of the internal reinforcement during a direct tension test.

The special manufacturing of internally gauged reinforcing rebars has been presented in section 5.1 and their geometrical and mechanical characteristics can be found in Table 5.2. Similarly, details on how the pre-cracks were induced around the perimeter of the ties are given in section 5.2 and the final tie characteristics can be found in Tables 5.6 and 5.7. The induced pre-cracks allowed to make the most of the internal gauging, so that first transversal cracks appeared at specific locations where lecture of reinforcement strain was assured.

5.4.1 Crack pattern

In Figures 5.52 and 5.53 the final crack pattern of the notched ties is shown, with cracks numbered according to appearance order. As expected, first cracks appeared at the pre-induced cracks, where the weakest sections were found. If crack pattern of non-precrack ties (see Figure 5.26) is compared with crack pattern of notched ties (see Figures 5.52 and 5.53), splitting cracks appearing for the 19-170 tie still appear in the 19-170-N tie. However whilst only transverse cracks appeared in the 16-170 tie, splitting and transverse cracks appear for the notched tie, 16-170-3N. These new splitting cracks were formed as a result of the reduction in concrete section (i.e. as a result of the increase in reinforcement ratio).

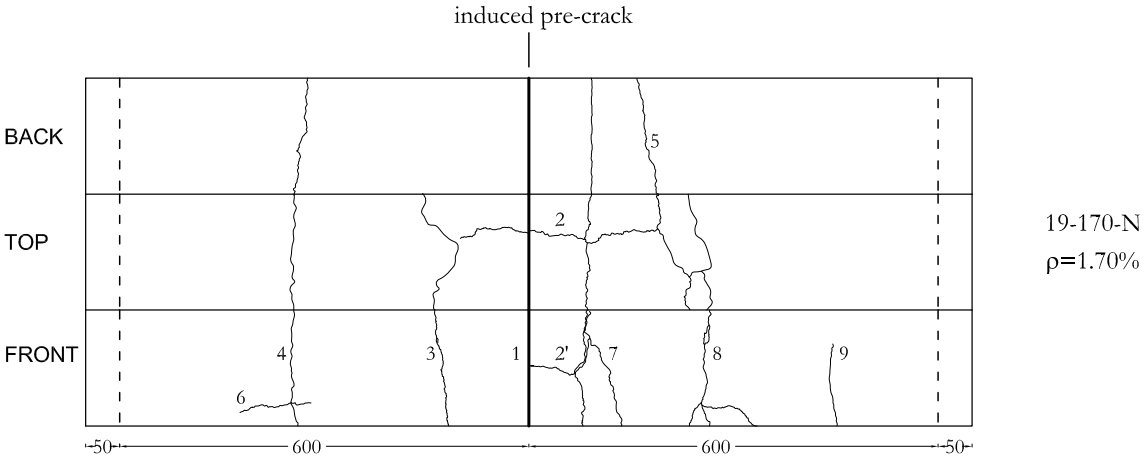

Figure 5.52: Final crack pattern for 19-170-N tie (units in mm).

5.4.2 Reinforcement strain distribution

In this section, the reinforcement strain distributions obtained through the internal strain gauging on reinforcing rebars are presented and analyzed. Differences in cracking behaviour observed during the tests are accompanied with evidences in the strain distributions.

It has to be noticed that in the strain distribution profiles presented hereafter, lines have been plotted to connect individual strain measurement readings. Although, these connecting lines may not reflect real behaviour between strain gauged points, they give a reasonable pattern on global strain distribution.

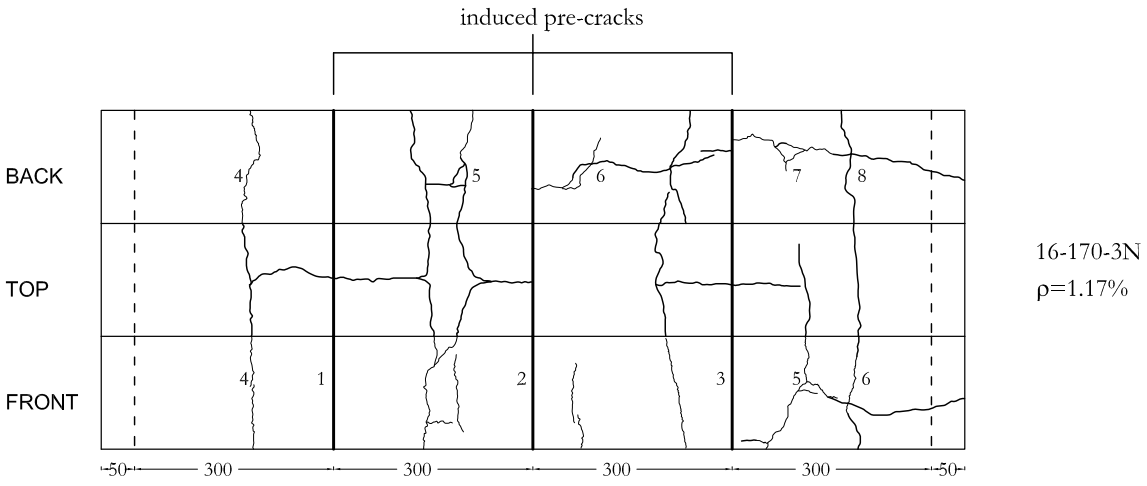

Figure 5.53: Final crack pattern for 16-170-3N tie (units in mm).

16-170-3N tie

The reinforcement strain distributions during crack formation of the three induced cracks are shown in Figure 5.54. Strain measurements are shown before and after each crack formation when the specimen is loaded back to the same load. The composite action that contributes to the high initial stiffness of RC tie is present along the whole tie, except near notched sections and near the ends of the tie, where reinforcement strain increases because concrete carries no tension.

After the three induced cracks were formed, load was further increase. Reinforcement strain distributions at higher load stages during the crack propagation phase are shown in Figure 5.55. After the formation of the third induced crack, splitting cracks started to appear. This behaviour is evidenced in the strain distribution through the plateau in strain values observed next to the notched sections. This plateau is the result of the rapid loose in bond behaviour happening when splitting cracks appear. The formation of complementary transverse cracks is not visible in the strain distribution because of the higher effect of splitting cracks.

19-170-N tie

Similarly to previous tie, the reinforcement strain distributions for the whole loading procedure are shown in Figures 5.56-5.58. Hereafter, the crack formation will

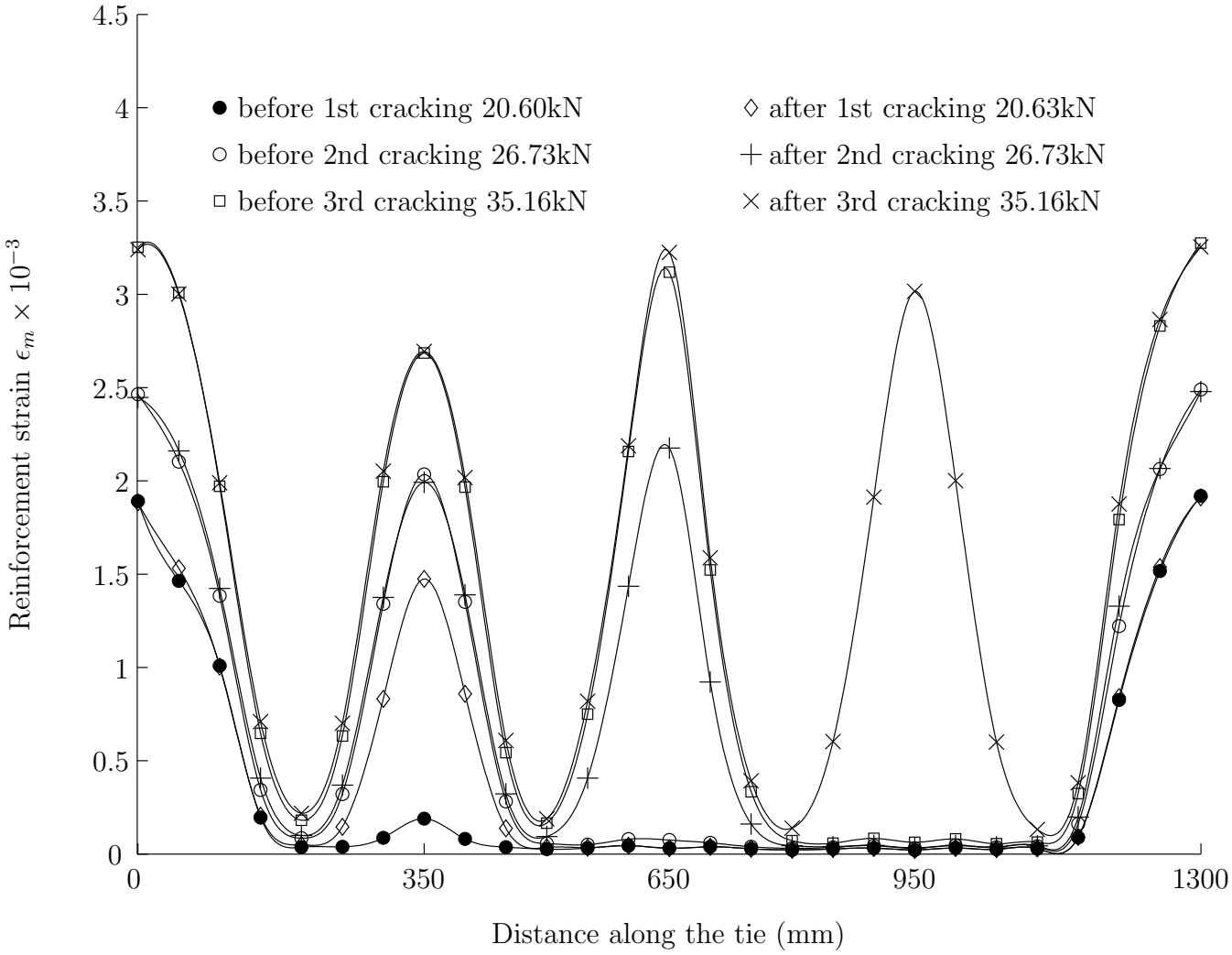

Figure 5.54: Strain distribution during crack formation of the three induced cracks for specimen 16-170-3N when specimen is loaded back to the same loading.

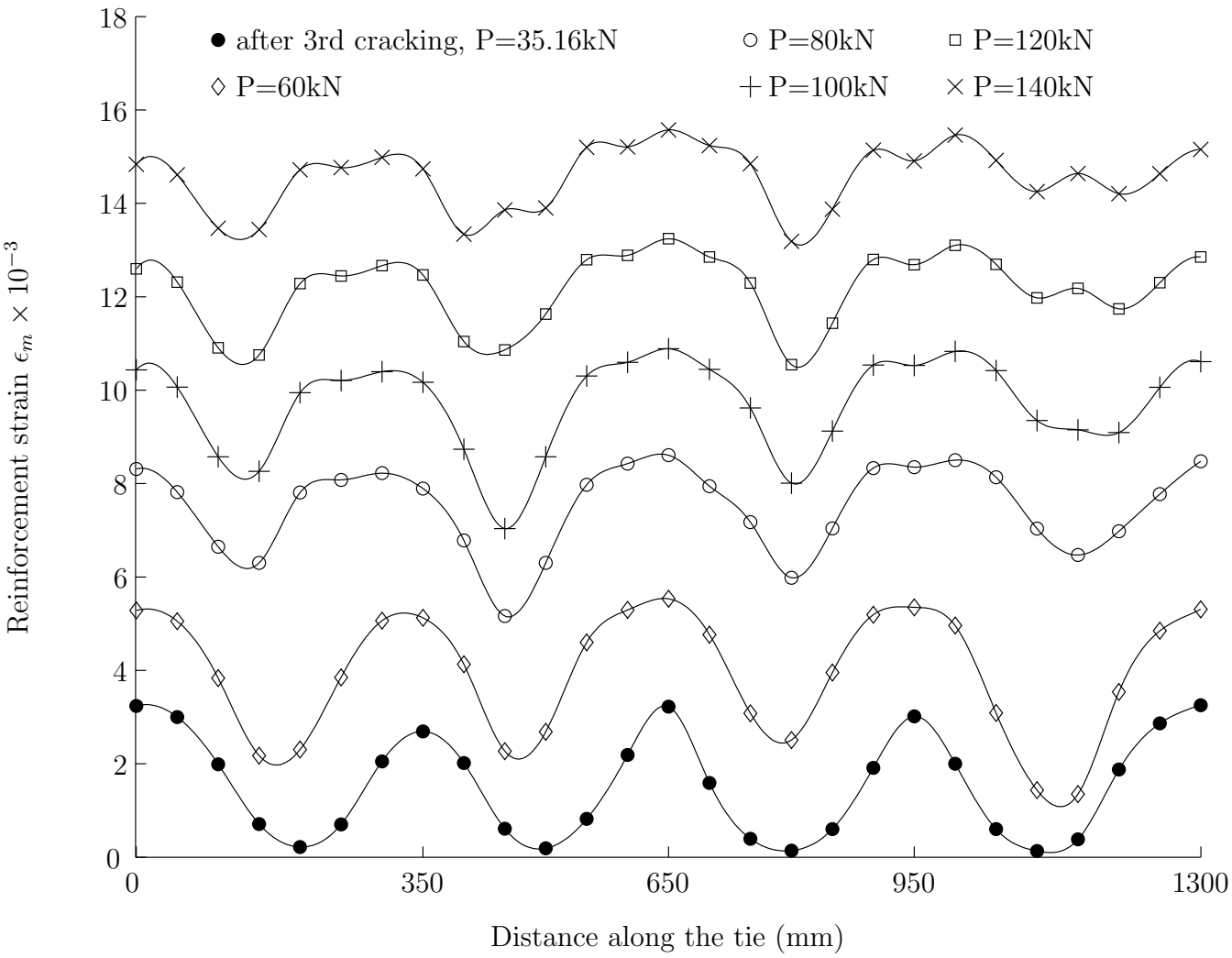

Figure 5.55: Strain distribution at post-cracking stage for specimen 16-170-3N.

be explained with the help of both crack pattern (shown in Figure 5.52) and reinforcement strain profiles (shown in Figures 5.56-5.58).

The reinforcement strain profiles for the crack formation of cracks 1-4 are shown in Figure 5.56. For tie 19-170-N, only one induced crack was formed at midway section (crack 1, P=35kN). After this first crack formation, and due to low concrete cover, a splitting crack appeared on the right side (crack 2, P=48.5kN). This new crack formation made the peak value of reinforcement strain to move to the right. The formation of crack 3 was accompanied with a new peak in reinforcement distribution on the left side (crack 3, P=55kN). The distance between first and third crack was not long enough to allow for composite action to be recovered. After this third crack, the tie could not be loaded back to the same loading without any new crack formation. Crack number 4 appeared when previous loading level was being recovered, at a loading level with P=49.5kN. For this whole loading procedure, no cracks appeared on the right hand side of the tie, and composite action was possible.

Reinforcement strain profiles related to the formation of cracks 5-9 are shown in Figure 5.57. To better connect previous and actual strain profiles, the reinforcement strain distribution related to the formation of crack 4 at a load level of P=49.5kN is repeated in Figure 5.57. Transverse crack number 5 was detected at the back side of the tie before splitting crack number 6 became visible (i.e. before crack 6 propagated until the face of the tie). However, strain profile evidences that both crack were formed together at a load level of P=59kN. Formation of crack number 7 is not clearly visible in the reinforcement strain distribution because it formed very close to previously existing crack number 2. Again, no possibility of loading back the tie was possible and crack number 7 appeared at P=57kN. The short crack spacing avoided the recovering of composite action between cracks (at the left hand side of the tie). Load was further increase until crack number 8 appeared for P=60kN and last crack number 9 started to appear at P=62kN. The final crack pattern was achieved at P=70kN, with all cracks being clearly visible through reinforcement strain profile.

Finally, reinforcement strain distributions during crack maturity are shown in Figure 5.58. At this stage, no more new cracks appeared and only the opening of

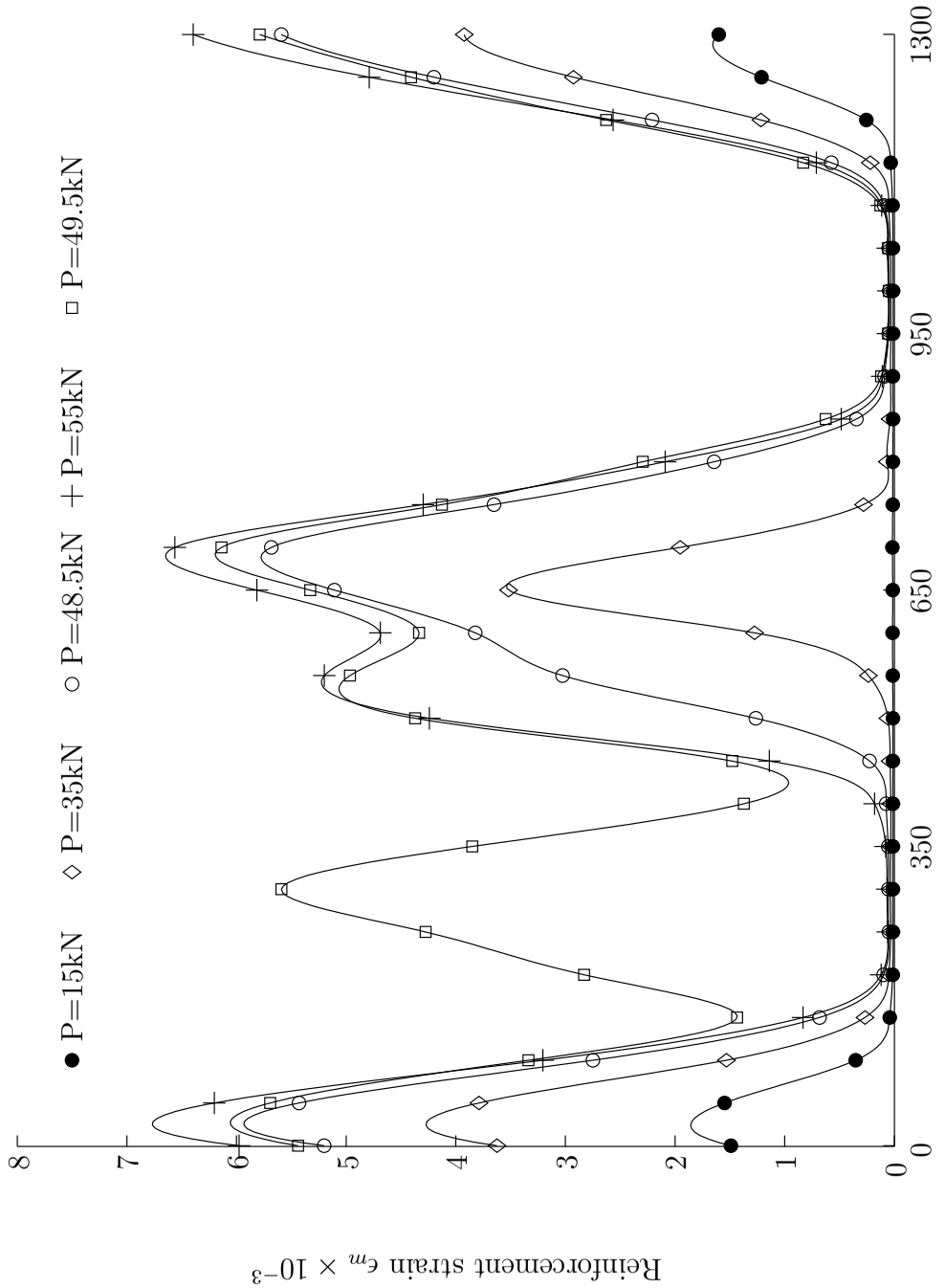

Figure 5.56: Strain distribution during formation of cracks 1 to 4 for specimen 19-170-N.

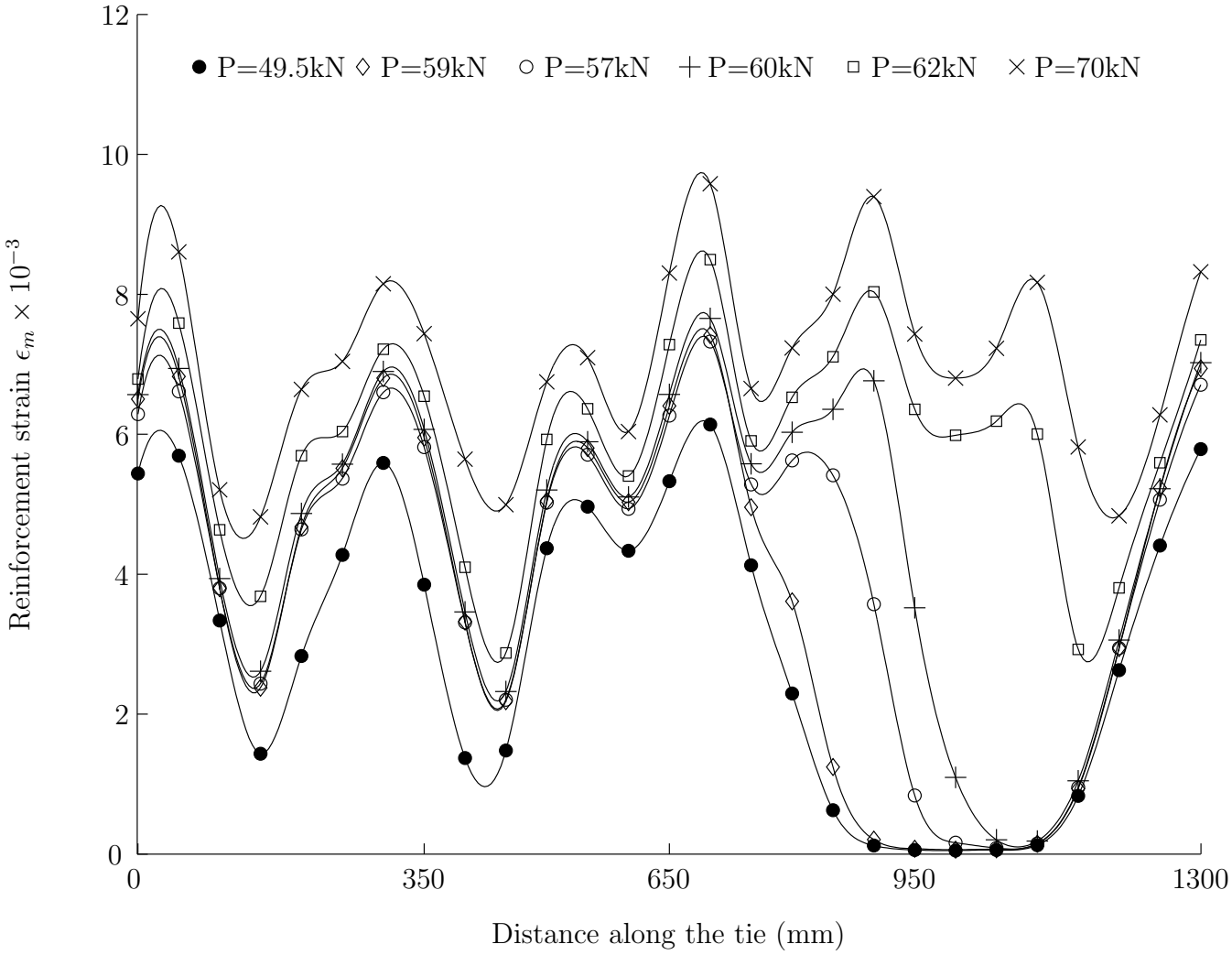

Figure 5.57: Strain distribution during formation of cracks 5 to 9 for specimen 19-170-N.

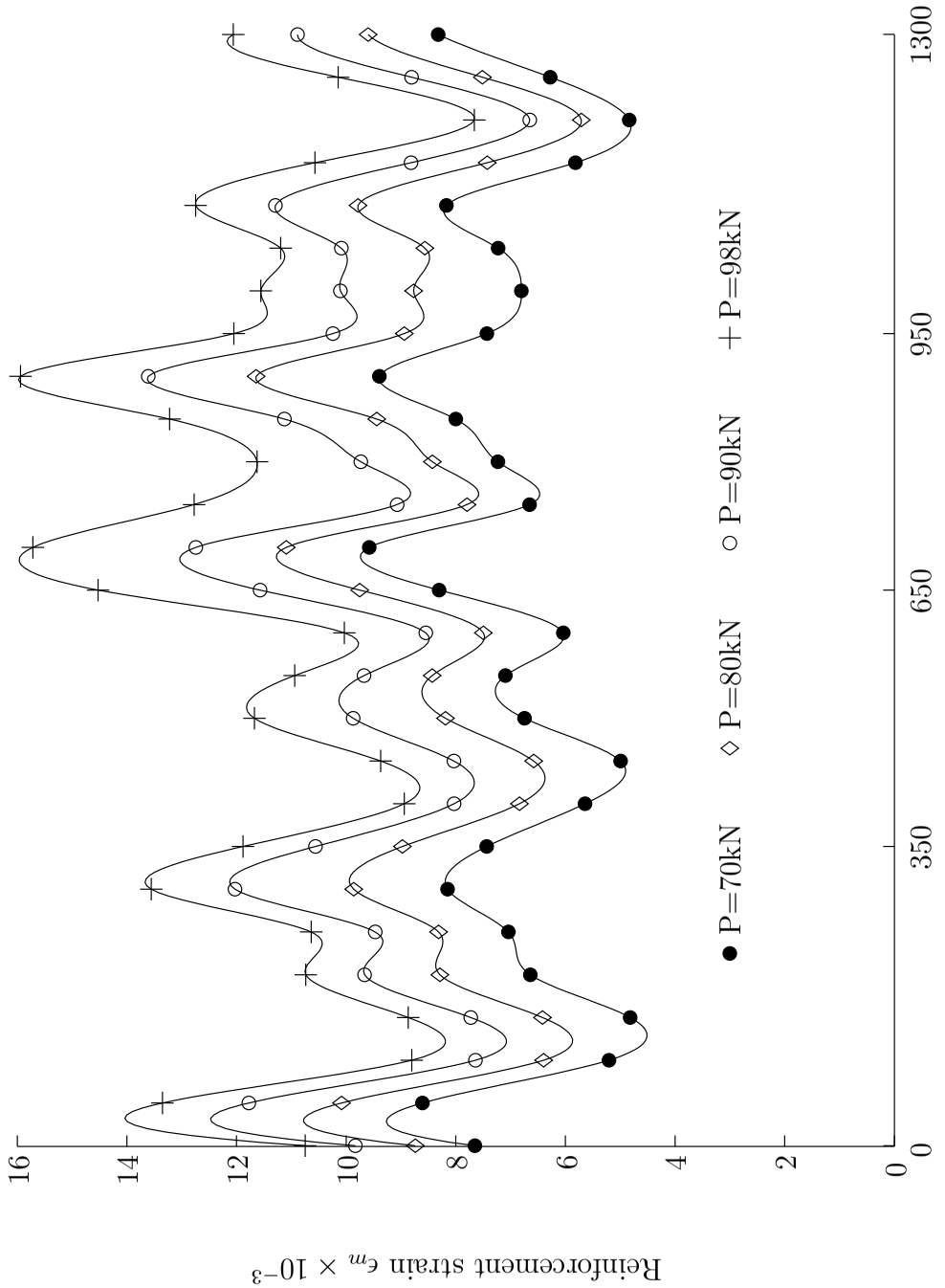

Figure 5.58: Strain distribution during crack maturity for specimen 19-170-N.

the existing ones was possible. Any further increase in load was accompanied with a parallel shift of the strain distribution.

Similarities are found when strain profiles belonging to different ties are compared. For early loading stages, when no crack has formed, composite action is possible almost along the whole tie, except for those regions next to the tie ends. From first cracking load on, cracks start to appear wherever the concrete tensile strength is attained, therefore corroborating to the reduction in member stiffness. The recovering of composite action after a new crack formation is only possible if enough crack spacing is provided. Moreover, early splitting cracks appear next to the reduced notched sections, because of the low concrete cover. Once crack maturity is attained, the strain profile shifts to higher reinforcement strain values.

5.5 Concluding remarks

Chapter 5 presents detailed information on the experimental research work on GFRP RC ties, concerning the test design, specimens manufacturing, testing and data analysis.

Tensile tests performed on GFRP bars confirmed their brittleness. The suitability and optimization of the gripping arrangement developed for the tensile tests have been demonstrated. Specially, the centering aligning system has been confirmed to provide good results avoiding the introduction of flexural loads. The proper adaptation of this gripping arrangement to the set-up of GFRP RC ties was also successful.

The tensile behaviour of GFRP RC ties was compared to proposals of ACI and EC2. Clear overestimation of member stiffness was found in ACI 224.2R predictions, even when the reduction factor firstly introduced for ACI FRP RC flexural code was adapted to ACI tensile code. Different theoretical background considered in EC2 provided more accurate predictions. Moreover, the differences in tensile cracking behaviour occurring when splitting cracks appear can be modelled through variation of β_1 coefficient.

Results indicate that a dependence of maximum, minimum and average crack spacing on reinforcement ratio can be derived. Moreover, close agreement was found between maximum over average and minimum over average crack spacing.

EC2 provisions of crack spacing do not provide accurate results when applied to GFRP RC ties. Although the dependence of crack spacing on d_b/ρ_{eff} was confirmed with experimental results, EC2 proposal of an additional dependence on the concrete cover does not seem directly applicable to RC tensile members. Therefore, based on experimental results an equation which describes the relationship between crack spacing and d_b/ρ_{eff} has been proposed. However, more experimental data is needed to arrive to a more general conclusion.

Linear progression of maximum and minimum crack width with mean crack width were found. Although crack width provision make reference to the influence of ρ in crack width, no clear evidences have been found in the test performed in this dissertation because of the ambiguity derived from the combined action of bar diameter, concrete cover and reinforcement ratio.

Crack width calculated according to EC2 recommendations clearly overestimated experimental values. The poor accuracy is related to inaccurate predictions on crack spacing. However, great improvement in EC2 crack width provisions was found when crack spacing proposal presented in this dissertation is considered.

Empirical formula for the calculation of crack width of steel RC ties proposed by ACI underpredicts experimental values. By contrast, the formula proposed in the code for FRP RC flexural members gives accurate predictions. The accuracy of the flexural code is thought to be linked with the change in formula dependencies, as the influence of reinforcement stress was removed and new dependence on reinforcement strain was introduced. Therefore, similar adaptation would be required in the code for tensile members.

The internal strain gauging on additional RC ties was proven to be useful to obtain the reinforcement strain profile along the whole tie. The analysis of strain

readings at different load levels is presented as an useful tool to analyze cracking behaviour and understand the evolution of crack pattern until crack stabilization phase is attained. At crack maturity no changes in the shape of the reinforcement strain profile are observed, however a shift of the whole profile to higher tensile strain values took place. Besides, the process of stress redistribution after crack formation can be studied through the study of the reinforcement strain profiles.

Chapter 6

Modeling cracking behaviour of FRP RC ties

6.1 Introduction

The post-cracking structural behaviour of reinforced concrete members is affected by the interaction between the reinforcing bar and the surrounding concrete. This interaction allows the intact concrete between cracks to contribute to carry tensile stresses and provides stiffness (*tension stiffening* effect). Different strategies have been proposed to study the cracking behaviour of RC members. Some studies remove any effect of the consequences of the bond behaviour on the constitutive equations of both the reinforcing and the surrounding materials, and relate it to an effective cross-sectional area that reduces as long as the cracking process progresses [6, 56]. Some others couple the additional stiffness on the post-cracking stage of RC members with the constitutive behaviour of one of the two materials involved in the bond forces system. In this sense, some works have been presented where the stress-strain constitutive equation of the embedded reinforcing material has been modified [5, 63, 64], whilst other studies include the additional stiffness in the constitutive equation of the surrounding concrete [57–59, 66, 67]. A third group of studies does not modify neither the effective cross-sectional area nor the material constitutive equations, but proposes to specifically include the interaction between materials. To this end, the theoretical model that describes the cracking behaviour is considered and different techniques are used to solve the system of differential equations

that governs the bond problem. At early stages, the solving technique consisted on the analytical solution of the system of differential equations [67, 74–79]. Although this technique gives an exact solution of the problem, it has an important drawback that only simple bond-slip laws can be used (i.e. lineal, constant and/or bilinear laws). Hence, the solution of the system of differential equations through numerical procedures has become more popular, with either finite differences methods technique [80–82, 95, 96] or finite element methods [66, 100].

In this chapter, a numerical procedure for the study of the cracking behaviour of RC tensile members is presented. Based on the system of differential equations that govern the bond problem, an iterative computation of slip and reinforcement and concrete strain profiles along the RC tie is conducted. Moreover, the transmission of the bond forces that appear between reinforcement and concrete is modelled through the relationship between bond stresses and slip (i.e. the bond-slip law). The numerical procedure is versatile enough to consider not only simple bond-slip law previously used in the literature, but also any experimental bond-slip law, so that the behaviour characterized in bond tests can be included in the model. Due to its flexibility, the numerical procedure is thereafter used to conduct a parametric study on the influence that the variables involved in the bond problem (f_c', ρ, n) can have on the cracking behaviour of RC ties.

6.2 Cracking phenomenon and governing equations

Before cracking, stresses and strains in an RC element in tension are uniform along the length of the member. Forces equilibrium and compatibility of strains are linked together by assuming linear elastic material behaviour for both the concrete and the reinforcement. Therefore, the applied load is shared between the concrete and the reinforcement in relation to their respective rigidities. At this uncracked stage, no differences between reinforcement and concrete strain exist and therefore no slip occurs. Once concrete tensile strength, f_{ct}, is reached first primary crack appears. Due to crack formation, the tensile concrete stress at crack location drops to zero, and a redistribution of reinforcement and concrete strains takes place, so that strains are

no longer equal along the total length of the member and slip occurs. The applied axial load can be further increased until concrete tensile strength is again attained at any other section and new cracks appear. The process continues until final crack configuration is attained.

According to the explained cracking phenomenon, the theoretical study of RC ties beyond the cracking load is related to the analysis of concrete and reinforcement strain distribution along the RC member, which in turn is based on the solution of the differential equation that describes the bond problem. Hereafter, the rational derivation of the differential equation is presented, where the following assumptions have been considered:

- The rebar and concrete follow the Hooke's law.
- No tensile softening behaviour is considered in the constitutive equations for concrete.
- Stresses are assumed to be constant on the whole cross section.

Let us consider a block of a RC member subjected to uniaxial tensile force P as shown in Figure 6.1(a). The x-axis has its origin midway between the two cracks. Because of symmetry only one half-member is analyzed. Let us consider a section at a distance x from the origin, so that the free-body diagram of the right hand side is shown in Figure 6.1(b). The reinforcement and concrete interfaces related to an infinitesimal element of length dx are shown in Figure 6.1(c). The equilibrium equations read:

$$dF_c(x) = A_c d\sigma_c(x) = -p_r \tau(x) dx \tag{6.1}$$

$$dF_r(x) = A_r d\sigma_r(x) = p_r \tau(x) dx \tag{6.2}$$

where p_r is the perimeter of the bar, $\tau(x)$ is the the bond stress, A_c and A_r are the cross sectional area of concrete and reinforcement, respectively, $d\sigma_c(x)$ and $d\sigma_r(x)$ are the tensile stresses in the concrete and in the rebar at a distance x from the origin, respectively, and $dF_r(x)$ and $dF_c(x)$ are the axial force in the concrete and

in the rebar at a distance x from the origin, respectively.

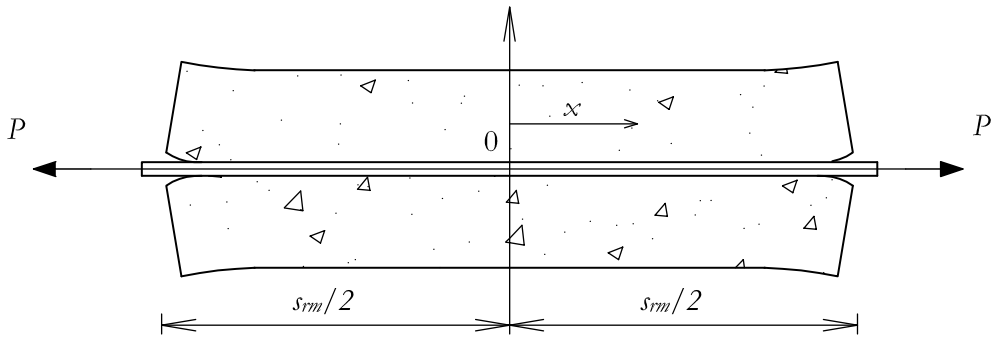

(a) block of RC member in tension

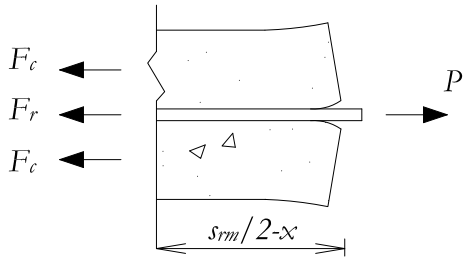

(b) arbitrary section

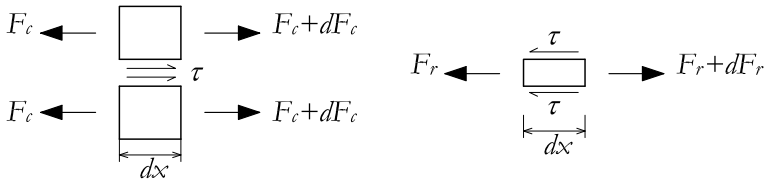

(c) concrete and reinforcement interfaces

Figure 6.1: Free-body diagrams of RC tie.

The slip at the reinforcement-concrete interface is defined by:

$$s(x) = u_r(x) - u_c(x) \tag{6.3}$$

where $s(x)$ is the slip, and $u_r(x)$ and $u_c(x)$ are the displacements along the x-axis of the reinforcement and concrete, respectively. The uniaxial constitutive relationship for the linear elastic concrete and reinforcement elements are:

$$F_c(x) = E_c A_c \epsilon_c(x) \tag{6.4}$$

$$F_r(x) = E_r A_r \epsilon_r(x) \tag{6.5}$$

where $F(x)$ is the axial force along the x-axis, E is the elastic moduli and $\epsilon(x)$ is the axial strain at a distance x. The subscripts c and r refer to concrete and reinforcement, respectively. Finally, the equilibrium equation for the block shown in Figure 6.1(b) reads:

$$P = \sigma_r(x) A_r + \sigma_c(x) A_c \tag{6.6}$$

The first and second derivatives of Equation 6.3 read:

$$\frac{ds(x)}{dx} = \epsilon_r(x) - \epsilon_c(x) \tag{6.7}$$

$$\frac{d^2 s(x)}{dx^2} = \frac{d\epsilon_r(x)}{dx} - \frac{d\epsilon_c(x)}{dx} \tag{6.8}$$

Substituting Equations 6.4 and 6.5 into Equation 6.8, yields:

$$\frac{d^2 s(x)}{dx^2} = \frac{dF_r(x)}{E_r A_r dx} - \frac{dF_c(x)}{E_c A_c dx} \tag{6.9}$$

Substituting the value of $\frac{dF_r(x)}{dx}$ and $\frac{dF_c(x)}{dx}$, derived from Equations 6.1 and 6.2, into Equation 6.9 results in:

$$\frac{d^2 s(x)}{dx^2} = \frac{\tau(x) p_r}{A_r E_r} (1 + n\rho) \tag{6.10}$$

Equation 6.10 is a differential equation with two unknown functions, $\tau(x)$ and $s(x)$ that are related through the bond-slip relationship.

6.2.1 Analytical solution for B.E.P. bond-slip law

In this section, the differential equation (Equation 6.10) is solved assuming a bond-slip law equal to the ascending branch of the B.E.P. bond-slip law [42] (Section 2.3.6), shown next:

$$\tau = \tau_m \left(\frac{s}{s_m} \right)^{\alpha} \tag{6.11}$$

Substituting Equation 6.11 into Equation 6.10 yields:

$$\frac{d^2 s(x)}{dx^2} = \frac{(1+n\rho)\, p_r}{A_r E_r} \frac{\tau_m}{s_m^\alpha} s^\alpha \tag{6.12}$$

Boundary conditions are needed to solve Equation 6.12. Therefore, the physical behaviour taking place in a concrete block between two cracks is hereafter explained with the help of Figure 6.2, with the origin of the x-axis at the midway section between two cracks.

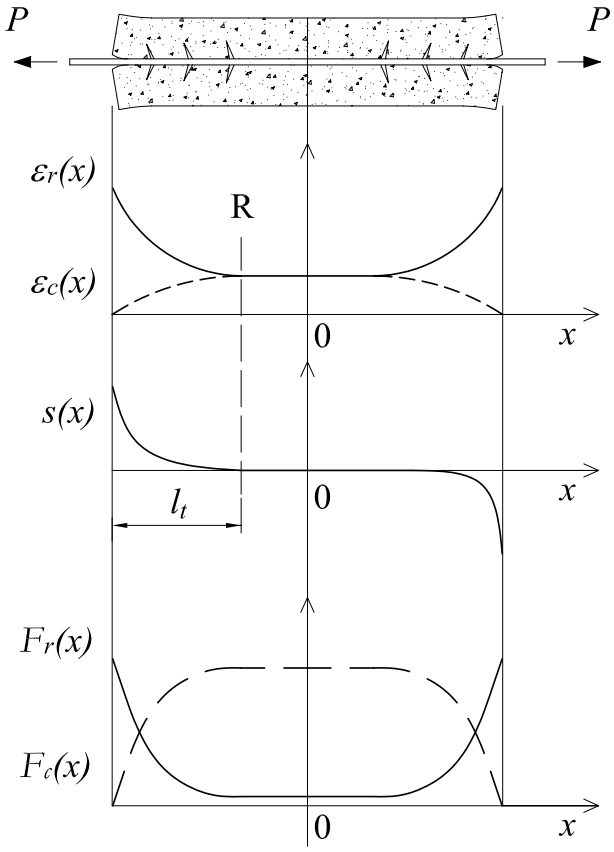

Figure 6.2: Strain, slip and load distribution along a concrete block.

A tie subjected to a tensile load P lower than the firs-cracking load P_{crack} is considered. At the end faces, assumed to behave as crack faces, the reinforcement takes the entire tensile force whilst concrete carries no tension. Due to bond effects, forces are transferred from reinforcement to concrete through the transfer length l_t. This force transfer ends with concrete strain becoming equal to reinforcement strain at

a section R. From this section on, composite action ensures both strains remaining constant, and equal to their common value, along the remaining length of the half-member. At this point, two different situations are possible: if both strains become equal at a section inside the half-member length, composite action can be assured from R section to the midway section. Contrariwise, the reinforcement strain will be larger than the concrete strain if this fictitious R section falls outside the half concrete block.

The differences in physical behaviour are described with different boundary conditions, and therefore, different solutions of the differential equation (Equation 6.12) are expected. Henceforth, the analytical solution for the case when composite action is possible (i.e. when R section falls inside the half concrete block) is derived. The derivation of the solution for cases where composite action is not possible implies a higher mathematical handling, which is not the aim of this dissertation.

The solution of the cases where composite action is possible is obtained through the solution of the limit case when R section falls at midway section between two cracks. The assumed situation (Figure 6.3) is described with the following boundary conditions: $s(0)$=0 and s'(0)=0. If these conditions are assumed, the final solution of Equation 6.12 is:

$$s(x) = \left[\frac{\tau_m p_r \left(1 + n\rho\right)}{2 A_r E_r s_m^{\alpha}} \frac{\left(1-\alpha\right)^2}{\left(1+\alpha\right)} \right]^{\frac{1}{1-\alpha}} x^{\frac{2}{1-\alpha}} \tag{6.13}$$

Back to the equilibrium equation for the reinforcement (Equation 6.2), the tensile stress in reinforcement at any position along the tie can be defined as:

$$\frac{d\sigma_r(x)}{dx} = \frac{\tau_m p_r}{A_r s_m^{\alpha}} s(x)^{\alpha} \tag{6.14}$$

Substituting Equation 6.13 into Equation 6.14 and integrating, the tensile stress in reinforcement along the x-axis can be expressed as:

$$\sigma_r(x) = K_a x^{\frac{(1+\alpha)}{1-\alpha}} + C \tag{6.15}$$

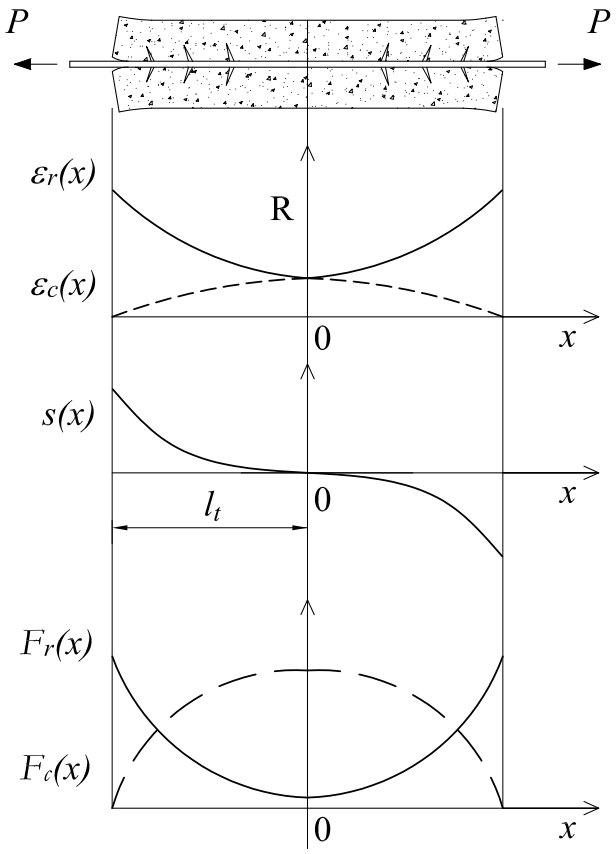

Figure 6.3: Strain, slip and load distribution with R at midway section.

where K_a is a constant coupling the mechanical and geometrical characteristics of the reinforced concrete tie and the shape of the bond-slip curve:

$$K_a = \left(\frac{\tau_m p_r}{A_r s_m^{\alpha}}\right)\left[\frac{\tau_m p_r\,(1+n\rho)}{2E_r A_r s_m^{\alpha}}\frac{(1-\alpha)^2}{(1+\alpha)}\right]^{\frac{\alpha}{(1-\alpha)}}\left(\frac{1-\alpha}{1+\alpha}\right) \tag{6.16}$$

Evaluating Equation 6.15 for x=0 sets the value of the integration constant C of Equation 6.15.

$$C = \frac{nP_{crack}}{A_c(1+n\rho)} = nf_{ct} \tag{6.17}$$

In a similar way, the concrete stress distribution can be also obtained. Moreover, concrete and reinforcement strain distribution, ϵ_c(x) and ϵ_r(x), can be derived through the materials' constitutive equations (Equations 6.4-6.5).

Equations 6.13 and 6.15 have been deduced for the limit situation of section R falling at midway section between two cracks. In the case of section R falling inside the half-member length, composite action is assured along the remaining length of the half-member, with s=0 and $\epsilon_r = \epsilon_c = \epsilon_{comp} = \frac{P}{A_c E_c (1+n\rho)}$. Moreover, solving Equation 6.15 for $\sigma_r = \frac{P_{crack}}{A_r}$, the transfer length reads:

$$l_t = \left(\frac{P_{crack}}{A_r(1+n\rho)} \frac{1}{K_a} \right)^{\left(\frac{1-\alpha}{1+\alpha}\right)} \tag{6.18}$$

However, although finding the solution for the differential equation gives the exact distribution of slip, stresses and strains along the tie, it is not always possible to analytically solve the problem. In fact, the exact solution of the bond problem has only been previously presented for those cases assuming a constant bond-slip law [67, 74] a linearly dependent bond-slip law [74, 77, 79] or a bond-slip law equal to that of the ascending branch of the MC90 [75]. Therefore, for a general bond-slip law, a numerical procedure is needed to solve the stress distribution along the cracked member.

6.2.2 Proposed numerical approach

The rational derivation of the differential equation that governs the bond problem has been introduced in section 6.2.1. Depending on the complexity of the bond-slip law, a straightforward solution of the differential equation is not always possible. As an alternative, a mathematical non-linear model based on existing previous works [80, 81, 96] is presented in this section.

Numerical procedure

The mathematical solving procedure is presented next with the help of Figures 6.2 to 6.9, with the origin of the x-axis at the midway section between two cracks, and L_B defined as half length of the concrete block studied.

The stress and strain conditions of a reinforced concrete tie before first cracking can be modelled as the reinforced concrete block shown in Figure 6.2. As far as the tensile load applied P is lower than the first-cracking load, and assuming that

the transfer length is lower than half the length of the tie, composite action between midway section and section R is assured. As load is increased, concrete strain increases up to a point where the concrete tensile strength is reached. Due to non-homogeneity in concrete material, crack can appear in any section between section R and the halfway section.

Within the numerical procedure presented, the following assumptions have been considered:

- Concrete tensile strength f_{ct} is assumed to be constant along the reinforced tie.
- Cracks appear always at the halfway section between two cracks.
- No damaged length next to the crack section has been introduced to account for bond deterioration at the crack section (i.e. bond forces start to act from the very beginning after cracked section).

The tie is subdivided in n discrete elements with small length Δx. The procedure starts at the cracking load level $P = P_{crack}$, when concrete tensile strength f_{ct} has been reached (see Figure 6.4). Stress and strain at the halfway section are evaluated by equilibrium equation (Equation 6.6) and imposing symmetry conditions. Using Equations 6.2, 6.7 and 6.6, the stress and stain distributions at the end of the first subinterval of length Δx measured from the halfway section are obtained. The procedure is extended to every contiguous discrete element and the condition of σ_c=0 at x=L_B is imposed. With the help of this condition, reinforcement and concrete stress distribution are found and respective strain distributions are computed as $\epsilon_r(x) = \frac{\sigma_r(x)}{E_{FRP}}$ and $\epsilon_c(x) = \frac{\sigma_c(x)}{E_c}$.

Based on the comparison of the reinforcement strain values at each subinterval, the transfer length, l_t is computed and compared to L_B. At this point, two cases can be found. If $l_t \leq L_B$ /2 a new crack appears and composite action is still assured in the two new blocks (Figure 6.5). Therefore, new cracking will again take place at each concrete block without any increase in the applied load P (Figure 6.6). However, going back to Figure 6.4, if $l_t > L_B$ /2 a new crack forms but composite

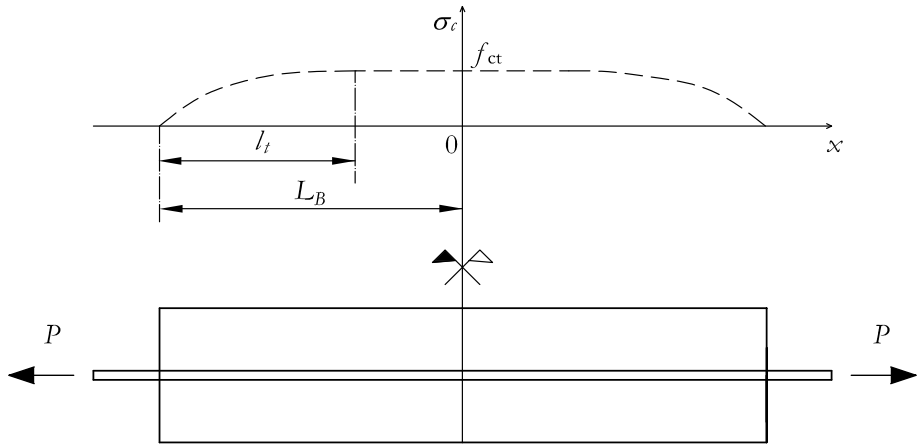

Figure 6.4: Concrete stress distribution when f_{ct} attained at midway section (unknown l_t).

action is no longer assured in the two new blocks (Figure 6.7).

Whichever the case, a situation where the tie is defined through a number of identical concrete blocks, with no possible composite action and whose maximum concrete stress does not attain f_{ct}, is achieved. Therefore, further analysis is conducted on a representative block and the complete stress and strain distributions will be formed through concatenation of concrete blocks' results.

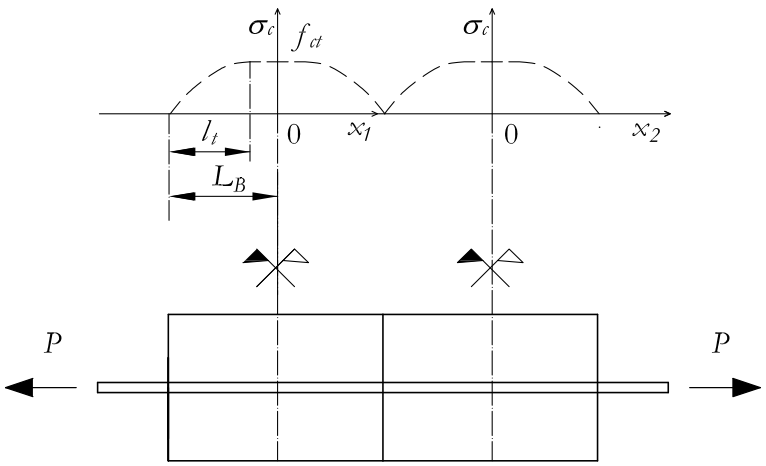

Figure 6.5: Tie divided in two concrete blocks with active composite action.

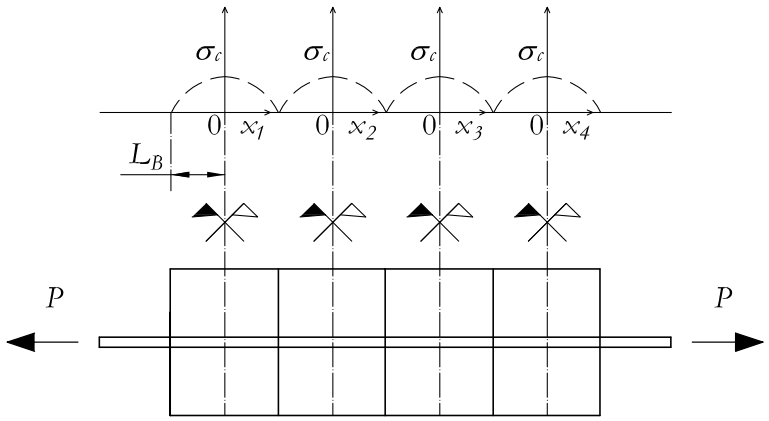

Figure 6.6: Tie divided in four concrete blocks without composite action.

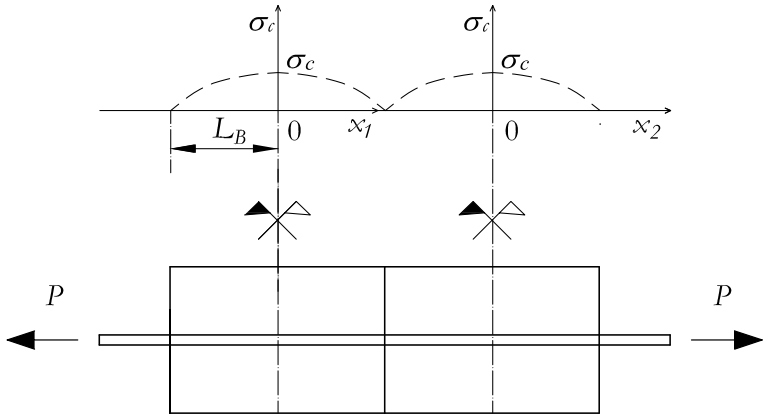

Figure 6.7: Tie divided in two concrete blocks without composite action.

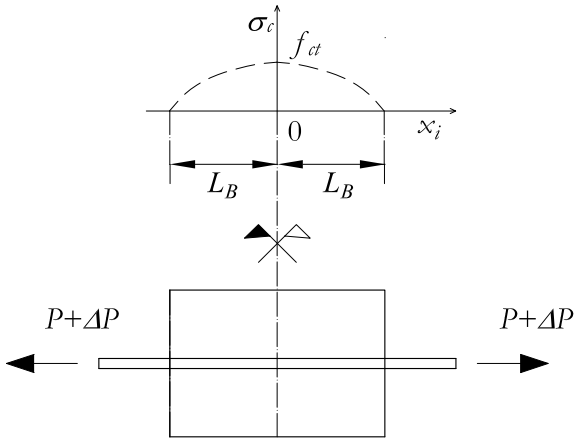

Figure 6.8: Representative concrete block at maximum crack spacing configuration.

For each concrete block, the new origin is located at the halfway section and L_B is updated to represent concrete block half length. From this point on, load is further increased until σ_c reaches the concrete tensile strength f_{ct} (see Figure 6.8). During this process the block between two cracks is called to be in a transient state. Stress and strain conditions are as follows: the slip is zero in the halfway section between the cracks (x_i=0) where concrete tensile strength has been reached. At a distance x=L_B, the tensile strain in concrete is zero. ΔP represents the new unknown increment of applied load P to calculate. This cracking configuration represents maximum crack spacing configuration.

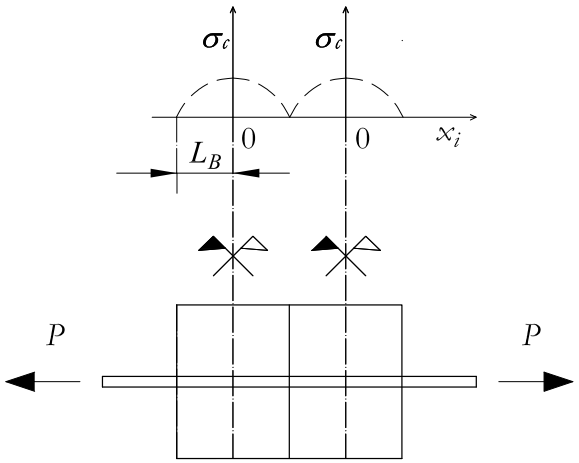

Figure 6.9: Representative concrete block at minimum crack spacing configuration

Once f_{ct} is reached at half section of the concrete block, a new crack forms (Figure 6.9). Therefore, new origin for x axis is defined and new value for L_B is assigned. This cracking configuration represents minimum crack spacing configuration. From this situation on, an alternative iteration between situations in Figures 6.8 and 6.9 will take place. The reinforcement average strain ϵ_m is evaluated as:

$$\epsilon_m = \frac{1}{L_B} \int_0^{L_B} \epsilon_r(x) dx \tag{6.19}$$

Due to the simplification of the model for cracks appearing always at the midway section between two cracks, once a cracking configuration is reached, crack will appear at all the existing concrete blocks. Therefore, the appearance of cracks will happen as shown in Figure 6.10.

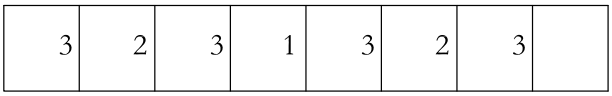

Figure 6.10: Correspondence between crack formation numbering and final crack pattern.

The steps of the complete algorithm are presented in detailed in the flow diagram shown in Figure 6.11. Two subroutines referred as LMAX.m and LMIN.m are used to compute for the situations described in Figures 6.8 and 6.9, respectively. The internal steps of these two subroutines are shown in Figure 6.12 and 6.13.

Some comments on presented flow diagrams are:

- In the main algorithm, presented in Figure 6.11, the computation of transfer length, l_t, is needed to determine whether an increase of load is needed to cause second cracking or not. Therefore, the transfer length will determine the number of cracks that suddenly appear at P_{crack}. Transfer length is defined as the distance between crack section where the whole load is applied to reinforcement, and the section where the composite action is recovered (i.e. where concrete strain equals reinforcement strain). Therefore, based on reinforcement strain profile, the transfer length is the distance between the section where $\epsilon_r = \frac{P}{A_r E_r}$ and the section where $\epsilon_r = \frac{P}{A_c E_c (1+n\rho)}$, hereafter referred to as ϵ_{ro} and ϵ_{comp}, respectively. Based on these two limit conditions, once the reinforcement strain profile has been determined after first cracking, the numerical model defines a tolerance $TOL1$ and compares the values of reinforcement strain at each subinterval. The transfer length is computed as the distance between the crack face and the first section where $\frac{\epsilon_r(x_i) - \epsilon_r(x_{i-1})}{\epsilon_{comp}} \leq TOL1$ holds true.

- Further cracking possibility is checked with a deformability criteria through reinforcement strain where, if $\epsilon_m > K_1 \epsilon_{crack}$, no more cracks will be allowed to appear and the model will be stopped.

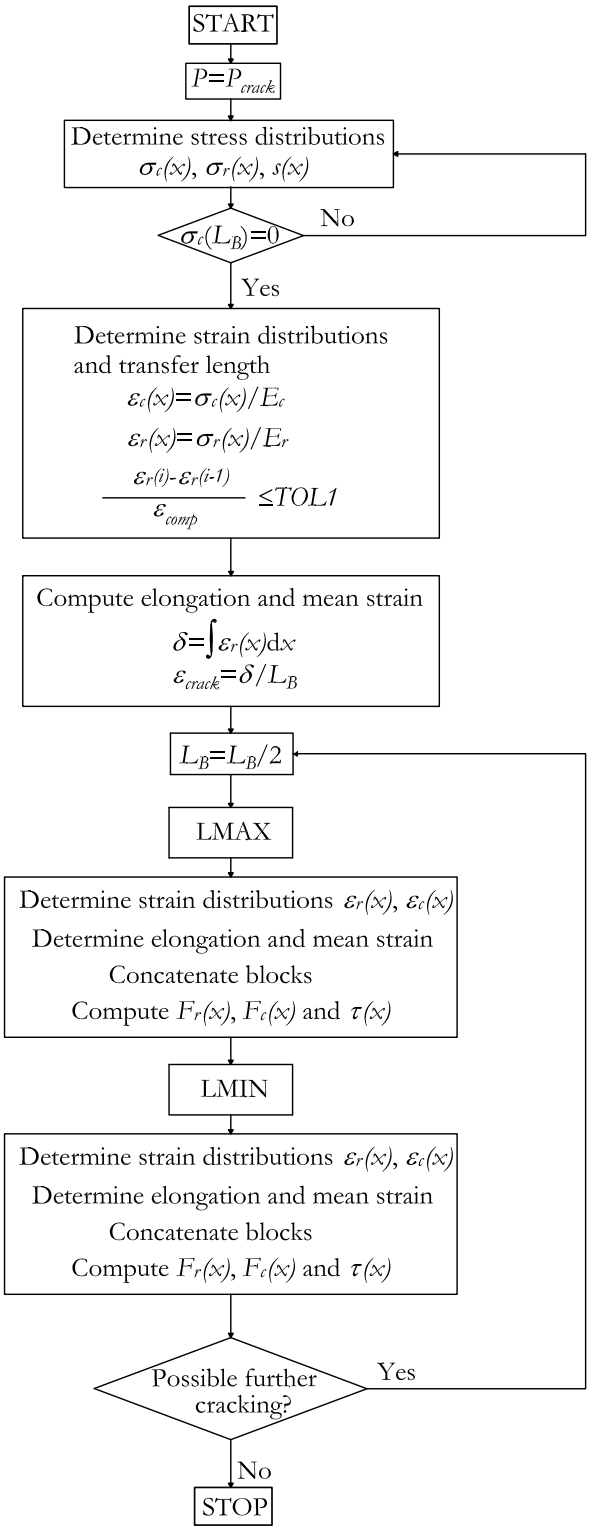

Figure 6.11: Outline of solution algorithm.

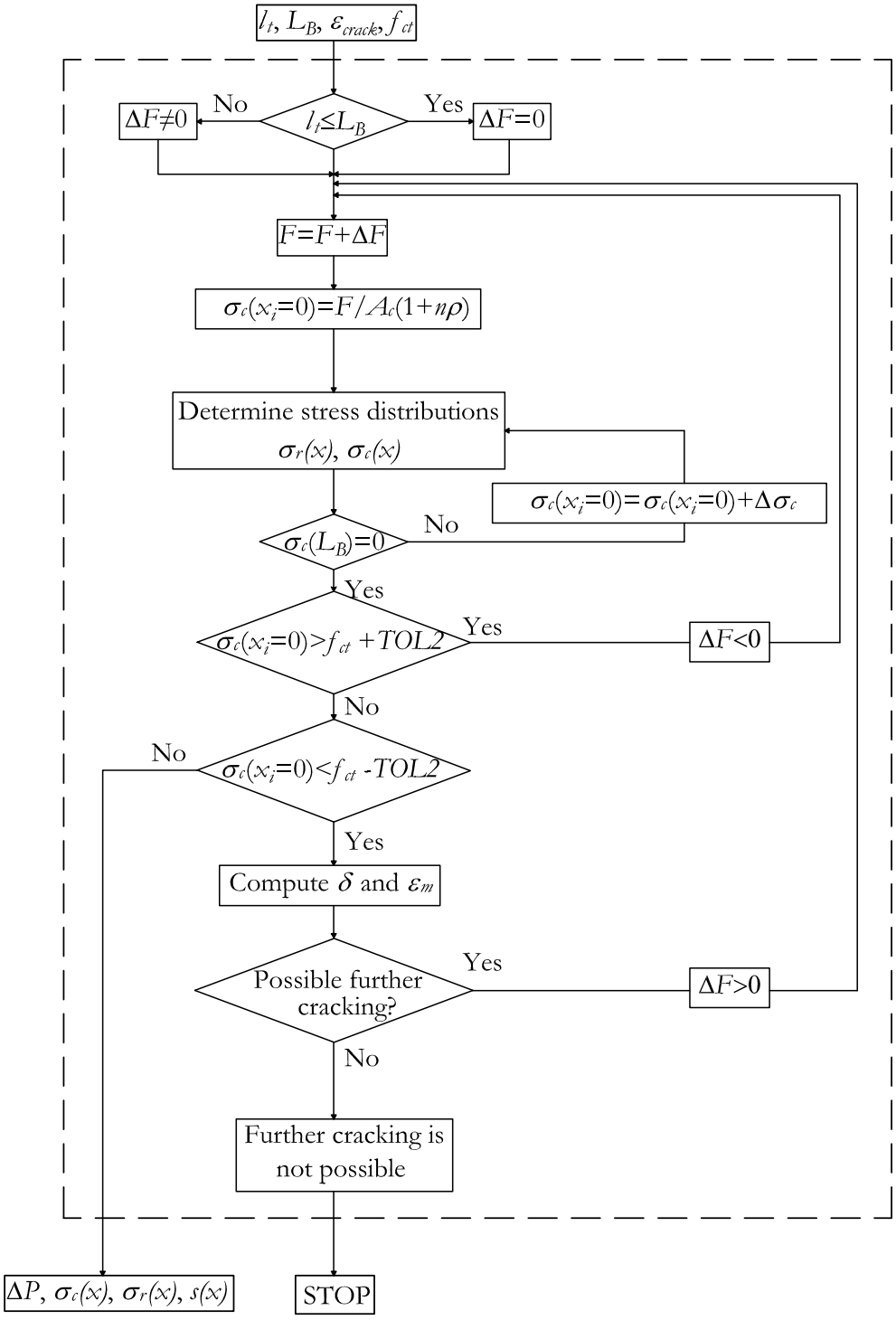

Figure 6.12: Outline of subroutine LMAX.m algorithm.

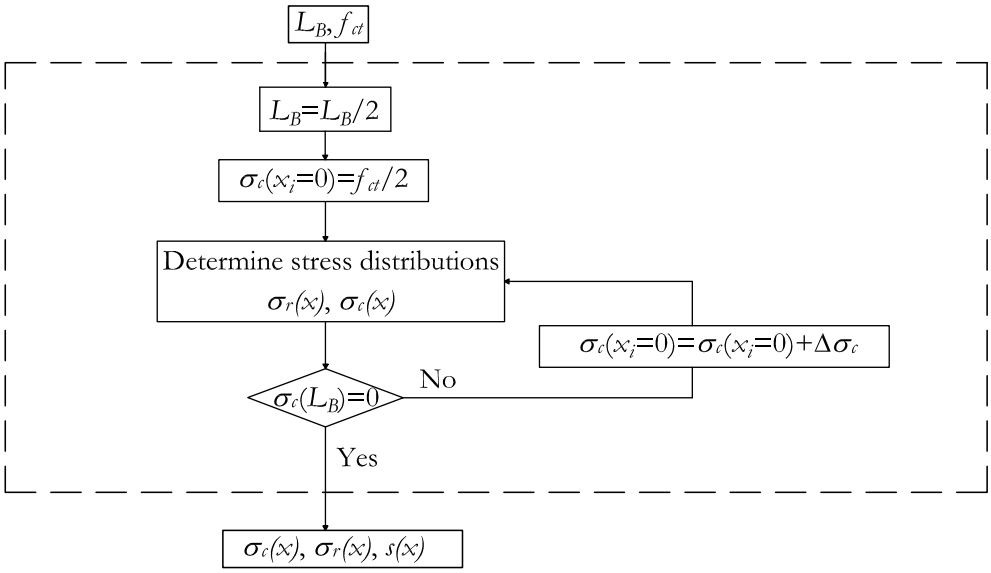

Figure 6.13: Outline of subroutine LMIN.m algorithm.

- In LMAX.m subroutine, presented in Figure 6.12, a tolerance is applied to check whether the concrete tensile strength, f_{ct}, has been attained or not at the halfway section. The value of the tolerance is $TOL2$.

6.3 Validation of the numerical procedure

The numerical procedure presented in Section 6.2.2 is henceforth validated by comparing the results obtained in an analytical study which uses the equations presented in Section 6.2.1 and experimental results obtained in the experimental program on FRP RC ties presented in Chapter 5.

6.3.1 Comparison between numerical and analytical results

In this section, the numerical model is validated through comparison with analytical results. To this end, the analytical solution of the differential equation with an assumed bond-slip law equal to the ascending branch of the B.E.P. model (previously presented in Equation 6.12) is compared to the numerical solution with the same bond-slip law (Equation 6.11) included in the numerical model.

The length of the RC tie to be modeled in the validation procedure is 1200mm. A GFRP reinforcing bar with d_b=12mm and E_{FRP}=38000MPa is used, and the concrete square section is 100×100mm. The characteristic compressive strength of concrete, f_{ck}, is assumed to be 25MPa; the mean axial tensile strength, f_{ctm}=2.565MPa, and the secant modulus of elasticity, E_{cm}=31.48GPa, are estimated according to EC2-04 [9] (Equations 6.20, 6.21 and 6.22). According to MC-90 [5], the characteristic bond-slip law values are assumed as follows: α=0.4, s_m=1 and τ_m=12.5MPa according to Equation 6.23.

$$f_{cm} = f_{ck} + 8 \tag{6.20}$$

$$f_{ctm} = 0.30\,(f_{ck})^{\frac{2}{3}} \tag{6.21}$$

$$E_{cm} = 22\left(\frac{f_{cm}}{10}\right)^{0.3} \tag{6.22}$$

$$\tau_m = 2.5\,(f_{ck})^{0.5} \tag{6.23}$$

The comparison between analytical and numerical results is done at three different loading levels (P=7, 14 and 21kN), all of them being lower than the cracking load P_{crack}. Numerical results on reinforcement strain distribution are compared in Figure 6.14(a) with analytical results obtained through stress distribution from Equation 6.15. Similarly, in Figure 6.14(b), the numerical distribution of the slip is compared to the analytical expression (Equation 6.13). An additional comparison is presented in Figure 6.15 for a tensile load equal to the first cracking load P_{crack}. The reinforcement strain distribution and the slip distribution are compared at both the pre and post-cracking situations.

The good agreement indicates that prediction on either reinforcement or concrete strain distribution, as well as slip distribution, using the presented numerical procedure is reliable. Moreover, the composite action still active in the stable situation after first cracking, shown in Figures 6.15(a) and 6.15(b), allows the second cracking occurring for the same load level, with no additional load required. However, the results for this second cracking are not shown because the analytical solution could

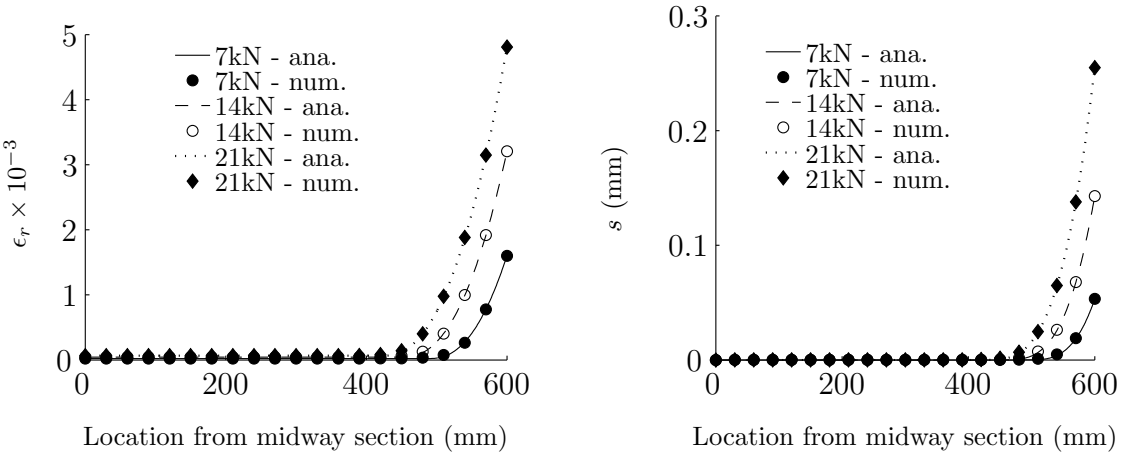

(a) Reinforcement strain (b) Rebar slip

Figure 6.14: Comparison between numerical and analytical results at three load levels lower than P_{crack}.

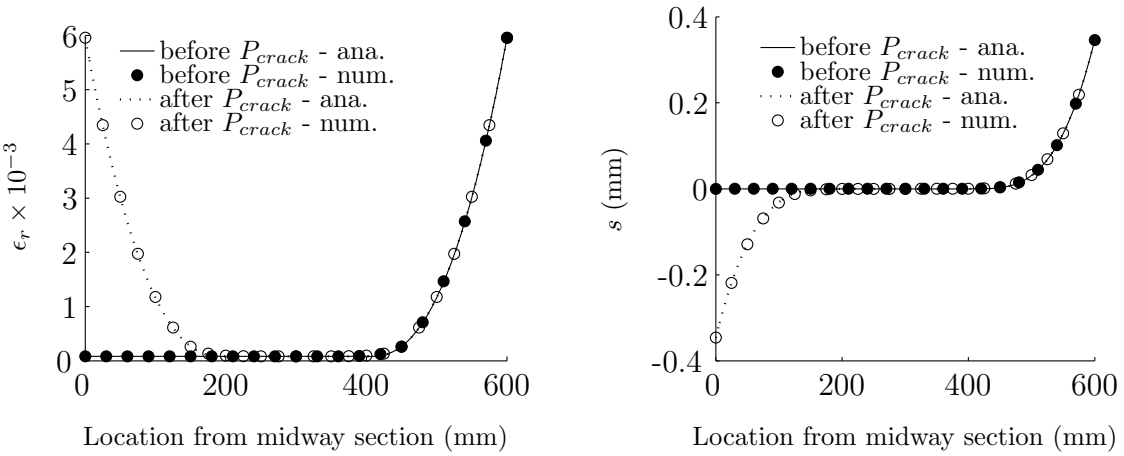

(a) Reinforcement strain (b) Rebar slip

Figure 6.15: Comparison between numerical and analytical results at cracking load level. Results are presented for the unstable state before cracking and for the stable one after cracking.

only be derived for the case when composite action is present.

The results confirm the validity of the presented numerical procedure to model how the bond behaviour affects the pre and post-cracking structural behaviour of reinforced concrete members. Therefore, once the bond-slip law related to the specific

reinforcing rebar is known, proper estimations on the behaviour of the reinforced concrete tie can be obtained.

6.3.2 Comparison between numerical and experimental results

The numerical approach is further validated with experimental results obtained in RC tensile tests. To this end, a first validation through reinforcement strain distribution obtained from a specially strain gauged notched tie is presented. Further on, numerical predictions on the tensile behaviour of RC ties are compared to experimental results and code predictions.

Results on reinforcement strain distribution

The numerical procedure is further validated through the comparison with experimental results on reinforcement strain profile. In Chapter 5, experimental results on two RC notched ties (referred to as 19-170-N and 16-170-3N) have been presented, where an special internally strain gauged rebar was used. The proposed instrumentation allowed to study the evolution of reinforcement strain distribution along the whole loading procedure. In this section, specimen 16-170-3N has been considered due to its more regular crack pattern. Accordingly, the geometrical and mechanical properties of tie 16-170-3N have been considered in the numerical simulation.

Due to inevitable scatter in concrete tensile strength, the pre-cracks opened in the chronological order shown in Figure 6.16. Therefore, to better compare numerical and experimental results, and to avoid random cracks distribution, the onset of the first, second and third crack are triggered in numerical simulation in keeping with the test results.

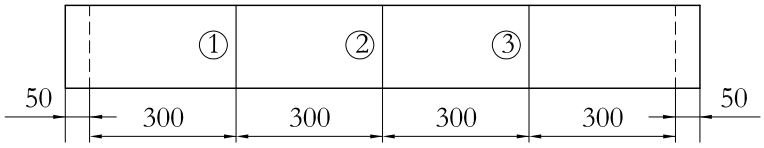

Figure 6.16: Experimental transverse cracks numbered according to appearance order.

Bond-slip law. Pull-out tests on GFRP rebars that were nominally equal to those used in the notched RC ties were performed. Results on these tests have been reported in Chapter 4. According to these results, different bond-slip laws were obtained for the loaded and unloaded end. Therefore, in the validation of the numerical procedure, simulations with experimental bond-slip relationships for the loaded and unloaded end (hereafter referred to as BSLE and BSUE, respectively) have been considered. However, although bond-slip laws obtained from pull-out tests represent the whole loading procedure, only the data up to the peak bond value has been necessary (see Figure 6.17).

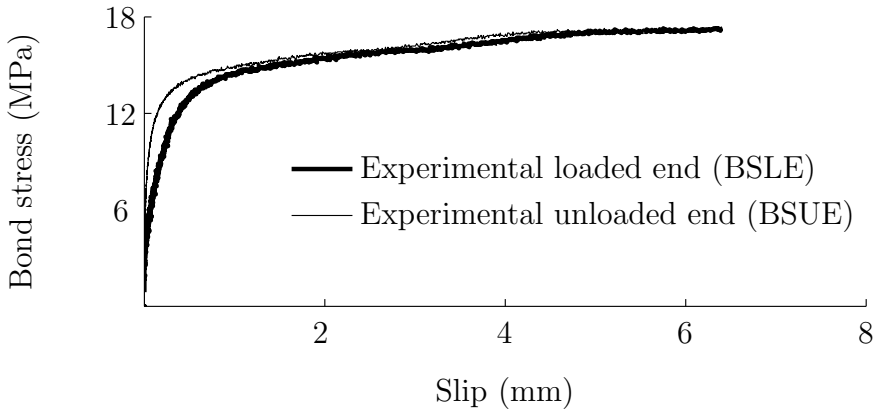

Figure 6.17: Experimental bond-slip law derived from pull-out test and considered in the validation of the numerical procedure.

In Figures 6.18-6.20, the reinforcement strain distributions along the tie obtained from the numerical simulations and the laboratory tests are compared. Numerical and experimental data are compared at loading levels causing first, second and third transverse crack formation (P=20.63, 26.73 and 35.16kN, respectively). At each load level, the reinforcement strain distributions active both before and after crack formation are shown. The presence of the new crack is reflected with a new peak in reinforcement strain distribution at new cracked section.

Close numerical strain distributions are obtained with both bond-slip laws (see Figures 6.17-6.20). However, numerical predictions with the loaded end bond-slip law (i.e. BSLE law) fall closer to experimental results than those obtained with

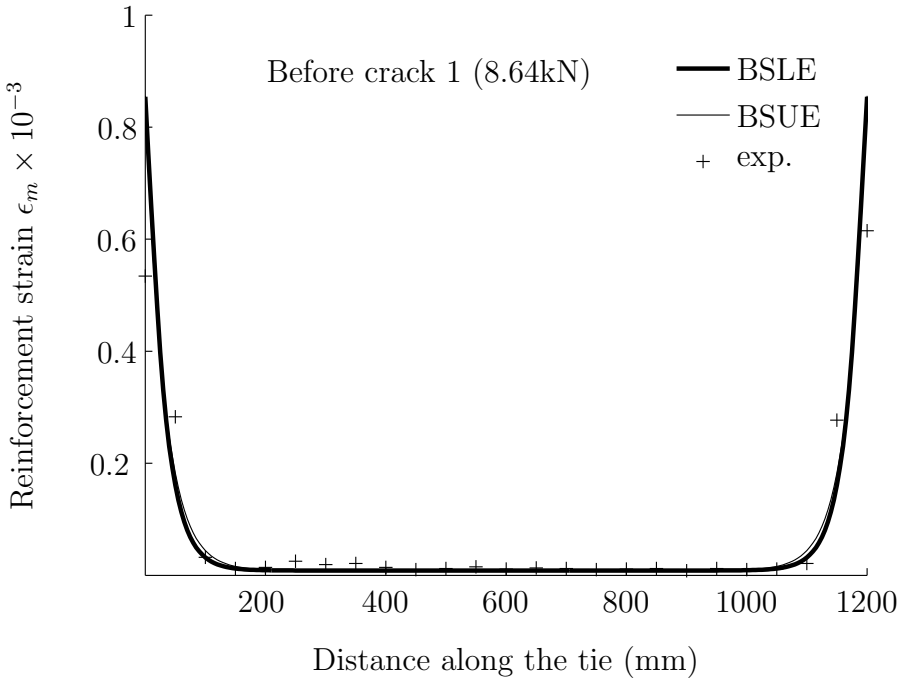

(a)

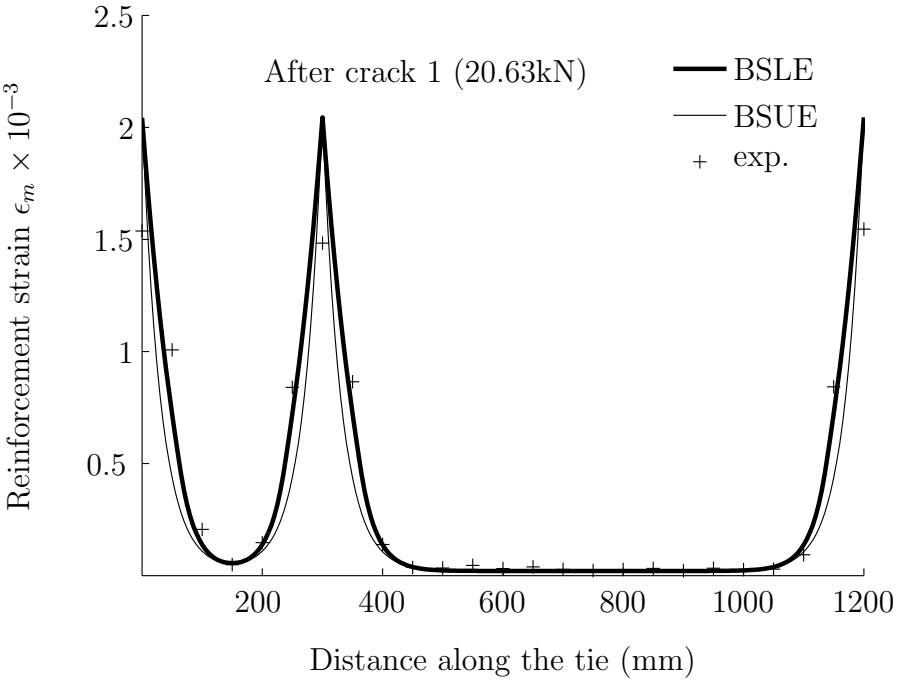

(b)

Figure 6.18: Comparison between numerical and experimental results on reinforcement strain (a) before and (b) after first transverse crack formation.

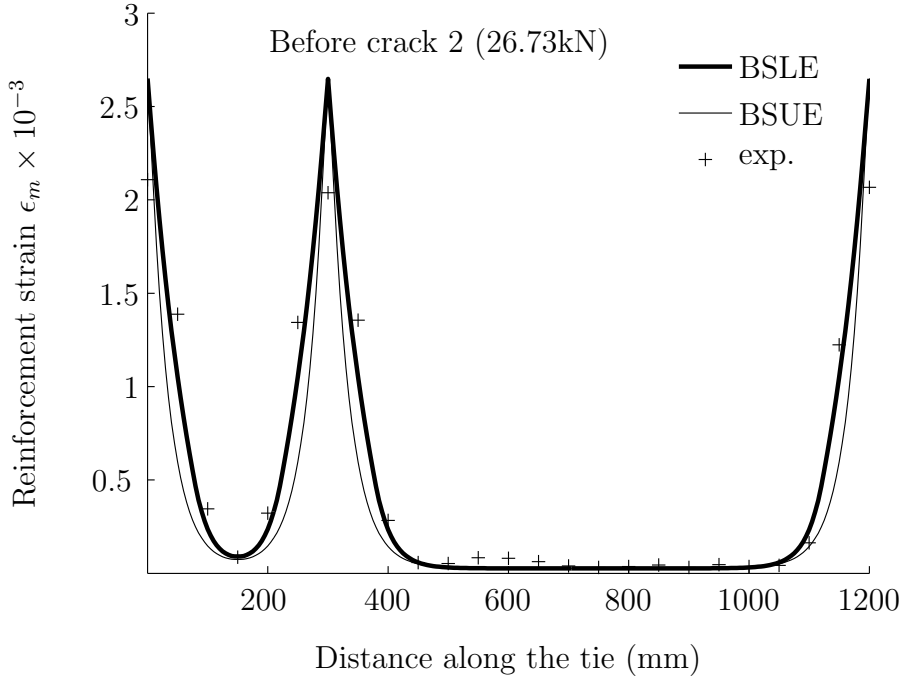

(a)

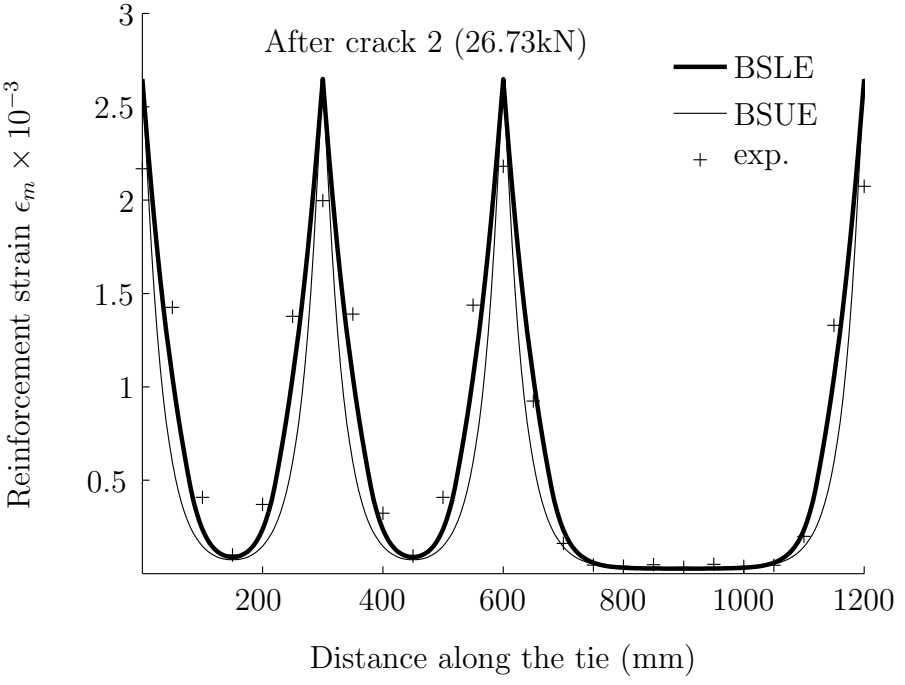

(b)

Figure 6.19: Comparison between numerical and experimental results on reinforcement strain (a) before and (b) after second transverse crack formation.

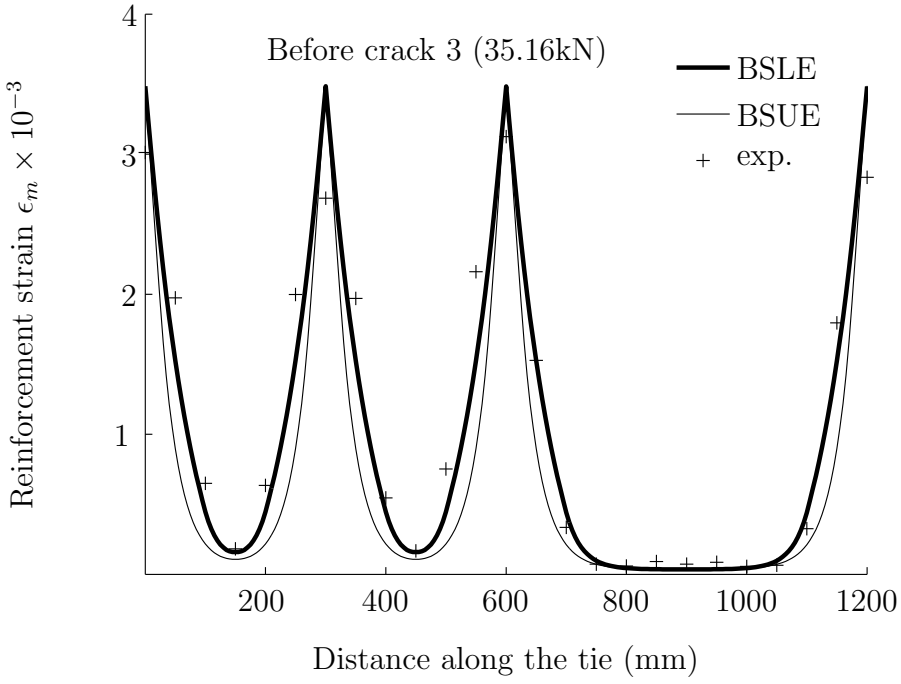

(a)

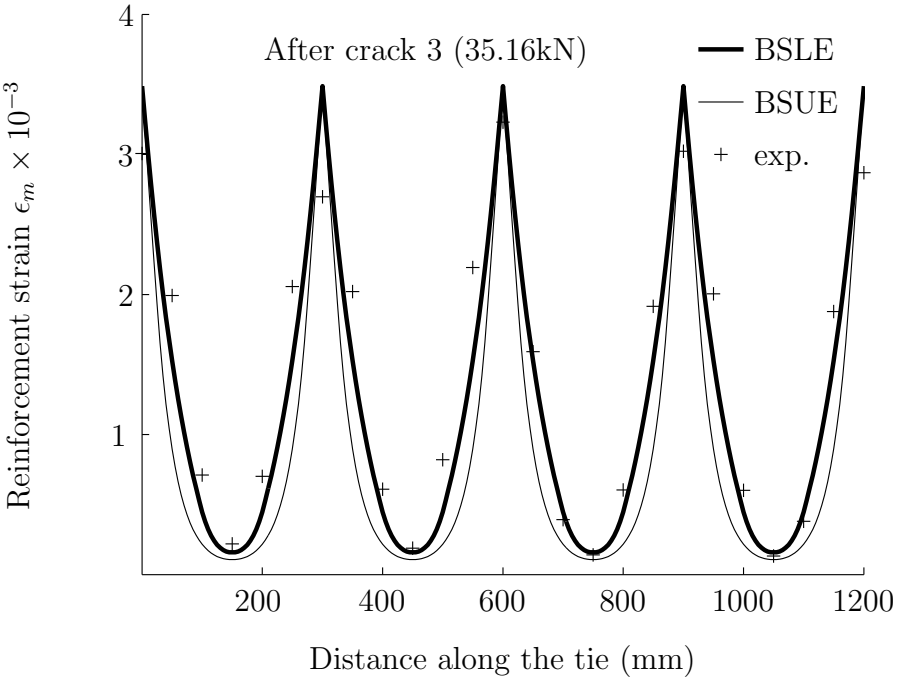

(b)

Figure 6.20: Comparison between numerical and experimental results on reinforcement strain (a) before and (b) after third transverse crack formation.

BSUE law. The agreement between numerical predictions and experimental data proves the validity of the proposed method to predict the contribution of each component (reinforcement and concrete) before and after cracking, therefore describing satisfactory the cracking behaviour in RC tensile members.

Although no experimental slip data is available, slip distributions obtained from numerical simulation are shown in Figures 6.21-6.23. The main visible difference arises in the maximum slip value attained at cracked sections. Because of the lower stiffness of the BSLE bond-slip law (see Figure 6.17), higher slips are obtained with BSLE simulation. Besides, numerical results confirms that although bond tests are normally performed until complete bond failure is observed at relative high slips (around 20-30mm), little slips arise in a RC tensile test and no use of the unloading branch of the bond-slip law is made.

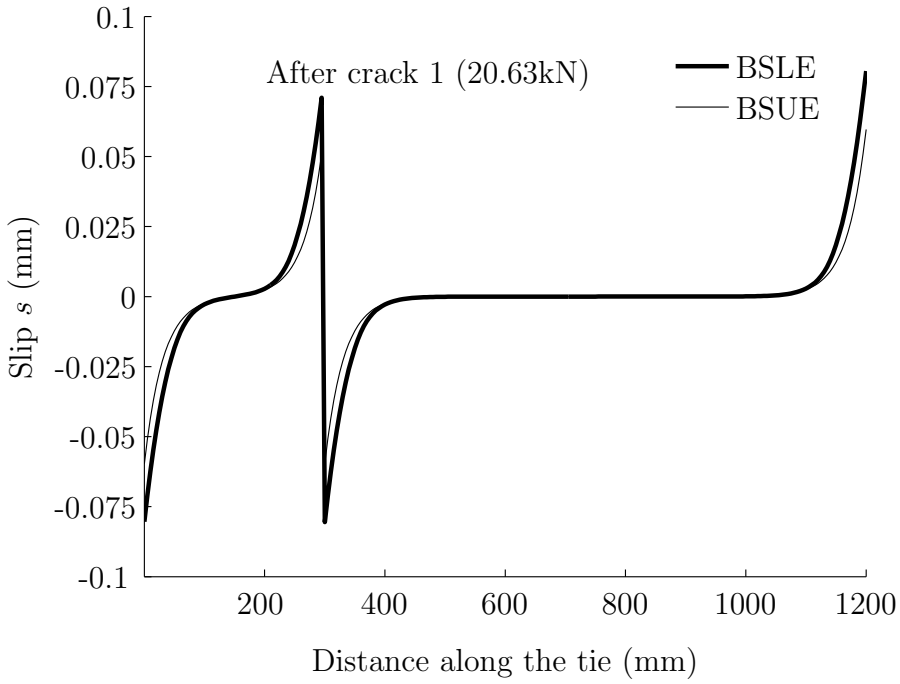

Figure 6.21: Numerical slip distributions at first cracking.

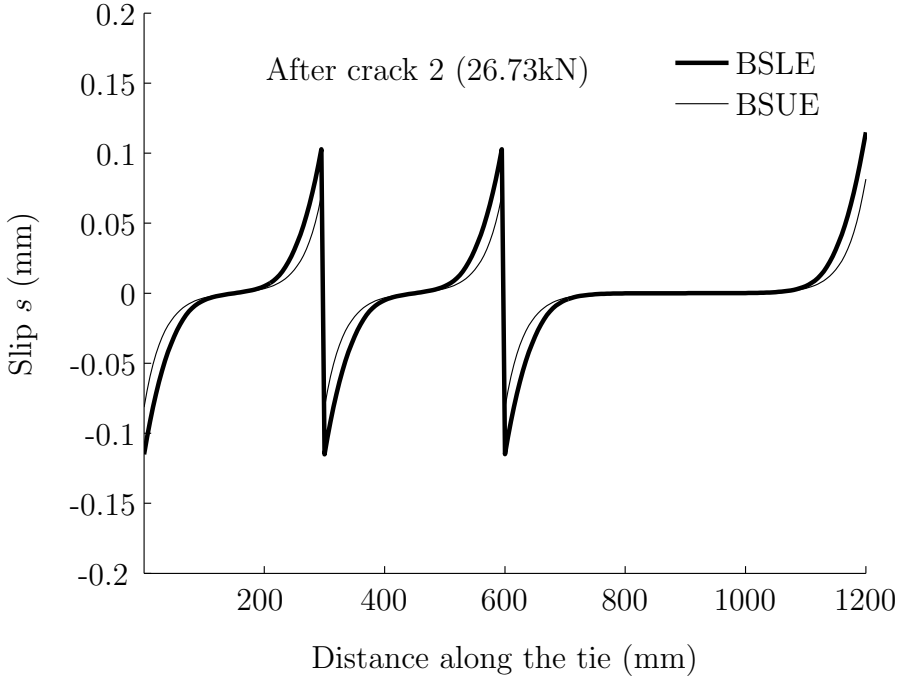

Figure 6.22: Numerical slip distributions at second cracking.

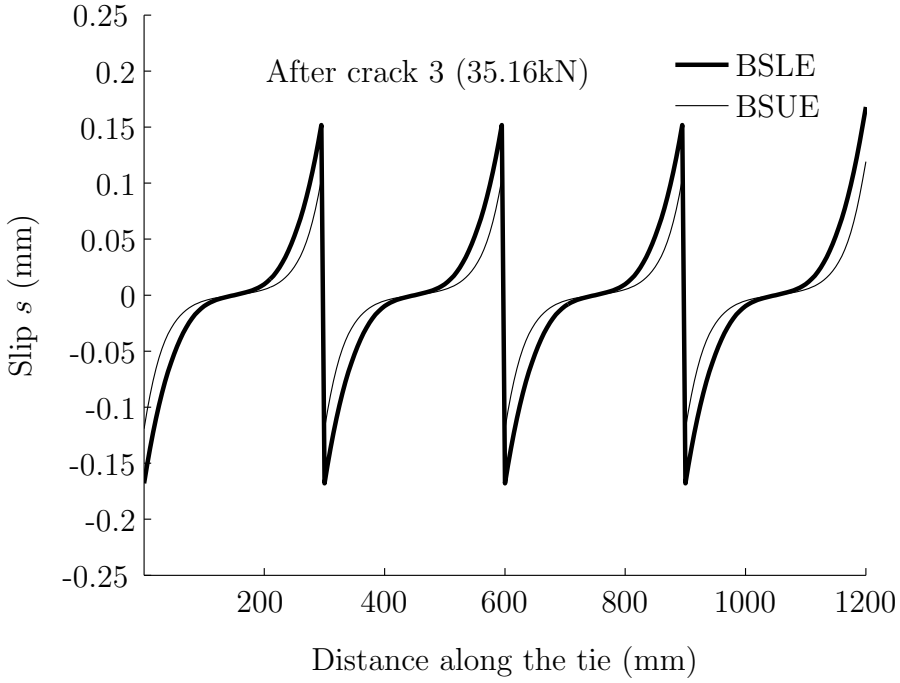

Figure 6.23: Numerical slip distributions at third cracking.

Results on tie tensile behaviour

Once the numerical model has been proven to be valid on describing the local behaviour of RC ties, the model validity on predicting the global behaviour is further validated through comparison between experimental and numerically predicted global RC ties tensile responses. The numerical model is used to simulate RC ties described and analyzed in Chapter 5. Similar to predictions of reinforcement strain distribution presented in previous section, the bond-slip laws used in the numerical predictions of the global tensile behaviour have been obtained from the experimental campaign on pull-out tests performed in this dissertation, whose results are presented in Chapter 4.

The characteristic form of the load-mean strain relationship of a RC tie obtained through the numerical model previously presented is described in Figure 6.24. After the initial branch with no cracks, concrete tensile strength is reached at P_{crack} and the first crack is about to appear. The opening of the crack is followed with an increase in the mean tie strain. Under load control test, an horizonal line in the $P-\epsilon_m$ curve is obtained (see Figure 6.24). After the first crack has formed, the load can increase until the tensile stress in concrete between two cracks reaches again the concrete tensile strength. This new points is unstable and next cracks can form in every midway section between previously existing cracks. Again an horizontal line depicts the opening of cracks. This pattern in $P-\epsilon_m$ behaviour is further repeated until no more cracks can form.

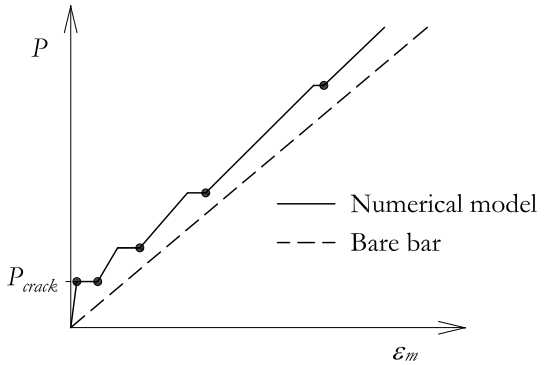

Figure 6.24: Numerically derived $P-\epsilon_m$ relationship.

For a given cracking load two different mean strains are possible, which are

related to the pre and post crack opening. In Figure 6.24, points that define the post crack opening situation are highlighted. These points will be used in the parametric study presented in the following section to qualitative define a conservative tension stiffening effect.

In Figures 6.25-6.28 the comparison of numerical predictions on member tensile behaviour with experimental responses is shown. Moreover, EC-2 predictions (Equation 5.6) with bond coefficient limit values are also plotted. A large plateau after P_{crack} is observed in the numerical predictions. This plateau is related to the multicrack formation that takes place at P_{crack} when the transfer length, l_t, is shorter than $L/4$, where L reads for the total length of the tie, and more than one crack can form. This multicracking is therefore responsible of a significant underestimation of the tension stiffening effect at early cracking stages. Although the assumptions of constant concrete tensile strength along the RC tie and crack formation prefixed at midway section between two existing cracks, numerical predictions follow the general trends of the experimental results (Figures 6.25-6.28) and set a range of possible responses of the tie that fits with limit responses obtained in EC-2 predictions.

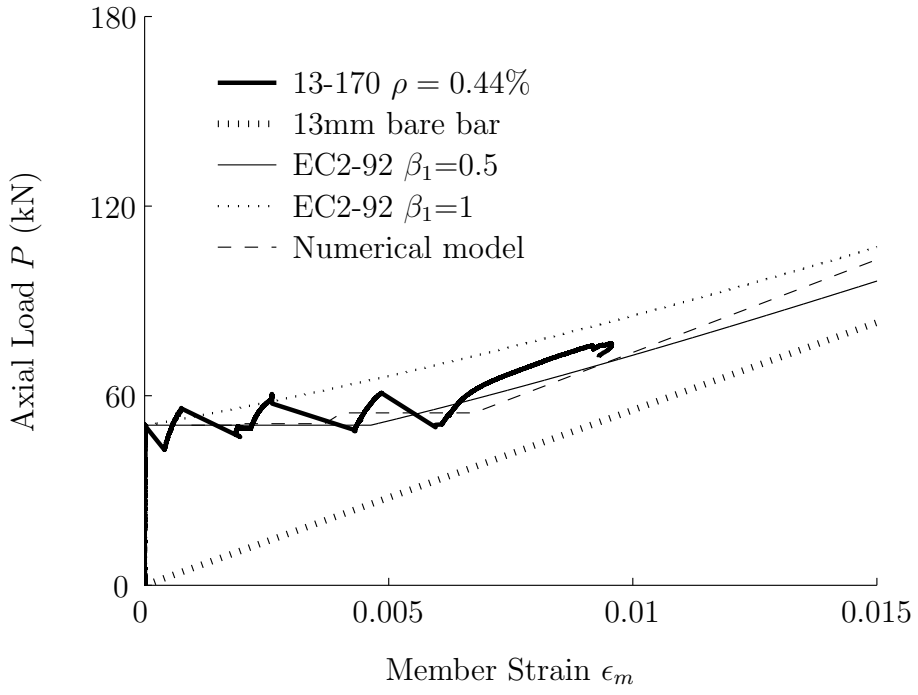

Figure 6.25: Numerical prediction on 13-170 tensile behaviour.

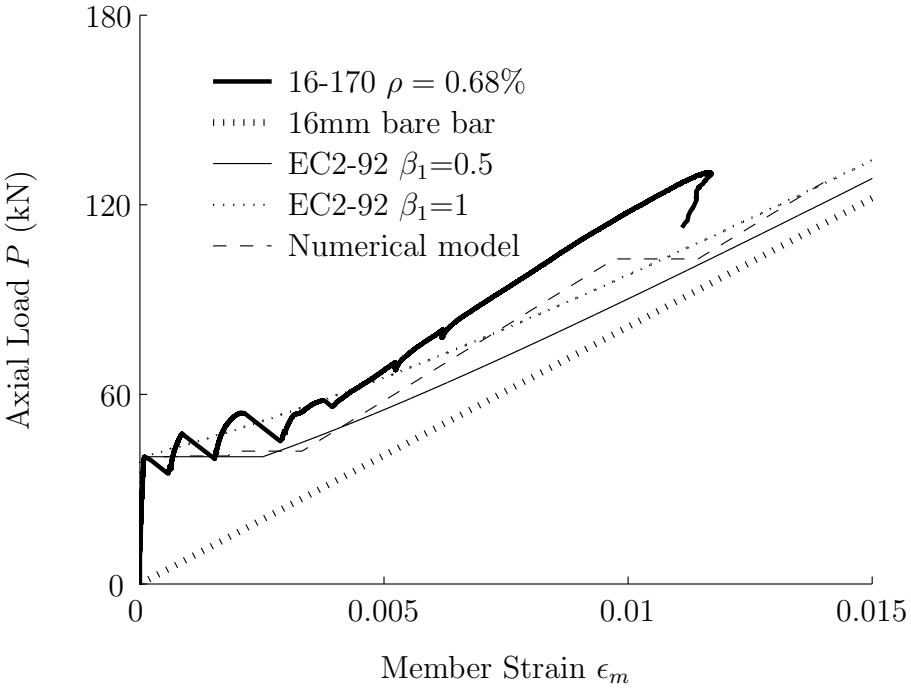

Figure 6.26: Numerical prediction on 16-170 tensile behaviour.

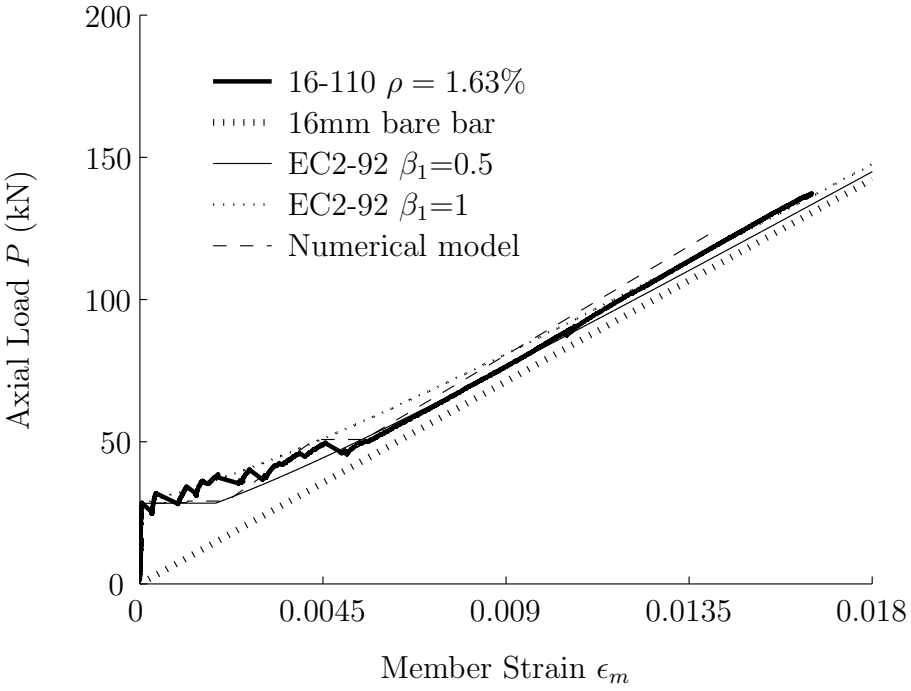

Figure 6.27: Numerical prediction on 16-110 tensile behaviour.

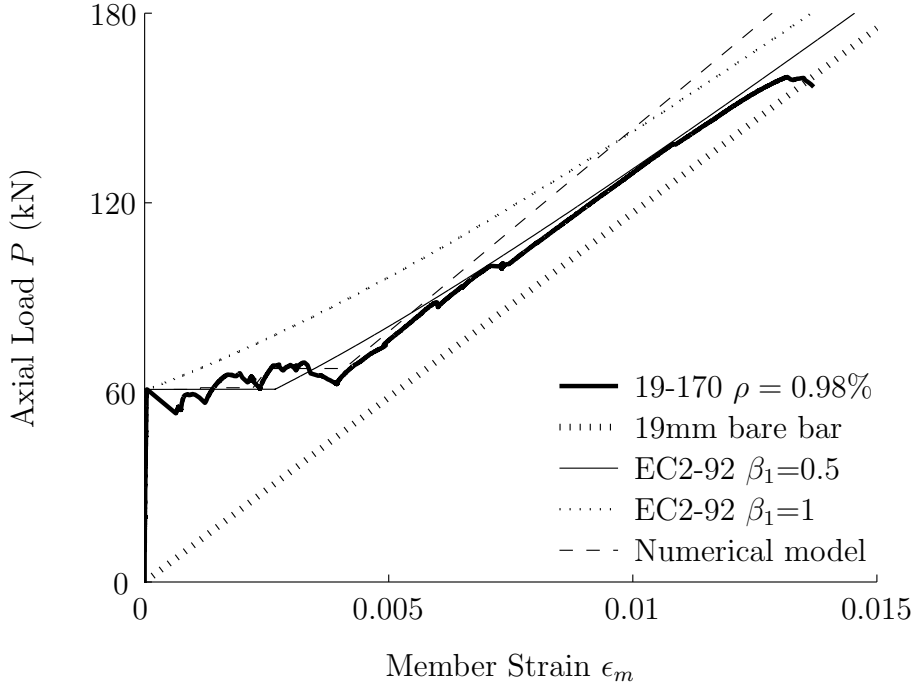

Figure 6.28: Numerical prediction on 19-170 tensile behaviour.

The experimental normalized concrete post-cracking response is compared to the numerical prediction of the tension stiffening effect in Figures 6.29 and 6.30. Although a slight underestimation at early cracking stages is visible, the numerical prediction of the tension stiffening effect reasonably fits the experimental behaviour.

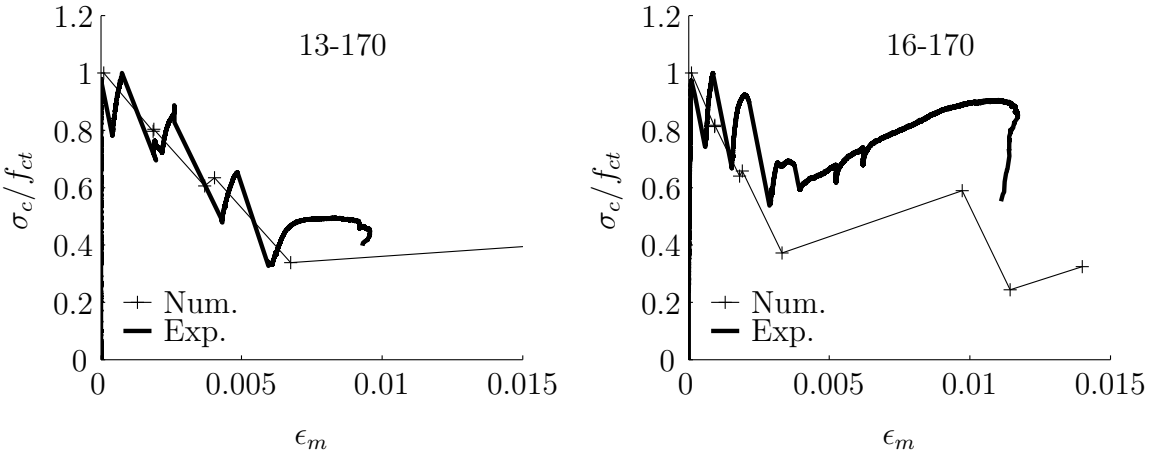

Figure 6.29: Experimental and numerical tension stiffening effect.

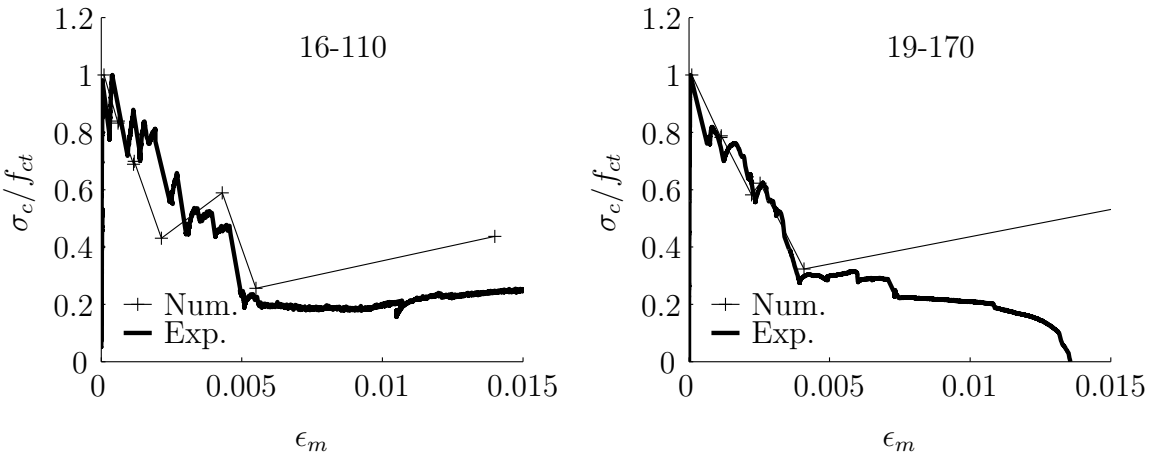

Figure 6.30: Experimental and numerical tension stiffening effect.

An additional check of the goodness of the numerical model to predict the cracking behaviour of FRP RC ties is performed hereafter. A comparison between numerical predictions and experimental results on three GFRP RC tensile tests presented in [68] is conducted. The ties are 1100mm length and concrete has a 100mm side square section. The concrete tensile and compressive strength are 2.6 and 48.8MPa, respectively. The secant modulus of elasticity, E_{cm}=37.28GPa, and the bond strength, τ_m=17.5MPa, are estimated according to Equation 6.22 and 6.23. In Table 6.1 the rebar size, d_r, of each test is presented, along with the reinforcement ratio, ρ, and the elastic modulus of the GFRP rebar, E_r.

Tie	Rebar diameter d_r (mm)	Reinforcement ratio, ρ (%)	Elastic Modulus E_r (GPa)
RS1	12.7	1.26	40.3
RS2	15.9	1.98	41.3
RS3	19.1	2.86	41.5

Table 6.1: Tie properties of RC ties tested in [68].

The numerically predicted $P - \epsilon_m$ relationships are compared to experimental responses in Figure 6.31. Although numerical responses and bare bar responses pass through the origin, an initial offset is applied to experimental results according to

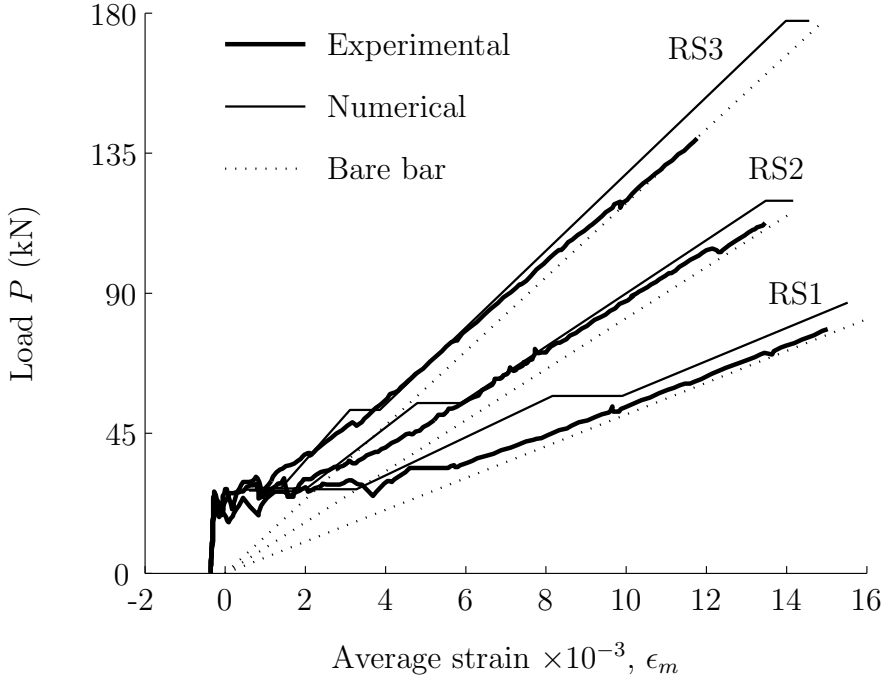

Figure 6.31: Comparison between experimental results presented in [68] and numerical $P - \epsilon$ relationships.

Bischoff indication on initial shortening caused by shrinkage effects. The responses obtained with the numerical model accurately predict experimental behaviour at all stages of the cracking process.

6.4 Parametric study on tension stiffening effect

The numerical model presented in Section 6.2.2 was used to predict the experimental results referring to either local behaviour (strain reinforcement) and global behaviour (tie overall deformability). The model is hereafter used to study the influence of the variables involved in the bond behaviour.

The study of the bond behaviour is related to study the tension stiffening effect. Traditionally, many experimental and analytical studies available in the literature present their results by either assigning, the bar tensile constitutive behaviour or the concrete tensile constitutive behaviour, the extra stiffness derived from bond

behaviour (see Figure 6.32). The former methodology is known as *tension stiffening strain* approach and assumes a perfect brittle concrete tensile behaviour, whilst the second is known as *load sharing* approach and assumes a perfect brittle rebar tensile behaviour [62]. In this section the *load sharing* approach is used to present the results of the parametric study on the bond behaviour and tension stiffening effect.

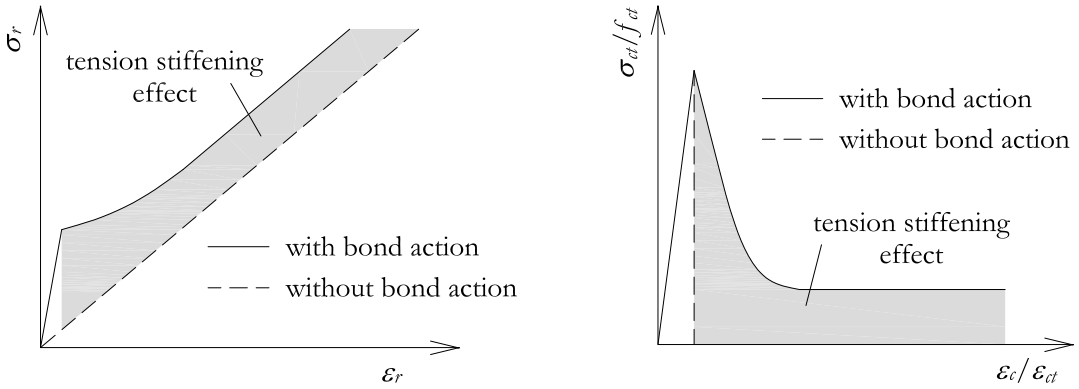

(a) *Tension stiffening strain* approach (b) *Load sharing* approach

Figure 6.32: Possible approaches to study the tension stiffening effect.

The numerical procedure is applied below to a 5000mm length RC tie with 170x170mm concrete cross section. A reinforcing rebar with diameter d_r=19mm and E_r=40000MPa is considered as internal reinforcement. Concrete properties needed in the numerical study (characteristic compressive strength, mean axial tensile strength and secant modulus of elasticity) are estimated according to EC2-04 [9] (Equations 6.20, 6.21 and 6.22). Besides, the ascending branch of the bond-slip law proposed in MC-90 [5], which is based in B.E.P. model [42], is assumed, with its characteristic values assumed as follows: α=0.4, s_m=1 and τ_m according to Equation 6.23.

6.4.1 Effect of concrete strength, f_c

The influence of concrete strength on tension stiffening effect is studied through numerical simulation on three RC ties with characteristic concrete compressive strength equal to 25, 40 and 50MPa. The related concrete and bond properties (f_{ctm}, E_{cm} and τ_m) are accordingly computed. Therefore, properties of f_{ctm}=2.56, 3.51 and 4.07MPa, E_{cm}=31.48, 35.22 and 37.27GPa and τ_m=12.5, 15.81 and 17.67MPa are

used for concrete 25, 40 and 50, respectively. The ties are named as CG25, CG40 and CG50, respectively.

Numerical results on cracking process for the three RC ties are presented in Table 6.2. Crack formation named as Pattern A, Pattern B, Pattern C, Pattern D, Pattern E and Pattern F refer to a final crack pattern of 1, 3, 7, 15, 31 and 63 cracks, equally distributed (see Figure 6.10).

Tie	Cracking load (kN)					l_t
	Pattern A	Pattern B	Pattern C	Pattern D	Pattern E	(mm)
CG25	75.1	75.1	75.1	77.6	120.1	261
CG40	102.5	102.5	102.5	105.0	155.0	252
CG50	118.9	118.9	118.9	121.4	181.4	248

Table 6.2: Numerical results of concrete strength influence.

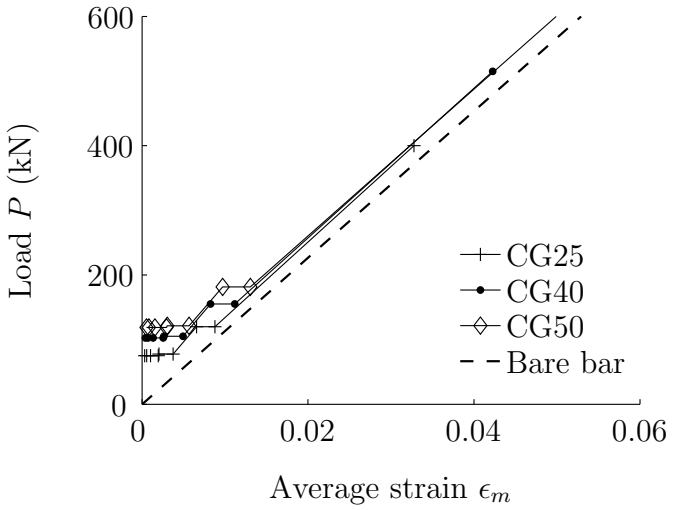

Figure 6.33: Effect of concrete strength on the $P - \epsilon_m$ relationship.

The differences in material properties derive in different $P - \epsilon_m$ relationships obtained for each RC tie (see Figure 6.33). However, normalized stress-strain relationships are obtained in Figure 6.34(a). Results are presented until ϵ_m/ϵ_{ct}=150

because no new cracks were formed beyond this point. The numerical results indicate that the concrete strength has little effect on the normalized post-cracking concrete tensile curve (i.e. representation of the tension stiffening effect) when other variables are kept constant.

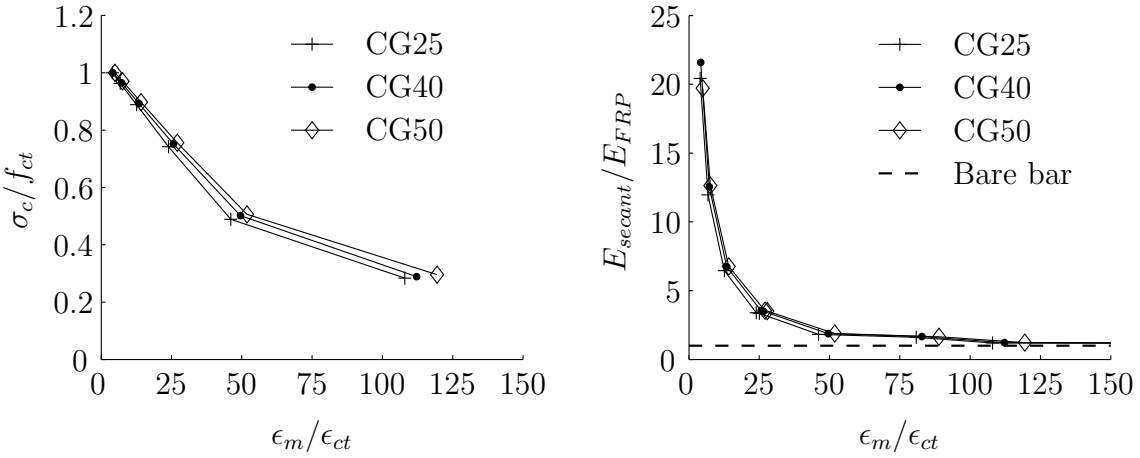

(a) Post-cracking response of concrete

(b) Tie secant modulus

Figure 6.34: Effect of concrete strength on tension stiffening effect.

The tension stiffening effect can also be studied through evolution of the secant modulus, which can be obtained from $P - \epsilon_m$ relationships. The tendency of an almost unperceptive influence of concrete strength on tension stiffening effect is also confirmed if the evolution of the secant modulus presented in Figure 6.34(b) is studied. According to Figure 6.34(b), an abrupt decay in RC tie stiffness takes place at first cracking. Afterwards, further crack formation is followed with stiffness decrease, until the point where crack stabilization phase is attained. From this point on, tie stiffness remains relatively close to bare bar stiffness.

6.4.2 Effect of reinforcement ratio, ρ

In this section the study of the effect of reinforcement ratio on tension stiffening effect is presented. Because of the interrelation existing between reinforcement ratio, ρ, rebar diameter, d_r, and concrete cross section, A_c, three different substudies are conducted. The first one considers the variation of the area of concrete (keeping d_r=ct), the second one considers the variation of the rebar diameter, d_r (keeping

A_c=ct) and the third one varies both the area of concrete and the rebar diameter so that their combination derives in a constant reinforcement ratio.

Effect of the area of concrete, A_c

Four different concrete areas have been considered to study the effect of this variable on tension stiffening. In this study, the concrete compressive strength is kept constant at 25MPa and therefore bond strength τ_m is also kept constant. Keeping a constant rebar diameter, d_r=19mm, the concrete areas have been selected to finally obtain the following reinforcement ratios: 0.9, 1.5, 3 and 4%. The studied ties are named as CS1, CS2, CS3 and CS4, respectively (see Table 6.3). It has to be noticed that the first case, CS1, with ρ=0.9% coincides with with previously presented CG25 simulation (included in Section 6.4.1).

Tie	Concrete area A_c (mm^2)	Reinforcement ratio, ρ (%)
CS1	28900	0.9
CS2	18902	1.5
CS3	9451	3.0
CS4	7088	4.0

Table 6.3: Concrete cross sections and reinforcement ratios.

Tie	Cracking load (kN)						l_t
	Pattern A	Pattern B	Pattern C	Pattern D	Pattern E	Pattern F	(mm)
CS1	75.1	75.1	75.1	76.3	116.3	-	261
CS2	49.4	49.4	49.4	50.0	65.3	-	219
CS3	25.2	25.2	25.2	25.5	28.6	61.1	186
CS4	19.1	19.1	19.1	19.3	21.1	38.6	171

Table 6.4: Numerical results of concrete cross area influence.

Similarly to previous section, the numerical results on cracking process are presented in Table 6.4. The smaller the value of l_t, the smaller the increase in load

needed to provoke fourth cracking and the more prone the tie is to have a denser crack pattern.

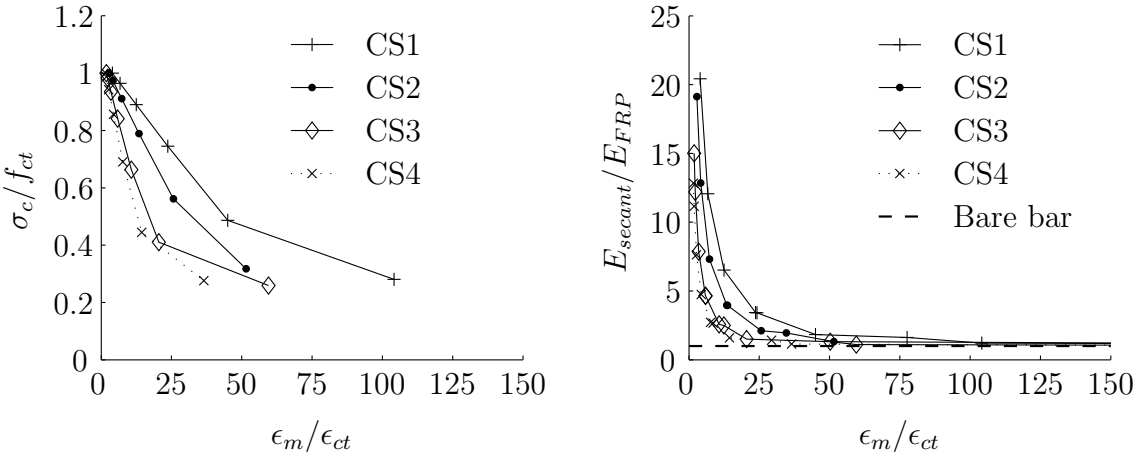

(a) Post-cracking response of concrete

(b) Tie secant modulus

Figure 6.35: Effect of concrete cross area on tension stiffening effect.

Numerical results on concrete normalized post-cracking response and the evolution of the secant modulus are presented in Figures 6.35(a) and 6.35(b). The results indicate that the change in reinforcement ratio, derived from the change in concrete cross area, has a significant effect on the representation of the tension stiffening effect through the normalized post-cracking concrete tensile behaviour, when other variables are kept constant. According to numerical results, the larger the reinforcement ratio, ρ, the lower the amount of tension stiffening effect available.

Effect of the rebar diameter, d_r

The analysis of the possible influence of the reinforcement ratio on the tension stiffening effect is further analyzed through the variation of the rebar diameter. All the remaining geometrical and characteristics of the RC tie are kept constant at their common value: concrete compressive strength is kept constant at 25MPa (i.e. the bond strength, τ_m is also kept constant), modulus of elasticity of the rebar is 40000MPa, RC tie length is equal to 5000mm and concrete has a 170mm side square section. The rebar diameter for each tie has been chosen so that the reinforcement ratios studied in the previous section are met (see Table 6.5).

Tie	Reinforcement area A_r (mm^2)	Rebar diameter d_r (mm)	Reinforcement ratio, ρ (%)
RD1	260.1	18.2	0.9
RD2	433.5	23.5	1.5
RD3	867.0	33.3	3.0
RD4	1156.0	38.4	4.0

Table 6.5: Ties geometrical properties.

Tie	Cracking load (kN)						l_t
	Pattern A	Pattern B	Pattern C	Pattern D	Pattern E	Pattern F	(mm)
RD1	75.0	75.0	75.0	76.2	118.8	-	269
RD2	75.5	75.5	75.5	76.8	114.3	-	265
RD3	77.0	77.0	77.0	79.5	112.0	532.0	258
RD4	77.9	77.9	77.9	80.4	112.9	497.9	238

Table 6.6: Numerical results of rebar size influence.

The numerical results on cracking process are presented in Table 6.6. Numerical results on concrete normalized post-cracking response and the evolution of the secant modulus are presented in Figures 6.36(a) and 6.36(b). The results indicate that the change in reinforcement ratio, caused by a change in rebar diameter, has a significant effect on the tension stiffening effect when other variables are kept constant. The numerical results confirm the trend stated in previous section, with larger reinforcement ratio developing lower amount of tension stiffening.

Effect of concrete section and rebar size, with ρ=ct

The comparison of numerical predictions for ties with equal reinforcement ratio, presented in Figures 6.35 and 6.36, depict that scarce differences are found for ties with identical reinforcement ratio (compare CS1 with RD1, CS2 with RD2, CS3 with RD3 and CS4 with RD4) and reasonable agreement is observed. However, in the cases which have been analyzed only one geometrical property was varied (either

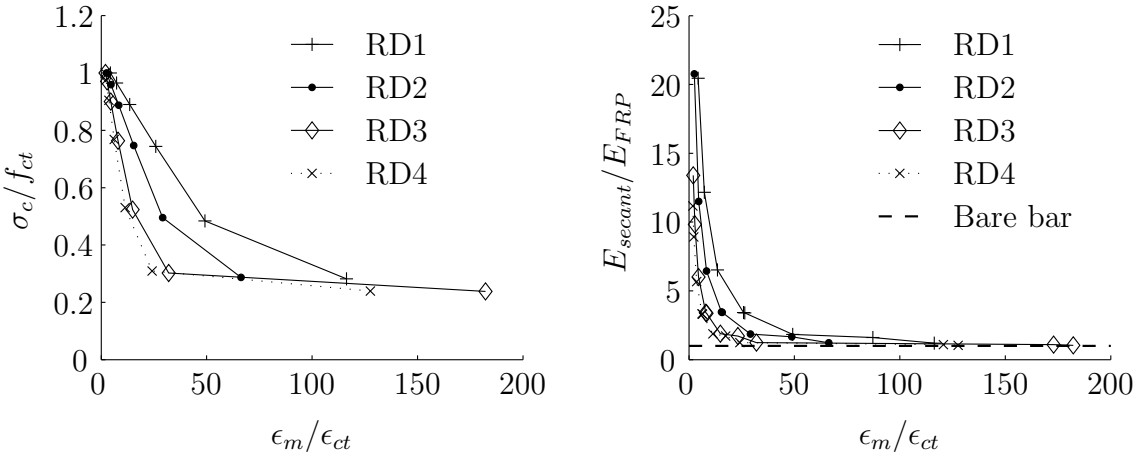

(a) Post-cracking response of concrete

(b) Tie secant modulus

Figure 6.36: Effect of rebar size on tension stiffening effect.

the concrete area or the rebar size). In this section, the numerical model is used to study the possible influence of the variation of both geometrical properties in such a way that the reinforcement ratio is kept constant at 1.5%. Similarly to previous sections, the remaining tie characteristics are kept constant. Three combinations of geometrical properties are considered (see Table 6.7).

Tie	Rebar diameter d_r (mm)	Concrete square section (mm^2)	Reinforcement ratio, ρ (%)
CR1	12	7540	1.5
CR2	16	13404	1.5
CR3	19	18902	1.5

Table 6.7: Combinations of concrete section and rebar diameter (i.e. section properties) considered in the study.

The numerical results on cracking process are summarized in Table 6.8. Numerical results on concrete normalized post-cracking response and the evolution of the secant modulus are presented in Figure 6.37. The results depict that tension stiffening effect is dependent on reinforcement ratio but less dependent on how the rebar size and concrete section are combined to obtained a fixed reinforcement ratio.

Tie	Cracking load (kN)						l_t
	Pattern A	Pattern B	Pattern C	Pattern D	Pattern E	Pattern F	(mm)
CR1	19.7	19.7	19.7	19.9	22.1	45.8	172
CR2	35.0	35.0	35.0	35.7	43.2	133.2	207
CR3	49.4	49.4	49.4	50.7	65.7	-	232

Table 6.8: Numerical results of section properties influence.

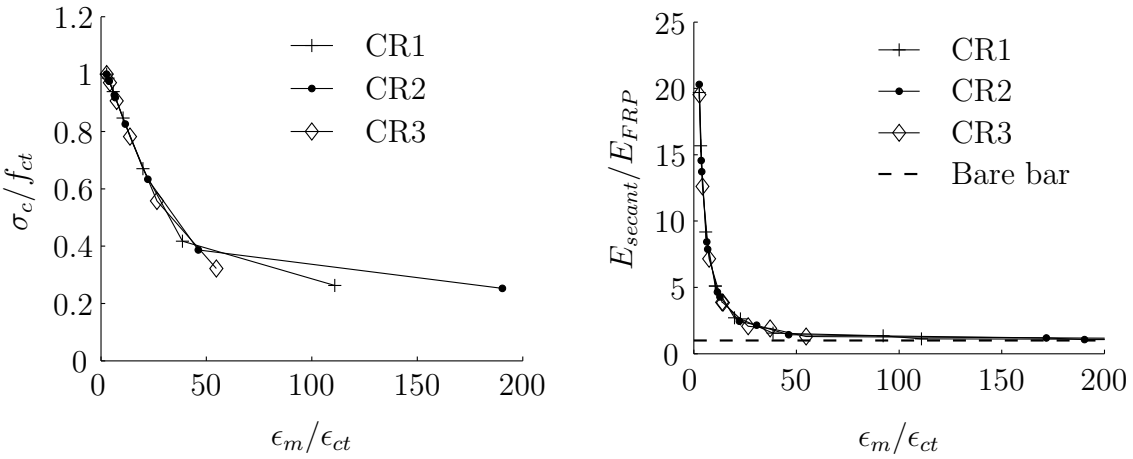

(a) Post-cracking response of concrete

(b) Tie secant modulus

Figure 6.37: Effect of the variation of RC tie geometrical properties (with ρ kept constant) on tension stiffening effect.

6.4.3 Effect of modular ratio, n

One of the main differences between traditional steel reinforcement and FRP reinforcement is the wider range of modulus of elasticity presented for the case of carbon FRP and glass FRP rebars. Therefore, numerical simulation on RC ties with varying modular ratio are conducted in this section. The numerical procedure is applied to 50000mm length RC ties with a 19mm diameter rebar and reinforcement ratio ρ=1.5%. The concrete compressive strength is kept constant at 25MPa and related concrete properties and bond strength values are accordingly estimated. The reinforcing rebar modulus of elasticity is varied so that modular ratio equals n =1, 2, 3, 4, 5 and 6. Therefore, the names used to refer to these ties are MR1, MR2, MR3, MR4, MR5 and MR6, respectively.

Tie	n	Cracking load (kN)						l_t
		Pattern A	Pattern B	Pattern C	Pattern D	Pattern E	Pattern F	(mm)
MR1	1	49.2	49.2	49.2	49.8	61.1	241.1	215
MR2	2	49.9	49.9	49.9	50.6	70.6	-	268
MR3	3	50.7	50.7	50.7	51.9	86.9	-	306
MR4	4	51.4	51.4	51.4	52.6	102.6	-	336
MR5	5	52.1	52.1	52.1	53.3	118.3	-	361
MR6	6	52.8	52.8	52.8	56.6	131.6	-	382

Table 6.9: Numerical results of modular ratio influence.

The numerical results on cracking process are presented in Table 6.9. Increases in transfer length are comparatively larger when compared to those obtained within the study of the influence of either the concrete tensile properties or tie reinforcement ratio. The transfer length somehow represents the transmission of forces between the two materials, and based on the larger differences in transfer length values obtained in the study, it can be concluded that the modular ratio has a noticeable effect on the tension stiffening effect of the RC tie.

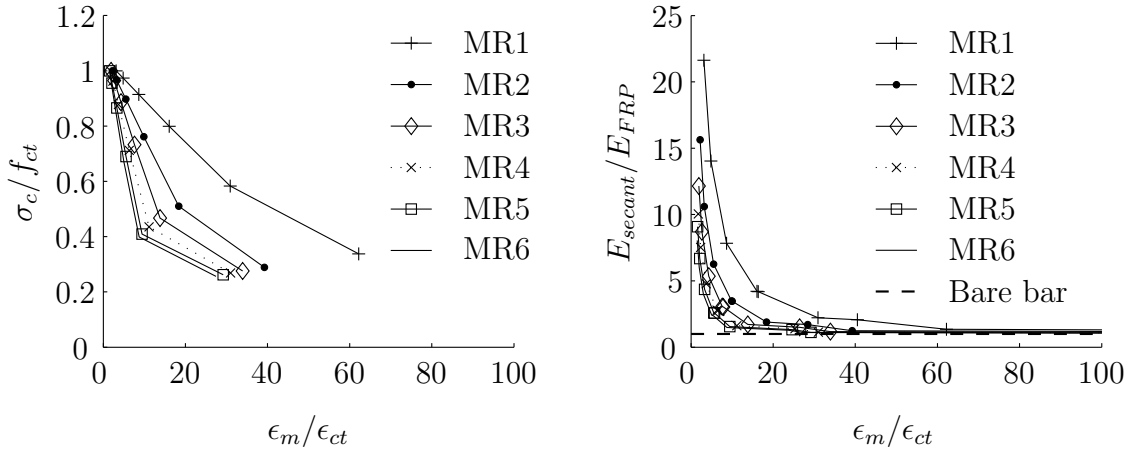

(a) Post-cracking response of concrete

(b) Tie secant modulus

Figure 6.38: Effect of modular ratio on tension stiffening effect.

Numerical results on concrete normalized post-cracking response and the evolution of the secant modulus are presented in Figure 6.38. According to results, the variation of the modular ratio, through variations in the modulus of elasticity of the reinforcing material, exerts an influence on the tension stiffening effect. Larger amounts of tension stiffening effect are expected for ties with lower modular ratio. This conclusion is in agreement with Bischoff proposal [68], which states that, as far as shrinkage is taken into account, the tension stiffening effect in FRP RC ties can be modeled as:

$$\frac{\sigma_c}{f_{ct}} = e^{-1100(\epsilon_m - \epsilon_{cr})\frac{E_{FRP}}{200}} \tag{6.24}$$

where $\frac{E_{FRP}}{200}$ is a factor that normalizes the tie response respect the modulus of elasticity of steel. However, Bischoff and co-autors [68] stated that tension stiffening effect is insensitive to changes in reinforcement ratio. This statement is in contradiction with numerical results presented in this dissertation and results presented in [70, 123].

6.4.4 Effect of the bond strength, τ_m

In previous section the study of the possible variables that may influence the tension stiffening behaviour was focused on RC tie geometrical and mechanical properties. As indicated at the beginning of Section 6.4, the ascending branch of the bond-slip law proposed in B.E.P. model was assumed, with its characteristic values assumed as α=0.4, s_m=1 and τ_m according to Equation 6.23.

MC-90 establishes the bond strength to be dependent on the concrete grade (Equation 6.23), independently on the rebar size or rebar external configuration. However, results presented in Chapter 4 demonstrate that different bond strengths are obtained for rebars with same surface configuration but different rebar size and for rebars with same diameter but different surface configuration. Therefore, it is worth studying the possible influence of the bond strength on the tension stiffening effect of an RC ties.

The numerical model is applied to a RC tie with same geometric characteris-

tics as those in previous section (i.e. L=5000mm, d_r=19mm and b=170mm) and constant concrete compressive strength (f_c=25MPa). Typical bond strength values range from 5 to 30MPa (see Chapter 4). Therefore, three intermediate values have been considered in the study (τ_m=5, 15 and 30MPa). An additional study which assumes an unattainable bond strength equal to 100MPa has been also considered.

Tie	Cracking load (kN)						l_t
	Pattern A	Pattern B	Pattern C	Pattern D	Pattern E	Pattern F	(mm)
T5	75.1	75.1	75.1	120.1	-	-	512
T15	75.1	75.1	75.1	76.3	98.8	-	278
T30	75.1	75.1	75.1	75.7	79.4	139.4	177
T100	75.1	75.1	75.1	76.3	87.6	127.6	104

Table 6.10: Numerical results of τ_m influence.

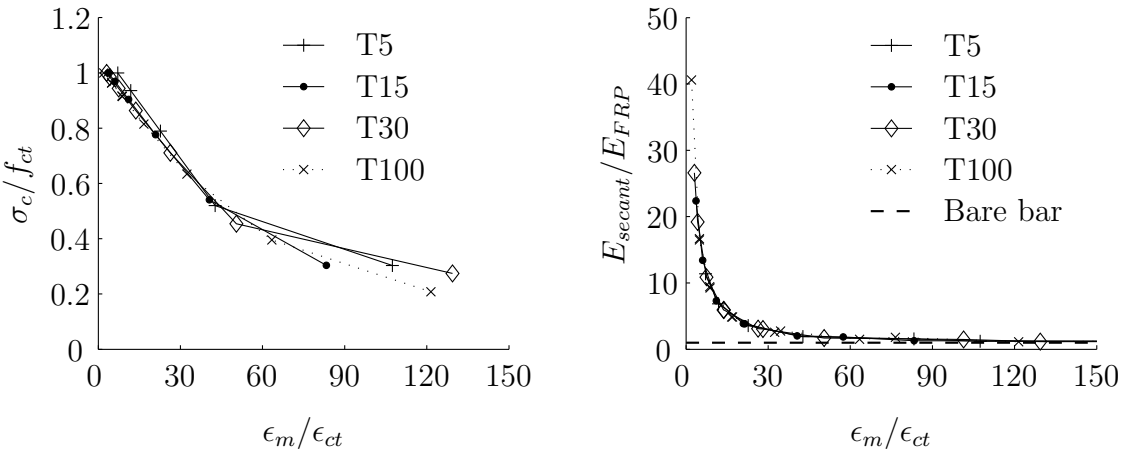

(a) Post-cracking response of concrete

(b) Tie secant modulus

Figure 6.39: Effect of τ_m on the tension stiffening effect.

Numerical results are presented in Table 6.10. In general, the larger the stiffness of the bond-slip law is, the faster the bond forces are transferred (i.e. the larger the τ_m value is, the shorter the transfer length needed), and the smaller the increase in load needed to cause further cracking. However, although different bond strength values require different transfer length to transfer the forces from reinforcement to

concrete, similar amounts of tension stiffening effect are obtained in Figure 6.39.

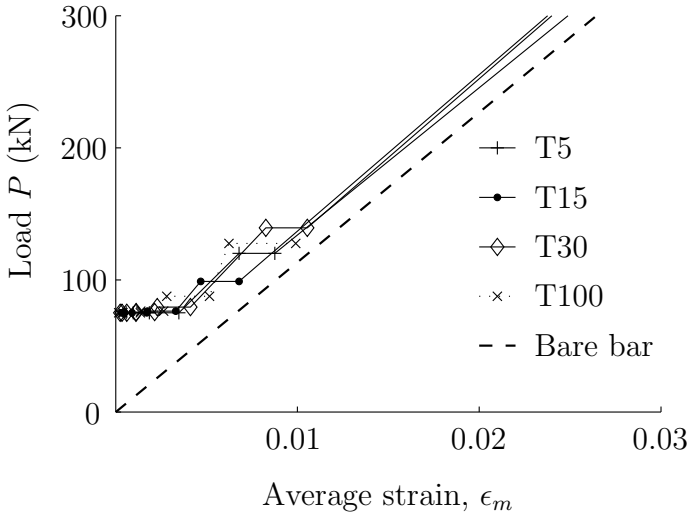

Figure 6.40: Effect of bond strength on the $P - \epsilon$ relationship.

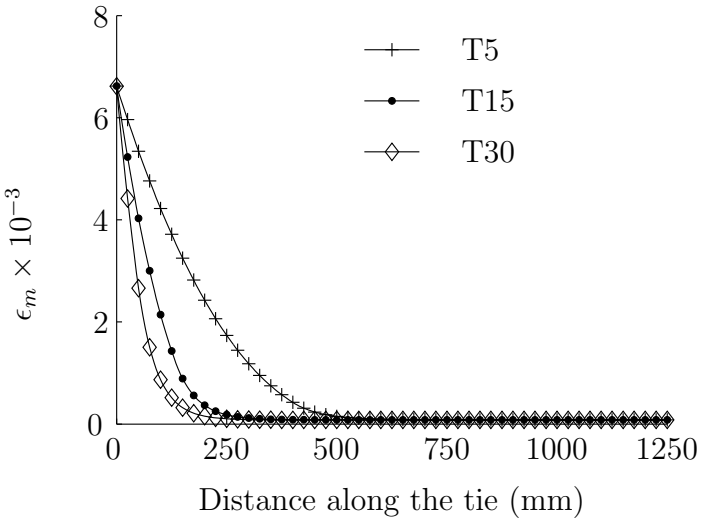

Figure 6.41: Effect of bond strength on the reinforcement strain profile.

The differences in bond behaviour when different bond strength values are considered are not visible in the representation of the tension stiffening effect proposed in Figure 6.39 (derived as shown in Figure 6.24), but are clearly visible in the representation of the load-mean strain relationship and the reinforcement strain profile, shown in Figures 6.40 and 6.41, respectively. The higher the bond strength value, the smaller

the transfer length necessary to transfer the load and the denser the final crack pattern for a given load. Nevertheless, differences in the crack formation phase are visible in Figure 6.40.

6.4.5 Effect of the rebar perimeter, p_r

Transfer length has an important role in the development of tension stiffening effect. The transmission of forces from reinforcement to concrete takes place at the interface between the two materials. Actually, the analytical expression of the transfer length, presented in Equation 6.18, is dependent on the K_a constant which, in turn, is dependent on both the bond strength and the perimeter of the reinforcing bar (see Equation 6.16).

Numerical results presented in previous section demonstrate that, the differences which arise because of different bond strength values are not appreciable in the final tension stiffening representation, but have an effect on the materials strain profile and the cracking load pattern. A similar study on the possible effect of the reinforcing bar perimeter is shown next.

Tie	Rebar perimeter p_r (mm)	Section shape
PER1	30.0	undefined
PER2	59.7	circular
PER3	84.2	rectangular, $b = 4a^*$
PER4	100.0	undefined
PER5	150.0	undefined

* a and b are dimensions of the rectangle

Table 6.11: Variations in perimeter.

The numerical model is applied to a RC tie with same geometric characteristics as those in previous section (i.e. L=5000mm, d_r=19mm and b=170mm) and constant concrete compressive strength (f_c=25MPa). Reinforcing bars with circu-

lar section are traditionally used in reinforced concrete, and therefore a perimeter of $p_r = \pi d_r$ is usually considered. In this section, different shapes for the reinforcing bar are considered so that different perimeters are obtained (see Table 6.11). The reinforcing area and the reinforcement ratio are kept constant at the values $A_r = \frac{\pi d^2}{4} = 283.528 mm^2$ and $\rho = 0.98\%$, respectively.

Tie	Cracking load (kN)						l_t
	Pattern A	Pattern B	Pattern C	Pattern D	Pattern E	Pattern F	(mm)
PER1	75.1	75.1	75.1	90.1	-	-	515
PER2	75.1	75.1	75.1	76.3	116.3	-	435
PER3	75.1	75.1	75.1	75.7	89.4	-	400
PER4	75.1	75.1	75.1	75.7	83.2	238.2	375
PER5	75.1	75.1	75.1	75.1	78.8	133.8	305

Table 6.12: Numerical results of perimeter influence.

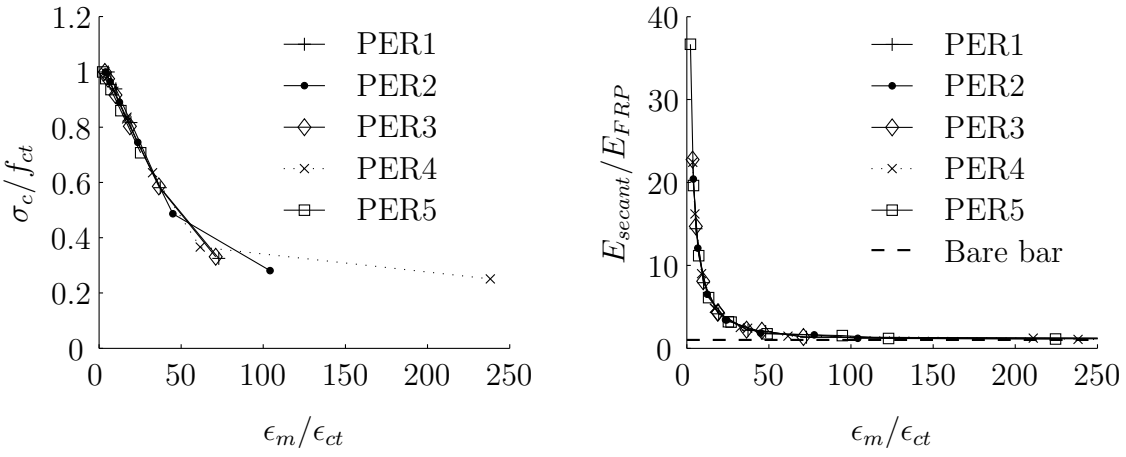

(a) Post-cracking response of concrete

(b) Tie secant modulus

Figure 6.42: Effect of rebar perimeter on the tension stiffening effect.

Numerical results are presented in Table 6.12. Similar to the case of bond strength, the larger the perimeter of the reinforcing bar is, the faster the bond forces are transferred (i.e. the larger the p_r value is, the shorter the transfer length

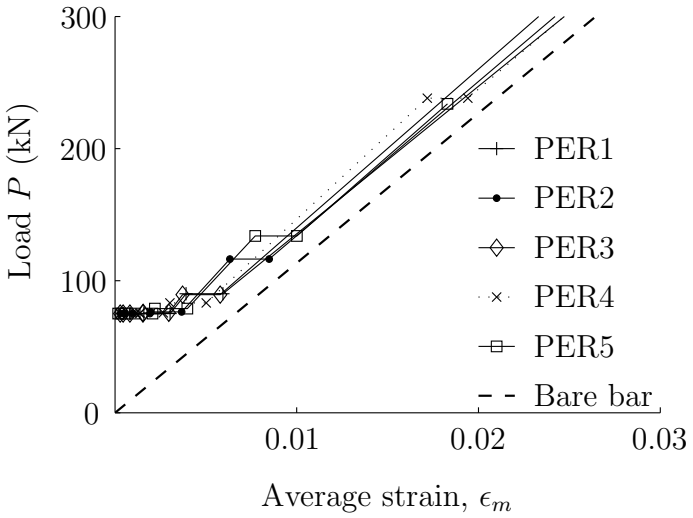

Figure 6.43: Effect of rebar perimeter on the $P - \epsilon$ relationship.

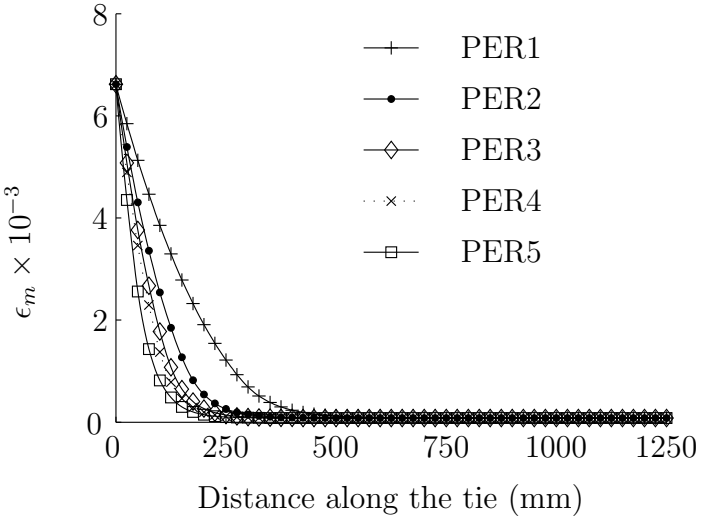

Figure 6.44: Effect of rebar perimeter on the reinforcement strain profile.

needed), and the smaller the increase in load needed to cause further cracking. Similar to the case of the role of bond strength, the differences in bond behaviour when the rebar perimeter is changed are not perceivable in the representation of the tension stiffening effect proposed in Figure 6.42. The differences can be observed in Figures 6.43 and 6.44, with the representation of the load-mean strain relationship and the reinforcement strain profile, respectively.

Numerical results presented in previous section, demonstrate that whichever the change in either bond strength value or rebar perimeter, no variation of the amount of tension stiffening effect in the final RC tie is observed. However, the transmission of forces between the two materials is governed by the bond strength and the reinforcing bar perimeter, and therefore different materials strain profiles and different cracking stages are expected when the variables are independently modified.

Based on previous results, one may expect that the combination of these two parameters is the key parameter of the transmission process. In the following, bond strength and rebar perimeter are varied so that their product is kept constant at a force transfer ratio equal to 750N/mm (see Table 6.13).

Tie	Bond strength τ_m (MPa)	Rebar perimeter p_r (mm)
RAT1	5	150
RAT2	25	30
RAT3	50	15

Table 6.13: Constant force transfer ratio.

The numerical model is applied to a RC tie with same geometric characteristics as those in previous section (i.e. L=5000mm, d_r=19mm and b=170mm) and constant concrete compressive strength (f_c=25MPa). The reinforcing area and the reinforcement ratio are kept constant at the values A_r=$\frac{\pi d^2}{4}$=$283.528mm^2$ and $\rho = 0.98\%$, respectively.

According to numerical results presented in Table 6.14, similar transfer length are obtained when load transfer ratio is kept constant, irrespective of the individual values of bond strength and rebar perimeter. Similarly, the loads which cause cracking are also similar. Therefore, for a given load transfer ratio, and whatever the combination of bond strength and rebar perimeter, same amount of tension stiffening effect is expected (see Figure 6.45). Moreover, similar load-mean strain relationship and materials strain profile are also expected (see Figures 6.46 and 6.47).

Tie	Cracking load (kN)					l_t
	Pattern A	Pattern B	Pattern C	Pattern D	Pattern E	(mm)
RAT1	75.1	75.1	75.1	76.3	116.3	405
RAT2	75.1	75.1	75.1	77.6	122.6	390
RAT3	75.1	75.1	75.1	77.6	122.6	400

Table 6.14: Numerical results of constant transfer ratio study.

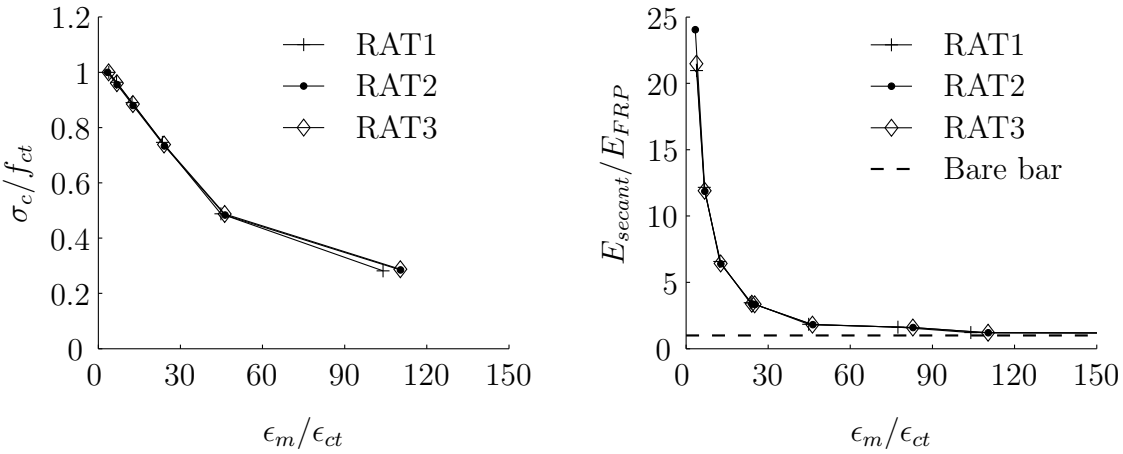

(a) Post-cracking response of concrete

(b) Tie secant modulus

Figure 6.45: Tension stiffening for constant force transfer ratio.

6.5 Concluding remarks

Numerical modelling of the bond problem present in RC ties was proposed. The model reproduces the experimental data obtained in the experimental campaign presented in Chapter 5. The verification of the model was performed by comparing data on reinforcement strain distribution and $P - \delta$ relationships.

A parametric study on the possible influence of the variables involved in the bond problem on the tension stiffening effect was conducted through simulations with the numerical model presented. The study of the possible influences was analysed by two different representations of the tension stiffening effect. The first one

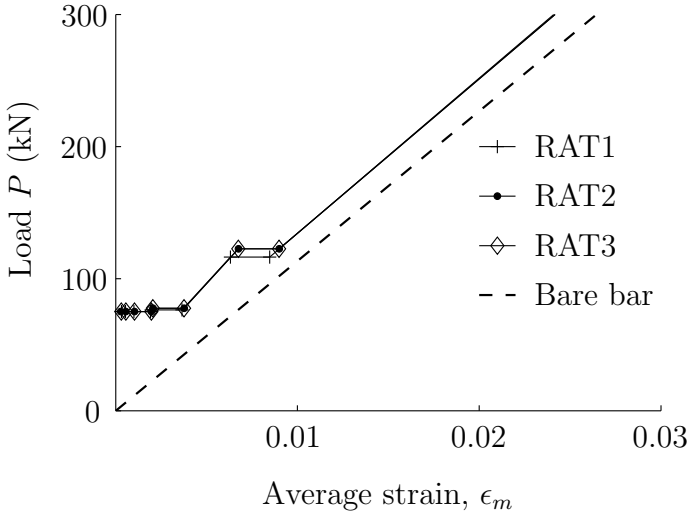

Figure 6.46: $P - \epsilon$ relationship for constant force transfer ratio.

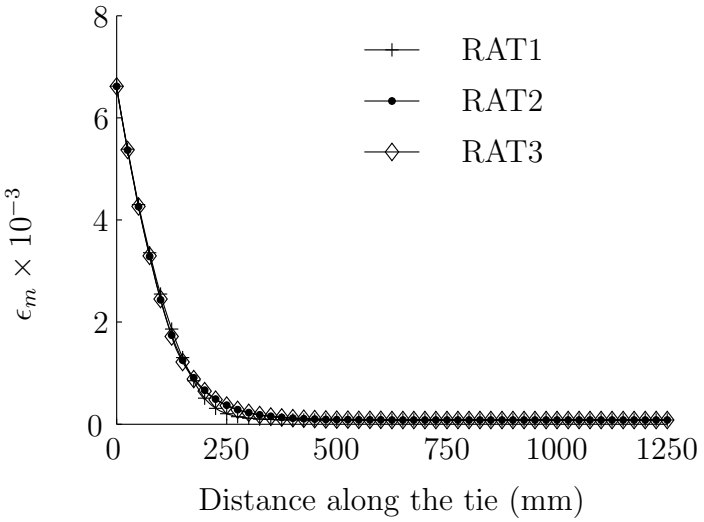

Figure 6.47: Reinforcement strain profile for constant force transfer ratio.

consisted in a normalized concrete post-cracking tensile behaviour, whilst the second one represented the RC tie secant stiffness. Similar trends on the dependencies of the tension stiffening effect were found.

In this sense, tension stiffening effect was found to be less sensitive to changes in concrete compressive strength. Besides, any change in concrete cross section or rebar diameter, that would produce a change in reinforcement ratio, causes a signif-

icant effect on tension stiffening effect (i.e. larger reinforcement ratio develop lower amount of tension stiffening). However, the tension stiffening effect is dependent on reinforcement ratio but independent on how the rebar size and concrete section are combined to obtained a fixed reinforcement ratio. Similarly, the ratio of the modulus of elasticity of the materials, n, appeared to have an influence with larger additional post-cracking stiffness available when lower E_{FRP} values are considered.

Likewise, tension stiffening effect was found to be less sensitive to changes in bond strength and rebar perimeter. These variables play a role in the load transfer process, which is studied through the reinforcement strain profile and the $P-\epsilon_m$ relationship. The larger the load transfer ratio is, the shorter the transfer length. Load transfer ratio is directly proportional to bond strength and rebar perimeter.

Chapter 7

Conclusions and future work

7.1 Thesis achievements

7.1.1 General

This study is focused on the bond-behaviour between FRP and concrete, with the aim of contributing to the experimental database and providing comprehensive understanding on the role of the variables involved. This bond-behaviour has been initially studied through pull-out tests, where the influence of the characteristics of reinforcing rebar (type of fibre, rebar surface configuration and rebar diameter) and surrounding concrete compressive strength on bond behaviour are reflected in the experimentally derived bond-slip laws. Afterwards, the study moved to direct tensile tests to analyze how the interaction between the two materials may affect the behaviour of GFRP RC cracked ties. To this end, load-deformation response, crack spacing and crack width results were used. Besides, a numerical procedure has been used to solve the analytical model that describes the bond phenomenon, so that the possible influence of different bond performances (represented with different bond-slip laws), and materials' mechanical and geometrical properties on the cracking phenomenon is analyzed.

7.1.2 Bond behaviour between FRP rebars and concrete in pull-out tests

Pull-out tests have been used to analyze the bond behaviour between different kinds of carbon and glass FRP bars, with different surface configurations, and two different concrete strengths. The results confirmed the trend of rebars with larger diameter developing lower bond strength, specially for high concrete strength series. An increase in bond strength and changes in failure surface were observed when the concrete compressive strength was increased. However, for sand coated rebars, the change in failure surface was associated with a change in failure mode from pull-out to debonding of the sand coating layer. In addition, the higher bond forces developed for higher concrete compressive strength were associated with splitting failure mode for steel rebars and FRP rebars with large surface deformations.

The analysis of the influence of the surface treatment on bond behaviour confirmed the existence of different bond mechanisms for different surface treatments. Sanding lead to an increase in chemical bond at early stages. However, once the bond strength was reached, the sand coating surface debonded from the rebar and an abrupt decay of bond stresses occurred. For the case of smooth bars, chemical adhesion and friction force, with low mechanical bearing forces, were the active bond mechanisms. Finally, for deformed and indented bars, bearing resistance, generated by the crushed concrete which sticks in the front of the surface lugs and/or deformations, governed the bond behaviour.

The influence of rebar surface treatment on bond strength was less important in the low concrete strength series than in the high concrete strength series (in which bond strength influence was more pronounced). For indented rebars the influence of the surface geometry was analyzed using the Concrete Lug Ratio (CLR), whilst a new geometrical ratio named "area-to-surface" ratio, a_s, was proposed for the analysis of deformed rebars. Whenever the CLR ratio was kept constant for different rebar sizes of indented bars, the trend of larger diameters developing lower bond strength held true. Besides, an increase in the CLR ratio made the bond strength to increase. In the case of deformed rebars, the larger the value of a_s was, the

larger the bearing resistance generated, and therefore the higher the bond strength developed. Nevertheless, the highest a_s values increased the radial stress on the specimen, therefore inducing a splitting failure mode.

Moreover, the initial stiffness of the derived bond-slip laws was not mainly influenced by the rebar diameter. Nevertheless, changes in the initial stiffness due to a change in concrete compressive strength were observed for some specimens of GFRP rebars. The slip values obtained for GFRP were greater than those for CFRP bars. There was also a difference in the first loading branch between the bond-slip law of steel rebars compared to that of FRP rebars, since there was a high level of stiffness with no slip in the steel rebars, whereas the FRP rebars developed slip from the beginning.

7.1.3 Bond behaviour between FRP rebars and concrete in tensile tests

Direct tensile tests were carried out to study the post-cracking response of GFRP RC ties with four different reinforcement ratios. The post-cracking tie stiffness was proven to be overpredicted in ACI 224.2R, where the benefits of the bond-behaviour are accounted for by computing an effective cross-sectional area that reduces beyond the cracking load. In contrast, the use of a modified constitutive law for the embedded reinforcement proposed in EC2 and MC90 was found to better predict the member deformability.

The ratio of crack stabilization load to first cracking load was found to be dependent on the reinforcement ratio. Similarly, a decrease in crack spacing values with increasing reinforcement ratio was observed. The experimental ratios of maximum to average crack spacing and minimum to average crack spacing fall between the ranges of [1.33, 1.54] and [0.67, 0.77] proposed in previous studies on flexural members, respectively.

Crack spacing was found to be dependent on the ratio of rebar diameter to effective reinforcement ratio as stated in EC-2 provisions. However, the EC2 proposal

for the additional dependence on the concrete cover does not seem directly applicable to RC tensile members. Therefore, a linear relationship for the dependence of average crack spacing on the ratio of rebar diameter to effective reinforcement ratio was adjusted, where concrete cover was not included. However, more experimental data is needed to arrive to a more general conclusion.

Although crack width was overestimated in EC2 provisions, the crack width code formulas were proven to be valid and contingent on good provisions of crack spacing. Reasonable agreement between experimental and predicted crack width was found when the crack spacing adjustment proposed in this dissertation was considered. Besides, based on experimental results, the influence of the reinforcement stress on crack width could be removed in predictive formula proposed in ACI code for RC ties. Alternatively, and similar to the code for FRP RC flexural members, a dependence on reinforcement strain could be introduced.

The internal strain gauging on additional RC ties was proven to be effective to obtain the reinforcement strain profile along the whole tie. The analysis of strain readings at different load levels was presented as a useful tool to analyze cracking behaviour and understand the evolution of crack pattern until crack stabilization phase is attained. At crack maturity no changes in the shape of the reinforcement strain profile were observed, however a shift of the whole profile to higher tensile strain values took place. Besides, the process of stress redistribution after crack formation could be studied through the study of the reinforcement strain profiles.

7.1.4 Modeling cracking behaviour of FRP RC ties

Numerical modelling of the bond problem present in RC ties was proposed. The model is based on the bond-slip reponse and takes into account the variables involved in the cracking process. Although being simple, the model is versatile to include any bond-slip law different to those usually assumed in available numerical works. Moreover, reinforcement and concrete mechanical and geometrical characteristics can also be changed. The verification of the model was performed by comparing data on reinforcement strain distribution and $P - \delta$ relationships. The model was found to satisfactorily reproduce the experimental data obtained in the experimen-

tal campaign presented in Chapter 5.

A parametric study on the possible influence that the variables involved in the bond problem can have on the cracking behaviour of RC ties was conducted through simulations with the numerical model presented. The possible influences were analyzed by two different representations. The first one consisted in a normalized concrete post-cracking tensile behaviour, whilst the second one represented the RC tie secant stiffness. Similar trends on their dependencies were found.

Tension stiffening effect was found to be less sensitive to changes in concrete compressive strength. Besides, any change in concrete cross section or rebar diameter, that would reproduce a change in reinforcement ratio, caused a significant effect on tension stiffening effect (i.e. larger reinforcement ratio develop lower amount of tension stiffening). However, the tension stiffening effect was dependent on reinforcement ratio but independent on how the rebar size and concrete section were combined to obtain a fixed reinforcement ratio. Similarly, the ratio of the modulus of elasticity of the materials appeared to have an influence with larger additional post-cracking stiffness available when lower values for the reinforcing bar's modulus of elasticity were considered. Likewise, tension stiffening effect was found to be less sensitive to changes in bond strength and rebar perimeter. These variables play a role in the load transfer process which was studied through the reinforcement strain profile and the $P - \epsilon_m$ relationship. The larger the load transfer ratio is, the shorter the transfer length. Moreover, transfer ratio is directly proportional to bond strength and rebar perimeter.

7.2 Future work

Based on the findings of this study, the following suggestions for future investigations are drawn:

- Propose a more general bond-slip law model which explicitly includes the effects of the surface configuration and rebar diameter. The model should be fed with experimental data available in the literature. In case more experimental

data is needed, an additional experimental work on pull-out tests would be performed.

- Conduct an experimental program on beam test to investigate the bond behaviour without the compression action in the concrete.

- Analytically and numerically study the concrete cover influence on the cracking behaviour of RC ties. The existence of a possible effective area of concrete in tension should also be studied.

- Create a numerical model to simulate the cracking behaviour of FRP RC flexural elements, and check whether the dependencies found in RC ties are still valid. In parallel, flexural elements with internally strain gauged FRP reinforcement should be tested to understand and analyze how the reinforcement strain profile evolves. The strain profile would also be valid to validate the reliability of the numerical model.

- A detailed numerical study of the load-deformation response of FRP RC ties using FEM should be carried out to complement the results obtained in the present work. The study could also analyze whether the introduction of a cohesive crack, in a fracture mechanics framework, would make any significant influence on the modelling results of cracking behaviour of FRP RC ties.

- Investigate how bond deterioration in the damaged areas near cracks can affect the bond-slip behaviour.

- A random concrete tensile strength distribution should be included in the numerical model so that only one crack forms at an aleatory section when the cracking criteria is attained.

- Introduce the effect of reinforcement strain into the bond-slip model, so that reinforcement strain would control the extent of secondary cracking causing the reduction of stiffness of the interface.

Bibliography

[1] Zhao, W.. Crack and deformation behaviour of FRP reinforced concrete structures, PhD Thesis, University of Sheffield. 1999.

[2] Neocleous, K.. Design and safety philosophy for concrete structures reinforced with Fiber Reinforced Polymers (FRP), PhD Thesis, University of Sheffield. 1999.

[3] CEB Bulletin 151. Bond Action and Bond Behaviour of Reinforcement, State-of-the-Art Report. CEB, Comité Euro International du Béton. París. 1982.

[4] Eurocode 2: Design of Concrete Structures-Part 1: General Rules and Rules for Buildings, DD ENV 1992-1-1:1992. CEN (Comité Européen de Normalisation), Brussels. 274p. 1992.

[5] CEB-FIP Model Code 1990: Design Code. Comité Euro International du Béton-Fédération International de la Précontraint. London, Thomas Telford Service LTD. 437p. 1993.

[6] ACI 224.2R-92. Cracking of Concrete Members in Direct Tension. ACI Committee 224, American Concrete Institute. Detroit (USA) . 1992.

[7] FIB Bulletin 10. Bond of Reinforcement in Concrete, State-of-the-Art Report. FIP. Fédération International de la Précontraint. Lausanne, Switzerland. 434p. 2000.

[8] ACI 318R-95. Building Code Requirements for Structural Concrete and Commentary. ACI Committee 318, American Concrete Institute. Farmington Hills, Michigan (USA). 1995.

[9] Eurocode 2: Design of Concrete Structures-Part 1: General Rules and Rules for Buildings, BS EN 1992-1-1:2004. CEN (Comité Européen de Normalisation), Brussels. 230p. 2004.

[10] Pilakoutas, K., Achillides, Z., Waldron, P.. Non-ferrous reinforcement in concrete structures. In: Topping, E.M.L.&.B., editor. Centenary Conference on Innovation in Civil and Structural Engineering. Civil-Comp Ltd; 1997, p. 47–58.

[11] Achillides, Z.. Bond behaviour of FRP bars in concrete, PhD Thesis, University of Sheffield. 1998.

[12] Kanakubo, T., Yonemaru, K., Fukuyama, H., Fujisawa, M., Sonobe, Y.. Bond performance of concrete members reinforced with FRP bars. In: Nanni, , Dolan, C., editors. First International Symposium on Non-Metallic (FRP) Reinforcement for Concrete Structures. 1993, p. 767–788.

[13] Makitani, E., Irisawa, I., Nishiura, N.. Investigation of bond in concrete member with fibre reinforced plastic bars. In: Nanni, , Dolan, C., editors. First International Symposium on Non-Metallic (FRP) Reinforcement for Concrete Structures. 1993, p. 315–332.

[14] Larralde, J., Silva-Rodriguez, R.. Bond and slip of frp rebars in concrete. Journal of Materials in Civil Engineering 1993;5(1):30–40.

[15] Benmokrane, B., Tighiouart, B., Chaallal, O.. Bond strength and load distribution of composite gfrp reinforcing bars in concrete. ACI Materials Journal 1996;93(3):246–253.

[16] EUROCRETE Project. The development of non-ferrous reinforcement for concrete structures - Final Report. Prepared by Euro-Project (LTTC) Ltd, 109p. 1997.

[17] Achillides, Z., Pilakoutas, K.. Bond behavior of fiber reinforced polymer bars under direct pullout conditions. Journal of Composites for Construction 2004;8(2):173–181.

[18] Tepfers, R.. Bond clause proposal for FRP-bars/rods in concrete based o CEB/FIP Model Code 90. Part 1: Design bond stress for FRP reinforcing bars. Structural Concrete 2006;7(2):47–55.

[19] Cosenza, E., Manfredi, G., Realfonzo, R.. Development length of FRP straight rebars. Composites Part B-Engineering 2002;33(7):493–504.

[20] Al-Zahrani, M.M., Al-Dulaijan, S.U., Nanni, A., Bakis, C.E., Boothby, T.E.. Evaluation of bond using FRP rods with axisymmetric deformations. Construction and Building Materials 1999;13(6):299–309.

[21] Benmokrane, B., Zhang, B.R., Chennouf, A.. Tensile properties and pullout behaviour of afrp and cfrp rods for grouted anchor applications. Construction and Building Materials 2000;14(3):157–170.

[22] Chaallal, O., Benmokrane, B.. Pullout and Bond of Glass-Fiber Rods Embedded in Concrete and Cement Grout. Materials and Structures 1993;26(3):167–175.

[23] Nanni, A., Al-Zahrani, M.M., Al-Dulaijan, S.U., Bakis, C.E., Boothby, T.E.. Bond of FRP reinforcement to concrete - experimental results. In: Taerwe, L., editor. Second International Symposium on Non-Metallic (FRP) Reinforcement for Concrete Structures. 1995, p. 135–145.

[24] Lee, J.Y., Kim, T.Y., Kim, T.J., Yi, C.K., Park, J.S., You, Y.C., et al. Interfacial bond strength of glass fiber reinforced polymer bars in high-strength concrete. Composites Part B-Engineering 2008;39(2):258–270.

[25] CSA S806-02. Design and Construction of Building Components with Fibre-Reinforced Polymers. CSA Standard, Canadian Standards Association. Canada. 187p. 2002.

[26] AL-Mahmoud, F., Castel, A., Francois, R., Tourneur, C.. Effect of surface pre-conditioning on bond of carbon fibre reinforced polymer rods to concrete. Cement and Concrete Composites 2007;29(9):677–689.

[27] Hao, Q.D., Wang, Y.L., He, Z., Ou, J.P.. Bond strength of glass fiber reinforced polymer ribbed rebars in normal strength concrete. Construction and Building Materials 2009;23(2):865–871.

[28] Freimanis, A.J., Bakis, C.E., Nanni, A., Gremel, D.A.. A comparison of pull-out and tensile behaviours of FRP reinforcement for concrete. In: H, S., editors, E.M., editors. Second International Conference on Composites in Infrastructure. 1998,.

[29] Malvar, L.J.. Tensile and bond properties of GFRP reinforcing bars. ACI Materials Journal 1995;92(3):276–285.

[30] Malvar, L.J., Cox, J.V., Cochran, K.B.. Bond between carbon fiber reinforced polymer bars and concrete. I: Experimental study. Journal of Composites for Construction 2003;7(2):154–163.

[31] Cox, J.V., Cochran, K.B.. Bond between carbon fiber reinforced polymer bars and concrete. II: Computational modeling. Journal of Composites for Construction 2003;7(2):164–171.

[32] Tepfers, R., Karlsson, M.. Pull-out and tensile reinforcement splice tests using FRP C-Bars. In: Third International Symposium on Non-Metallic (FRP) Reinforcement for Concrete Structures. 1997, p. 357–364.

[33] Tastani, S.P., Pantazopoulou, S.J.. Bond of GFRP bars in concrete: Experimental study and analytical interpretation. Journal of Composites for Construction 2006;10(5):381–391.

[34] Aiello, M.A., Leone, M., Pecce, M.. Bond performances of FRP rebars-reinforced concrete. Journal of Materials in Civil Engineering 2007;19(3):205–213.

[35] Pecce, M., Manfredi, G., Realfonzo, R., Cosenza, E.. Experimental and analytical evaluation of bond properties of GFRP bars. Journal of Materials in Civil Engineering 2001;13(4):282–290.

[36] Tighiouart, B., Benmokrane, B., Gao, D.. Investigation of bond in concrete member with fibre reinforced polymer (FRP) bars. Construction and Building Materials 1998;12(8):453–462.

[37] Ehsani, M.R., Saadatmanesh, H., Tao, S.. Design recommendations for bond of gfrp rebars to concrete. Journal of Structural Engineering-ASCE 1996;122(3):247–254.

[38] Benmokrane, B., Masmoudi, R.. FRP C-Bar as reinforcing rod for concrete structures. In: El-Badry, M., editor. Second International Conference on Advanced Composite Materials in Bridges and Structures. 1996, p. 181–188.

[39] Belarbi, A., Wang, H.. Bond-slip response of FRP reinforcing bars in fiber reinforced concrete under direct pullout. In: International Conference on Fiber Composites, High Performance Concretes and Smart Materials. 2004, p. 409–419.

[40] RC6. Bond Test for Reinforcing Steel. 2. Pull-out Test, 1983. RILEM Technical Recommendations for the Testing and Use of Construction Materials. E&FN Spon. London (United Kingdom). p 218-220. 1994.

[41] Won, J.P., Park, C.G., Kim, H.H., Lee, S.W., Jang, C.I.. Effect of fibers on the bonds between FRP reinforcing bars and high-strength concrete. Composites Part B-Engineering 2008;39(5):747–755.

[42] Eligehausen, R., Popov, E.P., Bertero, V.V.. Local bond stress-slip relationships of deformed bars under generalized excitations. Tech. Rep. Report 83/23; 1983.

[43] Cosenza, E., Manfredi, G., Realfonzo, R.. Analytical modelling of bond between FRP reinforcing bars and concrete. In: Taerwe, L., editor. Second International Symposium on Non-Metallic (FRP) Reinforcement for Concrete Structures. 1995, p. 164–171.

[44] Cosenza, E., Manfredi, G., Realfonzo, R.. Behavior and modeling of bond of FRP rebars to concrete. Journal of Composites for Construction 1997;1(2):40–51.

[45] Focacci, F., Nanni, A., Bakis, C.E.. Local bond-slip relationships for FRP reinforcement in concrete. Journal of Composites for Construction 2000;4(1):24–31.

[46] Greco, C., Manfredi, G., Pecce, M., Realfonzo, R.. Experimental analysis of bond between GFRP deformed rebars and concrete. In: ed I. Crivelli Visconti, , editor. Eighth European Conference on Composite Materials,; vol. 2. 1998, p. 301–308.

[47] Okelo, R., Yuan, R.L.. Bond strength of fiber reinforced polymer rebars in normal strength concrete. Journal of Composites for Construction 2005;9(3):203–213.

[48] Ehsani, M.R., Saadatmanesh, H., Tao, S.. Design recommendations for bond of GFRP rebars to concrete. Journal of Structural Engineering-ASCE 1996;122(3):247–254.

[49] Bakis, C.E., Uppuluri, V.S., Nanni, A., Boothby, T.E.. Analysis of bonding mechanisms of smooth and lugged FRP rods embedded in concrete. Composites Science and Technology 1998;58(8):1307–1319.

[50] Achillides, Z., Pilakoutas, K.. FE modelling of bond interaction of FRP bars to concrete. Structural Concrete 2006;7(1):7–16.

[51] Jendele, L., Cervenka, J.. Finite element modelling of reinforcement with bond. Computers and Structures 2006;84(28):1780–1791.

[52] Tvergaard, V.. Effect of fibre debonding in a whisker-reinforced metal. Materials Science and Engineering A 1990;125(2):203–213.

[53] Chaboche, J.L., Girard, R., Schaff, A.. Numerical analysis of composite systems by using interphase/interface models. Computational Mechanics 1997;20(1-2):3–11.

[54] Lin, G., Geubelle, P.H., Sottos, N.R.. Simulation of fiber debonding with friction in a model composite pushout test. International Journal of Solids and Structures 2001;38(46-47):8547–8562.

[55] Alfano, G., Sacco, E.. Combining interface damage and friction in a cohesive-zone model. International Journal for Numerical Methods in Engineering 2006;68(5):542–582.

[56] Branson, D.E.. Deformation of concrete structures. New York: Mc Graw-Hill; 1977.

[57] Scanlon, A., Murray, D.W.. Time-dependent reinforced concrete slab deflections. Journal of the Structural Division 1974;100(9):1911–1924.

[58] Lin, C.S., Scordelis, A.C.. Nonlinear analysis of rc shells of general forms. Journal of the Structural Division 1975;101(3):523–538.

[59] Gilbert, R.I., Warner, R.F.. Tension-stiffening in reinforced concrete slabs. Journal of the Structural Division 1978;104(12):1885–1900.

[60] Torres, L., Lopez-Almansa, F., Bozzo, L.M.. Tension-stiffening model for cracked flexural concrete members. Journal of Structural Engineering-ASCE 2004;130(8):1242–1251.

[61] Kaklauskas, G., Ghaboussi, J.. Stress-strain relations for cracked tensile concrete from rc beam tests. Journal of Structural Engineering-ASCE 2001;127(1):64–73.

[62] Bischoff, P.H.. Effects of shrinkage on tension stiffening and cracking in reinforced concrete. Canadian Journal of Civil Engineering 2001;28(3):363–374.

[63] Lee, G.Y., Kim, W.. Cracking and Tension Stiffening Behavior of High-Strength Concrete Tension Members Subjected to Axial Load. Advances in Structural Engineering 2009;12(2):127–137.

[64] Choi, C.K., Cheung, S.H.. A simplified model for predicting the shear response of reinforced-concrete membranes. Thin-Walled Structures 1994;19(1):37–60.

[65] Considère, A.. Influence des armatures métalliques sur les propriétés des mortiers et bétons (Influence of steel reinforcing on mortar and concrete properties. Part II). Le Génie Civil 1899;34(15):229–233.

[66] Stramandinoli, R.S.B., Rovere, H.L.L.. An efficient tension-stiffening model for nonlinear analysis of reinforced concrete members. Engineering Structures 2008;30(7):2069–2080.

[67] Choi, C.K., Cheung, S.H.. Tension stiffening model for planar reinforced concrete members. Computers and Structures 1996;59(1):179–190.

[68] Bischoff, P.H., Paixao, R.. Tension stiffening and cracking of concrete reinforced with glass fiber reinforced polymer (GFRP) bars. Canadian Journal of Civil Engineering 2004;31(4):579–588.

[69] Kaklauskas, G., Gribniak, V., Bacinskas, D., Vainiunas, P.. Shrinkage influence on tension stiffening in concrete members. Engineering Structures 2009;31(6):1305–1312.

[70] Kaklauskas, G.. Flexural layered deformational model of reinforced concrete members. Magazine of Concrete Research 2004;56(10):575–584.

[71] Fields, K., Bischoff, P.H.. Tension Stiffening and Cracking of Hihg-Strength Reinforced Concrete Tension Members. ACI Structural Journal 2004;101(4):447–456.

[72] Wu, H.Q., Gilbert, R.I.. Modeling short-term tension stiffening in reinforced concrete prisms using a continuum-based finite element model. Engineering Structures 2009;31(10):2380–2391.

[73] Ferreira, A.J.M., Camanho, P.P., Marques, A.T., Fernandes, A.A.. Modelling of concrete beams reinforced with frp re-bars. Composite Structures 2001;53(1):107–116.

[74] Gupta, A.K., Maestrini, S.R.. Tension-stiffness model for reinforced-concrete bars. Journal of Structural Engineering-ASCE 1990;116(3):769–790.

[75] Russo, G., Romano, F.. Cracking response of RC members subjected to uniaxial tension. Journal of Structural Engineering-ASCE 1992;118(5):1172–1190.

[76] Yankelevsky, D.Z., Jabareen, M., Abutbul, A.D.. One-dimensional analysis of tension stiffening in reinforced concrete with discrete cracks. Engineering Structures 2008;30(1):206–217.

[77] Yankelevsky, D.Z.. A two-phase one dimensional model for steel-concrete interaction. Computers and Structures 1997;65(6):781–794.

[78] Yankelevsky, D.Z.. New finite element for bond slip analysis. Journal of Structural Engineering-ASCE 1985;111(7):1533–1542.

[79] Khalfalla, S.. Cracking analysis of reinforced concrete tensioned members. Structural Concrete 2006;7(3):111–116.

[80] Fantilli, A.P., Ferretti, D., Iori, I., Vallini, P.. Flexural deformability of reinforced concrete beams. Journal of Structural Engineering-ASCE 1998;124(9):1041–1049.

[81] Creazza, G., Dimarco, R.. Bending moment-mean curvature relationship with constant axial load in the presence of tension stiffening. Materials and Structures 1993;26(158):196–206.

[82] Aiello, M.A., Ombres, L.. Load-deflection analysis of FRP reinforced concrete flexural members. Journal of Composites for Construction 2000;4(4):164–171.

[83] Vollum, R.L., Afshar, N., Izzuddin, B.A.. Modelling short-term tension stiffening in tension members. Magazine of Concrete Research 2008;60(4):291–300.

[84] Ferracuti, B., Savoia, M.. Tension-stiffening law for FRP-reinforced concrete elements under service loadings. In: Chen, , Teng, , editors. International Symposium on Bond Behaviour of FRP in Structures. International Institute for FRP in Construction; 2005, p. 221–228.

[85] Aiello, M.A., Leone, M., Ombres, L.. Modeling of the behavior of concrete tension members reinforced with FRP rods. Mechanics of Composite Materials 2003;39(4):283–292.

[86] Aiello, M., Leone, M., Ombres, L.. Cracking analysis of fibre-reinforced polymer-reinforced concrete tension members. Proceedings of the Institution of Civil Engineers-Structures and Buildings 2004;157(1):53–62.

[87] Sooriyaarachchi, H.. Tension Stiffening effect in GFRP reinforced concrete elements, PhD Thesis, University of Sheffield. 2006.

[88] Sooriyaarachchi, H., Pilakoutas, K., Byars, E.. Tension Stiffening Behaviour of GFRP Reinforced Concrete. In: et al Shield, C.K., editor. Seventh International Symposium on Non-Metallic (FRP) Reinforcement for Concrete Structures. 2005, p. 975–990.

[89] Beeby, A.W., Scottt, R.H.. Cracking and deformation of axially reinforced members subjected to pure tension. Magazine of Concrete Research 2005;57(10):611–621.

[90] Beeby, A.W., Scott, R.H.. Mechanisms of long-term decay of tension stiffening. Magazine of Concrete Research 2006;58(5):255–266.

[91] Chan, H.C., Cheung, Y.K., Huang, Y.P.. Crack analysis of reinforced-concrete tension members. Journal of Structural Engineering-ASCE 1992;118(8):2118–2132.

[92] Abrishami, H.H., Mitchell, D.. Influence of splitting cracks on tension stiffening. ACI Structural Journal 1996;93(6):703–710.

[93] Tammo, K., Thelandersson, S.. Crack behavior near reinforcing bars in concrete structures. ACI Structural Journal 2009;106(3):259–267.

[94] Vecchio, F.J., Collins, M.P.. The modified compression-field theory for reinforced-concrete elements subjected to shear. Journal of the American Concrete Institute 1986;83(2):219–231.

[95] Aiello, M.A., Ombres, L.. Load-deflection analysis of concrete elements reinforced with frp rebars. Mechanics of Composite Materials 1999;35(2):111–118.

[96] Aiello, M.A., Ombres, L.. Cracking analysis of frp-reinforced concrete flexural members. Mechanics of Composite Materials 2000;36(5):389–394.

[97] Bouzaiene, A., Massicotte, B.. Hypoelastic tridimensional model for nonproportional loading of plain concrete. Journal of Engineering Mechanics-ASCE 1997;123(11):1111–1120.

[98] Massicotte, B., Nour, A., Ftima, M.B., Yildiz, E.. Epm3d - a user-supplied constitutive model for the nonlinear finite element analysis of reinforced concrete structures. Tech. Rep. TR-SR07-10; École Polytechnique de Montréal; 2007.

[99] Nour, A., Massicotte, B., Yildiz, E., Koval, V.. Finite element modeling of concrete structures reinforced with internal and external fibre-reinforced polymers. Canadian Journal of Civil Engineering 2007;34(3):340–354.

[100] Kwak, H.G., Song, J.Y.. Cracking analysis of rc members using polynomial strain distribution function. Engineering Structures 2002;24(4):455–468.

[101] Somayaji, S., Shah, S.P.. Bond stress versus slip relationship and cracking response of tension members. Journal of the American Concrete Institute 1981;78(3):217–225.

[102] Pedziwiatr, J.. The influence of the bond between concrete and reinforcement on tension stiffening effect. Magazine of Concrete Research 2009;61(6):437–443.

[103] ACI 318R-05. Building Code Requirements for Structural Concrete and Commentary. ACI Committee 318, American Concrete Institute. Farmimngton Hills, Michigan (USA). 2005.

[104] Sooriyaarachchi, H., Pilakoutas, K., Byars, E.. Models for tension stiffening for deflection of GFRP-RC. In: Taerwe, L., editor. Eighth International Symposium on Non-Metallic (FRP) Reinforcement for Concrete Structures. 2007, p. 108–115.

[105] Bischoff, P.H.. Reevaluation of deflection prediction for concrete beams reinforced with steel and fiber reinforced polymer bars. Journal of Structural Engineering-ASCE 2005;131(5):752–767.

[106] ACI 440.1R-06. Guide for the Design and Construction of Concrete Reinforced with FRPBars. ACI Committee 440, American Concrete Institute. Farmington Hills, Michigan (USA). 2006.

[107] Bischoff, P.H.. Deflection calculation of frp reinforced concrete beams based on modifications to the existing branson equation. Journal of Composites for Construction 2007;11(1):4–14.

[108] ACI 440.1R-03. Guide for the Design and Construction of Concrete Reinforced with FRP Bars. ACI Committee 440, American Concrete Institute. Farmington Hills, Michigan (USA). 2003.

[109] Rehm, G.. The fundamentals of bond between steel reinforcement and concrete. Deutscher Ausschuss für Stahlbeton 1961;(138):59.

[110] RC6. Bond Test for Reinforcing Steel. 2. Pull-out Test, 1983. RILEM Technical Recommendations for the Testing and Use of Construction Materials. E&FN Spon. London (United Kingdom). p 218-220. 1994.

[111] ACI 440.3R-04. Guide Test Methods for Fiber-Reinforced Polymers (FRPs) for Reinforcing or Strengthening Concrete Structures. ACI Committee 440, American Concrete Institute. Farmington Hills, Michigan (USA). 2004.

[112] Bazant, Z.P., Sener, S.. Size effect in pullout tests. ACI Materials Journal 1988;85(5):347–351.

[113] UNE-EN 12390-3:2003. Ensayos de Hormigón Endurecido. Parte 3: Determinación de la Resistencia a Compresión de probetas. AENOR, Asociación Española de Normalización y Certificación. Madrid. 20p. 2003.

[114] ASTM C 469-87. Standard Test Method for Static Modulus of Elasticity and Poisson's Ratio of Concrete in Compression. ASTM Standards, American Society for Testing and Materials. Philadelphia (USA). Philadelphia; 1987.

[115] H.A. Toutanji, H., Saafi, M.. Flexural behavior of concrete beams reinforced with glass fiber-reinforced polymer (GFRP) bars. ACI Structural Journal 2000;97(5):712–719.

[116] Masmoudi, R., Thériault, M., Benmokrane, B.. Flexural behavior of concrete beams reinforced with deformed fiber reinforced plastic reinforcing rods. ACI Structural Journal 1998;95(6):665–676.

[117] Benmokrane, B., Chaallal, O., Masmoudi, R.. Flexural response of concrete beams reinforced with FRP reinforcing bars. ACI Structural Journal 1996;93(1):46–55.

[118] Pecce, M., Manfredi, G., Cosenza, E.. Experimental response and code models of GFRP RC beams in bending. Journal of Composites for Construction 2000;4(4):182–190.

[119] Barris, C., torres, L., Turon, A., Baena, M., Catalan, A.. An experimental study of the flexural behaviour of GFRP RC beams and comparison with prediction models. Compos 2009;91(3):286–295.

[120] Borosnyói, A.. Serviceability of CFRP prestressed concrete beams, PhD Thesis, Budapest University of Technology and Economics. 2002.

[121] Piyasena, R.. Crack spacing, crack width and tension stiffening effect in reinforced concrete beams and one-way slabs, PhD Thesis, Griffith University. 2002.

[122] Wang, C., Salmon, C.. Reinforced Concrete Design. Harper Collins Publication Inc.; 1992.

[123] Kaklauskas, G., Girdzius, R., Bacinskas, D., Sokolov, A.. Numerical deformation analysis of bridge concrete girders. Baltic Journal of Road and Bridge Engineering 2008;3(2):51–56.

Appendix A

Experimental bond-slip laws

A.1 Series C2 concrete

A.1.1 Rebar R1

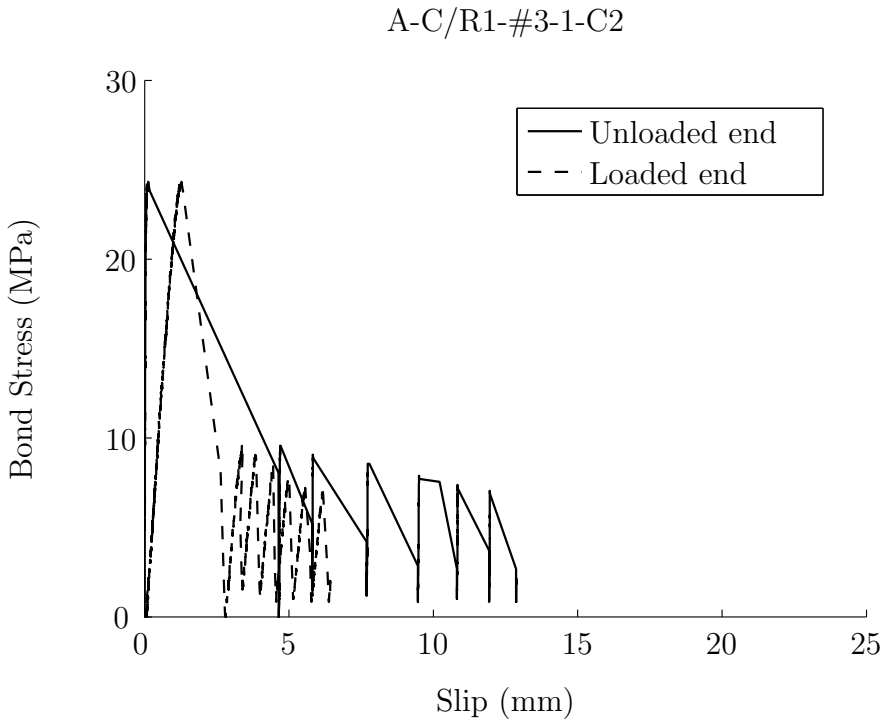

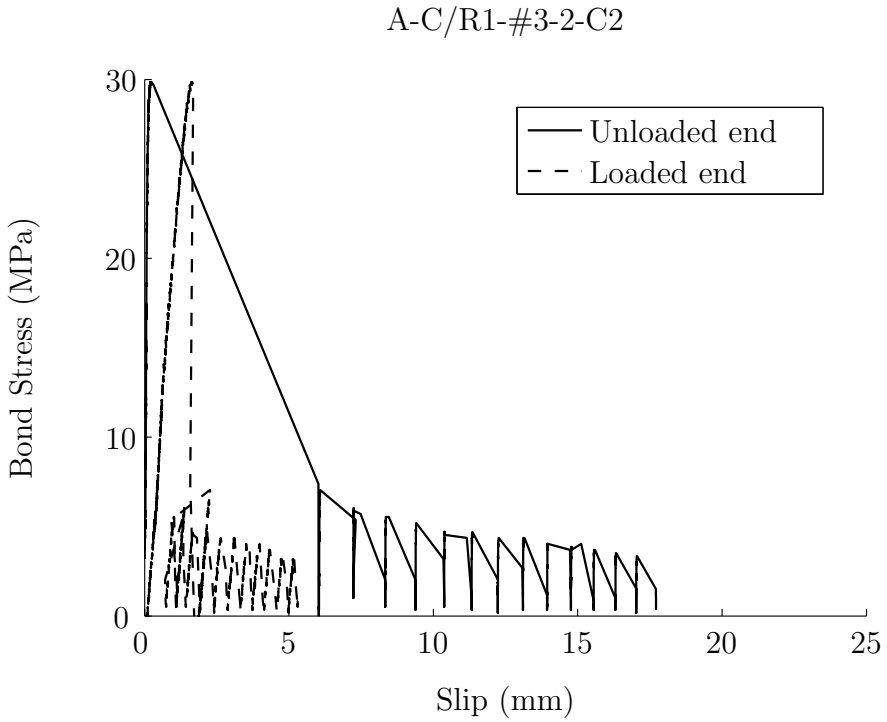

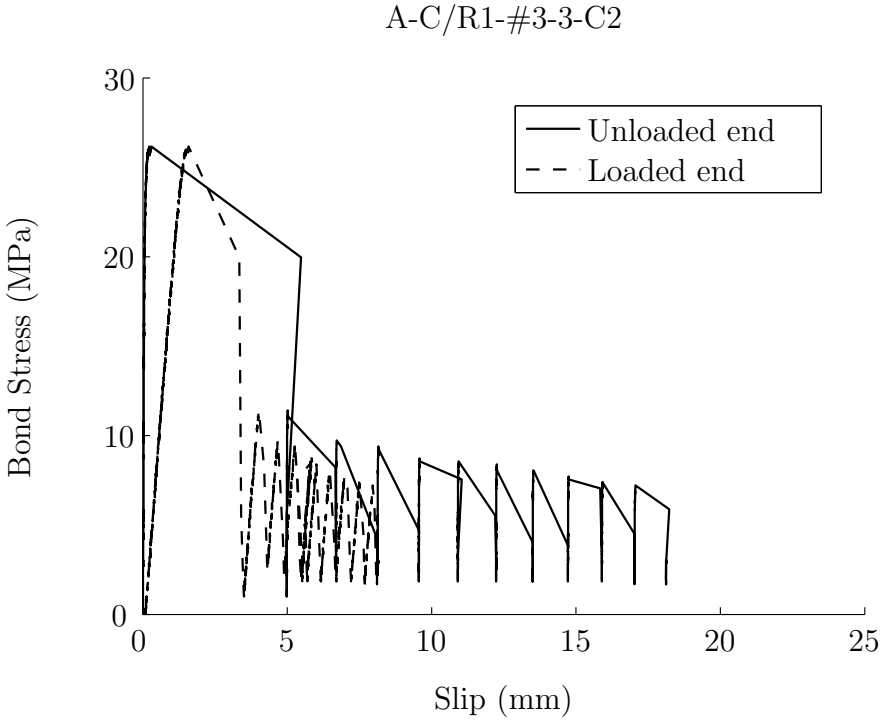
A-C/R1-#3-3-C2
Unloaded end
Loaded end
Bond Stress (MPa)
Slip (mm)
0
10
20
30
0
5
10
15
20
25

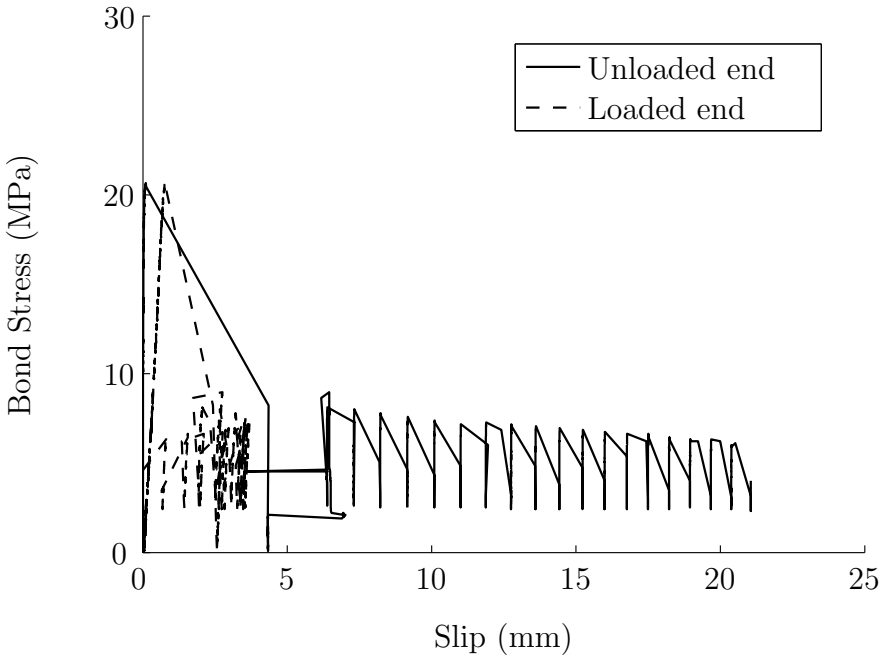
A-C/R1-#4-1-C2
Unloaded end
Loaded end
Bond Stress (MPa)
Slip (mm)
0
10
20
30
0
5
10
15
20
25

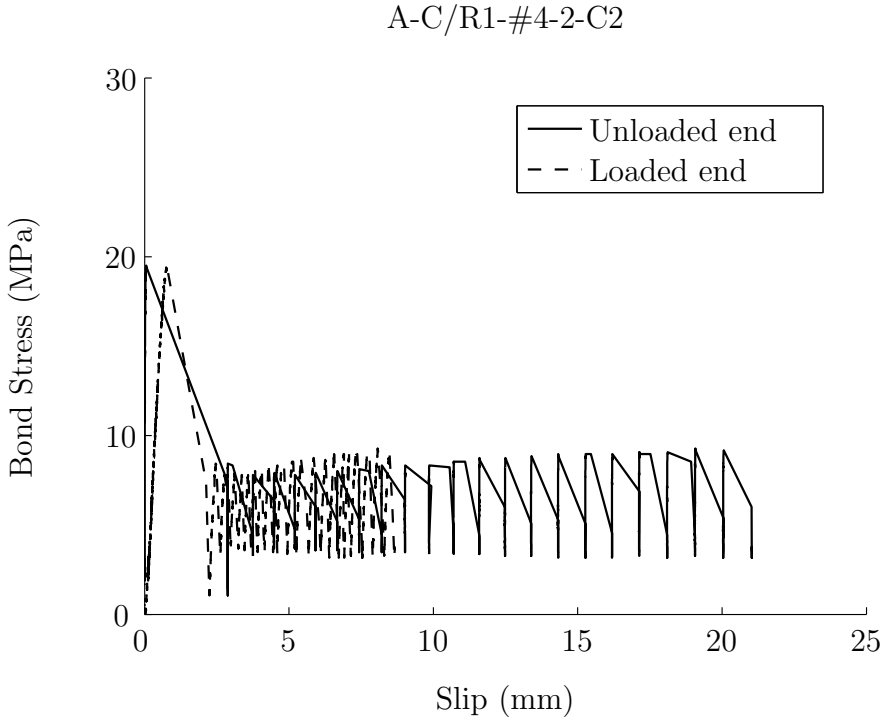
A-C/R1-#4-2-C2
Unloaded end
Loaded end
Bond Stress (MPa)
Slip (mm)
0
10
20
30
0
5
10
15
20
25

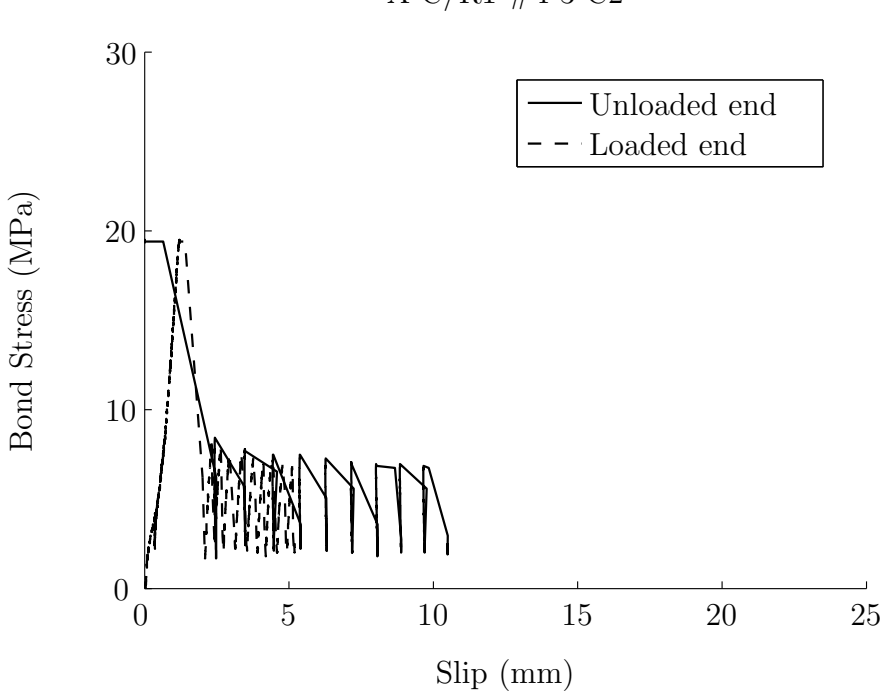
A-C/R1-#4-3-C2
Unloaded end
Loaded end
Bond Stress (MPa)
Slip (mm)
0
10
20
30
0
5
10
15
20
25

A.1.2 Rebar R2

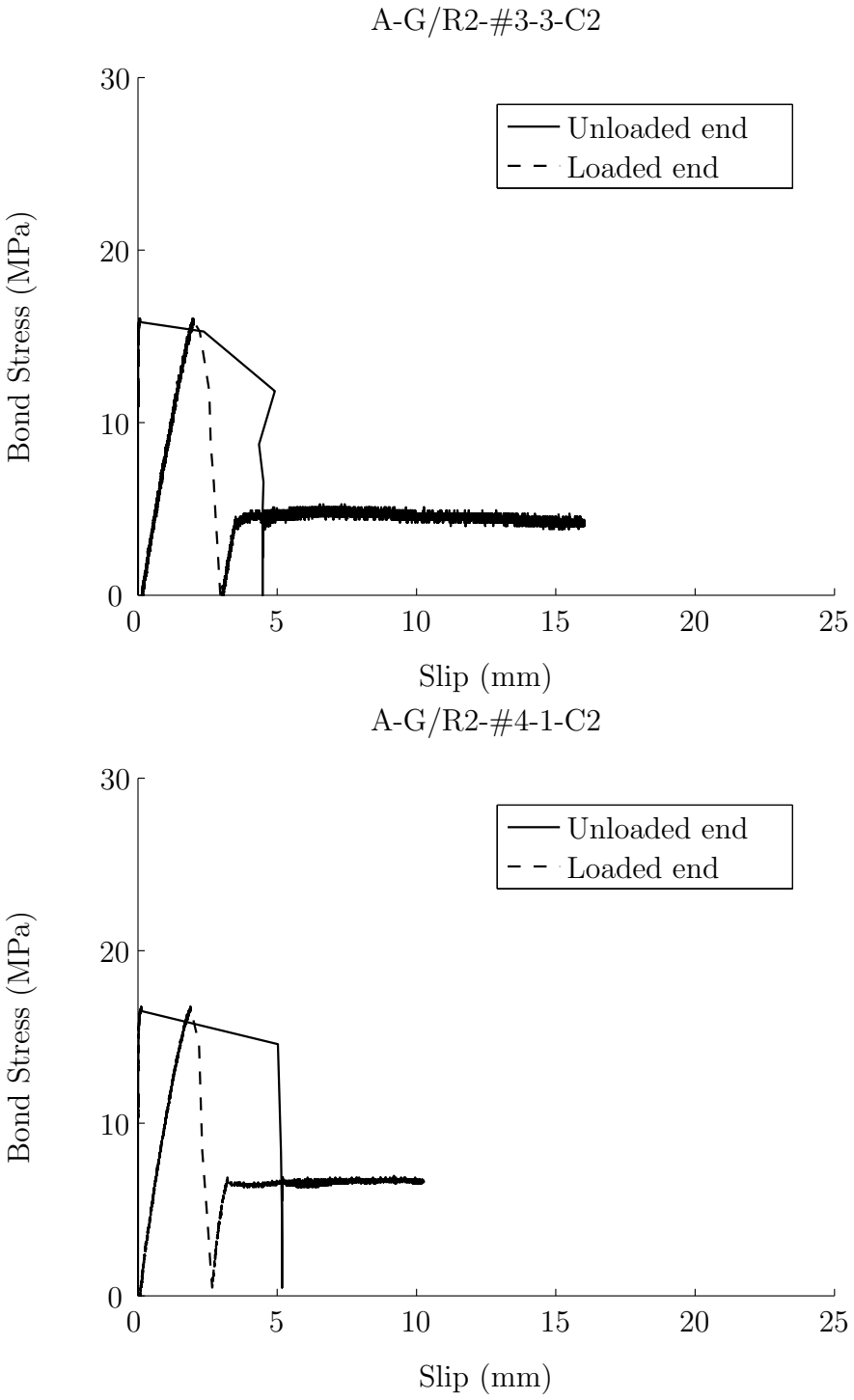
A-G/R2-#3-3-C2
Unloaded end
Loaded end
Bond Stress (MPa)
Slip (mm)
0
10
20
30
0
5
10
15
20
25
A-G/R2-#4-1-C2
Unloaded end
Loaded end
Bond Stress (MPa)
Slip (mm)

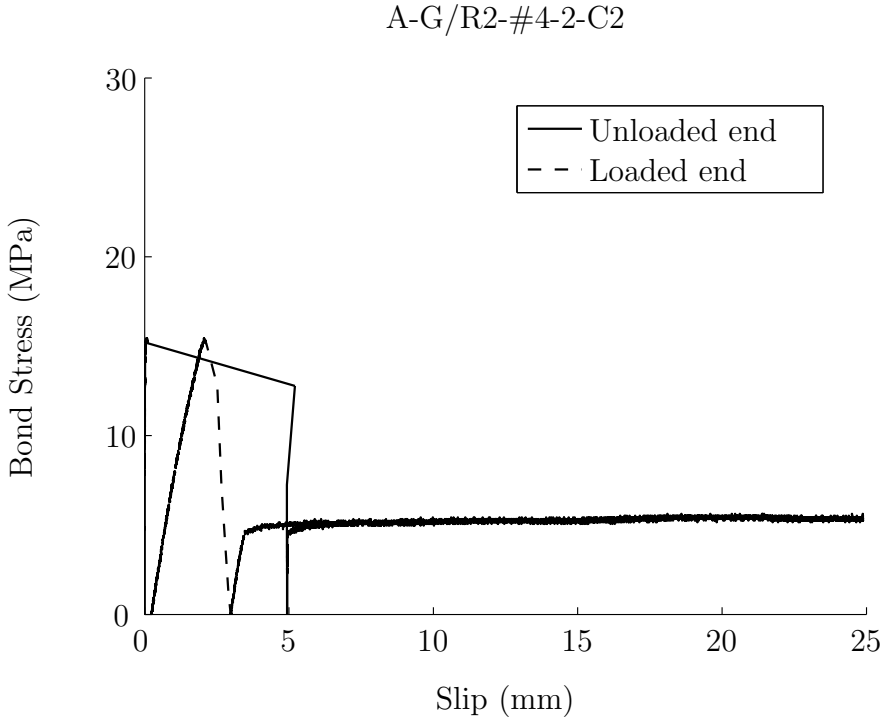
A-G/R2-#4-2-C2
Unloaded end
Loaded end
Bond Stress (MPa)
Slip (mm)
0
10
20
30
0
5
10
15
20
25

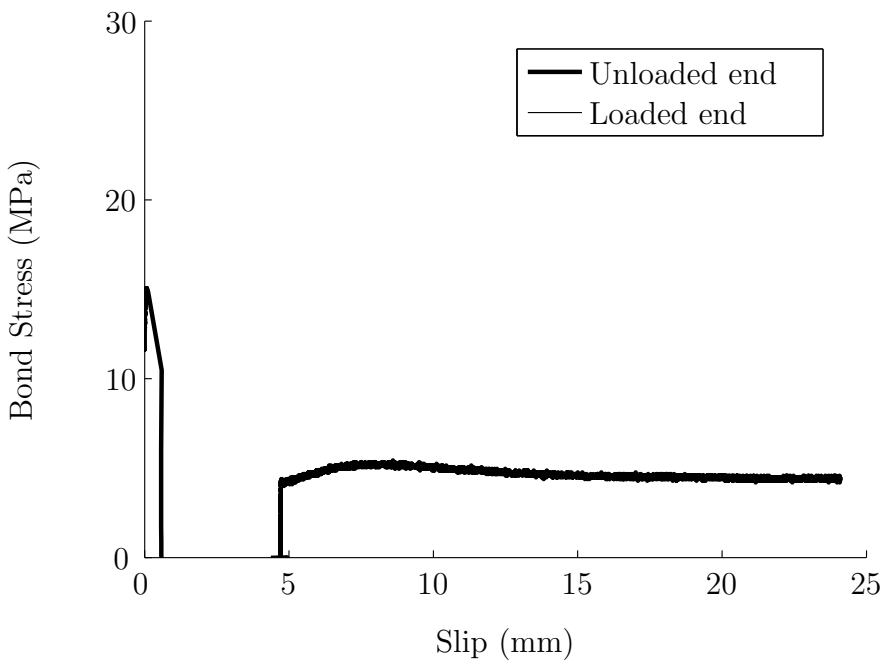
A-G/R2-#4-3-C2
Unloaded end
Loaded end
Bond Stress (MPa)
Slip (mm)
0
10
20
30
0
5
10
15
20
25

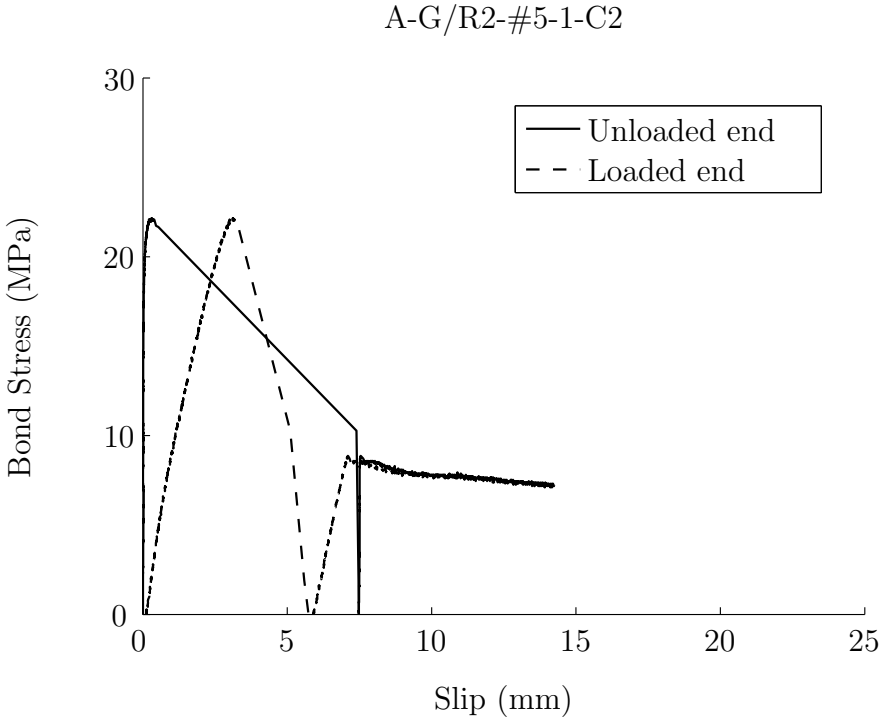
A-G/R2-#5-1-C2
Unloaded end
Loaded end
Bond Stress (MPa)
Slip (mm)
0
10
20
30
0
5
10
15
20
25

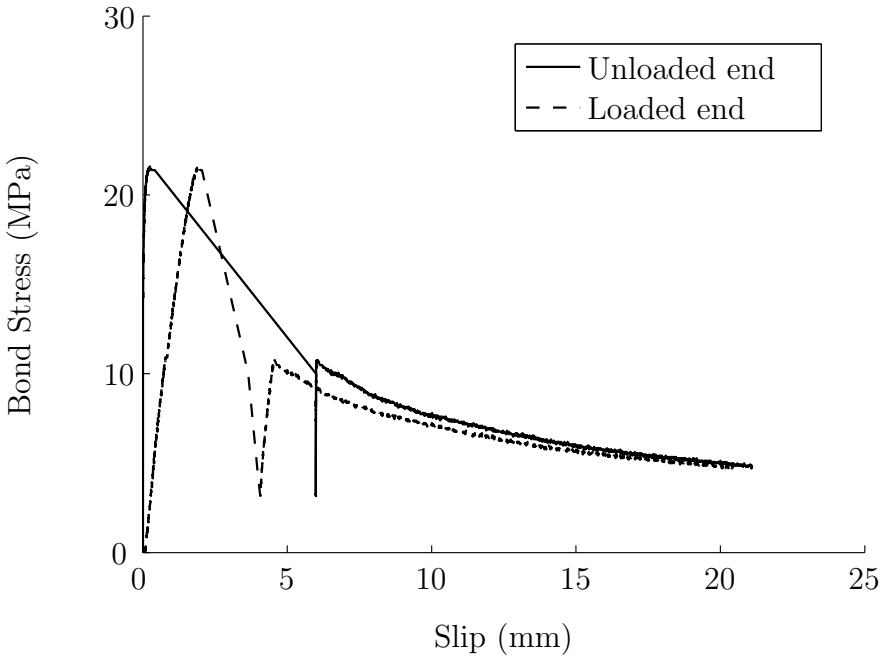
A-G/R2-#5-2-C2
Unloaded end
Loaded end
Bond Stress (MPa)
Slip (mm)
0
10
20
30
0
5
10
15
20
25

A-G/R2-#6-1-C2

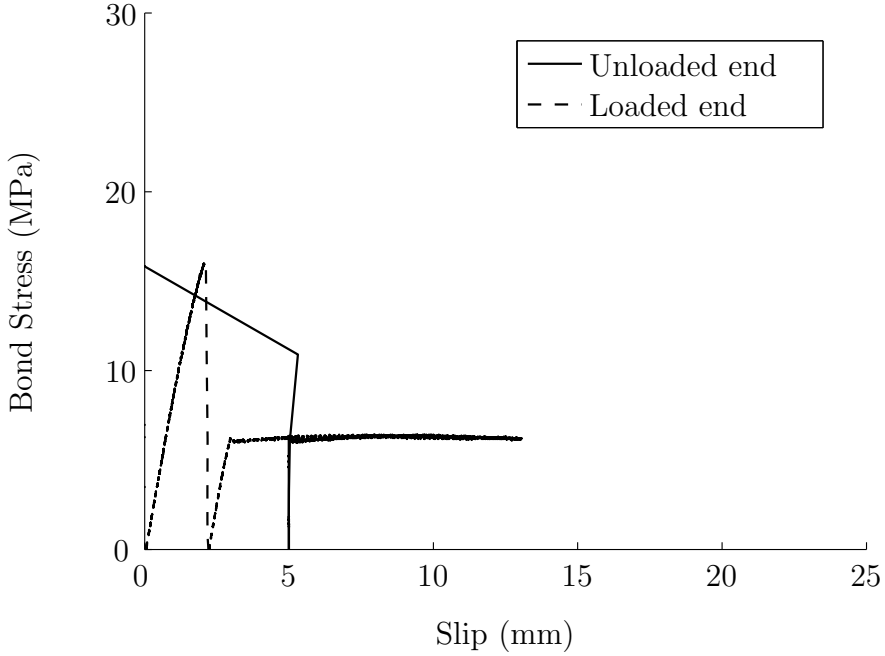

A-G/R2-#6-2-C2

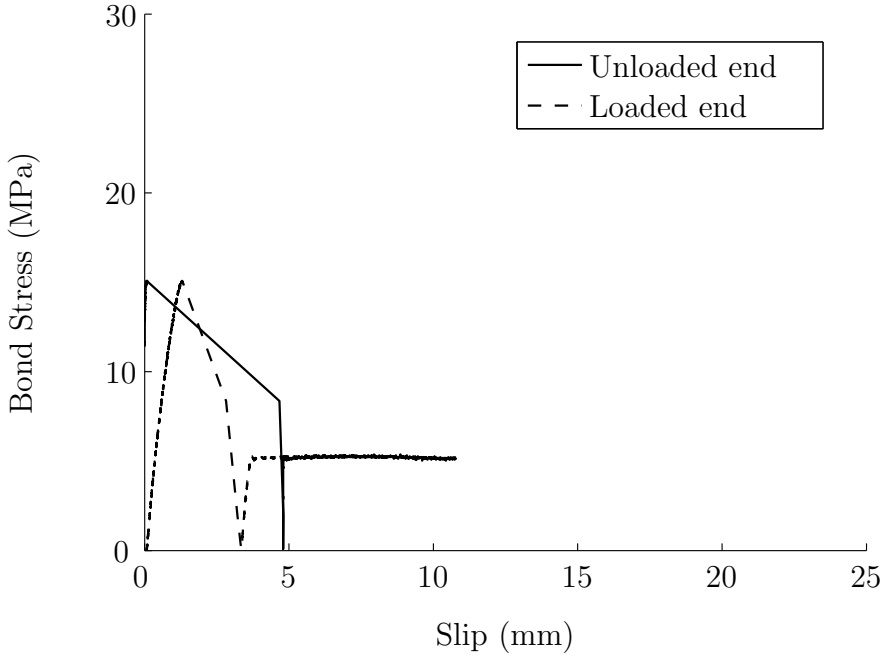

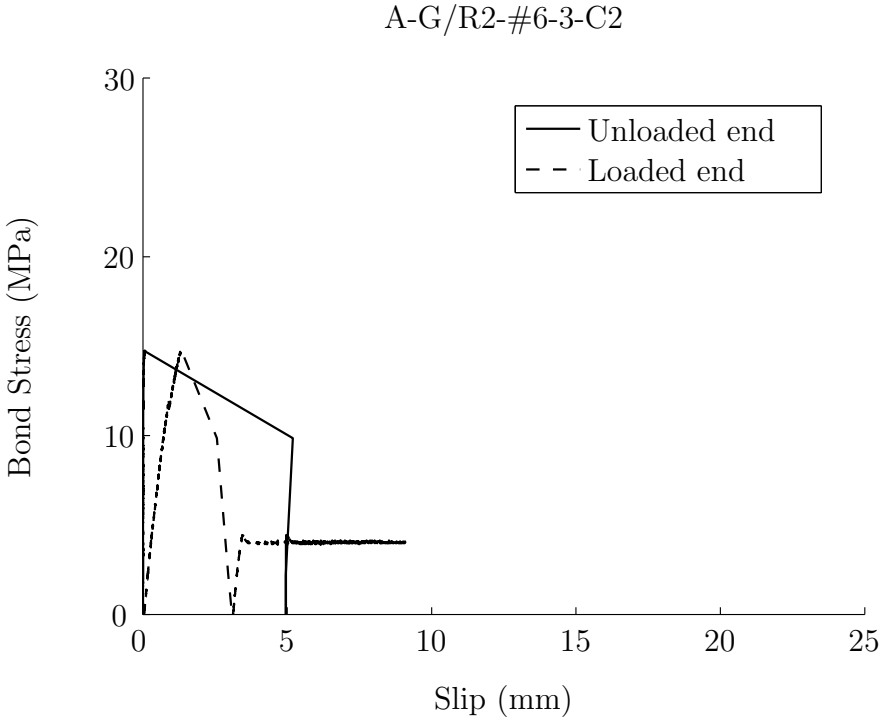
A-G/R2-#6-3-C2
Unloaded end
Loaded end
Bond Stress (MPa)
Slip (mm)
0
10
20
30
0
5
10
15
20
25

A.1.3 Rebar R3

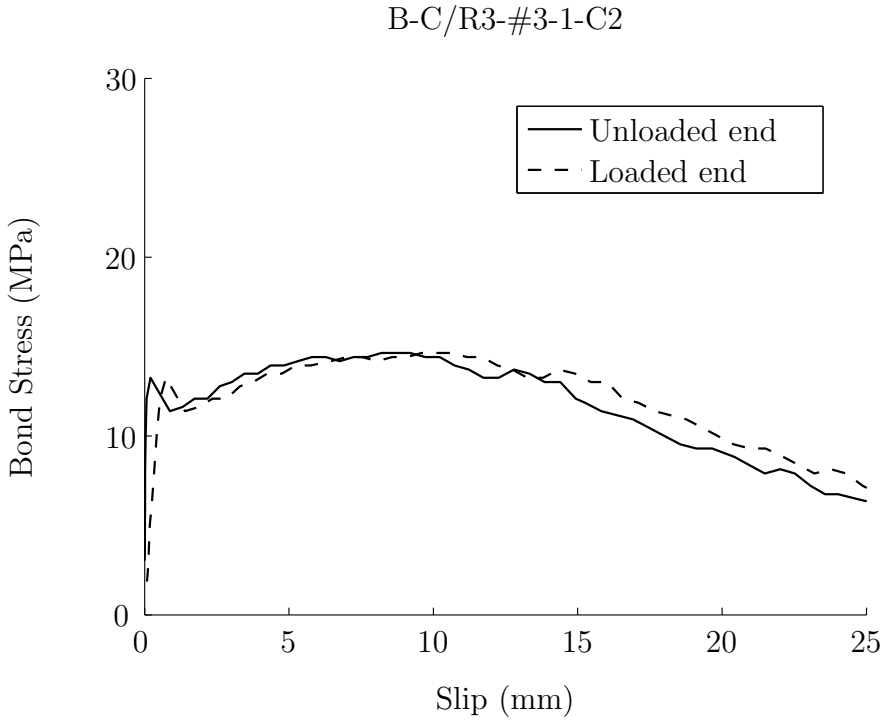
B-C/R3-#3-1-C2
Unloaded end
Loaded end
Bond Stress (MPa)
Slip (mm)
0
5
10
15
20
25
30

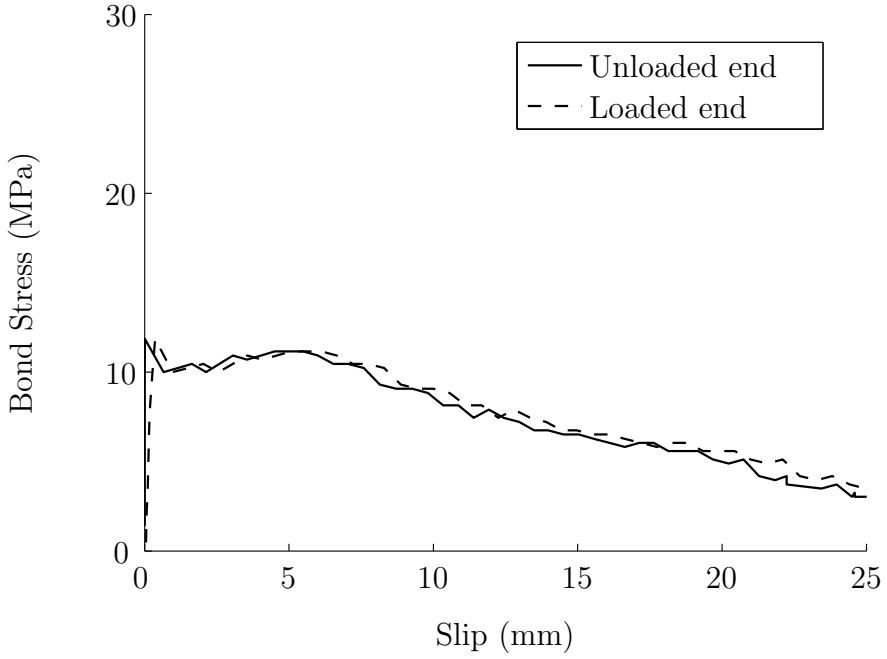
B-C/R3-#3-2-C2
Unloaded end
Loaded end
Bond Stress (MPa)
Slip (mm)
0
5
10
15
20
25
30

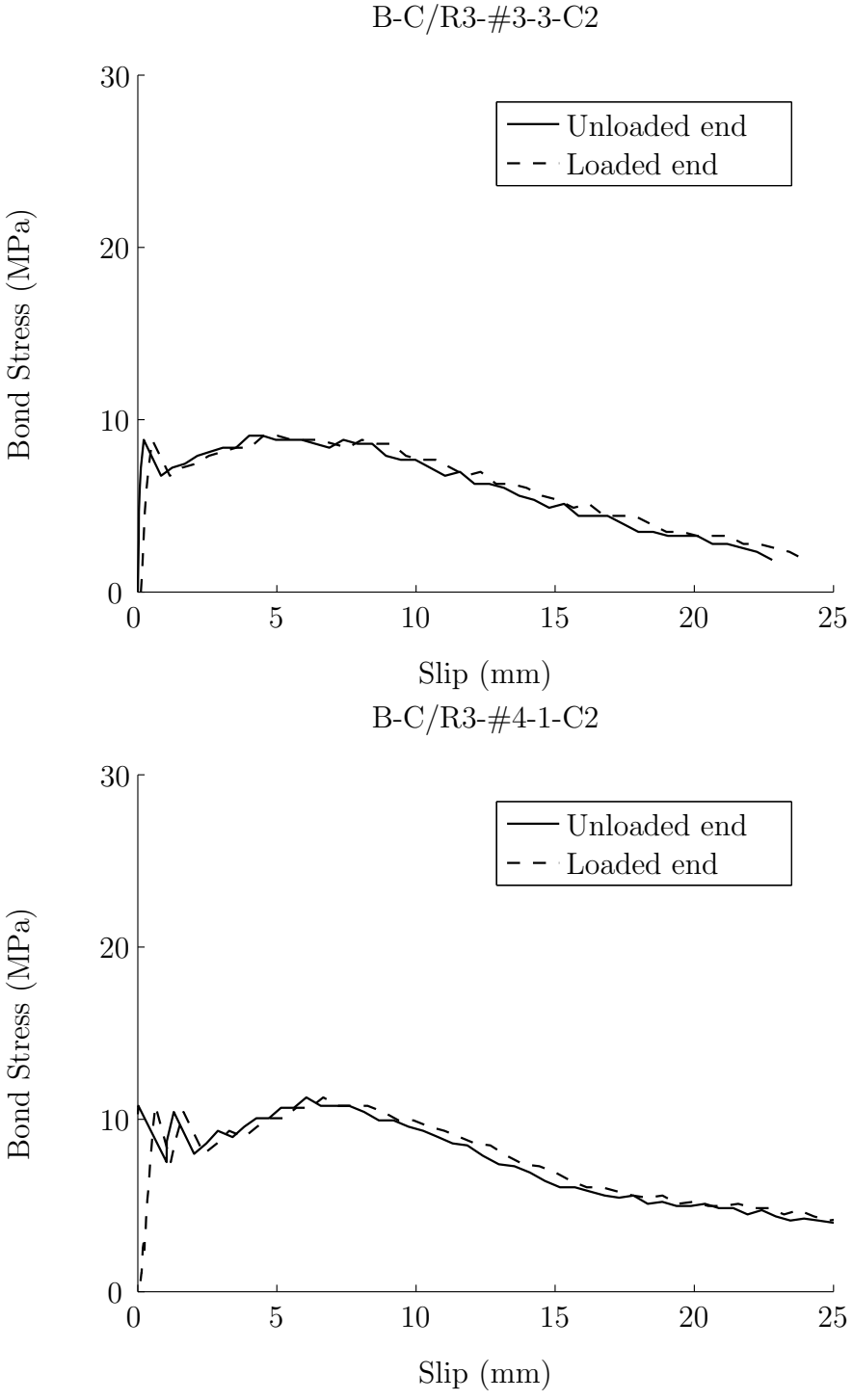
B-C/R3-#3-3-C2
Unloaded end
Loaded end
Bond Stress (MPa)
Slip (mm)
0
10
20
30
0
5
10
15
20
25
B-C/R3-#4-1-C2
Unloaded end
Loaded end
Bond Stress (MPa)
Slip (mm)
0
10
20
30
0
5
10
15
20
25

B-C/R3-#4-2-C2

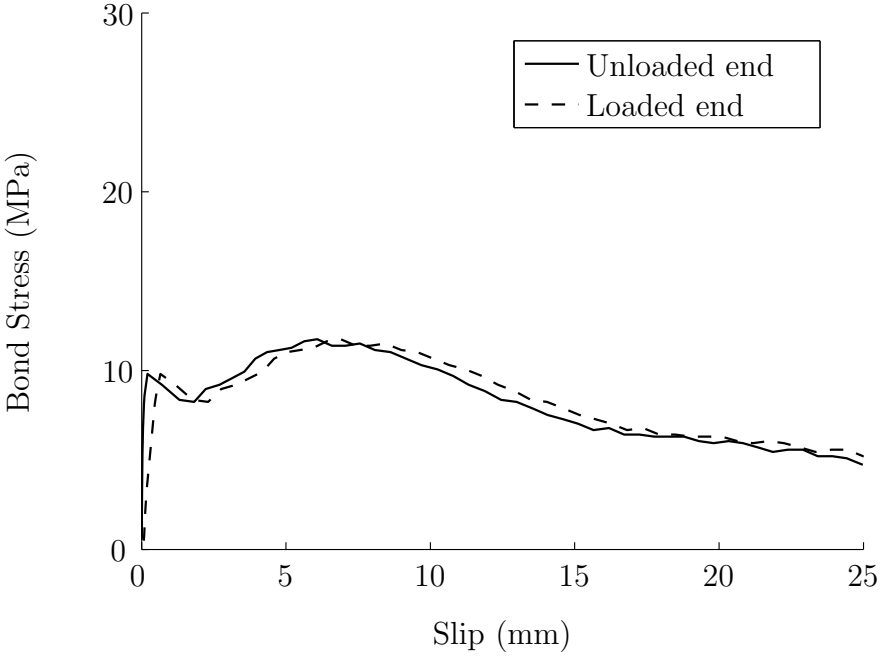

B-C/R3-#4-3-C2

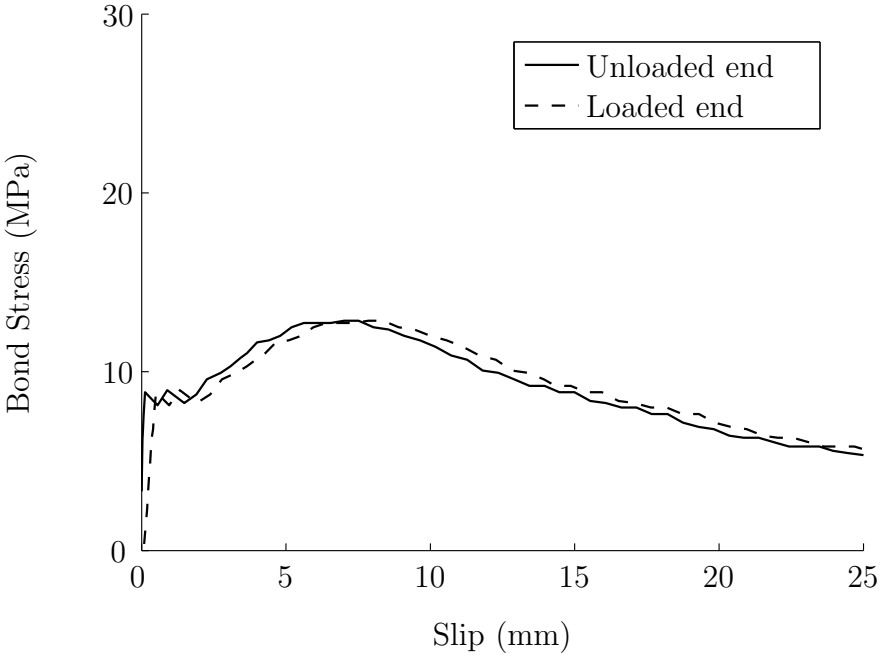

A.1.4 Rebar R4

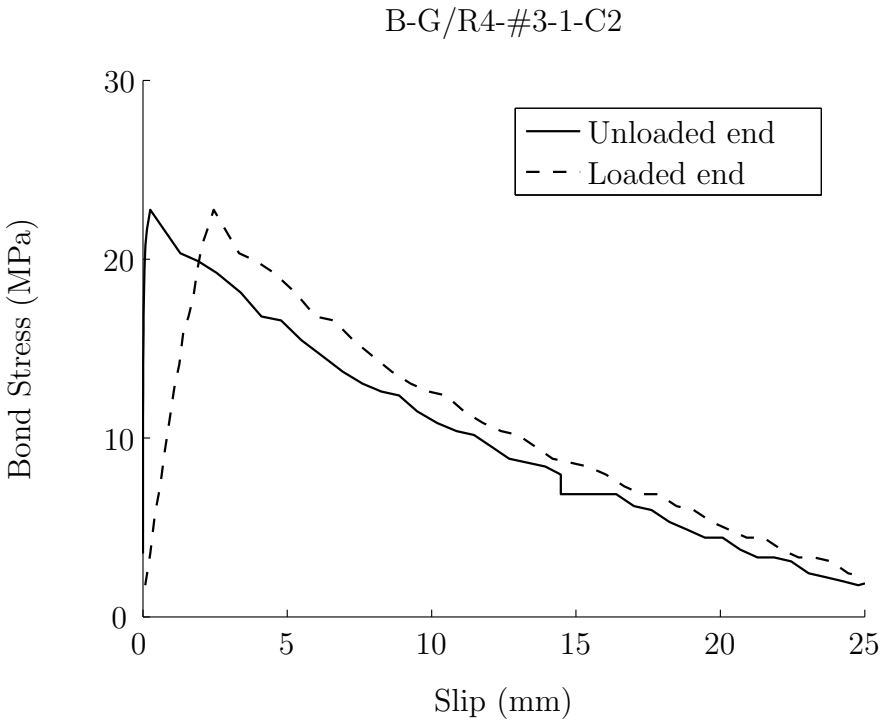
B-G/R4-#3-1-C2
Unloaded end
Loaded end
Bond Stress (MPa)
Slip (mm)
0
10
20
30
0
5
10
15
20
25

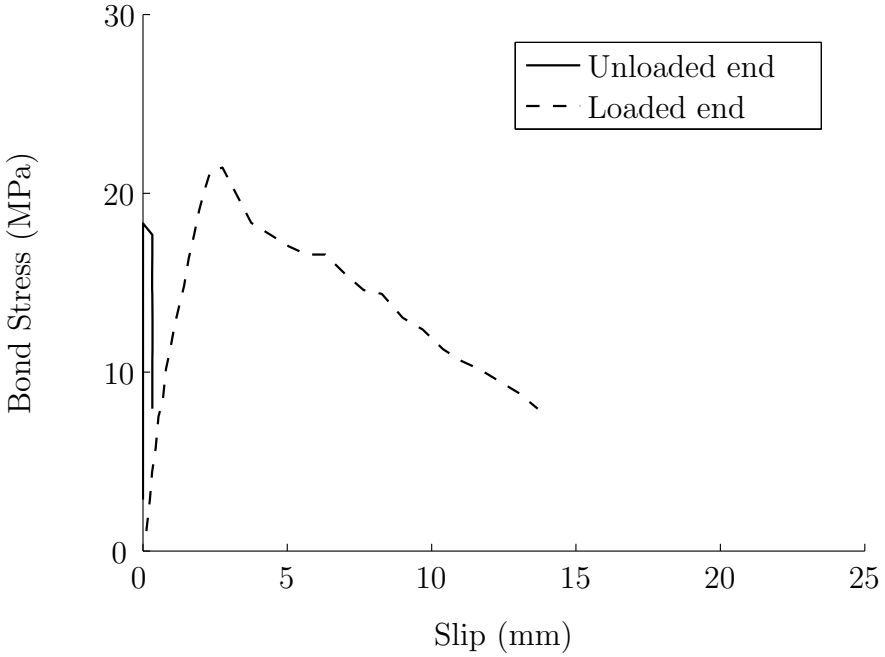
B-G/R4-#3-2-C2
Unloaded end
Loaded end
Bond Stress (MPa)
Slip (mm)
0
10
20
30
0
5
10
15
20
25

B-G/R4-#3-3-C2

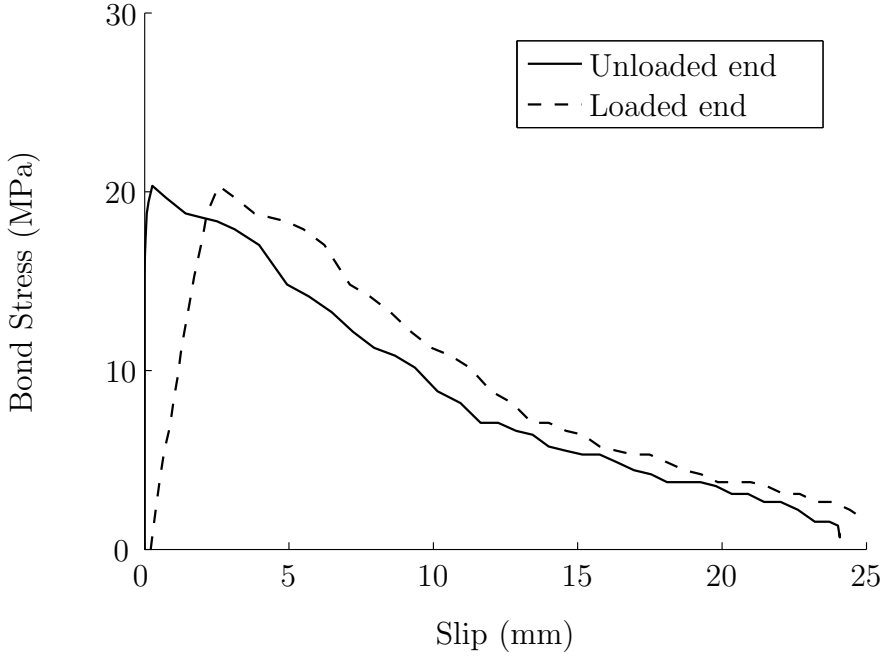

B-G/R4-#4-1-C2

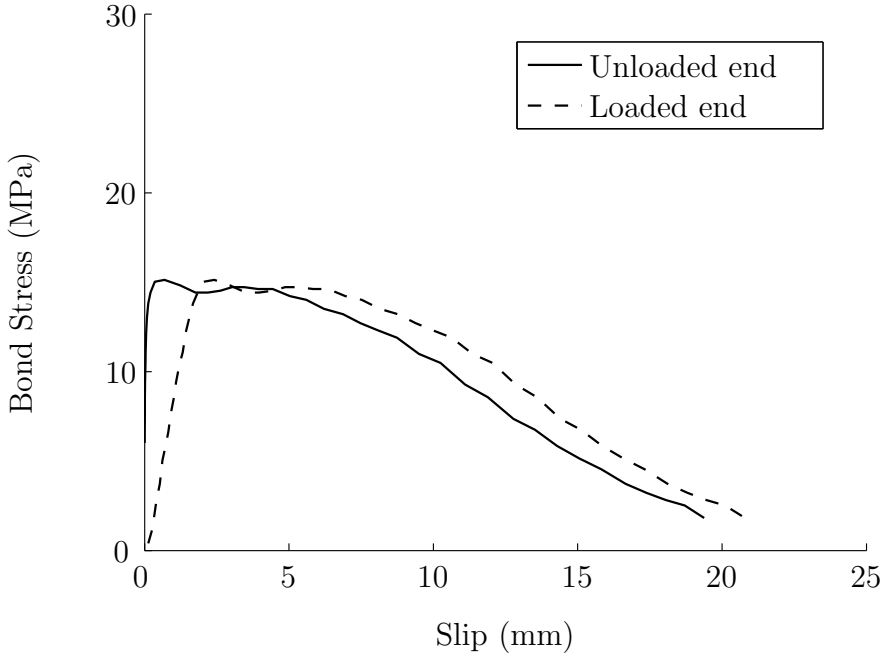

B-G/R4-#4-2-C2

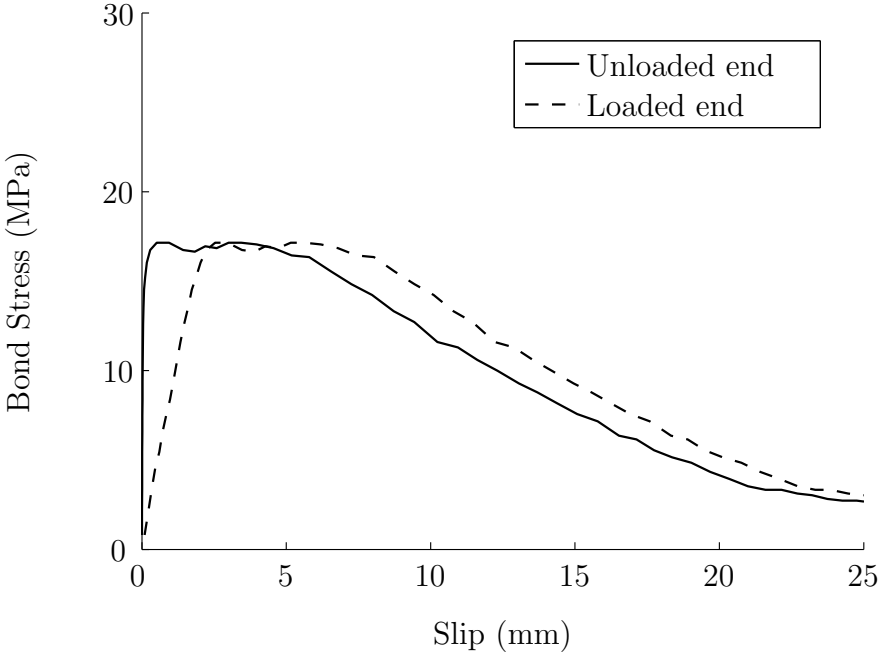

B-G/R4-#4-3-C2

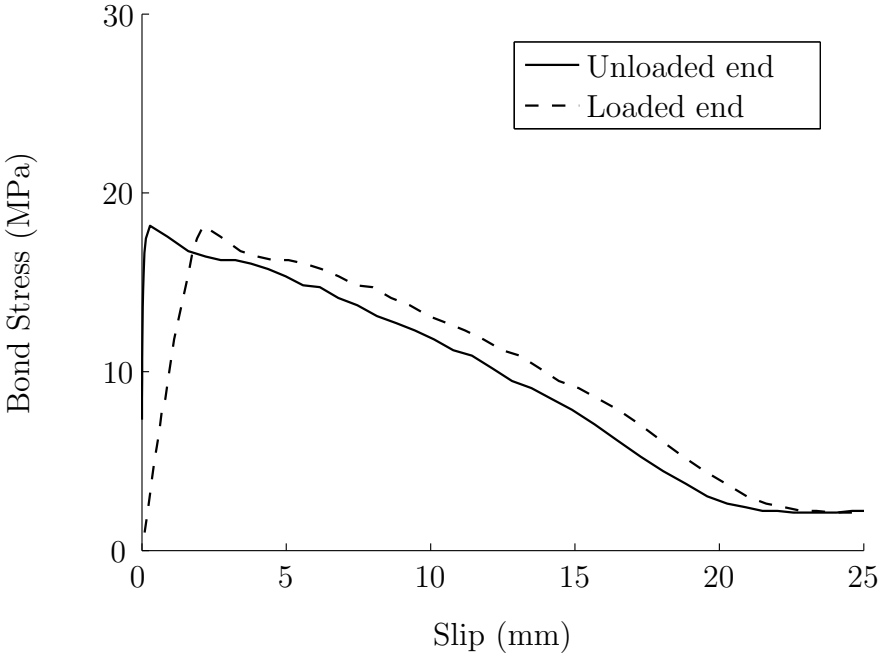

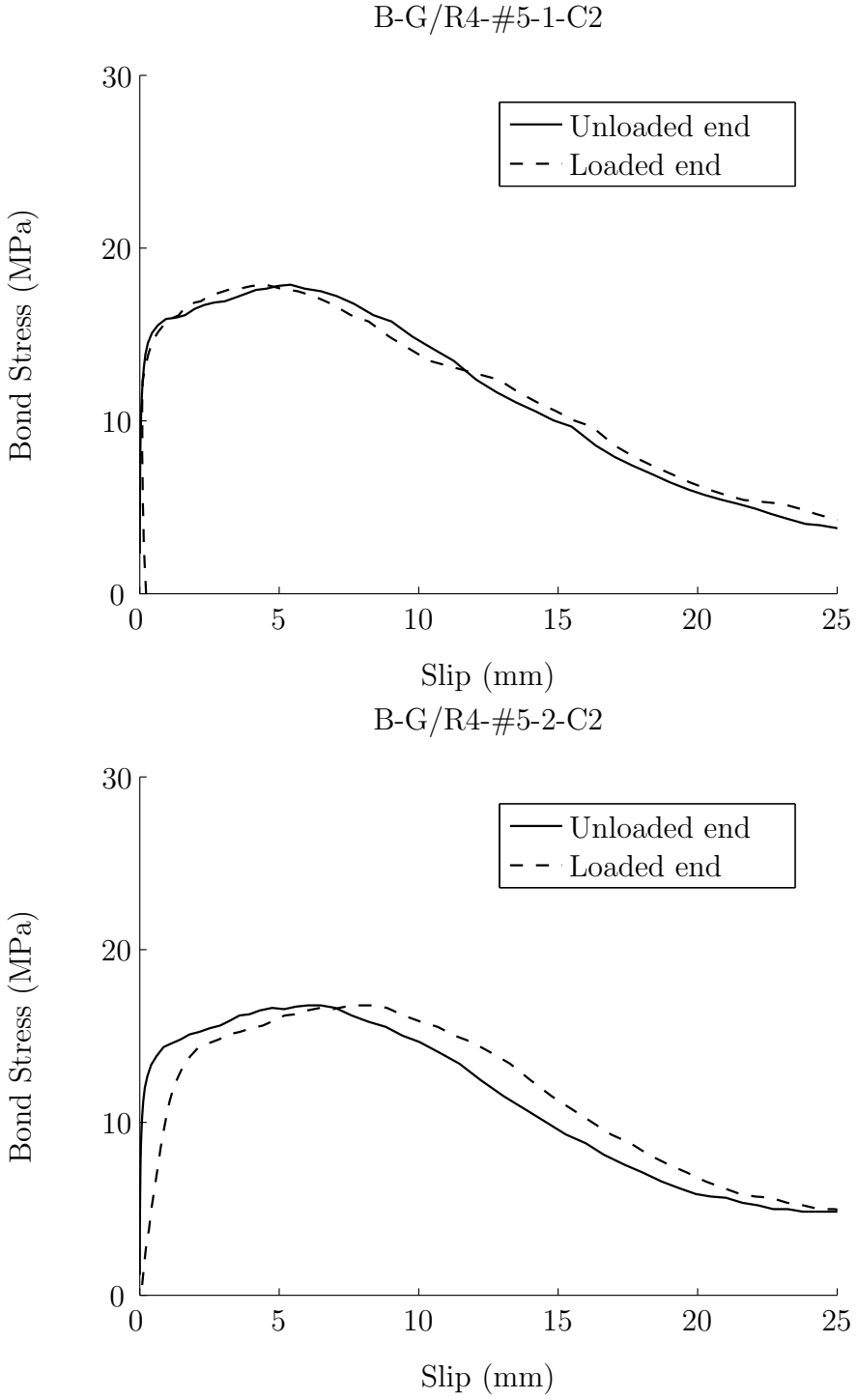
B-G/R4-#5-1-C2
Unloaded end
Loaded end
Bond Stress (MPa)
Slip (mm)
0
10
20
30
0
5
10
15
20
25
B-G/R4-#5-2-C2
Unloaded end
Loaded end
Bond Stress (MPa)
Slip (mm)

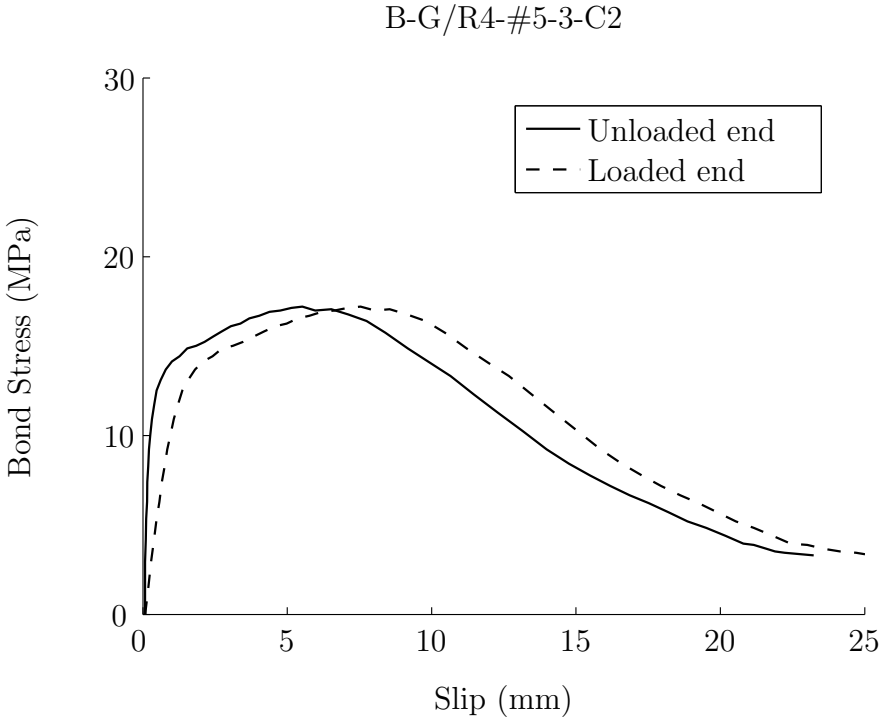
B-G/R4-#5-3-C2
Unloaded end
Loaded end
Bond Stress (MPa)
Slip (mm)
0
10
20
30
0
5
10
15
20
25

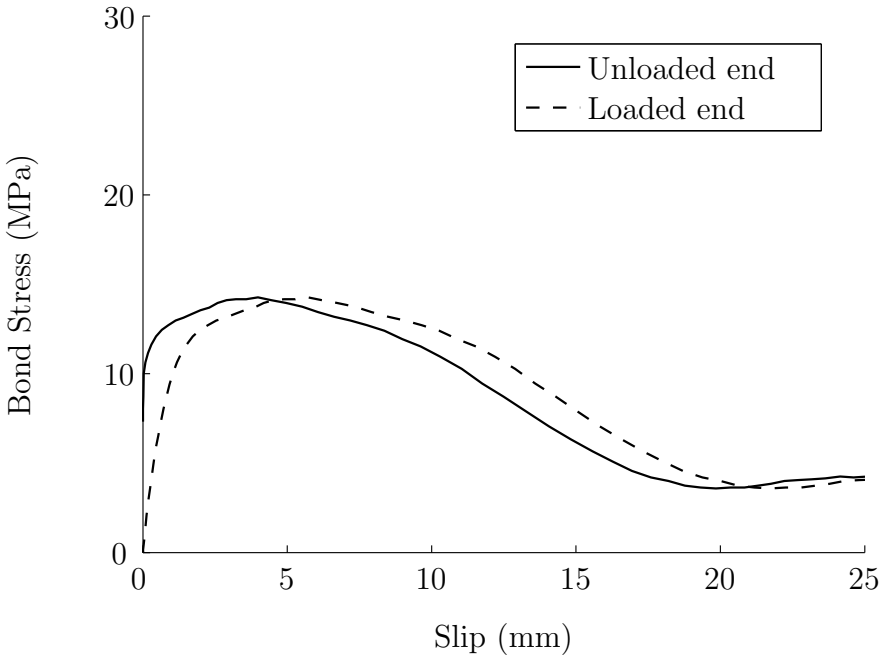
B-G/R4-#6-1-C2
Unloaded end
Loaded end
Bond Stress (MPa)
Slip (mm)
0
10
20
30
0
5
10
15
20
25

B-G/R4-#6-2-C2

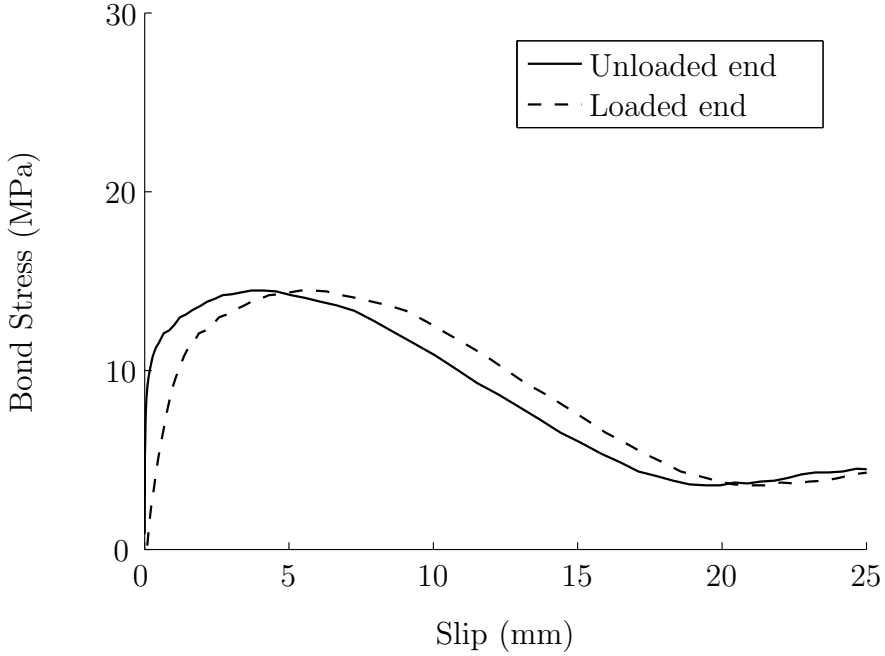

B-G/R4-#6-3-C2

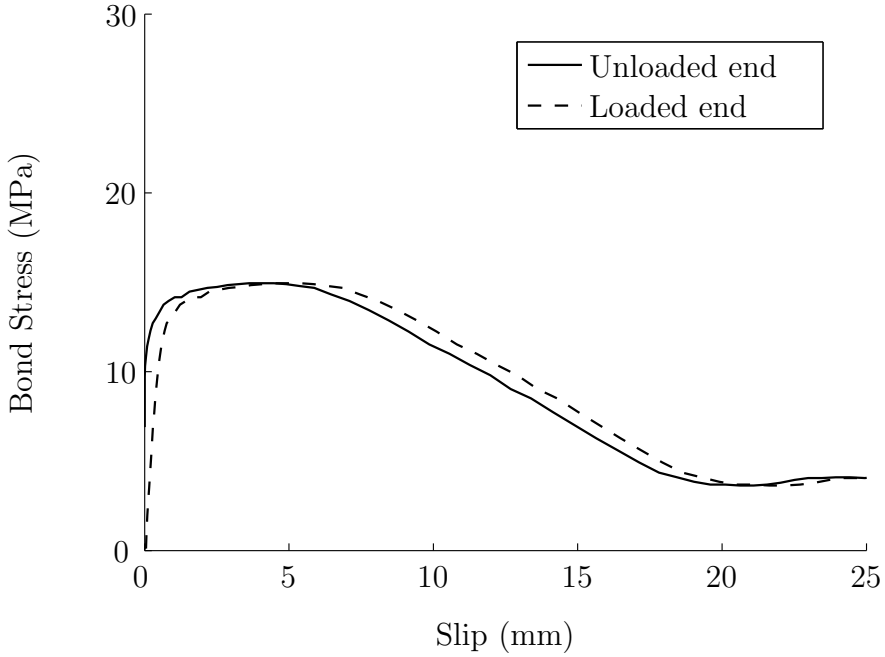

A.1.5 Rebar R5

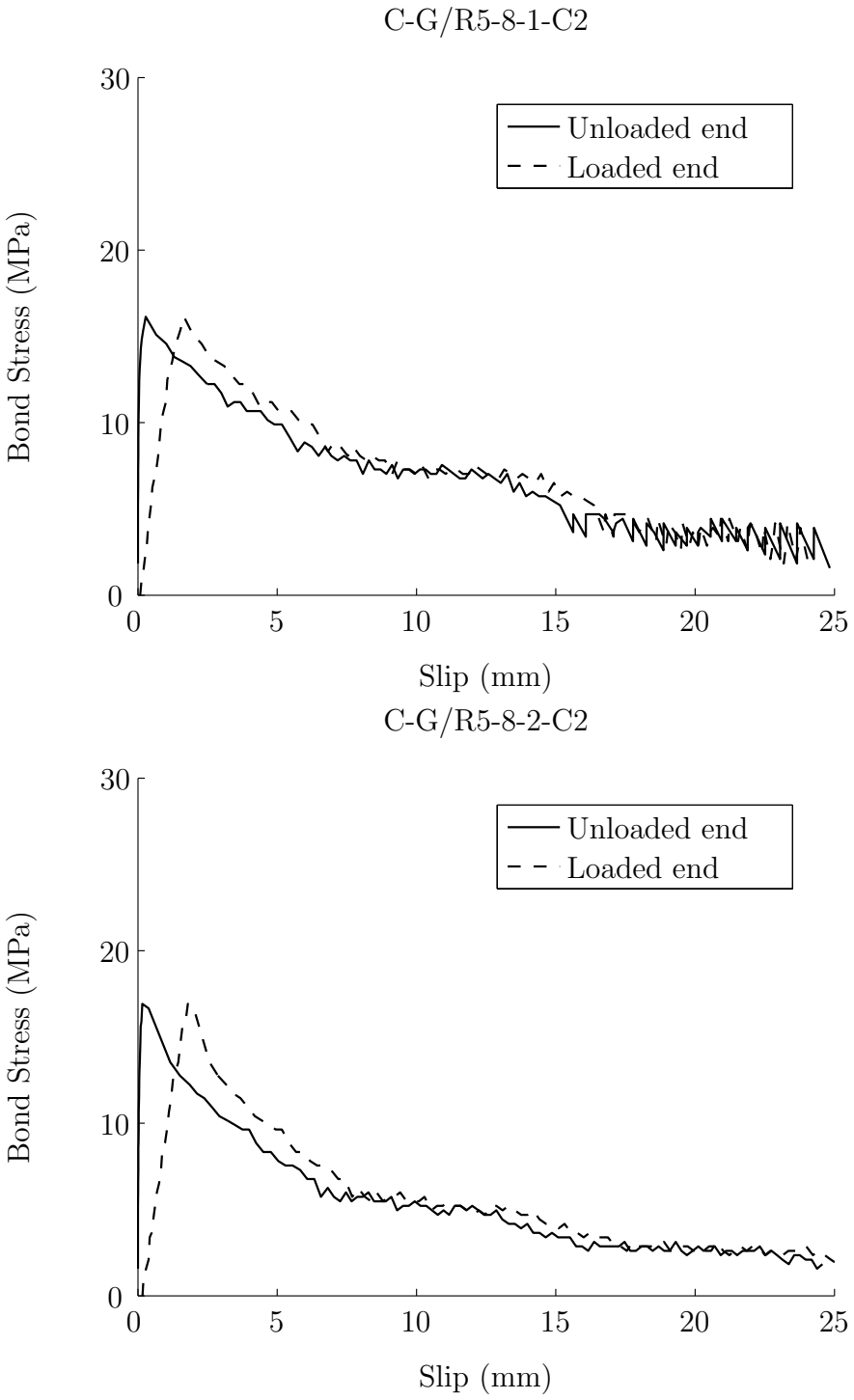
C-G/R5-8-1-C2
Unloaded end
Loaded end
Bond Stress (MPa)
Slip (mm)
0
10
20
30
0
5
10
15
20
25
C-G/R5-8-2-C2
Unloaded end
Loaded end
Bond Stress (MPa)
Slip (mm)

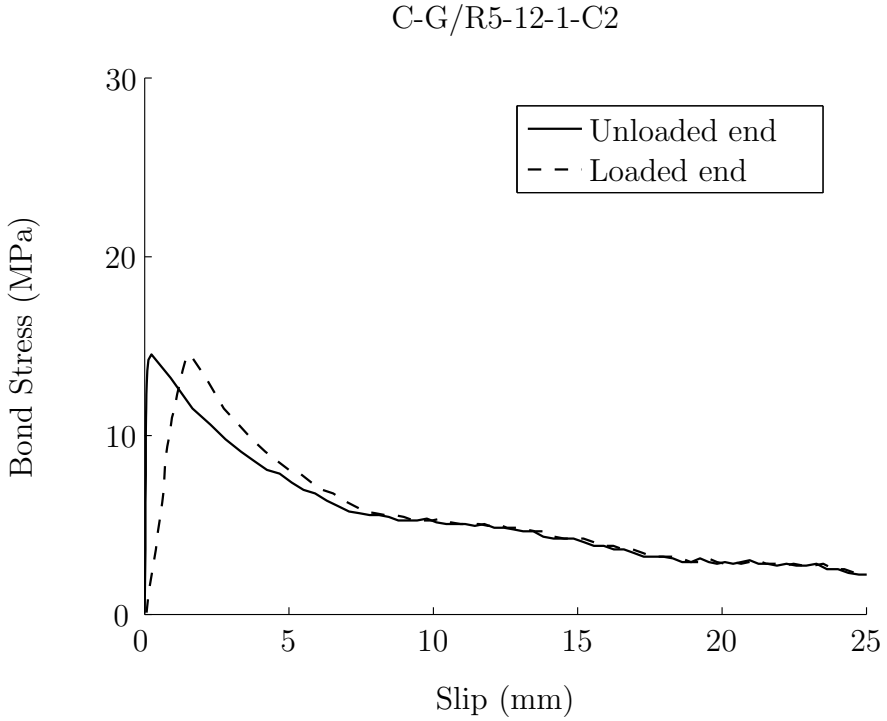
C-G/R5-12-1-C2
Unloaded end
Loaded end
Bond Stress (MPa)
Slip (mm)
0
10
20
30
0
5
10
15
20
25

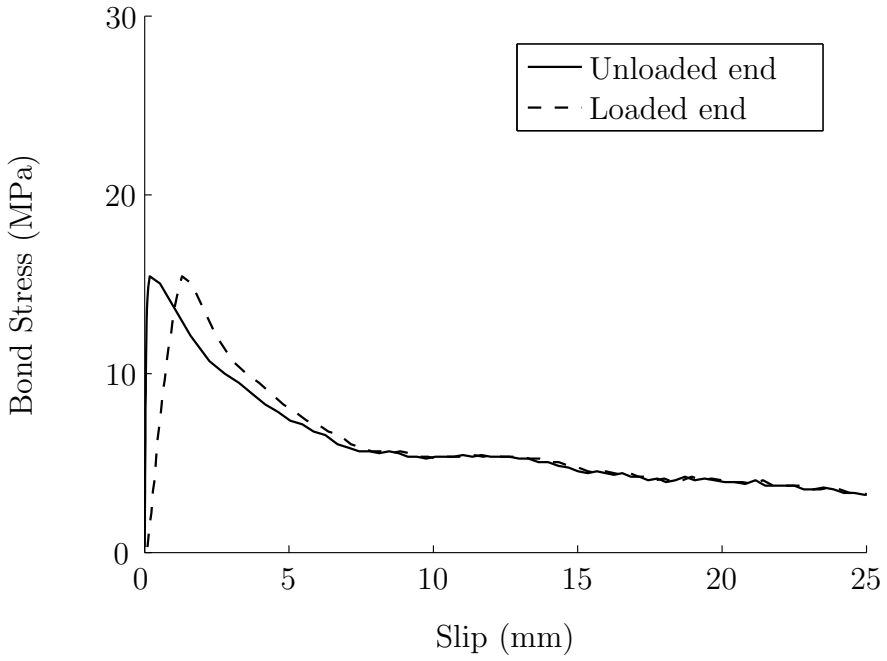
C-G/R5-12-2-C2
Unloaded end
Loaded end
Bond Stress (MPa)
Slip (mm)
0
10
20
30
0
5
10
15
20
25

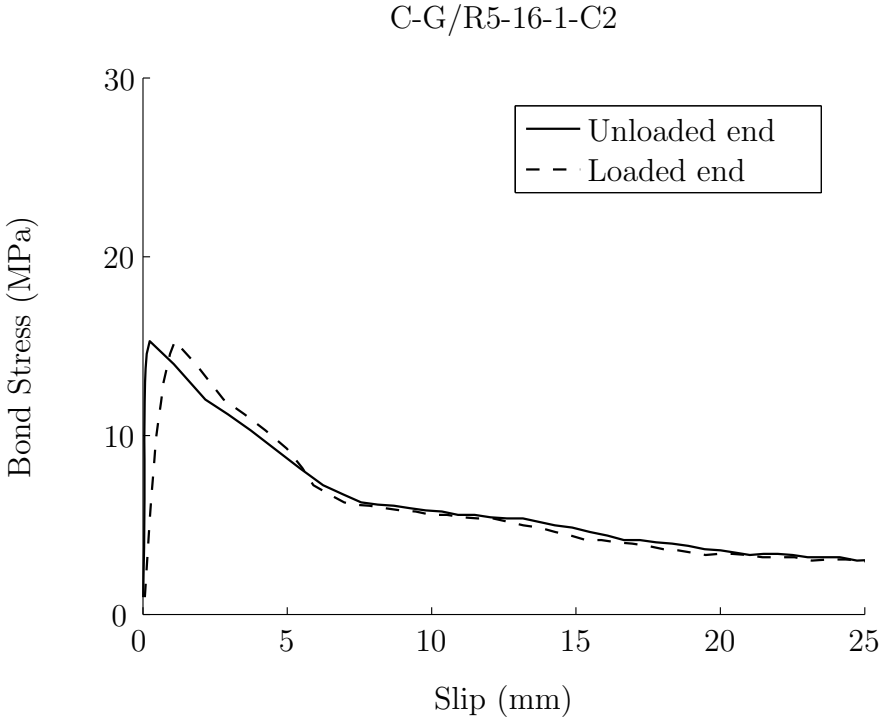
C-G/R5-16-1-C2
Unloaded end
Loaded end
Bond Stress (MPa)
Slip (mm)
0
10
20
30
0
5
10
15
20
25

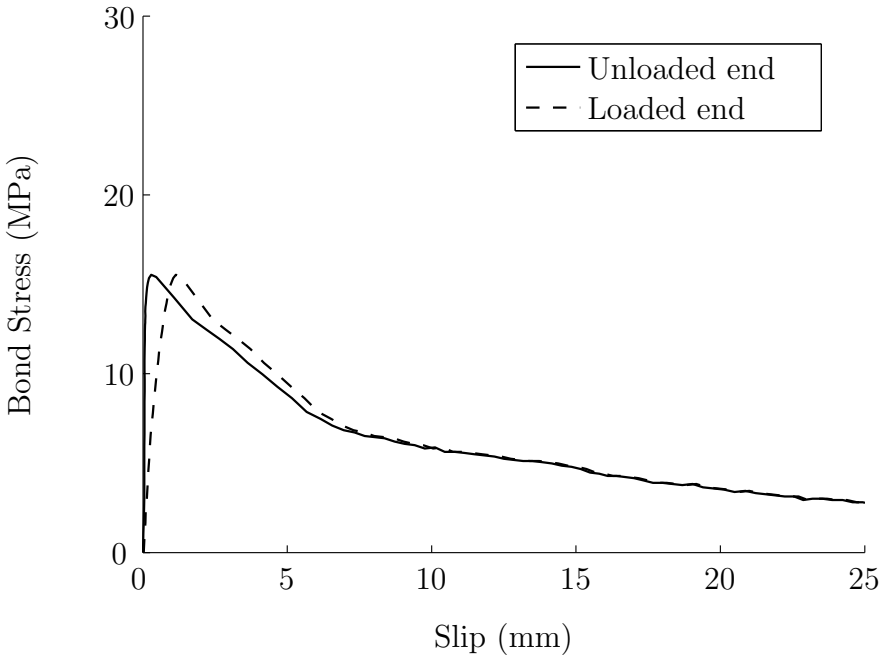
C-G/R5-16-2-C2
Unloaded end
Loaded end
Bond Stress (MPa)
Slip (mm)
0
10
20
30
0
5
10
15
20
25

A.1.6 Rebar R6

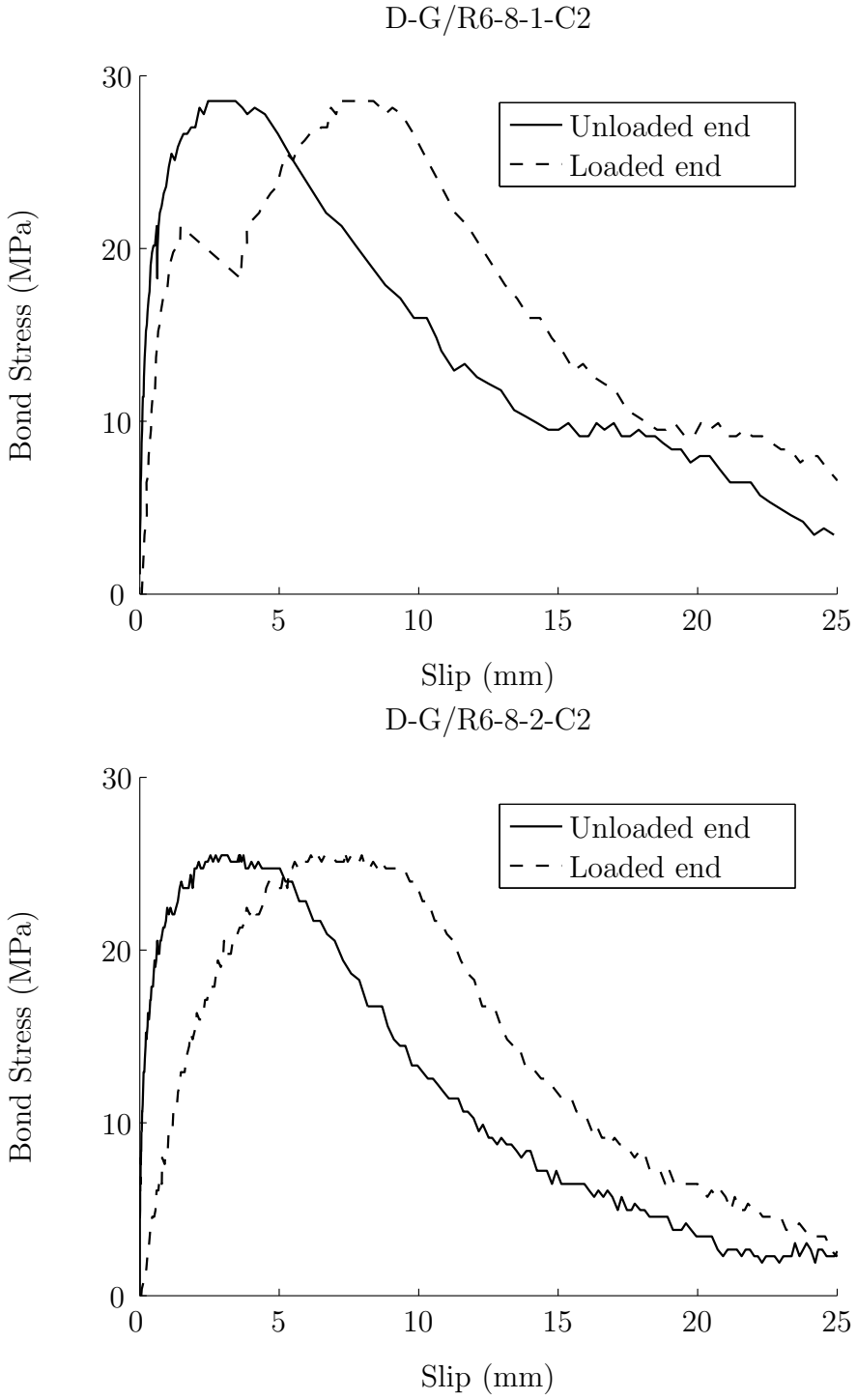
D-G/R6-8-1-C2
Unloaded end
Loaded end
Bond Stress (MPa)
Slip (mm)
0
10
20
30
0
5
10
15
20
25
D-G/R6-8-2-C2
Unloaded end
Loaded end
Bond Stress (MPa)
Slip (mm)

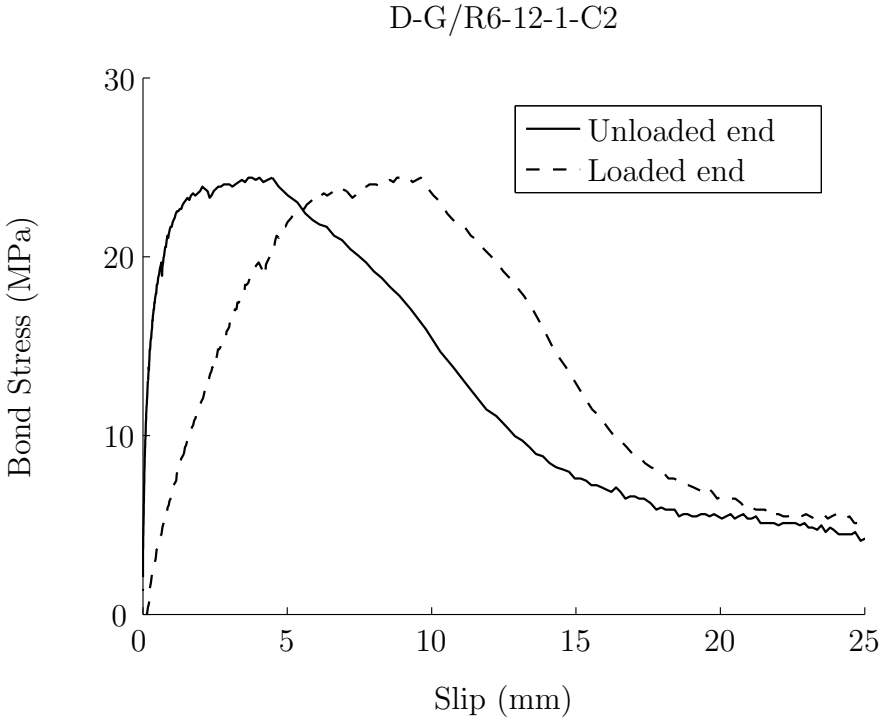
D-G/R6-12-1-C2
Unloaded end
Loaded end
Bond Stress (MPa)
Slip (mm)
0
10
20
30
0
5
10
15
20
25

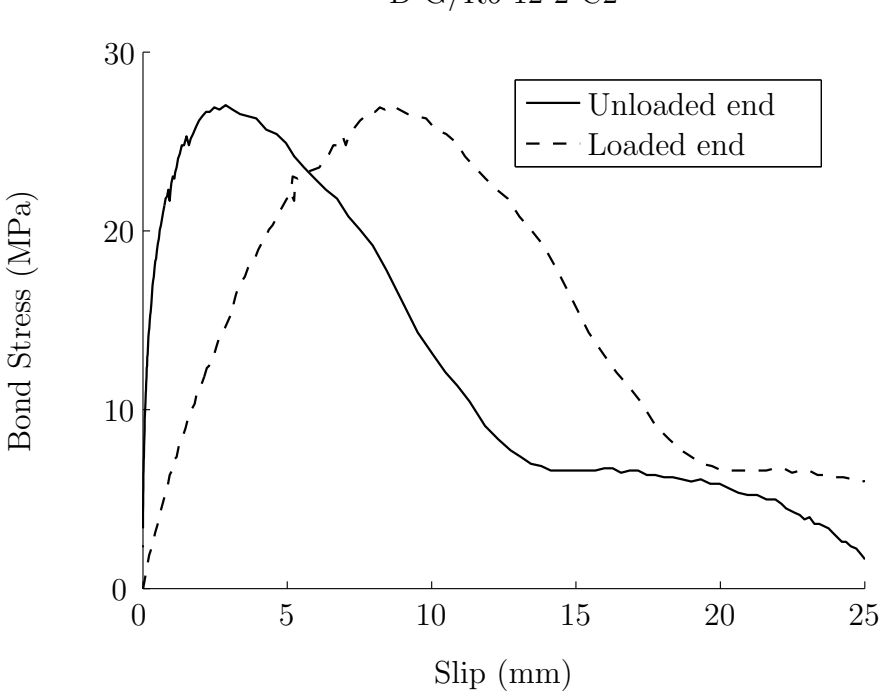
D-G/R6-12-2-C2
Unloaded end
Loaded end
Bond Stress (MPa)
Slip (mm)
0
10
20
30
0
5
10
15
20
25

D-G/R6-16-1-C2

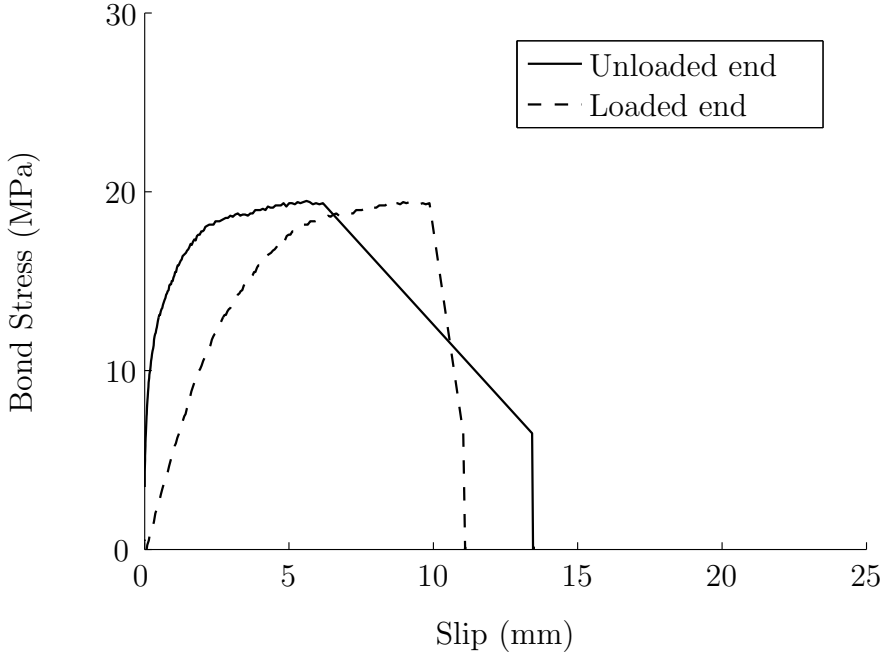

D-G/R6-16-2-C2

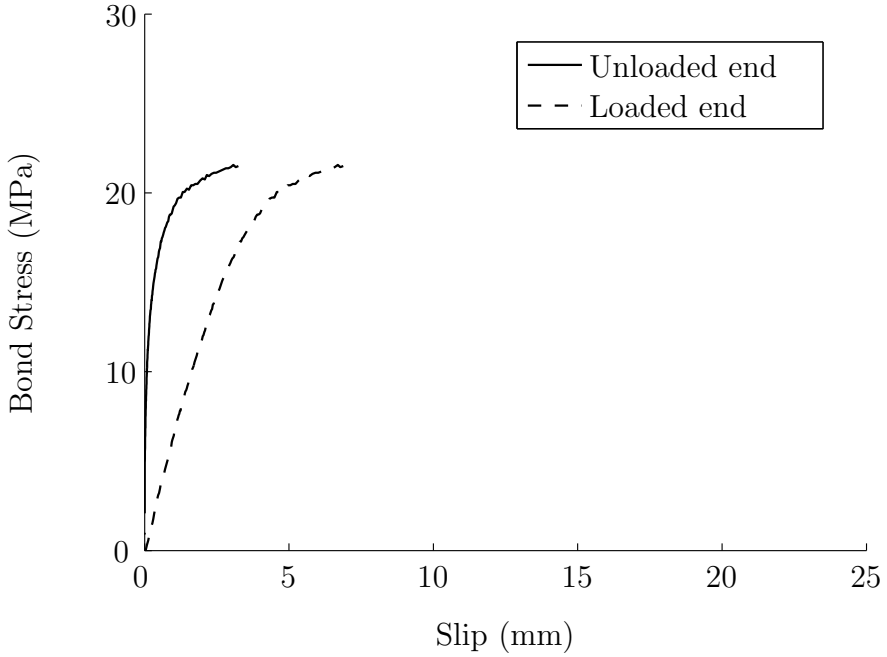

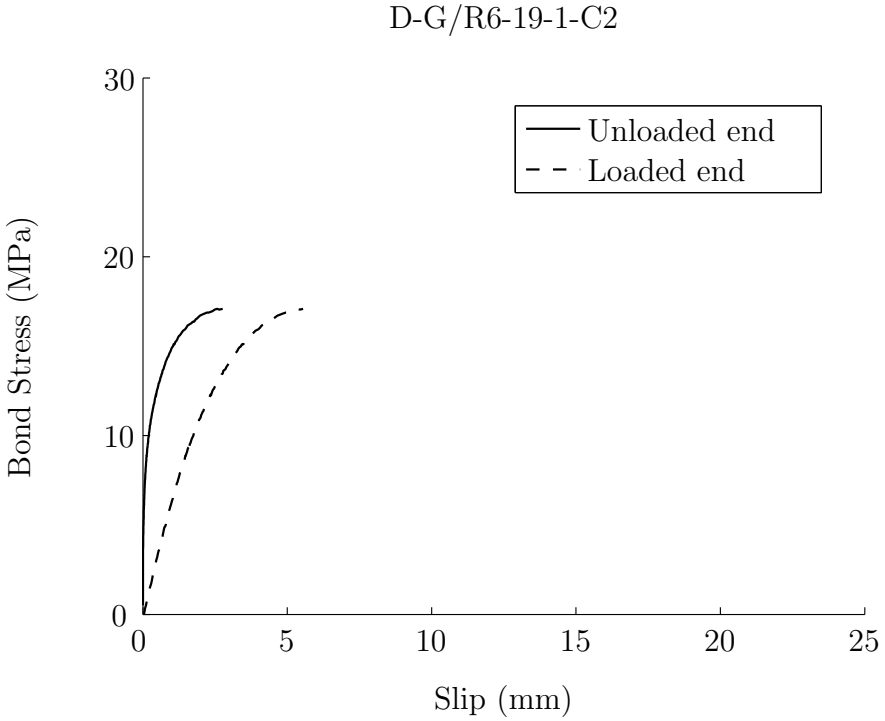
D-G/R6-19-1-C2
Unloaded end
Loaded end
Bond Stress (MPa)
Slip (mm)
0
10
20
30
0
5
10
15
20
25

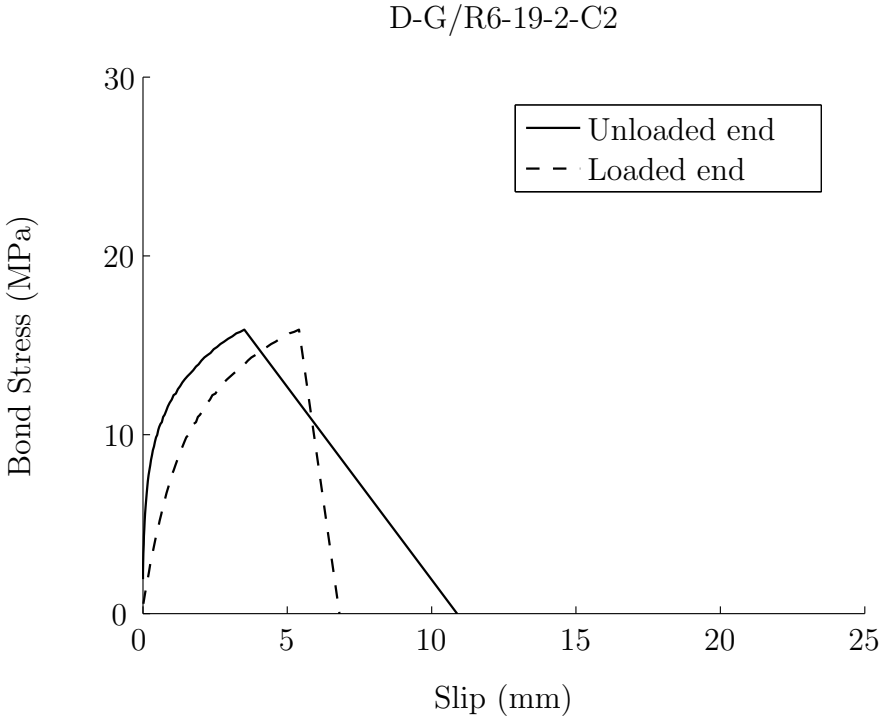
D-G/R6-19-2-C2
Unloaded end
Loaded end
Bond Stress (MPa)
Slip (mm)
0
10
20
30
0
5
10
15
20
25

A.1.7 Rebar R7

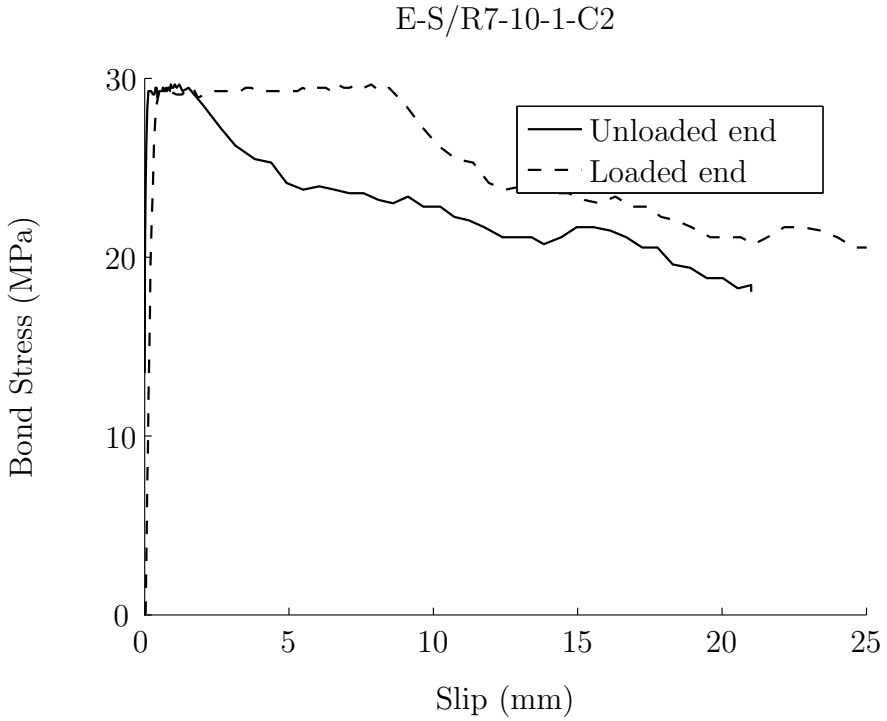
E-S/R7-10-1-C2
Unloaded end
Loaded end
Bond Stress (MPa)
Slip (mm)
0
10
20
30
0
5
10
15
20
25

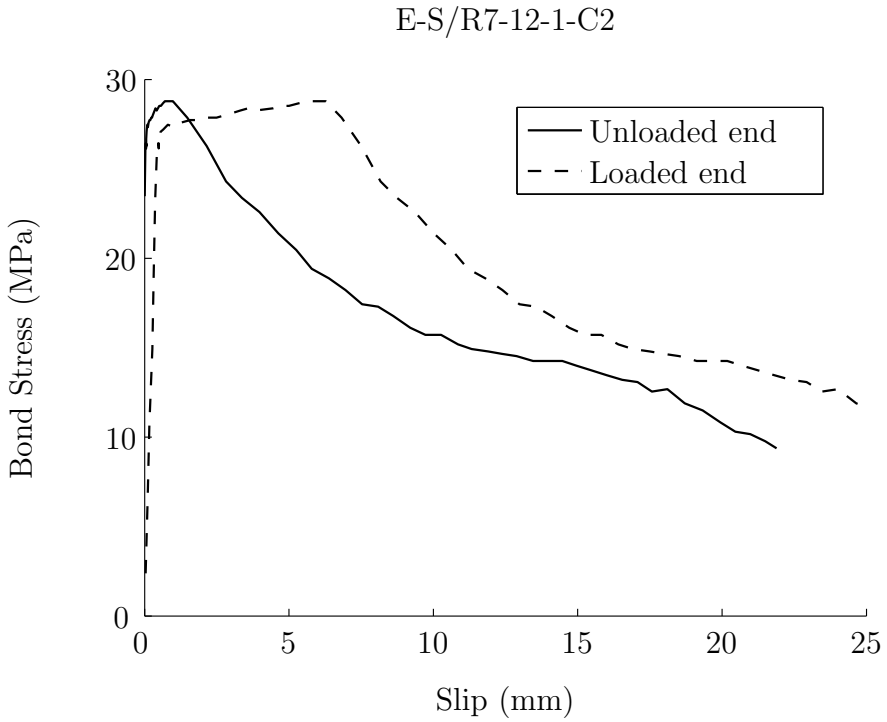
E-S/R7-12-1-C2
Unloaded end
Loaded end
Bond Stress (MPa)
Slip (mm)
0
10
20
30
0
5
10
15
20
25

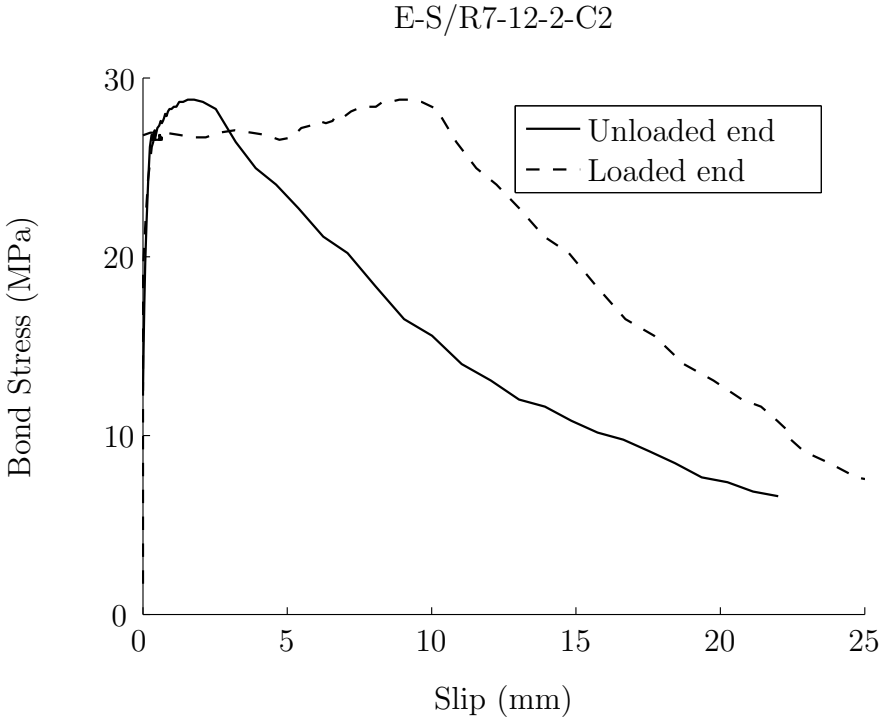
E-S/R7-12-2-C2
Unloaded end
Loaded end
Bond Stress (MPa)
Slip (mm)
0
10
20
30
0
5
10
15
20
25

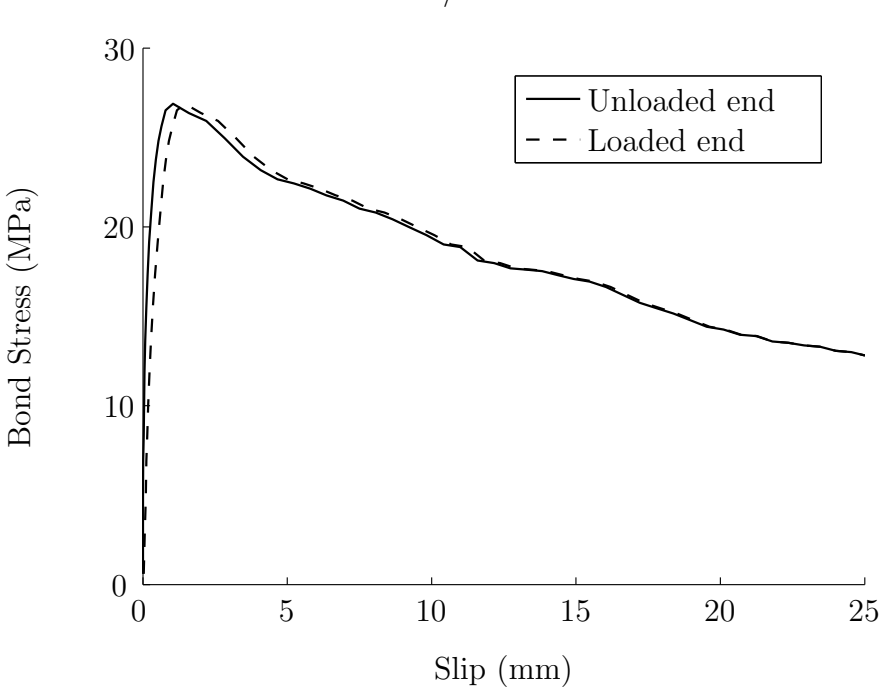
E-S/R7-16-1-C2
Unloaded end
Loaded end
Bond Stress (MPa)
Slip (mm)
0
10
20
30
0
5
10
15
20
25

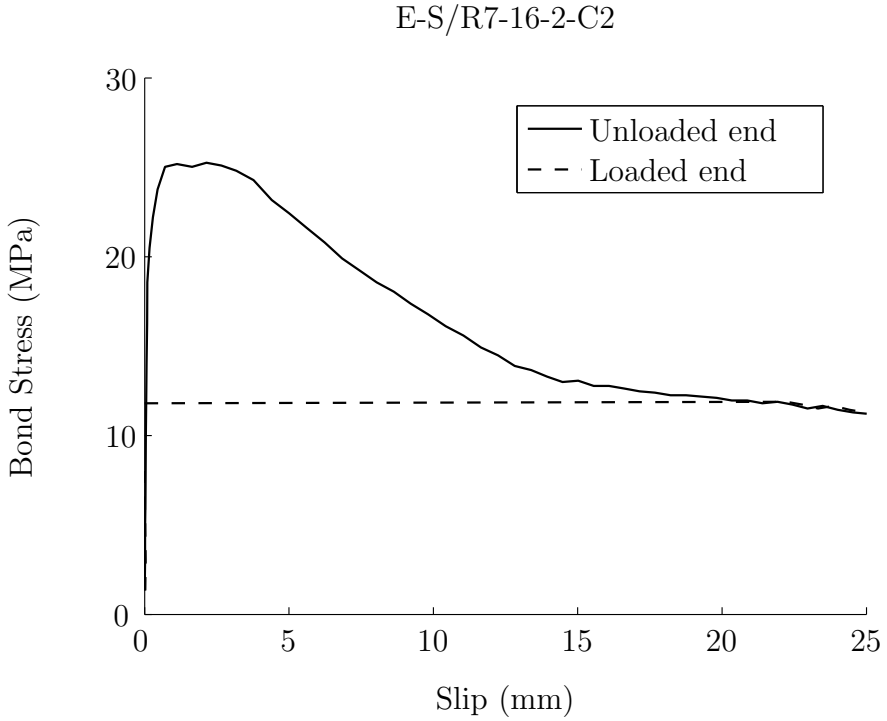
E-S/R7-16-2-C2
Unloaded end
Loaded end
Bond Stress (MPa)
Slip (mm)
0
10
20
30
0
5
10
15
20
25

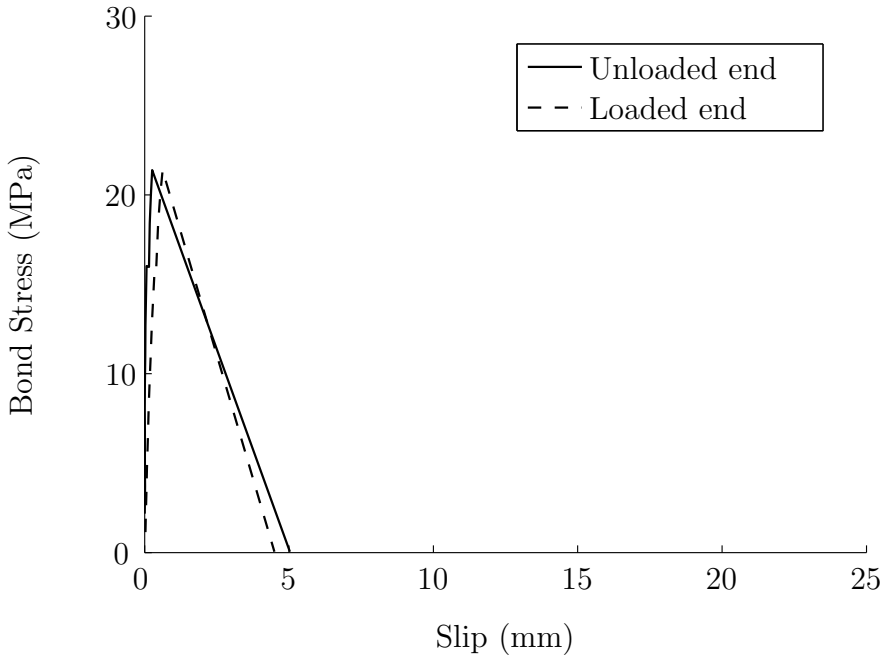
E-S/R7-20-1-C2
Unloaded end
Loaded end
Bond Stress (MPa)
Slip (mm)
0
10
20
30
0
5
10
15
20
25

A.2 Series C1 concrete

A.2.1 Rebar R1

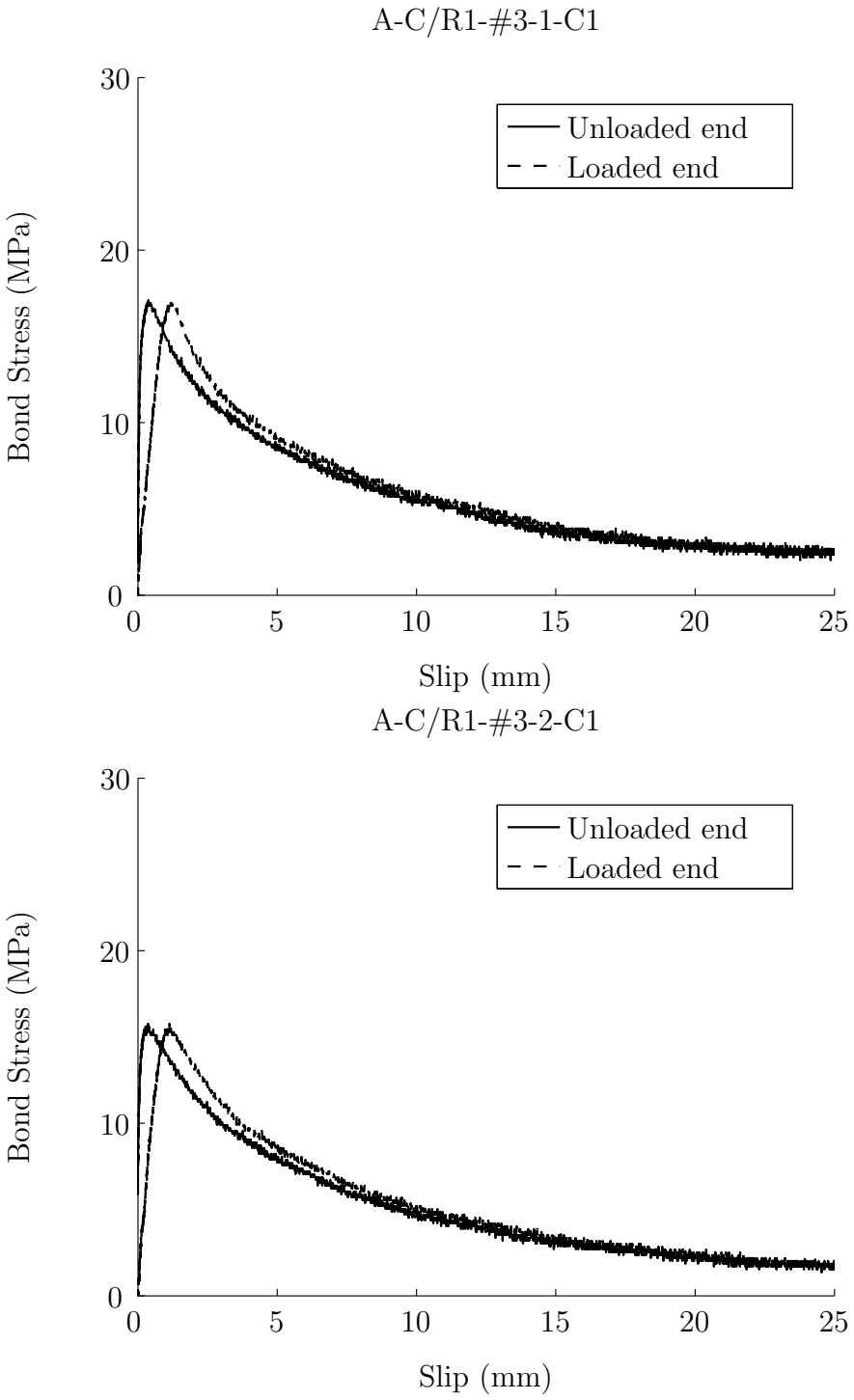

A-C/R1-#4-1-C1

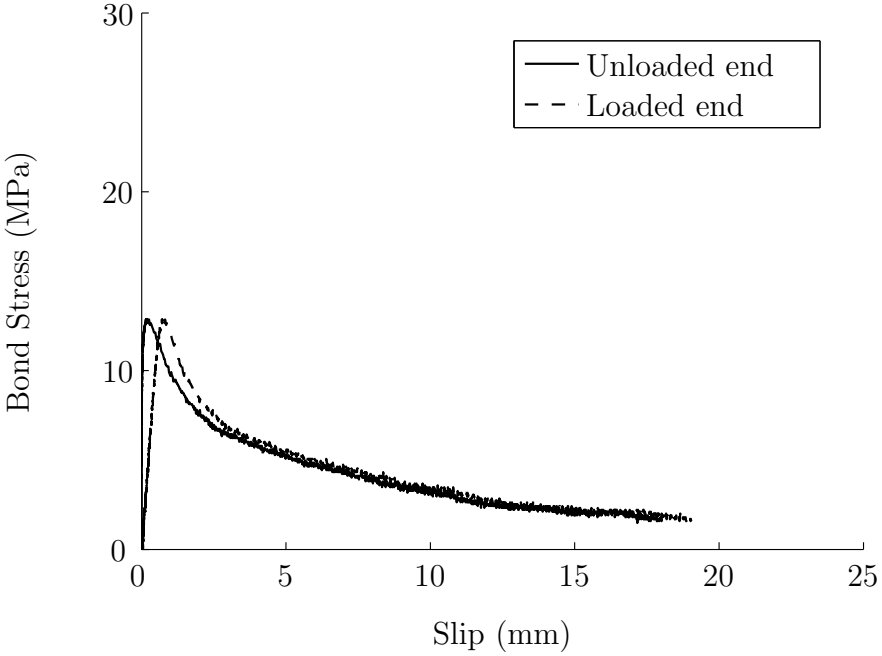

A-C/R1-#4-2-C1

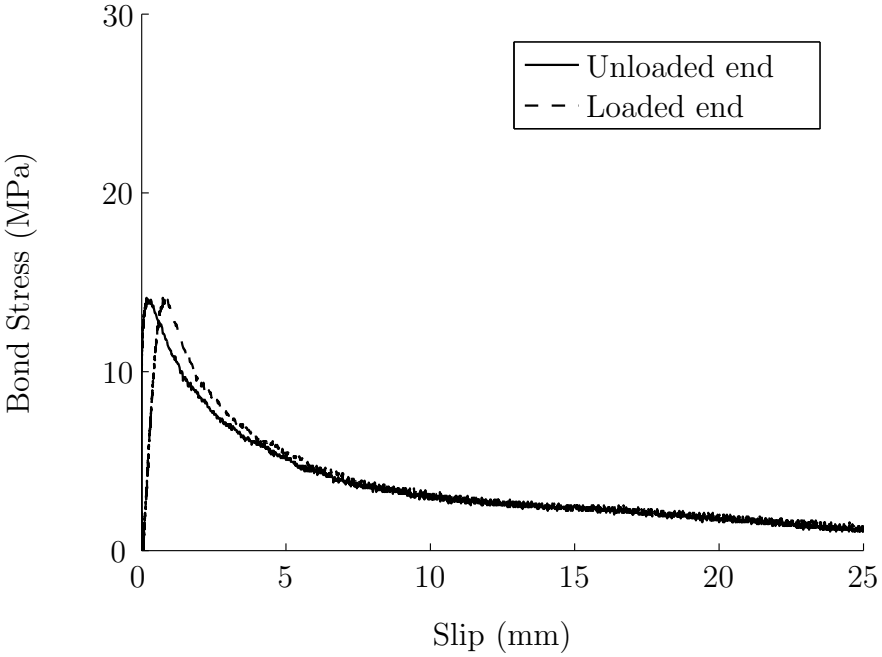

A.2.2 Rebar R2

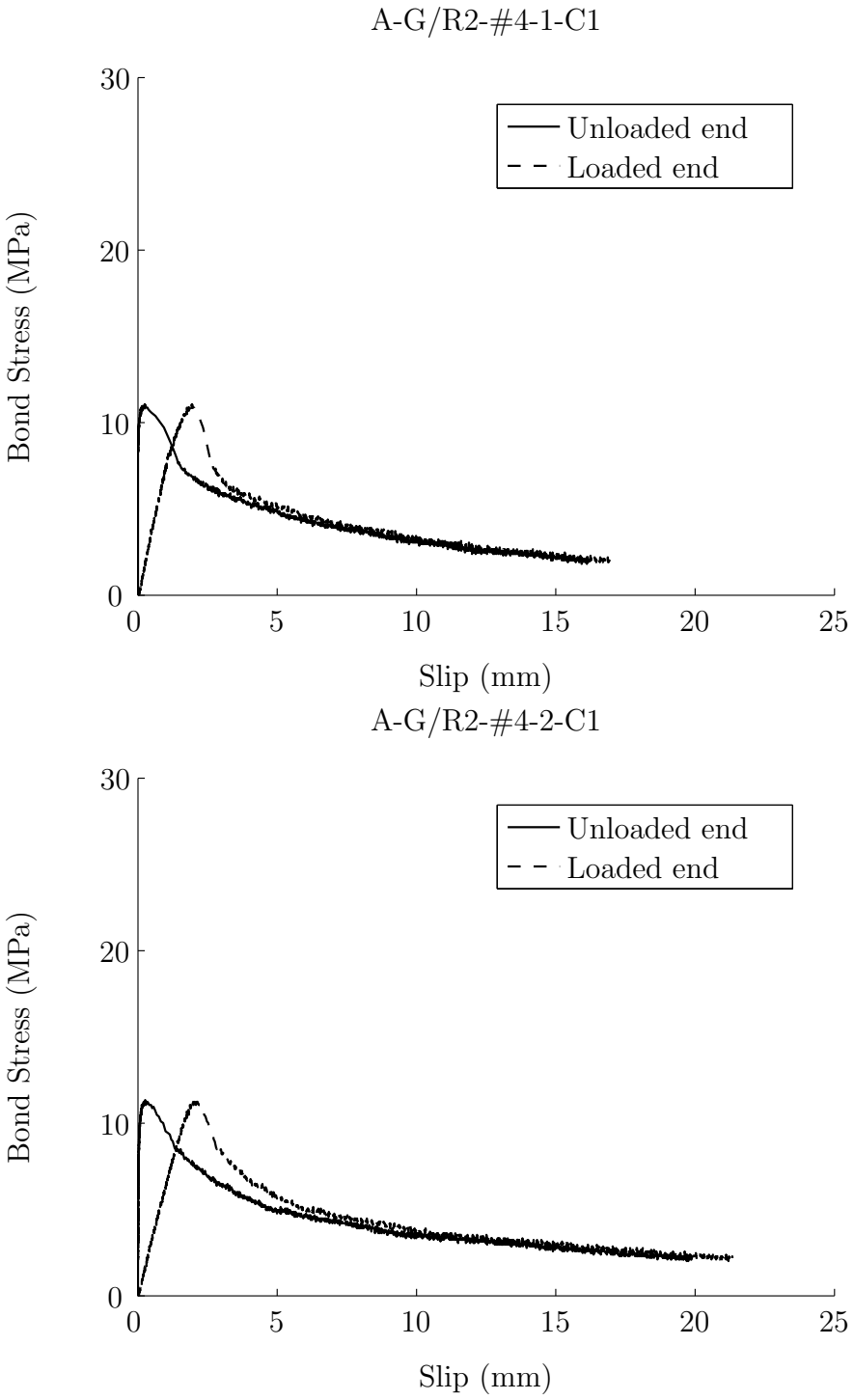
A-G/R2-#4-1-C1
Unloaded end
Loaded end
Bond Stress (MPa)
Slip (mm)
0
10
20
30
0
5
10
15
20
25
A-G/R2-#4-2-C1
Unloaded end
Loaded end
Bond Stress (MPa)
Slip (mm)

A-G/R2-#5-1-C1

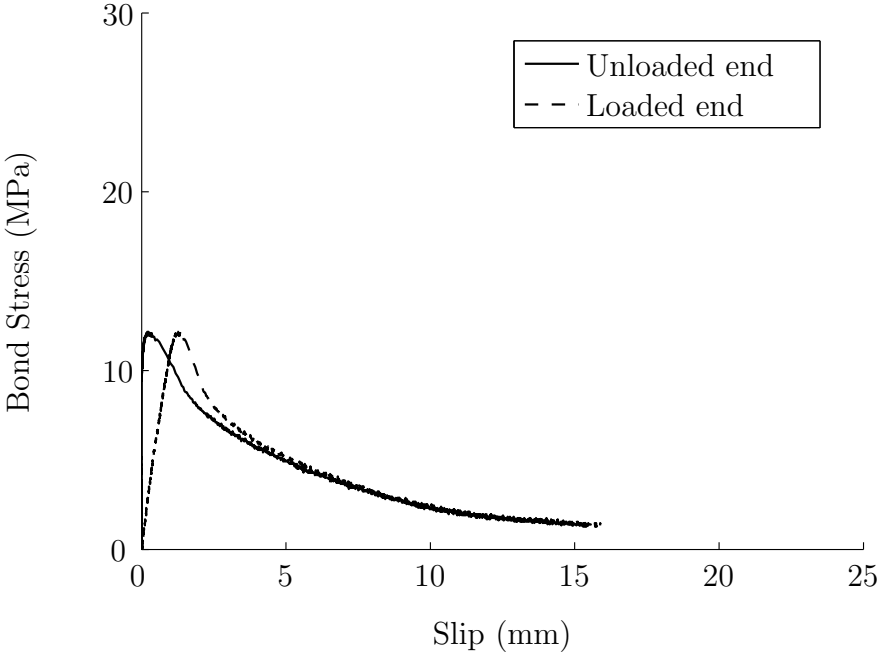

A-G/R2-#5-2-C1

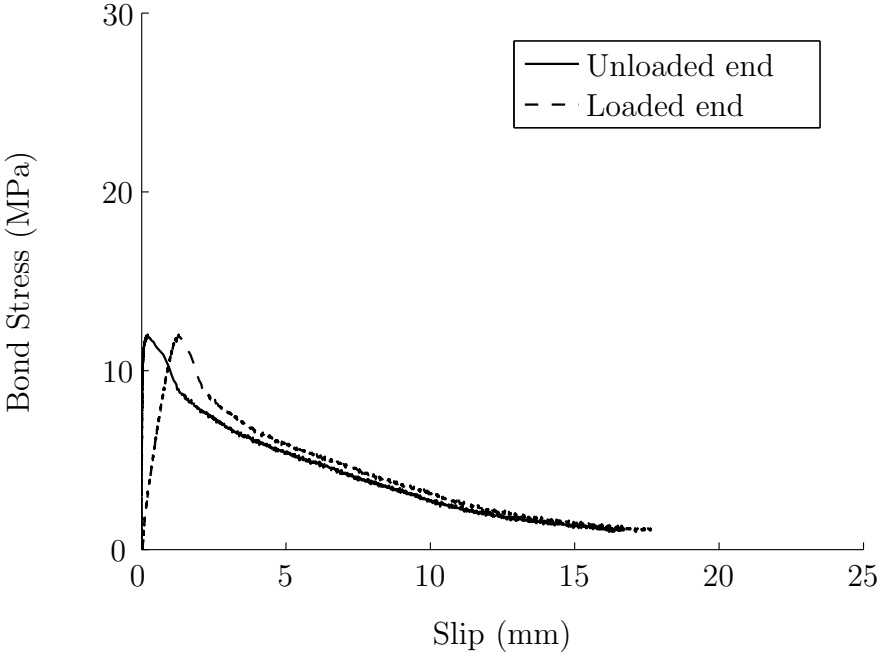

A.2.3 Rebar R3

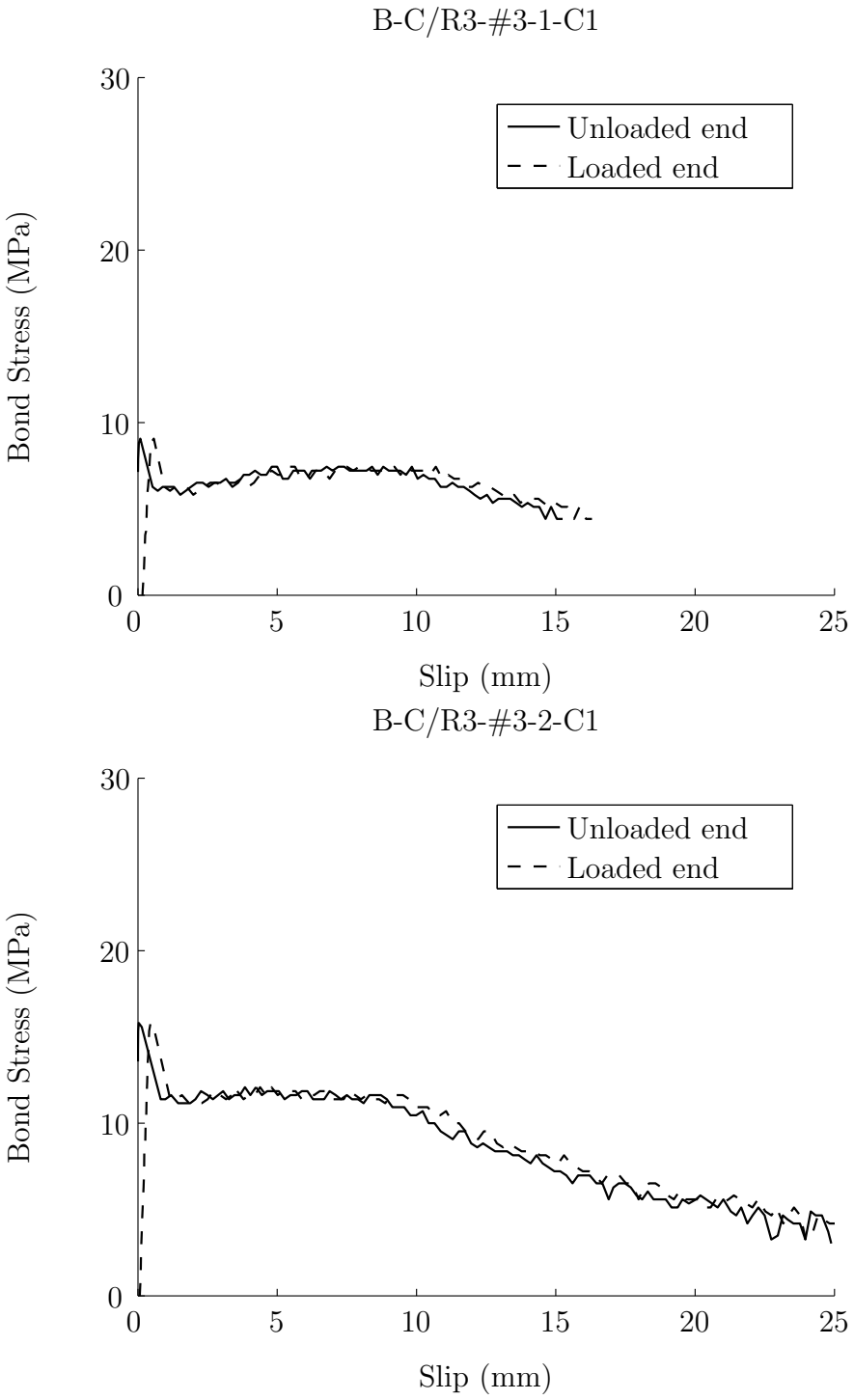
B-C/R3-#3-1-C1
Unloaded end
Loaded end
Bond Stress (MPa)
Slip (mm)
0
10
20
30
0
5
10
15
20
25
B-C/R3-#3-2-C1
Unloaded end
Loaded end
Bond Stress (MPa)
Slip (mm)
0
10
20
30
0
5
10
15
20
25

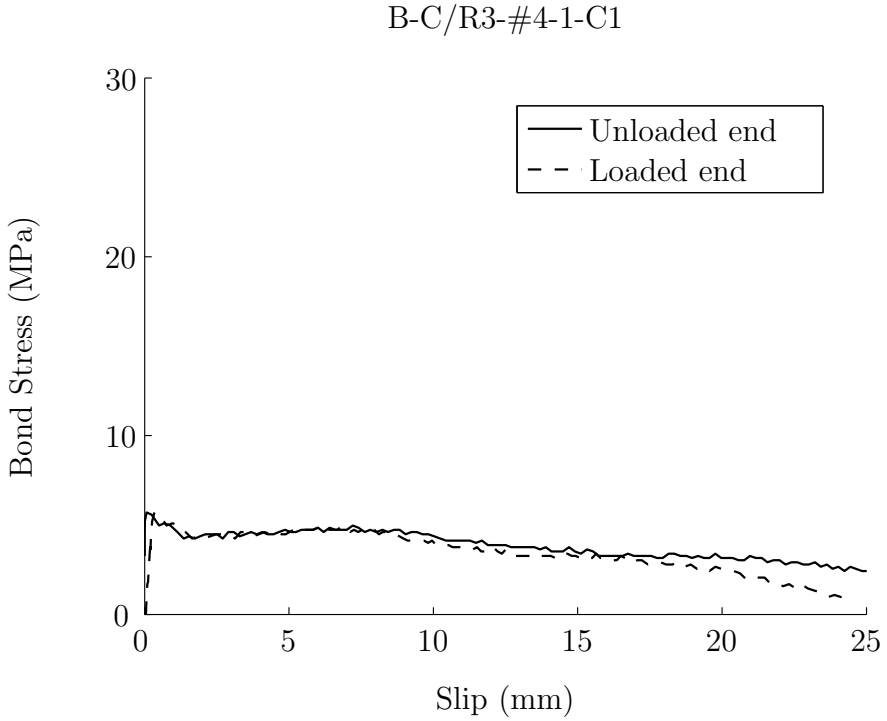
B-C/R3-#4-1-C1
Unloaded end
Loaded end
Bond Stress (MPa)
Slip (mm)
0
10
20
30
0
5
10
15
20
25

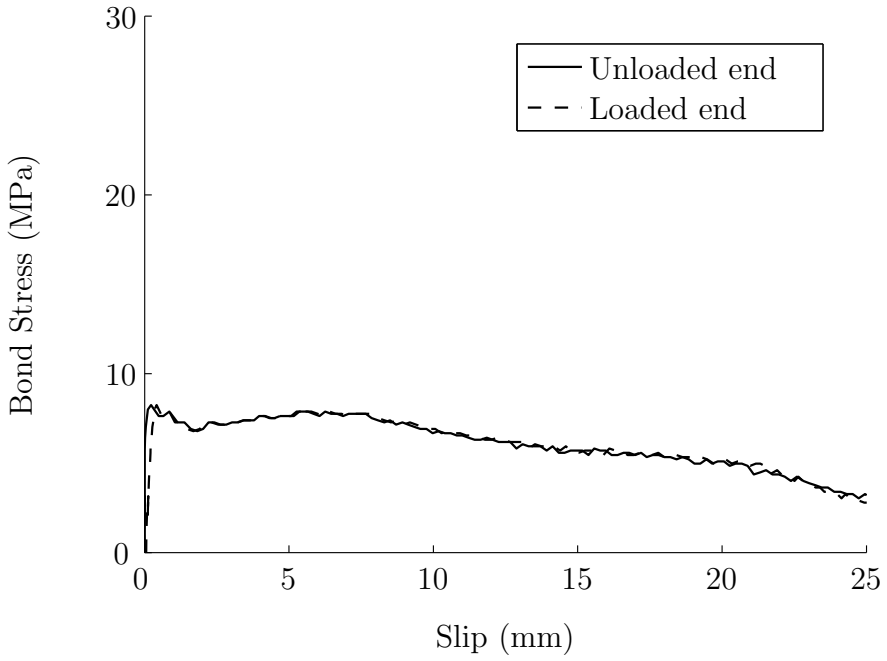
B-C/R3-#4-2-C1
Unloaded end
Loaded end
Bond Stress (MPa)
Slip (mm)
0
10
20
30
0
5
10
15
20
25

A.2.4 Rebar R4

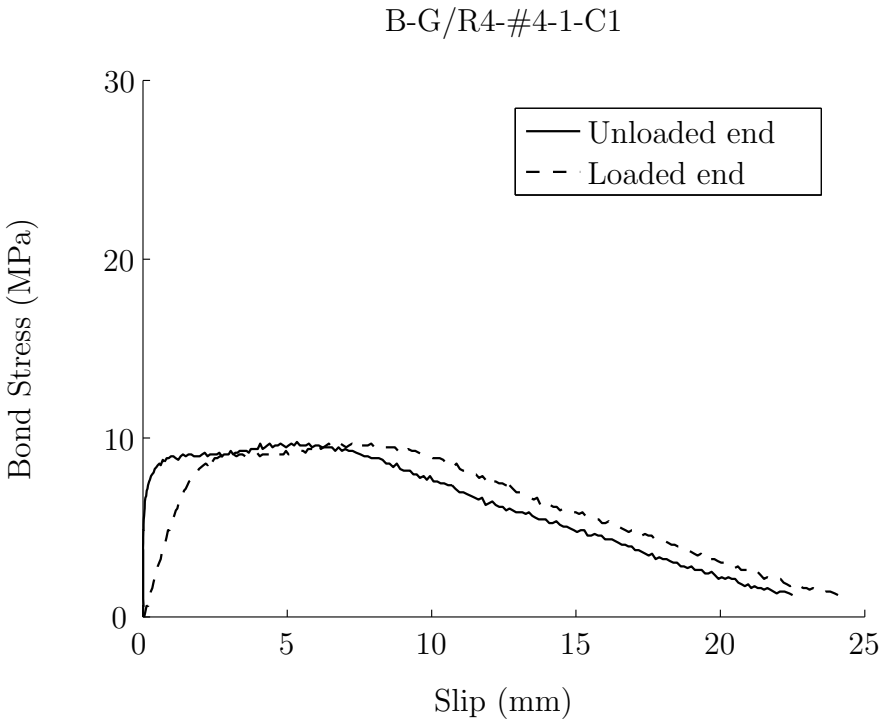
B-G/R4-#4-1-C1
Unloaded end
Loaded end
Bond Stress (MPa)
Slip (mm)
0
10
20
30
0
5
10
15
20
25

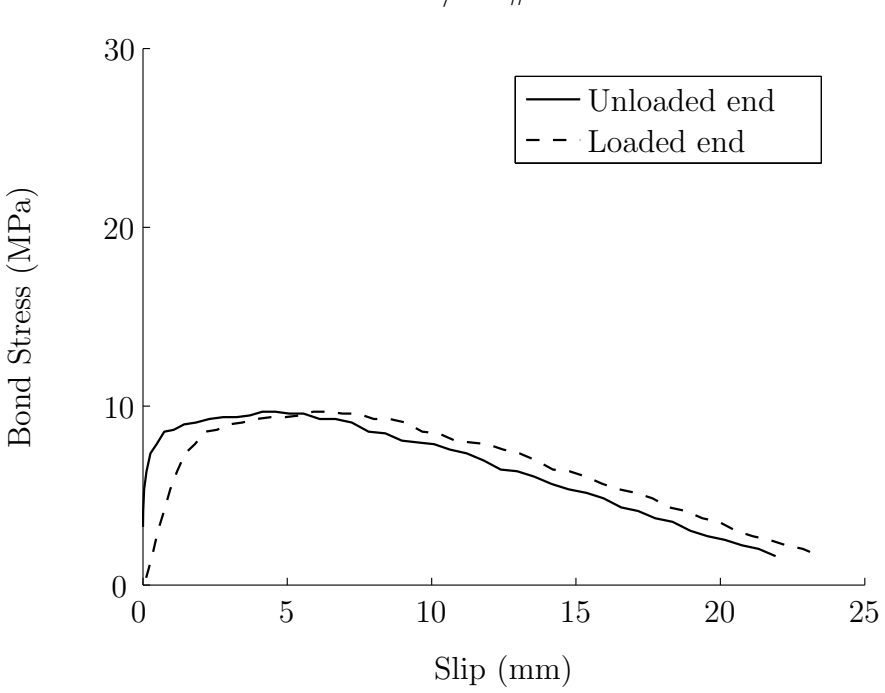
B-G/R4-#4-2-C1
Unloaded end
Loaded end
Bond Stress (MPa)
Slip (mm)
0
10
20
30
0
5
10
15
20
25

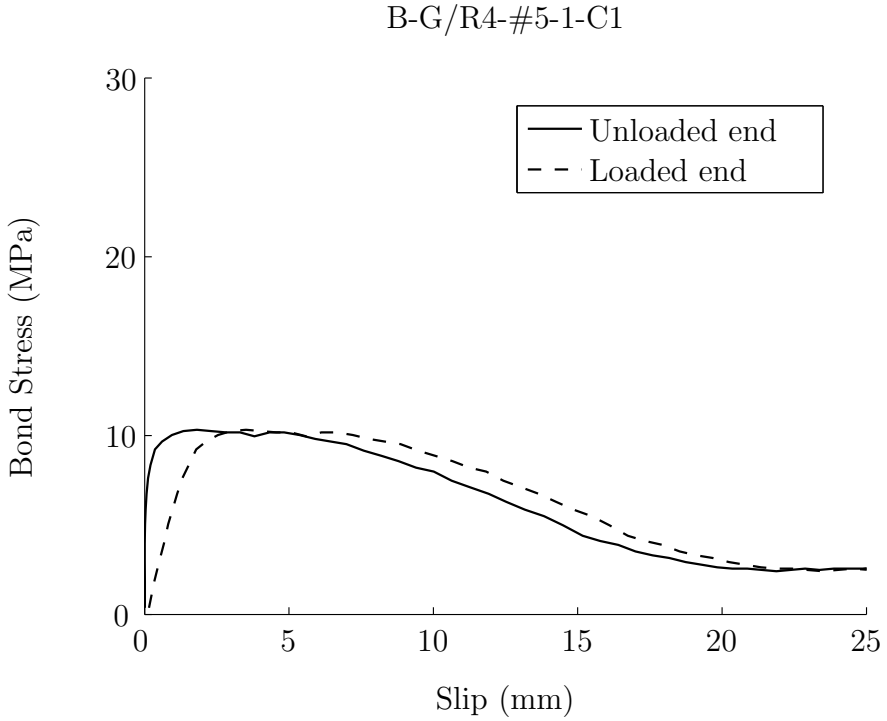
B-G/R4-#5-1-C1
Unloaded end
Loaded end
Bond Stress (MPa)
Slip (mm)
0
5
10
15
20
25
0
10
20
30

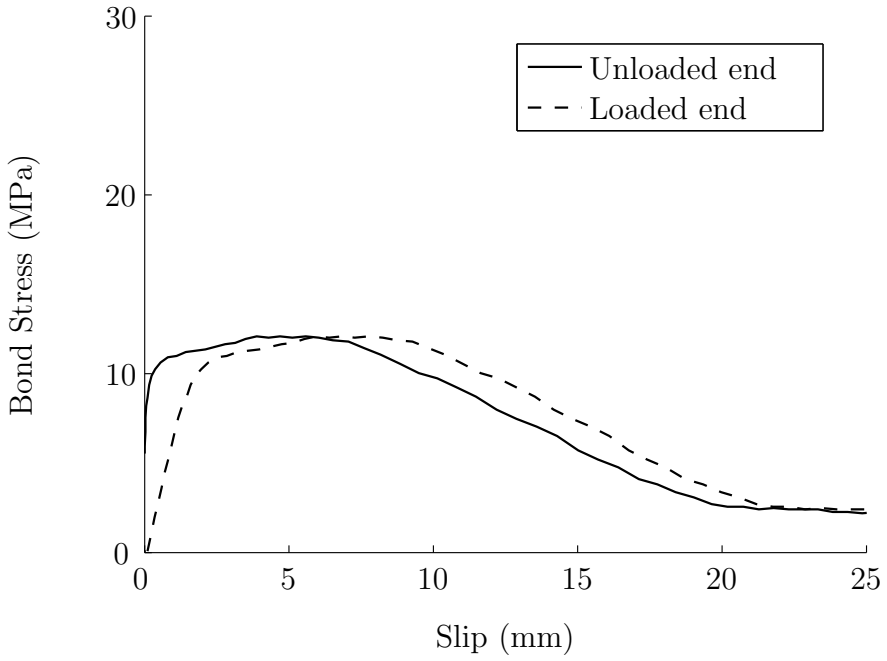
B-G/R4-#5-2-C1
Unloaded end
Loaded end
Bond Stress (MPa)
Slip (mm)
0
5
10
15
20
25
0
10
20
30

A.2.5 Rebar R5

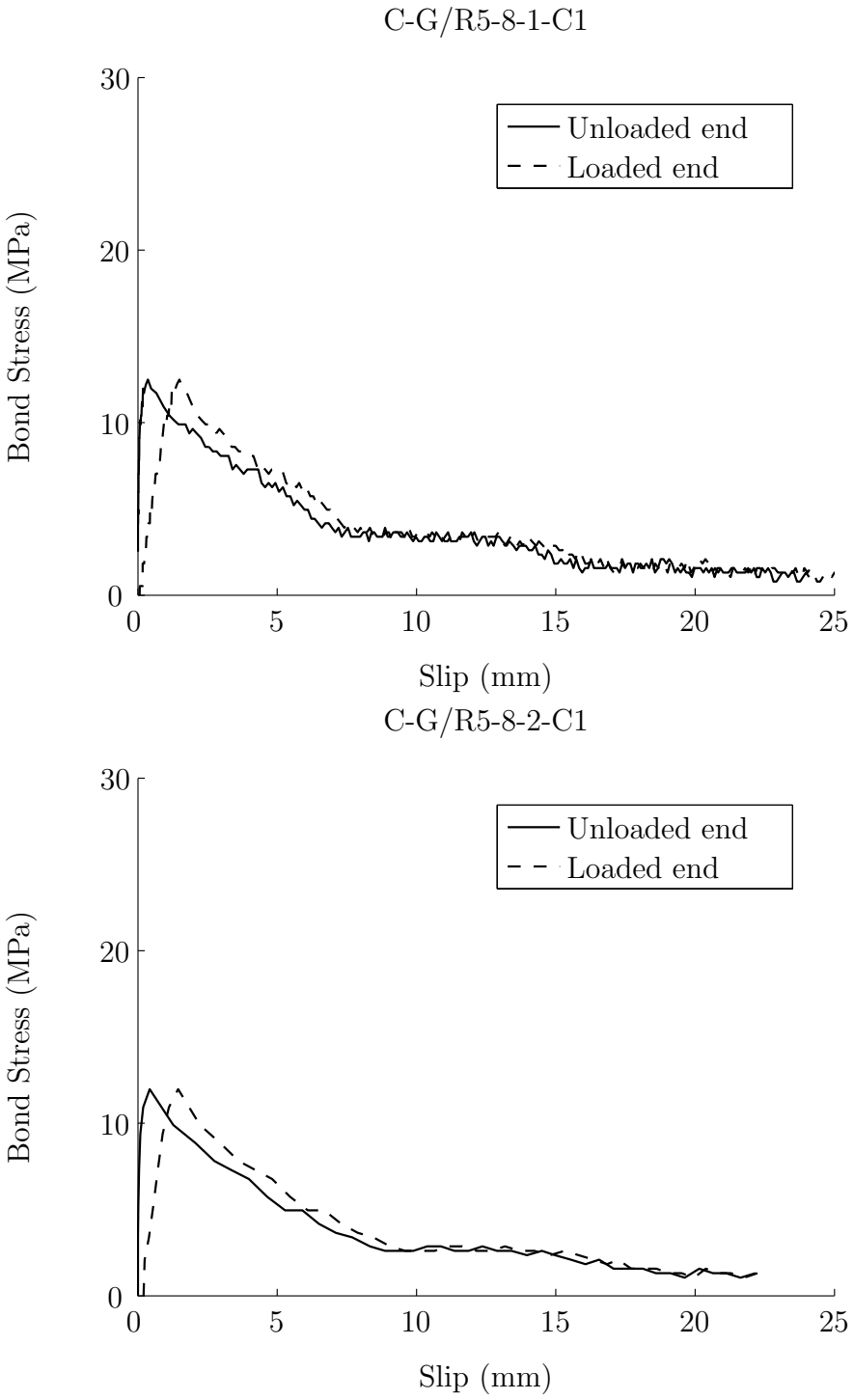
C-G/R5-8-1-C1
Unloaded end
Loaded end
Bond Stress (MPa)
Slip (mm)
0
10
20
30
0
5
10
15
20
25
C-G/R5-8-2-C1
Unloaded end
Loaded end
Bond Stress (MPa)
Slip (mm)

C-G/R5-12-1-C1

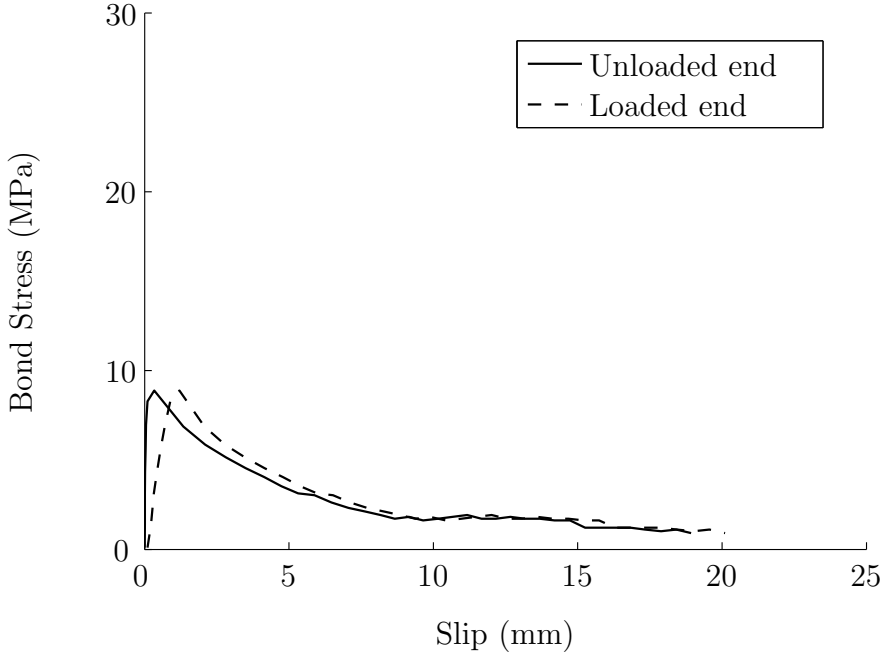

C-G/R5-12-2-C1

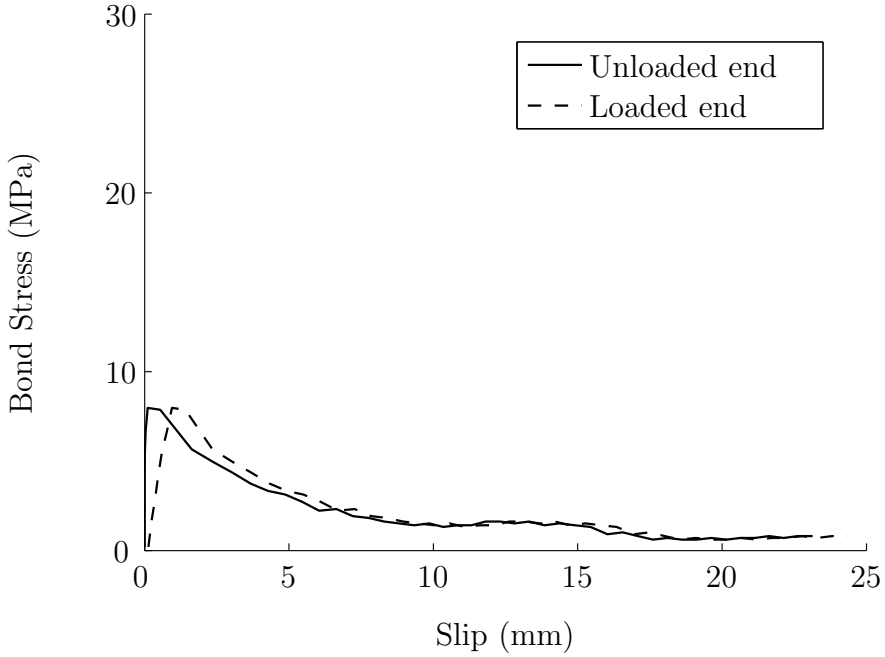

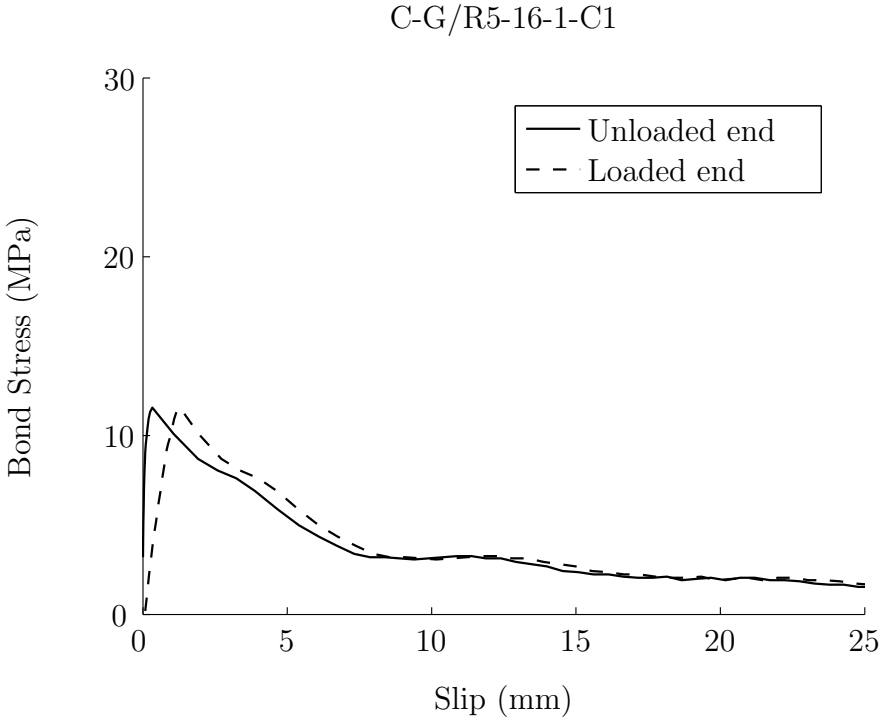
C-G/R5-16-1-C1
Unloaded end
Loaded end
Bond Stress (MPa)
Slip (mm)
0
10
20
30
0
5
10
15
20
25

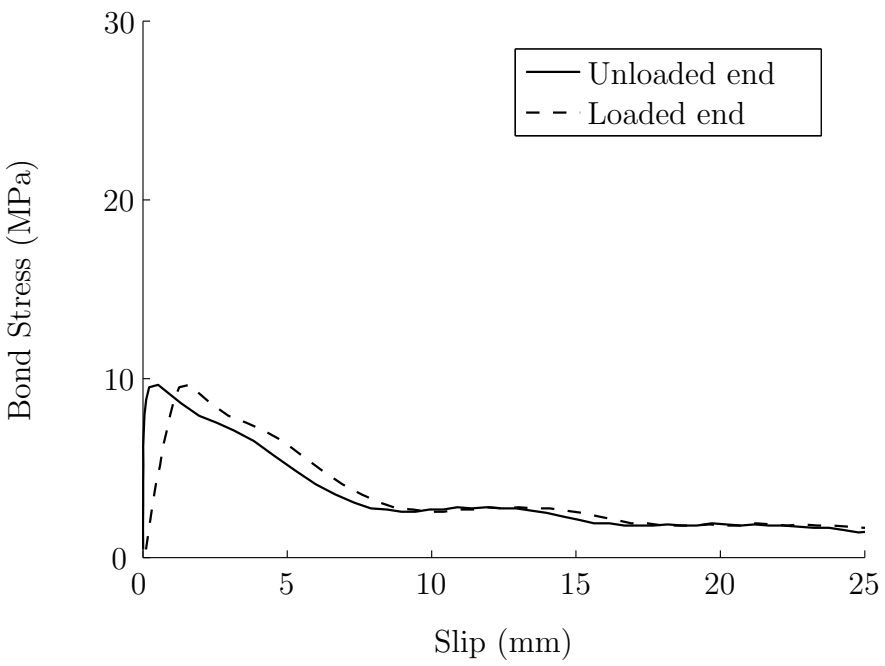
C-G/R5-16-2-C1
Unloaded end
Loaded end
Bond Stress (MPa)
Slip (mm)
0
10
20
30
0
5
10
15
20
25

A.2.6 Rebar R6

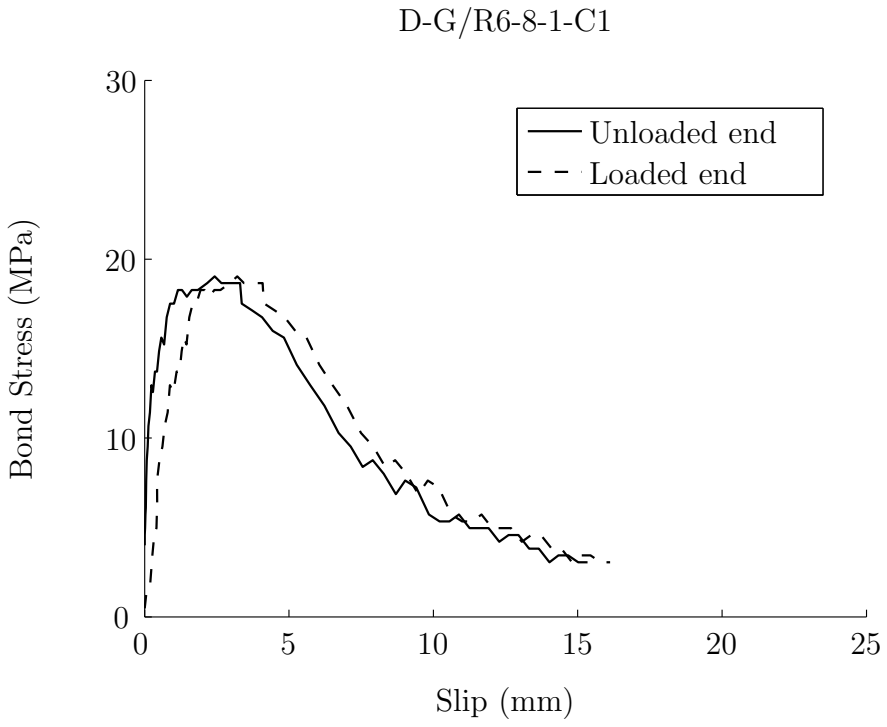
D-G/R6-8-1-C1
Unloaded end
Loaded end
Bond Stress (MPa)
Slip (mm)
0
5
10
15
20
25
30

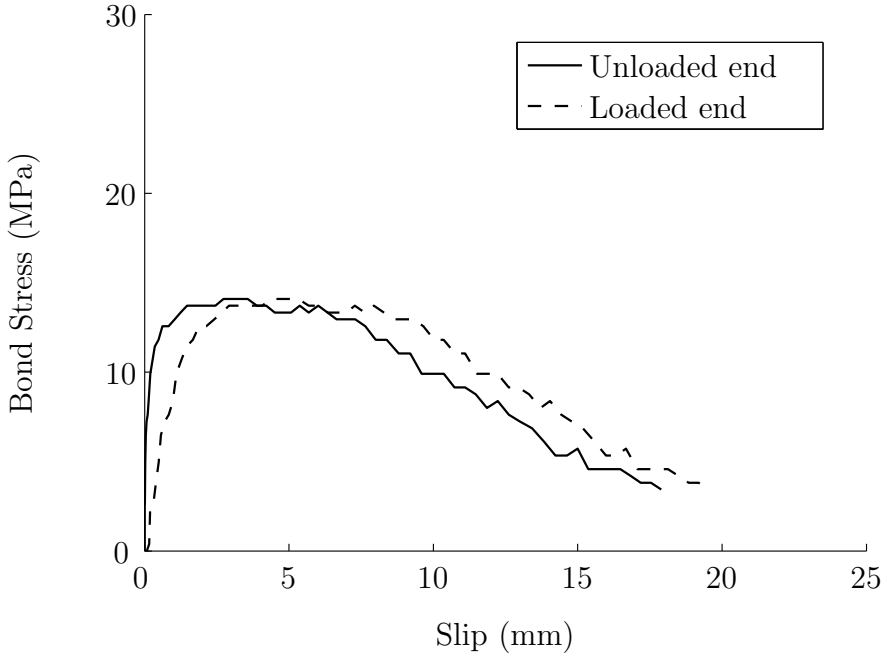
D-G/R6-8-2-C1
Unloaded end
Loaded end
Bond Stress (MPa)
Slip (mm)
0
5
10
15
20
25
30

D-G/R6-12-1-C1

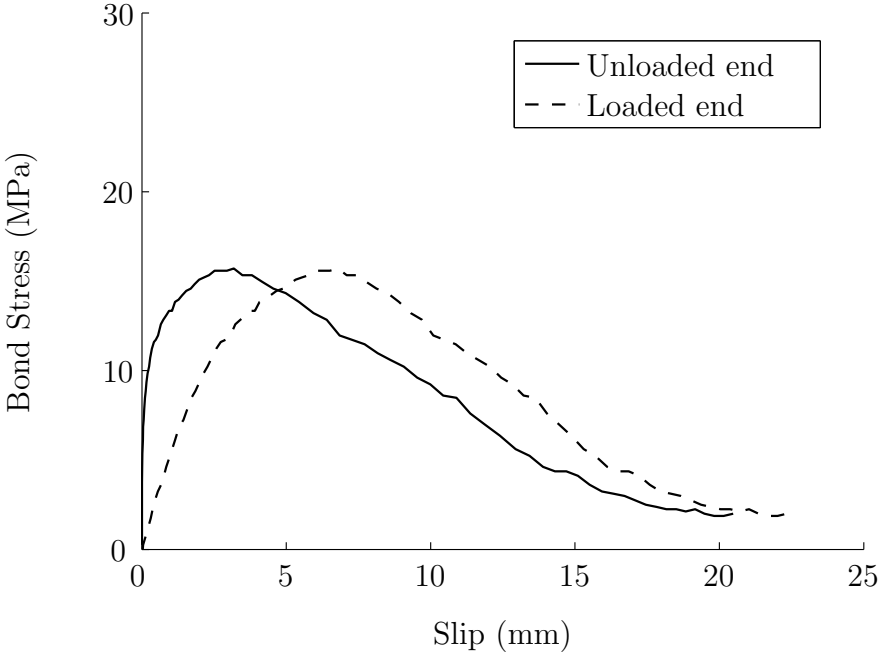

D-G/R6-12-2-C1

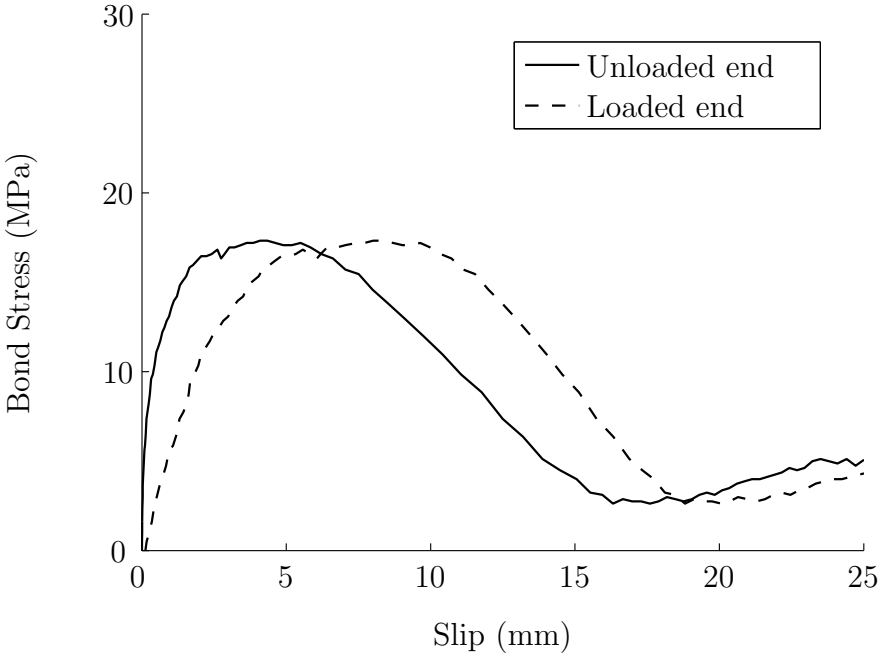

A.2.7 Rebar R7

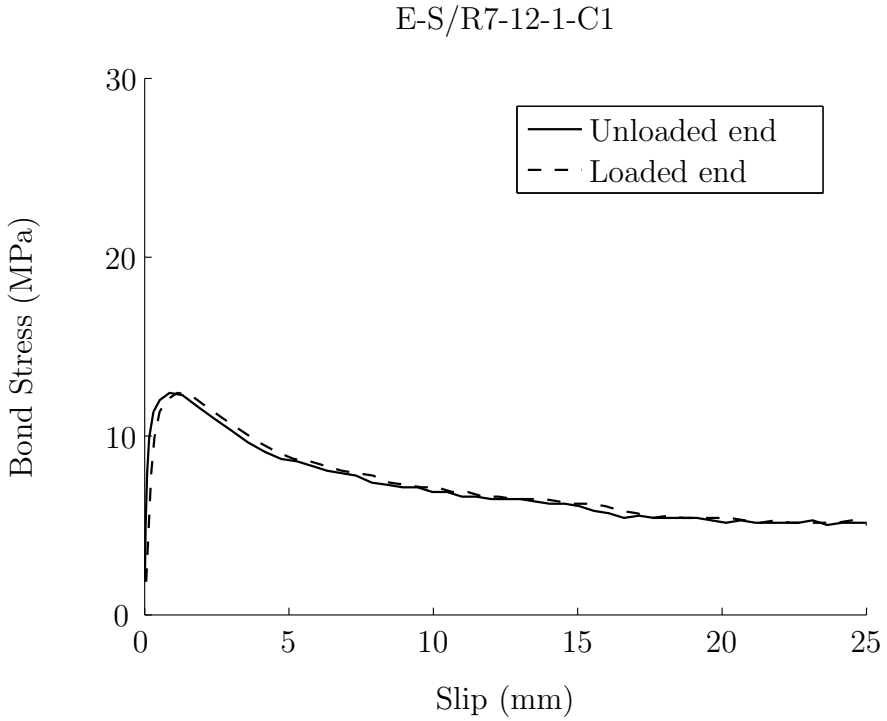
E-S/R7-12-1-C1
Unloaded end
Loaded end
Bond Stress (MPa)
Slip (mm)
0
5
10
15
20
25
30

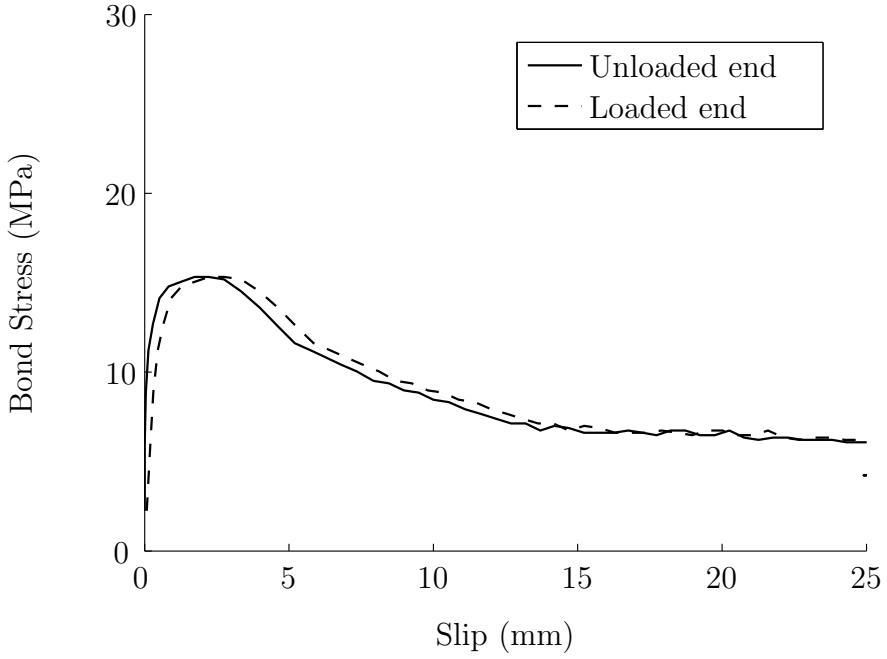
E-S/R7-12-2-C1
Unloaded end
Loaded end
Bond Stress (MPa)
Slip (mm)
0
5
10
15
20
25
30

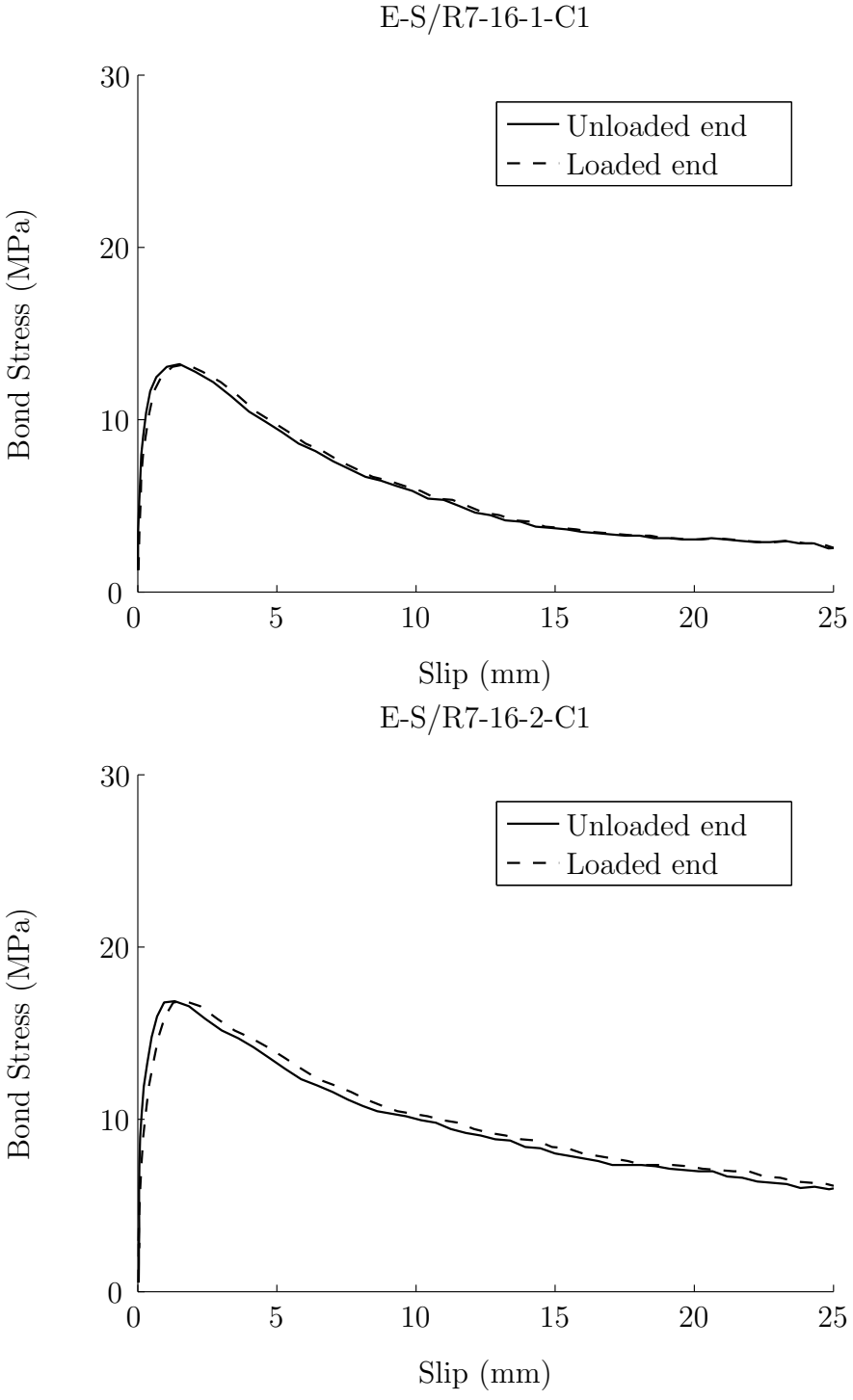
E-S/R7-16-1-C1
Unloaded end
Loaded end
Bond Stress (MPa)
Slip (mm)
0
10
20
30
0
5
10
15
20
25
E-S/R7-16-2-C1
Unloaded end
Loaded end
Bond Stress (MPa)
Slip (mm)
0
10
20
30
0
5
10
15
20
25

Appendix B

Experimental RC ties

B.1 13-170 RC tie

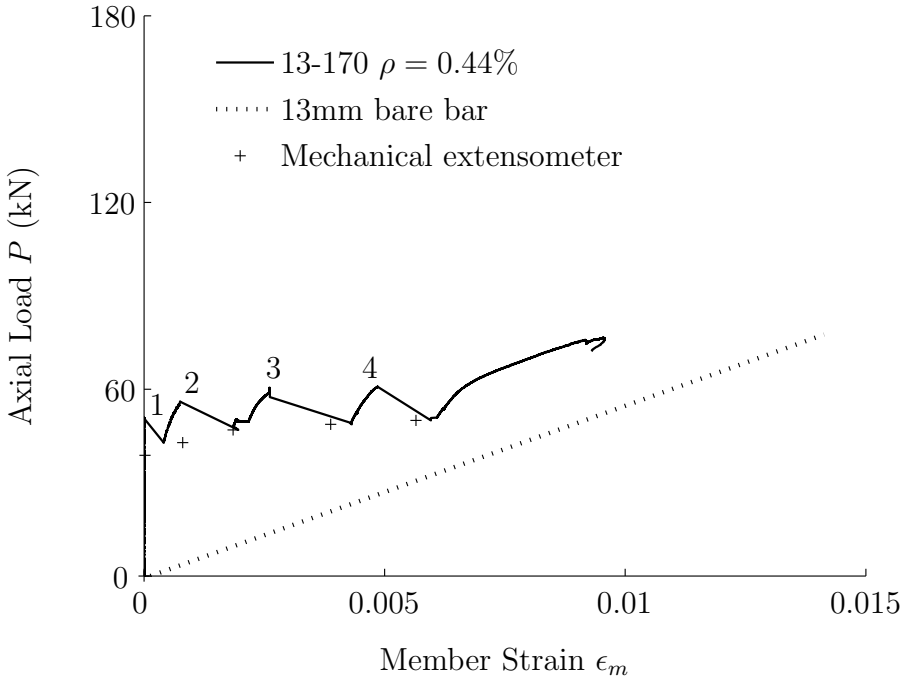

Figure B.1: Load-mean strain relationship (tie 13-170).

Tie failure:

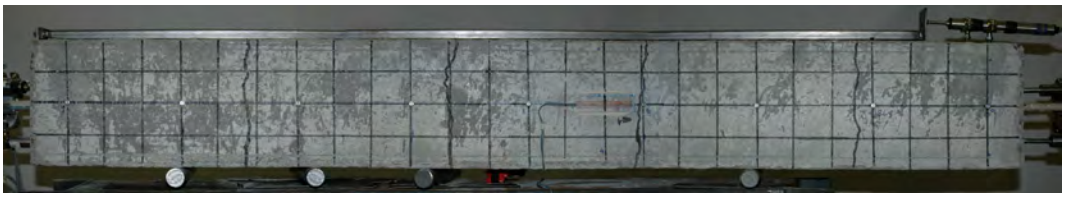

Figure B.2: Image final crack pattern (tie 13-170).

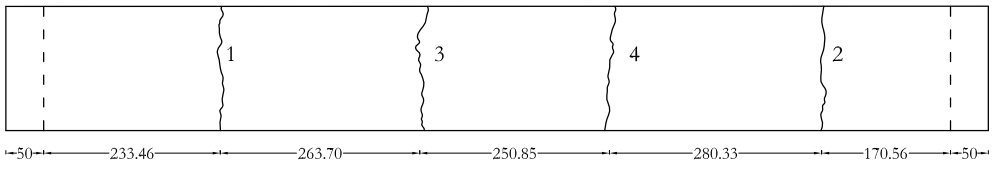

Figure B.3: Cracks number and locations (tie 13-170).

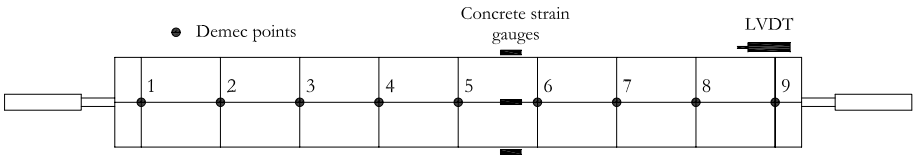

Figure B.4: Instrumentation (tie 13-170).

Load P	ΔL between demec points (mm)							
(kN)	1-2	2-3	3-4	4-5	5-6	6-7	7-8	8-9
0	0	0	0	0	0	0	0	0
2.23	-0.0016	0.0032	-0.0032	0	-0.0016	-0.0016	-0.0032	0
5.24	-0.0016	-0.0016	-0.0016	-0.0016	0	-0.0032	-0.0016	-0.0016
13.76	-0.0032	0	-0.0016	0.0016	0.0016	-0.0048	-0.0016	0
38.76	0.0016	0.0064	0.0048	0.0032	0.0048	0.0016	0.0016	0.0016
38.75	0	0.9136	0.0016	0.0064	0.008	0.0048	0.0032	0.0016
42.82	0	0.9296	0.0032	0.0096	0.0096	0.0064	0.0048	0.0032
49.90	0.0016	1.2144	0.0032	0.0128	0.0096	0.0144	0.9696	-0.0016
52.41	0.0016	1.6768	0	1.7616	0.008	0.016	1.192	-0.0016
53.84	0.0016	1.7696	-0.0016	1.9664	1.768	0.0032	1.2752	-0.0016

Table B.1: Length increment between demec points (tie 13-170).

Load P	Crack width (mm)						
(kN)	1^{st} crack	2^{nd} crack	3^{rd} crack	4^{th} crack	Max.	Min.	Ave.
42.82	1	-	-	-	1	1	1
49.90	1.5	1.1	-	-	1.5	1.1	1.3
52.41	1.9	1	2.1	-	2.1	1	1.67
53.84	1.9	1.8	2.2	1.9	2.2	1.8	1.95

Table B.2: Crack width measurements with optical magnifier (tie 13-170).

B.2 16-170 RC tie

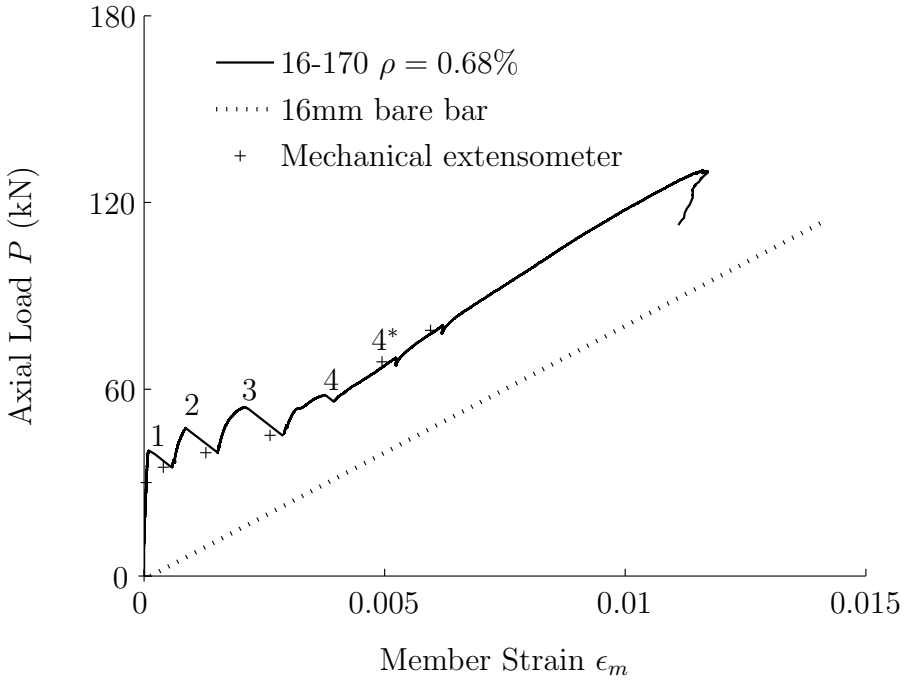

Figure B.5: Load-mean strain relationship (tie 16-170).

Tie failure:

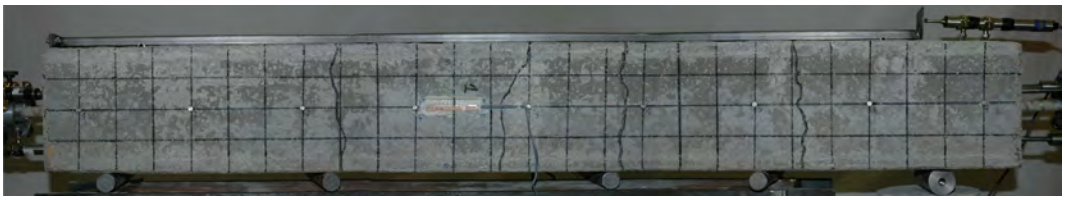

Figure B.6: Image final crack pattern (tie 16-170).

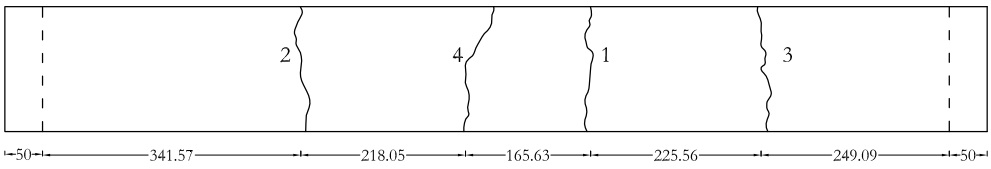

Figure B.7: Cracks number and locations (tie 16-170).

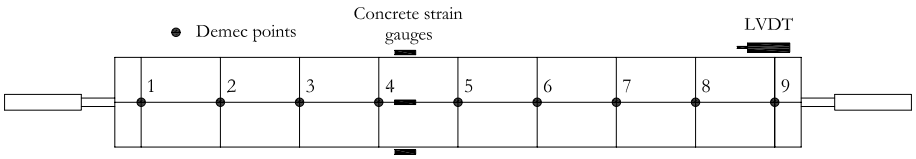

Figure B.8: Instrumentation (tie 16-170).

Load P	ΔL between demec points (mm)							
(kN)	1-2	2-3	3-4	4-5	5-6	6-7	7-8	8-9
0	0	0	0	0	0	0	0	0
2.74	0	0.0016	-0.016	0	0.0096	0.0016	0.0016	0
29.54	0.0016	0.0096	0	0.0048	0.016	0.008	0.008	0.0032
36.81	0.0032	0.0144	0	0.0048	0.4432	0.0032	0.008	0.0032
41.87	0.0032	0.016	0.7776	0.0032	0.7264	0.0048	0.0096	0.0032
48.28	0.0032	0.0176	0.984	-0.0016	1.1296	0.0016	1.008	0.0016
68.58	0.0048	0.0192	1.5856	0.7376	1.9872	0	1.5984	0.0032
78.93	0.0048	0.0192	1.8912	1.0544	2.24	0.0016	1.9328	0.0016

Table B.3: Length increment between demec points (tie 16-170).

Load P	Crack width (mm)						
(kN)	1^{st} crack	2^{nd} crack	3^{rd} crack	4^{th} crack	Max.	Min.	Ave.
36.81	0.2	-	-	-	0.2	0.2	0.2
41.87	0.8	0.9	-	-	0.9	0.8	0.85
48.28	1	1.1	1.1	-	1.1	1	1.07
68.58	3.2	1.4	1.6	0.8	3.2	0.8	1.75
78.93	4.1	2.1	1.9	0.7	4.1	0.7	2.2

Table B.4: Crack width measurements with optical magnifier (tie 16-170).

B.3 16-110 RC tie

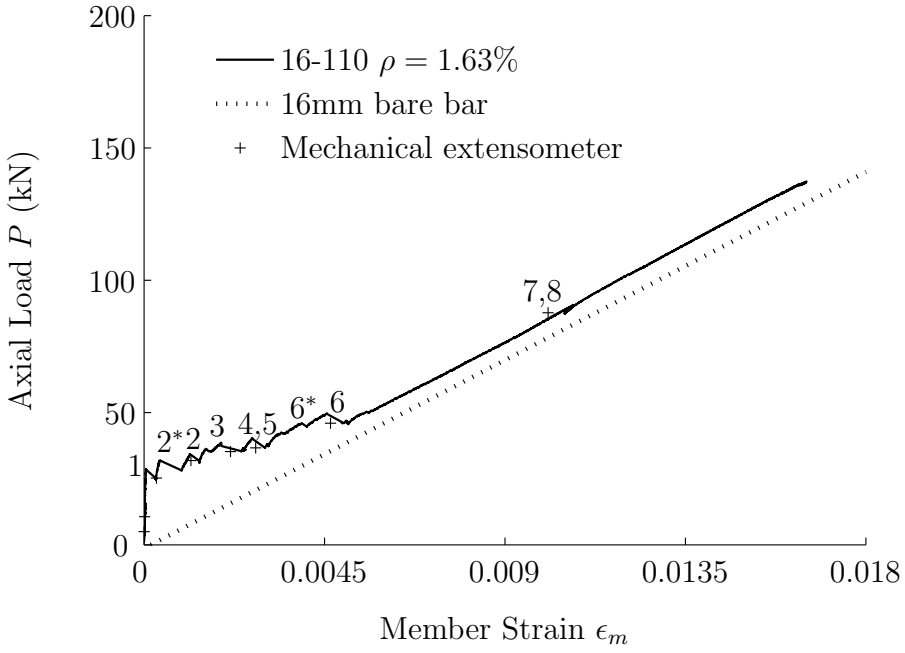

Figure B.9: Load-mean strain relationship (tie 16-110).

Tie failure:

Figure B.10: Image final crack pattern (tie 16-110).

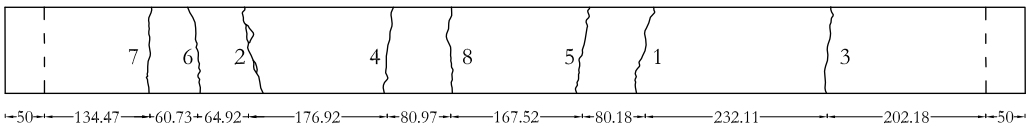

Figure B.11: Cracks number and locations (tie 16-110).

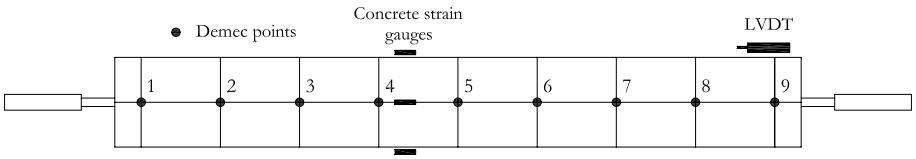

Figure B.12: Instrumentation (tie 16-110).

Load P	ΔL between demec points (mm)							
(kN)	1-2	2-3	3-4	4-5	5-6	6-7	7-8	8-9
0	0	0	0	0	0	0	0	0
5.31	0	0	0	0	0	0	0	0
10.56	0	0.0016	0.0032	0.0032	0.0064	0	0.0016	0.0016
25.15	0.0032	0.0048	0.008	0.0032	-0.0016	0.3456	0.0048	0.0032
31.68	0.0048	0.64	-0.0016	0.0048	-0.0224	0.7696	0.0048	0.0032
36.08	0.0048	0.8272	-0.0016	0.0064	0.152	1.1536	0.4496	-0.0016
37.76	0.0048	0.8304	0.6704	-0.0032	0.3216	1.0432	0.472	0.0016
46.18	-0.0096	1.744	1.3584	-0.0304	0.4816	1.2176	0.8512	-0.0288
87.69	0.7744	2.7232	2.7328	0.4368	0.9488	2.4144	2.112	-0.0496

Table B.5: Length increment between demec points (tie 16-110).

Load P	Crack width (mm)										
(kN)	1^{st}	2^{nd}	3^{rd}	4^{th}	5^{th}	6^{th}	7^{th}	8^{th}	Max.	Min.	Ave.
25.15	0.4	-	-	-	-	-	-	-	0.4	0.4	0.4
31.68	0.8	0.7	-	-	-	-	-	-	0.8	0.7	0.75
36.08	1.6	0.8	0.4	-	-	-	-	-	1.6	0.4	0.93
37.76	1.1	0.7	0.5	0.7	0.2	-	-	-	1.1	0.2	0.64
46.18	1.6	1.3	0.8	1.2	0.5	0.2	-	-	1.6	0.2	0.93
87.69	2.5	1.9	1.9	3	1.1	0.7	0.7	0.3	3	0.3	1.513

Table B.6: Crack width measurements with optical magnifier (tie 16-110).

B.4 19-170 RC tie

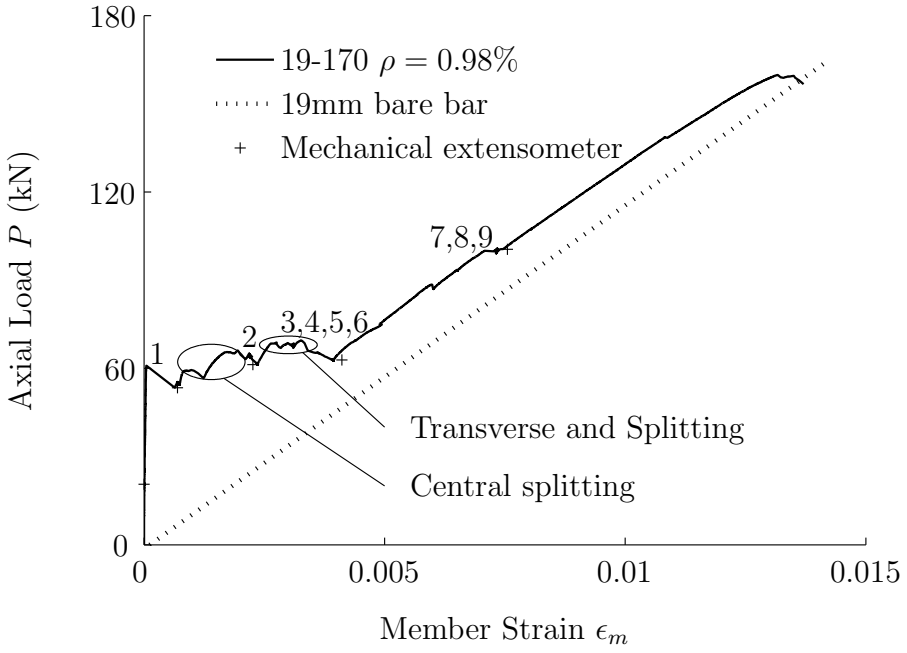

Figure B.13: Load-mean strain relationship (tie 19-170).

Tie failure:

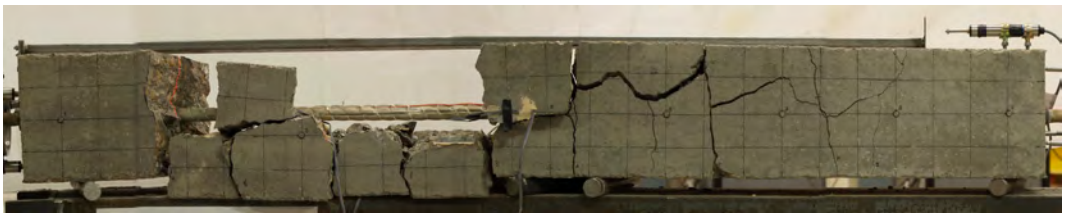

Figure B.14: Image final crack pattern (tie 19-170).

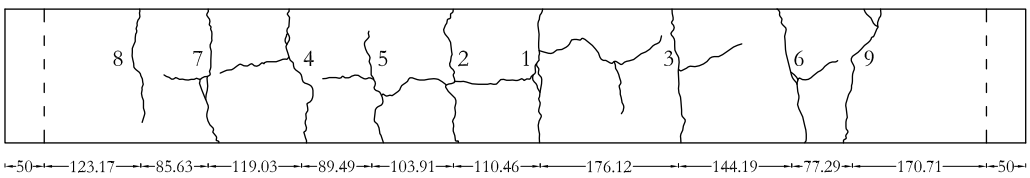

Figure B.15: Cracks number and locations (tie 19-170).

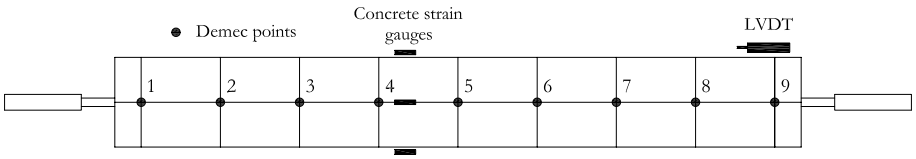

Figure B.16: Instrumentation (tie 19-170).

Load P	ΔL between demec points (mm)							
(kN)	1-2	2-3	3-4	4-5	5-6	6-7	7-8	8-9
20.60	0	0	0	0	0	0	0	0
54.90	0.0016	0.0048	0.0064	0.0032	0.8112	-0.0016	0.0084	0.0032
61.53	0	0.0048	0.0928	0.6928	1.9712	-0.0528	0	0.0048
62.84	0.0016	0.1536	0.7888	0.9008	1.6816	0.7312	0.6864	-0.008
100.23	0.4256	0.6864	1.2608	1.2544	2.36	0.992	2.0704	0.0112

Table B.7: Length increment between demec points (tie 19-170).

Load P	Crack width (mm)											
(kN)	1^{st}	2^{nd}	3^{rd}	4^{th}	5^{th}	6^{th}	7^{th}	8^{th}	9^{th}	Max.	Min.	Ave.
54.90	0.8	-	-	-	-	-	-	-	-	0.8	0.8	0.8
61.53	2	0.5	-	-	-	-	-	-	-	2	0.5	1.25
62.84	1.7	1.2	0.6	0.5	0.3	0.6	-	-	-	1.7	0.3	0.817
100.23	2.2	1.2	1.1	1.1	0.4	0.4	0.4	0.3	1.7	2.2	0.3	0.978

Table B.8: Crack width measurements with optical magnifier (tie 19-170).

B.5 16-170-2 RC tie

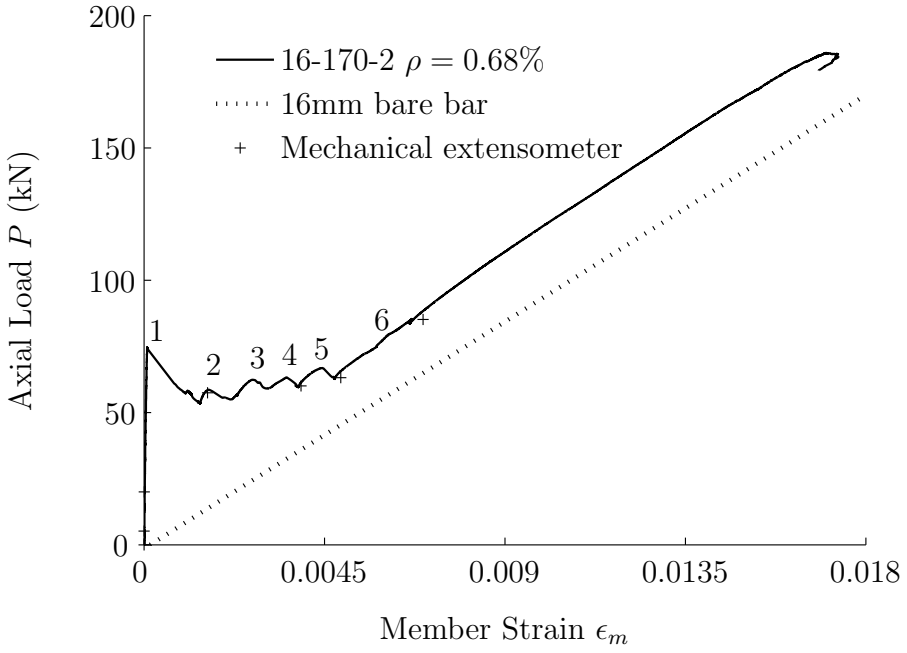

Figure B.17: Load-mean strain relationship (tie 16-170-2).

Tie failure:

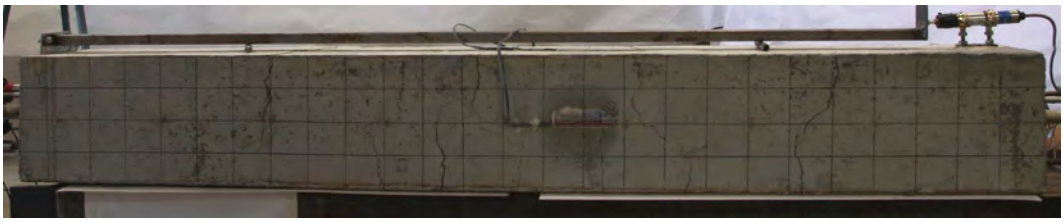

Figure B.18: Image final crack pattern (tie 16-170-2).

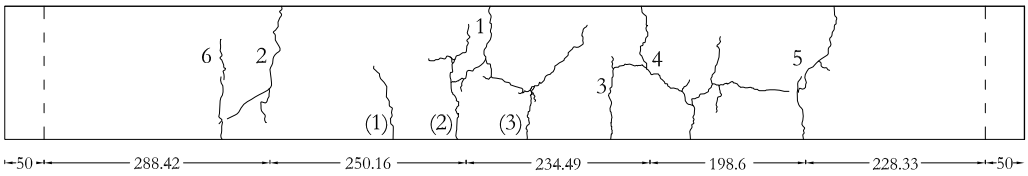

Figure B.19: Cracks number and locations (tie 16-170-2).

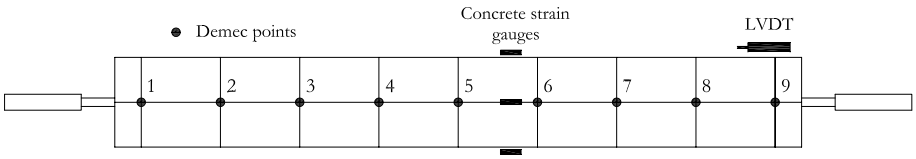

Figure B.20: Instrumentation (tie 16-170-2).

Load P	ΔL between demec points (mm)							
(kN)	1-2	2-3	3-4	4-5	5-6	6-7	7-8	8-9
0	0	0	0	0	0	0	0	0
5.19	0.0016	0.0016	-0.0016	0.0048	-0.0016	0	0	0.0032
20.02	0.0016	0.0016	0	0.016	-0.0176	0.0016	0.0032	0
57.47	.00640	0.0176	0.0732	1.5472	0.0256	0.0144	0.0096	0.0096
60.03	0.0032	0.896	0.5248	1.7488	0.6416	0.7088	0.0048	0.0064
63.18	0.0064	0.9824	0.5552	1.616	0.7344	0.928	1.3168	0.0048
85.12	0.0048	1.616	0.7264	2.2976	0.8848	1.2512	1.688	0.0032

Table B.9: Length increment between demec points (tie 16-170-2).

Load P	Crack width (mm)								
(kN)	1^{st}	2^{nd}	3^{rd}	4^{th}	5^{th}	6^{th}	Max.	Min.	Ave.
57.47	1.5	-	-	-	-	-	1.5	1.5	1.5
60.03	1.7	1	0.5	0.6	-	-	1.7	0.5	0.95
63.18	1.7	0.8	0.5	1	1.4	-	1.7	0.5	1.08
85.12	2.3	1.1	0.5	0.9	1.3	0.2	2.3	0.5	1.05

Table B.10: Crack width measurements with optical magnifier (tie 16-170-2).